Exciton Coupling in Homo- and Heterostacks of Merocyanine and Perylene Bisimide Dyes

Dissertation zur Erlangung des
naturwissenschaftlichen Doktorgrades
der Julius-Maximilians-Universität Würzburg

vorgelegt von
David Bialas
aus Würzburg

Würzburg 2017

Eingereicht bei der Fakultät für Chemie und Pharmazie am:

_____

Gutachter der schriftlichen Arbeit:

1. Gutachter: Prof. Dr. Frank Würthner

2. Gutachter:

Prüfer des öffentlichen Promotionskolloquiums

1. Prüfer:

2. Prüfer:

3. Prüfer:

Datum des öffentlichen Promotionskolloquiums:

_____

Doktorurkunde ausgehändigt am:

_____

Für meine Familie

Abbreviations

BODIPY	boron-dipyrromethene
br	broad
COSY	correlation spectroscopy
CP	cyclophane
CPK model	space-filling model
d	doublet
DCM	dichloromethane
dd	doublet of doublets
DFT	density functional theory
DMAP	4-dimethylaminopyridine
DMF	dimethylformamide
DNA	deoxyribonucleic acid
EDC	*N*-(3-dimethylaminopropyl)-*N*'-ethylcarbodiimide
ESI	electrospray ionization
GPC	gel permeation chromatography
h	hour
HOMO	highest occupied molecular orbital
HRMS	high-resolution mass spectrometry
HSQC	heteronuclear single quantum coherence
IC	internal conversion
ISC	intersystem crossing
LUMO	lowest unoccupied molecular orbital
m	multiplet
MCH	methylcyclohexane
min	minute
mp	melting point
NIR	near-infrared
NMR	nuclear magnetic resonance
NOESY	nuclear Overhauser effect spectroscopy
PBI	perylene bisimide
PCBM	[6,6]-phenyl-C_{61}-butyric acid methyl ester
ppm	parts per million

q	quartet
ROESY	rotating-frame Overhauser enhancement spectroscopy
rt	room temperature
s	singlet
SQ	squaraine
t	triplet
THF	tetrahydrofuran
TDDFT	time-dependent density functional theory
Ts	tosyl
UV/Vis	ultraviolet-visible

Table of Content

Chapter 1

Aim of the Thesis

About 80 years ago, the scientists Scheibe[1, 2] and Jelley[3, 4] made independently the unexpected observation that a concentrated aqueous solution of pseudoisocyanine chloride showed considerably different optical absorption bands compared to those observed for a solution of this dye in ethanol. Scheibe correctly ascribed these spectral changes to the formation of dye aggregates in water and proposed a 'vicinity effect' of the adjacent dyes.[1, 2] Nowadays, it is known that the spectral changes of dyes upon aggregation are caused by an electronic coupling between the constituent chromophores, which can be explained by the molecular exciton theory developed by Davydov[5] and Kasha[6-8] in the 1960s. Accordingly, dye aggregates can be classified as H- and J-aggregates depending on the arrangements of the chromophores which exhibit different optical properties, namely a hypsochromic (H-aggregate) or bathochromic shift (J-aggregate) of the absorption band compared to the respective monomer band.[9] Thus, it is possible to gain structural information on the arrangements of the chromophores within dye aggregates based on the spectral changes observed upon aggregation. In addition, so-called 'exciton coupling' not only affects the optical properties of dye aggregates but also enables coherent energy transport between chromophores as observed in the natural light-harvesting systems.[10, 11] Furthermore, various functional properties of organic semiconductors are affected by exciton coupling that are relevant for (opto-)electronic and photovoltaic applications.[12, 13] Therefore, much efforts have been made for the investigation of exciton coupling in order to gain insight into functional properties and structural information of dye aggregates.[14-19] Remarkably, research in this field remained focused on homoaggregates (*i.e.* aggregates comprising the same type of chromophores), whereas heteroaggregates based on different types of chromophores have rarely been investigated (note that we talk about different types of chromophores if there is a difference in the excited state energies of the monomeric chromophores).[20, 21] The reason why heteroaggregates have so far experienced considerably less attention than homoaggregates might be the synthetic challenges arising from the tendency of many chromophores to undergo narcissistic self-sorting, resulting in the preferential formation of homoaggregates.[22] In addition, an unequivocal characterization of the supramolecular structures of heteroaggregates is

challenging.[20, 23] However, dye aggregates comprising different types of chromophores may have exceptional properties that cannot be obtained upon self-assembly of the same type of chromophores into homoaggregates.[24, 25]

It is a common perception that exciton coupling between different types of chromophores is weak, resulting in insignificant spectral differences compared to the absorption spectra of the constituent chromophores.[26] Pronounced spectral changes upon aggregation are supposed to arise from exciton coupling only between the same type of chromophores within the heteroaggregates.[27] However, optical evidence for strong exciton coupling between different types of chromophores was obtained for mixed films composed of different dyes[28, 29] as well as for head-to-tail connected squaraine dye copolymers.[30] These examples illustrate an ambiguous state of knowledge for the exciton coupling in heteroaggregates.

Therefore, the main goal of this thesis was to gain further insight into the exciton coupling between different types of chromophores. For this purpose π-stacked dyes with distinct orientations of the chromophores are required. However, this is very challenging for supramolecular dye aggregates based on π-π-interactions since the prevailing dispersion interactions allow multiple arrangements of the chromophores with similar energies.[31, 32]

The class of merocyanine dyes are promising candidates towards this approach due to the high directionality of the intermolecular dipole-dipole interaction arising from their strong dipolar character.[33] Accordingly, these dyes form dimer aggregates in non-polar solvents with an antiparallel orientation of the ground state dipole moments. These well-defined aggregates can be used as model systems to elucidate the exciton coupling in heteroaggregates. Moreover, merocyanines exhibit intense, sharp absorption bands without pronounced vibronic progressions, which enables easy monitoring of the self-assembly process by UV/Vis spectroscopy.[34] However, since this class of dyes tends to undergo narcissistic self-sorting leading to homoaggregates (Figure 1a), sophisticated self-assembly strategies are necessary in order to obtain heteroaggregates. Based on earlier work on spacer-modulated differentiation between self-assembly and folding pathways for bis(merocyanine) dyes,[35] the linkage of two merocyanine chromophores with different conjugation length by appropriate spacer units was envisaged to obtain heteroaggregates of different size (Figure 1b). The optical absorption properties of these systems should be investigated by UV/Vis spectroscopy and rationalized by quantum chemical analysis. For

comparison, the optical properties of the homoaggregates of the respective bis(merocyanine) dyes comprising the same type of chromophores are also elucidated.

With the insights gained from the studies on merocyanine heteroaggregates, the exciton coupling between different types of perylene-3,4:9,10-bis(dicarboximide) (in short perylene bisimides; PBIs) chromophores within rigid cyclophanes has been approached. This class of dyes shows high potential for applications in organic electronics[36, 37] and photovoltaics[38, 39] due to their outstanding optical and electronic features. In contrast to merocyanines, the UV/Vis absorption spectra of PBI dyes usually show pronounced vibronic progressions leading to an exciton-vibrational coupling within PBI aggregates.[40, 41] Hence, quantum dynamical studies are necessary to gain insight into the optical properties of PBI aggregates.

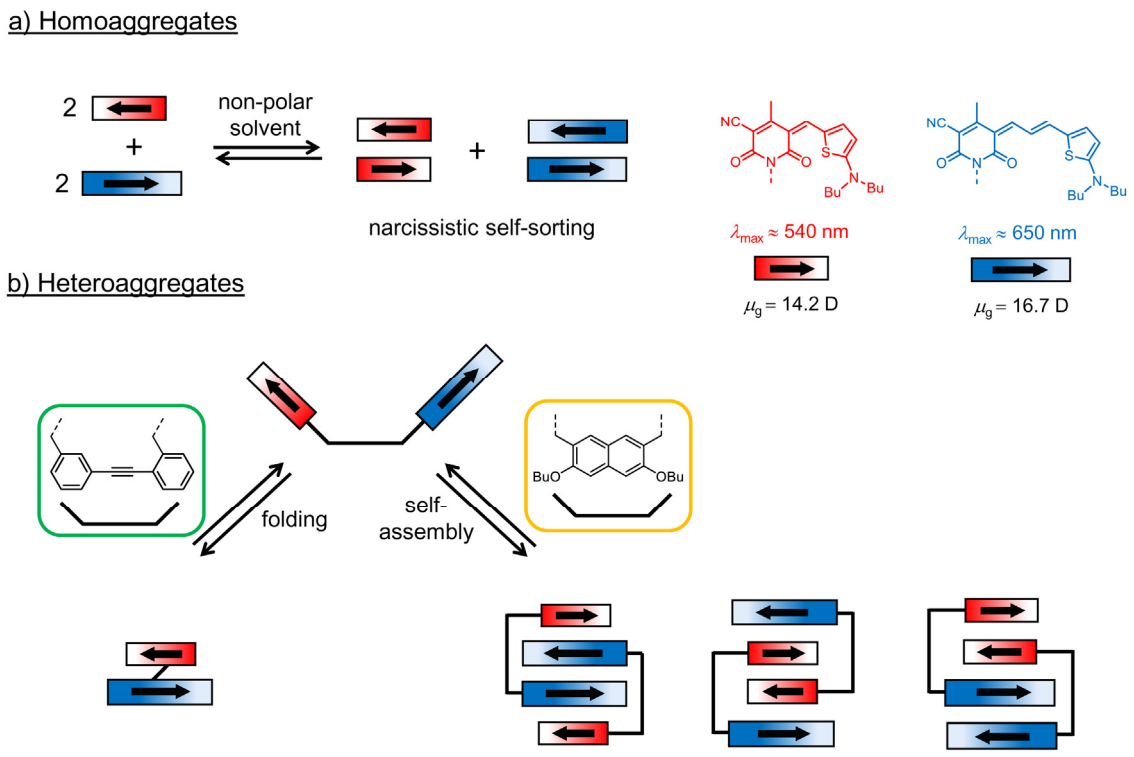

Figure 1. a) Schematic illustration of the narcissistic self-sorting of two different types of merocyanine chromophores resulting in the formation of homoaggregates. b) Folding (left) and self-assembly (right) of bis(merocyanine) dyes into double and quadruple dye stacks comprising different types of chromophores. The bold arrows illustrate the ground state dipole moments of the chromophores.

Finally, an additional goal was to construct well-defined supramolecular p/n-heterojunctions in solution based on bis(merocyanine)-C_{60} conjugates. These structures should serve as model systems for organic photovoltaics enabling studies on the

photoinduced electron transfer from the dye stack to the fullerene moieties by time-resolved transient absorption spectroscopy. This process represents a key step for the generation of charge carriers in organic photovoltaics and significantly affects the power conversion efficiency of the devices.[42]

Chapter 2 gives a short introduction into molecular exciton theory and the concept of the classification of dye aggregates into H- and J-aggregates is explained. Afterwards, further developments of the exciton theory, including the consideration of vibrational coupling in homoaggregates, are presented. The last part of this chapter deals with exciton coupling in multichromophoric systems comprising different types of chromophores.

Chapter 3 describes the synthesis and aggregation studies by UV/Vis spectroscopy of a bis(merocyanine) foldamer comprising different types of chromophores. The results obtained by quantum chemical analysis are discussed in comparison to the respective bis(merocyanine) dye comprising the same type of chromophores.

Chapter 4 deals with larger heteroaggregates obtained by self-assembly of a newly synthesized bis(merocyanine) dye in which two different types of chromophores are linked by a naphthalene unit. The optical properties of these quadruple dye stacks are compared to the ones formed upon self-assembly of the analogous bis(merocyanine) dye containing two identical chromophores.

In **Chapter 5** the exciton-vibrational coupling between same and different types of PBI chromophores, respectively, within rigid PBI cyclophanes are investigated.

Chapter 6 describes the synthesis and characterization of bis(merocyanine)-C_{60} conjugates and their self-assembly into well-defined supramolecular p/n-heterojunctions. Further, the results obtained from time-resolved femtosecond transient absorption spectroscopy of these systems are presented.

Chapter 7 summarizes the results of this thesis in English and German.

Chapter 2
Exciton Coupling in Dye Aggregates

Abstract: This chapter provides an overview on the formation of exciton states by the coupling of closely arranged chromophores, which significantly influences the optical properties of dye aggregates. First an introduction to Kasha's exciton theory is given that established structure-property relationships for homoaggregates, *i.e.* aggregates comprising the same type of chromophores. Afterwards, further developments of Kasha's theory including more sophisticated models that consider vibrational couplings are addressed. Finally, examples for exciton coupling in multichromophoric systems comprising different types of dyes are discussed. The focus of this state of knowledge chapter is the theoretical analysis of exciton coupling arising from Coulomb interaction between the transition dipole moments of the chromophores in dye aggregates.

2.1 Kasha's Exciton Theory

In the 1960s Davydov developed the molecular exciton theory to describe the optical properties of organic molecular crystals and could explain the characteristic line splitting (Davydov splitting) observed in the absorption spectra of the crystals.[5] In this model an excited molecule is treated as a Frenkel exciton, which represents a strongly Coulomb bound electron hole pair.[43] In a simplified picture, excitation leads to a state in which an electron is located in the lowest unoccupied molecular orbital (LUMO) and the corresponding hole in the highest occupied molecular orbital (HOMO). Due to intermolecular interactions the excitation is delocalized resulting in changes of the photophysical properties with respect to the isolated molecules. Kasha refined this model towards dye aggregates in solution and established structure-property relationships for dye assemblies.[6-8] In the following, the basic concept of Kasha's exciton theory will be explained for a dimer, which represents a most simple case. At this point we want to emphasize that this model was originally only applied to homoaggregates, *i.e.* aggregates comprising the same type of chromophores.

Under the assumption that the Born-Oppenheimer approximation is valid one can separate the nuclear and electronic wave functions.[44] In the following, only the electronic wave functions are considered. Then, the ground state wave function of a dimer (Φ_g) consisting of two identical chromophores 1 and 2 can be written as

$$\Phi_g = \varphi_1\varphi_2, \tag{1}$$

where φ_1 is the ground state wave function of chromophore 1 and φ_2 the ground state wave function of chromophore 2. The Hamiltonian $\hat{H}$ of the dimer is described as

$$\hat{H} = \hat{H}_1 + \hat{H}_2 + \hat{V}_{12} \tag{2}$$

with $\hat{H}_1$ and $\hat{H}_2$ being the Hamiltonians of the isolated chromophores 1 and 2, respectively, and $\hat{V}_{12}$ is a perturbation between both molecules. The ground state energy E_g of the dimer is obtained by applying the Hamiltonian on the ground state wave function:

$$\hat{H}\Phi_g = E_g\Phi_g. \tag{3}$$

In this way, we obtain for the ground state energy:

$$E_g = E_1 + E_2 + E_{vdW} \tag{4}$$

with $E_1 = \int\varphi_1\hat{H}\varphi_1 d\tau_1$ and $E_2 = \int\varphi_2\hat{H}\varphi_2 d\tau_2$ as the ground state energies of the isolated chromophores 1 and 2, respectively, and the van-der-Waals interaction energy E_{vdW} of the chromophores in the ground state, which corresponds to an energy lowering:

$$E_{vdW} = \iint\varphi_1\varphi_2\hat{V}_{12}\varphi_1\varphi_2 d\tau_1 d\tau_2. \tag{5}$$

The exciton wave function (Φ_e) of the dimer is written as

$$\Phi_e = c_1\,\varphi_1^*\varphi_2 + c_2\,\varphi_1\varphi_2^*, \tag{6}$$

where φ_1^* and φ_2^* represent localized excitations described by the excited state wave functions of the chromophores 1 and 2 with energies E_1^* and E_2^* (note that both energies are equal for the here discussed homodimer). Hence, the exciton state can be described as a linear combination of the two states where one of the chromophores is excited while the other one is in its ground state. By applying the Hamiltonian on the exciton wave function

$$\hat{H}\Phi_e = E_e\Phi_e \tag{7}$$

we obtain the eigenvalue equation for the dimer:

$$\begin{pmatrix} H_{11} & H_{12} \\ H_{12} & H_{11} \end{pmatrix}\begin{pmatrix} c_1 \\ c_2 \end{pmatrix} = E_e\begin{pmatrix} c_1 \\ c_2 \end{pmatrix} \tag{8}$$

with

$H_{11} = \iint\varphi_1^*\varphi_2\hat{H}\varphi_1^*\varphi_2 d\tau_1 d\tau_2$

$H_{12} = \iint\varphi_1^*\varphi_2\hat{H}\varphi_1\varphi_2^* d\tau_1 d\tau_2.$

The eigenvalues of the Hamiltonian matrix in equation (8) represent the two exciton state energies of the dimer:

$$E_e = E_1^* + E_1 + \iint\varphi_1^*\varphi_2\hat{V}_{12}\varphi_1^*\varphi_2 d\tau_1 d\tau_2 \pm \iint\varphi_1^*\varphi_2\hat{V}_{12}\varphi_1\varphi_2^* d\tau_1 d\tau_2. \tag{9}$$

The energy contribution $\iint\varphi_1^*\varphi_2\hat{V}_{12}\varphi_1^*\varphi_2 d\tau_1 d\tau_2$ can be interpreted as the van-der-Waals interaction between excited chromophore 1 and chromophore 2 in its ground state. The last term $\iint\varphi_1^*\varphi_2\hat{V}_{12}\varphi_1\varphi_2^* d\tau_1 d\tau_2$ is the so-called exciton coupling energy and, in the

following, denoted as J. This energy contribution arises from the exchange of excitation energy between the two chromophores and the energy difference between both exciton states (Davydov splitting)[5] amounts to $2J$.

The energy of the transition from the ground state to the exciton states (E_{eg}) is expressed by

$$E_{eg} = E_1^* - E_1 + \Delta E_{vdW} \pm J \tag{10}$$

with $\Delta E_{vdW} = \iint \varphi_1^* \varphi_2 \hat{V}_{12} \varphi_1^* \varphi_2 d\tau_1 d\tau_2 - \iint \varphi_1 \varphi_2 \hat{V}_{12} \varphi_1 \varphi_2 d\tau_1 d\tau_2$ as the difference of the van-der-Waals energies in the excited and ground state. This term is often assumed to be negative due to a larger polarizability of many π-conjugated chromophores in the excited than in the ground state,[45, 46] which results in larger intermolecular dispersion interactions in the excited state. However, solvatochromic effects may have a strong influence on the excitation energies in particular for dipolar chromophores such as merocyanines that is not taken into consideration by equation (10).

Kasha described the exciton coupling by the Coulomb interaction between the transition dipole moments $\boldsymbol{\mu}_{eg}$ of the chromophores and suggested the calculation of the exciton coupling energy by considering the point-dipole approximation. Assuming that the transition dipole moments of both chromophores are aligned in parallel planes, the exciton coupling energy can be calculated by

$$J = \frac{\mu_{eg}^2}{4\pi\varepsilon_0 r^3} (\cos\alpha - 3\cos\Theta_1 \cos\Theta_2), \tag{11}$$

where r is the center-to-center distance, α the rotational angle, and Θ_1 and Θ_2 are the slip angles of the transition dipole moments as depicted in Figure 2 and Figure 3. ε_0 is the vacuum permittivity. Hence, in addition to the magnitude of the square of the transition dipole moment the exciton coupling energy also depends on the arrangements of the chromophores, which significantly influences the absorption spectra of dye aggregates.

Figure 2a shows the exciton state diagram for parallel arrangements ($\alpha = 0°$) of the transition dipole moments as a function of the slip angle Θ ($\Theta_1 = \Theta_2$) at constant center-to-center distance r of the transition dipole moments. This representation is often used in the literature to explain the absorption properties of H- and J-aggregates despite the fact that it does not take into account the structural features of dye molecules (see later).[8, 47, 48]

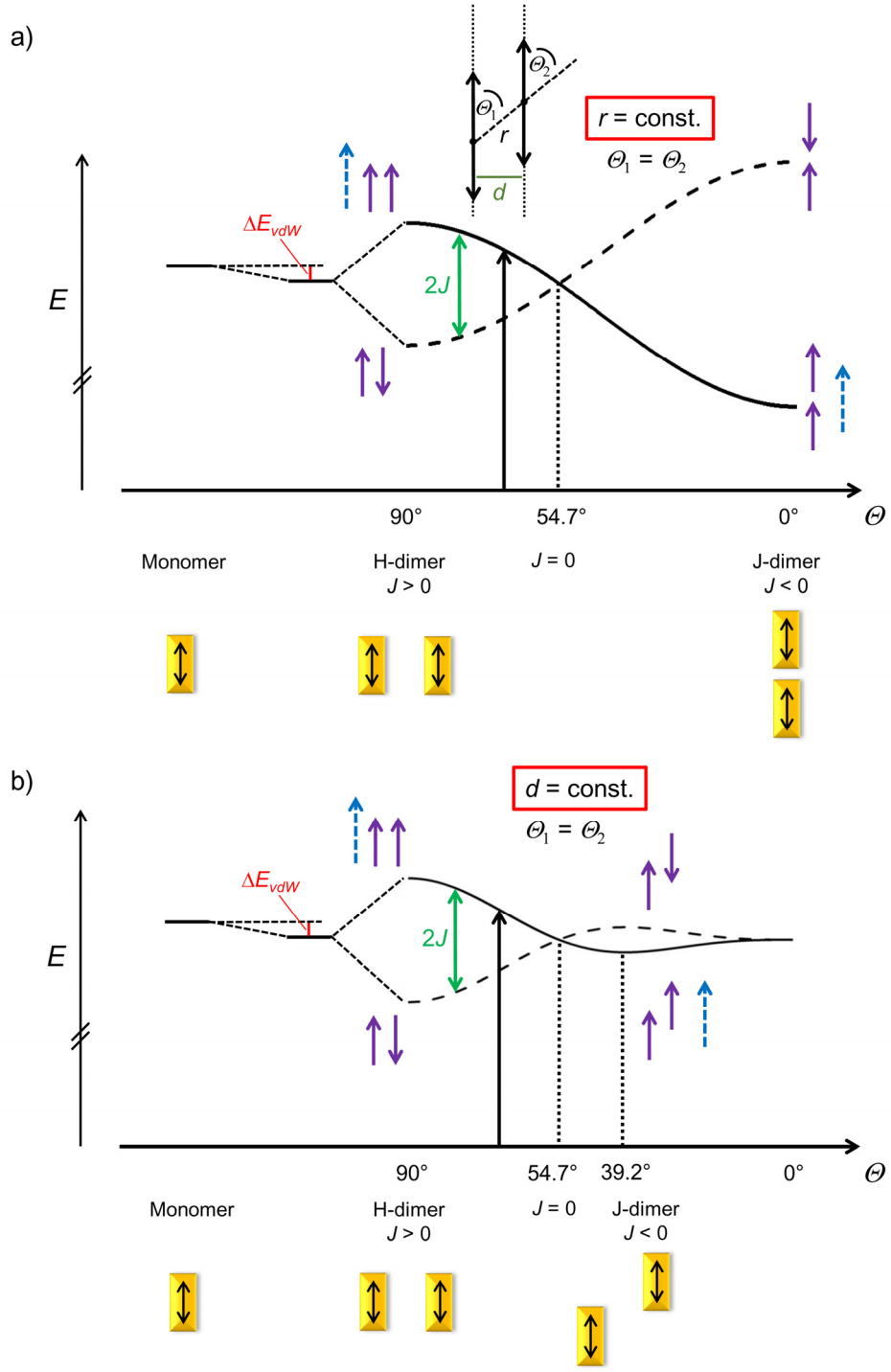

Figure 2. Exciton state diagram for two coupled transition dipole moments with linear alignment according to the point-dipole approximation. The dependence of the energy splitting from the slip angle Θ at a) fixed center-to-center distance r and b) fixed distance d between the axes of the transition dipole moments is shown. The black double arrows represent transition dipole moments and the violet arrows indicate their phase relations. In addition, the blue dashed arrows represent the overall transition dipole moments obtained by vector addition, black arrows indicate allowed transitions and J denotes the exciton coupling energy. ΔE_{vdw} is the energy stabilization due to van-der-Waals interactions.

Note that the ground state energy in Figure 2 is kept fixed and that the energy stabilization due to van-der-Waals interactions is displayed as a ΔE_{vdW} term. For a sandwich-type arrangement with parallel alignment of the transition dipole moments ($\Theta = 90°$) the exciton coupling energy J is positive according to equation (11). The resulting two exciton states differ in the phase relation of the coupled transition dipole moments. The overall transition dipole moment $\boldsymbol{\mu}_{eg}$ for the transition from the ground state to the respective exciton state of the dimer can be described as a linear combination of the coupled transition dipole moment vectors of the individual chromophores 1 and 2:

$$\boldsymbol{\mu}_{eg} = c_1\boldsymbol{\mu}_{eg,1} + c_2\boldsymbol{\mu}_{eg,2} \tag{12}$$

with the same coefficients c_1 and c_2 as in equation (6) that are obtained by determining the normalized eigenvectors of the Hamiltonian matrix in equation (8). For the lower exciton state the coefficients amount to $c_1 = -c_2 = \frac{1}{\sqrt{2}}$ representing an out-of-phase coupling and thus, the transition is forbidden. In contrast, the higher exciton state is characterized by an in-phase coupling ($c_1 = c_2 = \frac{1}{\sqrt{2}}$) leading to an allowed transition. Accordingly, aggregates in sandwich-type arrangement with parallel transition dipole moments show a hypsochromic shift of the absorption band with respect to the absorption band of the monomeric chromophores and are called H-aggregates (H denotes hypsochromic). This type of aggregates shows a quenching of the fluorescence. After photoexcitation to the highest exciton state, fast internal conversion to the lower exciton state occurs, which is a non-fluorescent dark-state. Thus, H-aggregates usually exhibit low fluorescence quantum yields and a large Stokes shift.[49, 50]

Upon decreasing the slip angle Θ the energy difference $2J$ between the two exciton states is reduced. At a slip angle of $\Theta = 54.7°$ ('magic angle') the exciton coupling energy J amounts to zero resulting in two degenerated exciton states. This situation corresponds to the crossing point in the exciton diagram shown in Figure 2a. In this case, the respective absorption spectrum exhibits only changes due to the van-der-Waals term ΔE_{vdW}. Upon further decreasing the slip angle, the exciton coupling energy J becomes negative. In this case, the higher exciton state shows an out-of-phase coupling of the transition dipole moments resulting in a repulsive Coulomb interaction, whereas the lower exciton state exhibits an in-phase coupling. Thus, the transition to the lower exciton state is strongly allowed while the transition to the higher exciton state is forbidden. As a consequence, the

absorption spectrum shows a bathochromic shift with respect to the absorption band of the monomeric chromophores.[9] These types of aggregates are called Scheibe- or J-aggregates (J denotes Jelley) named after their discoverers Scheibe[1, 2] and Jelley.[3, 4] In contrast to H-aggregates the lowest exciton state may be strongly fluorescent for J-aggregates, which usually results in intense emission bands with a very small Stokes shift.[9]

The problem with the commonly used Figure 2a is that dyes exhibit rather anisotropic shapes. Thus, whilst the close cofacial stacking at van-der-Waals distances of 3.3–3.5 Å is a common situation for many H-aggregates, there are no examples in the literature for J-aggregates composed of dyes at such close proximities because strong coupling requires large transition dipoles that are only given for extended π-systems. To comply with structural features of dye molecules we have accordingly added Figure 2b where the π-π-stacking distance is kept constant whilst the dyes are slipped with regard to each other. Accordingly, for J-aggregates a maximum of the energy splitting is observed at a slip angle of $\Theta = 39.2°$. For smaller Θ the Davydov splitting is reduced due to the increase of the center-to-center distance r of the transition dipole moments (equation (11)). For very large distances r ($\Theta \approx 0°$) no splitting is observed and the two chromophores can be described as isolated, non-interacting systems. It is apparent from Figure 2b that for a fixed distance d of the axes of the transition dipole moments the maximum exciton coupling energy is larger for H-aggregates than for J-aggregates. This is vice versa for the situation described in Figure 2a, where the maximum exciton coupling energy is significantly higher for J-aggregates which might lead to the wrong conclusion that exciton coupling is stronger in J-aggregates. This is only true for the same center-to-center distance r which is not realized in most dye aggregates. For chromophores with extended size, a head-to-tail arrangement usually exhibits larger distances r whereas a face-to-face orientation allows a π-π-stacking at short van-der-Waals distance. This short distance results in much stronger exciton coupling in H-aggregates than in the respective J-aggregates. It is striking that in Figure 2b only modest bathochromic shifts become possible by exciton coupling and that a significant contribution to the observed spectral shift may be attributed to the van-der-Waals term ΔE_{vdW}.

So far only linear arrangements ($\alpha = 0°$) of the transition dipole moments have been discussed leading to situations where only one of the two transitions is allowed (Figure 2). This is different in the case of oblique transition dipole moments ($\alpha \neq 0°$) as displayed in Figure 3. Here, the exciton state diagram for two transition dipole moments as a function

of the rotational angle α without transversal shift ($\Theta_1 = \Theta_2 = 90°$) is displayed. As dicussed above, for $\alpha = 0°$ two non-degenerated exciton states are present and only the transition to the highest exciton state is allowed. Upon increasing the rotational angle the exciton coupling energy J is decreasing, leading to a lower energy gap between both exciton states.[6] The overall transition dipole moment obtained by vector addition of the individual transition dipole moments is now different to zero for both exciton states. This results in two absorption bands in the absorption spectrum with a hypsochromic and a bathochromic shift with respect to the monomer absorption band.[35, 51, 52] For $\alpha = 90°$ the exciton splitting energy is zero resulting in two degenerated states as in the case of two parallelly aligned transition dipole moments under magic angle ($\Theta_1 = \Theta_2 = 54.7°$) but now both transitions are allowed.

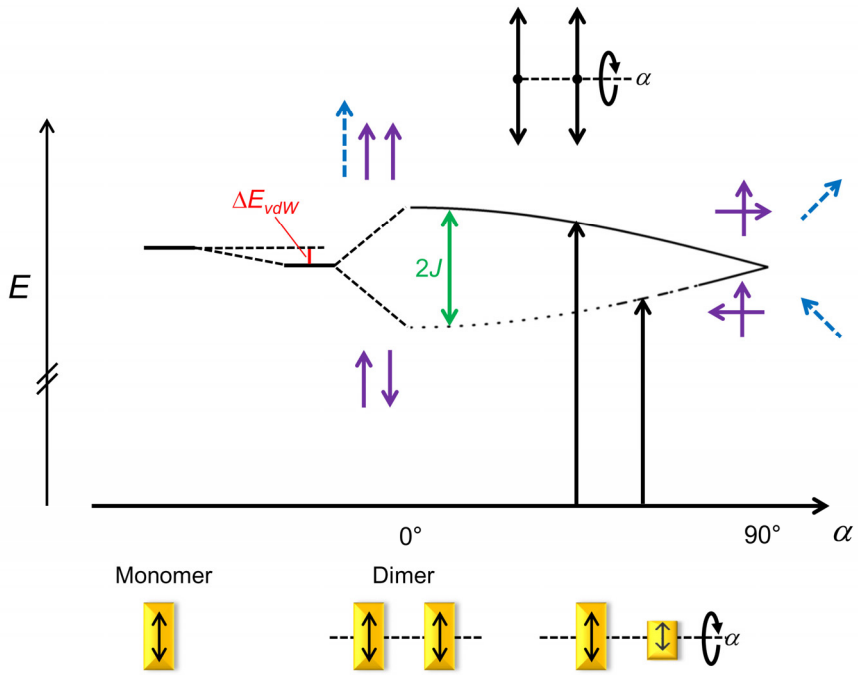

Figure 3. Exciton state diagram for two coupled transition dipole moments as a function of the rotation angle α according to the point-dipole approximation. The black double arrows represent transition dipole moments and the violet arrows indicate the phase relation between the coupled transition dipole moments. In addition, the blue dashed arrows represent the overall transition dipole moments obtained by vector addition and J denotes the exciton coupling energy. ΔE_{vdw} is the energy stabilization due to van-der-Waals interactions.

2.2 Further Development of Kasha's Exciton Theory

2.2.1 Transition Charges

Within Kasha's exciton theory the exciton coupling energy is determined by applying the point-dipole approximation assuming a Coulomb interaction between the transition dipole moments.[8] However, this approximation is only valid for distances between the chromophores that exceed the spatial extent of the transition dipole moment.[53] To adequately describe the exciton coupling for small distances one has to consider the dimension of the chromophores. Consequently, more sophisticated methods have been developed. The simplest one is the so-called extended dipole model developed by Kuhn *et al.*[54] Here, the transition dipole moment of a molecule is replaced by two transition charges $+q$ and $-q$ having a distance l (Figure 4), so that the following criterion is fulfilled:

$$\mu_{eg} = ql. \tag{13}$$

The exciton coupling energy is then defined as the Coulomb interaction energy between the respective transition charges:

$$J = \frac{q^2}{4\pi\varepsilon_0}\left(\frac{1}{r_1} + \frac{1}{r_2} - \frac{1}{r_3} - \frac{1}{r_4}\right), \tag{14}$$

where r_1, r_2, r_3 and r_4 are the distances between the charges as displayed in Figure 4. This model was applied to cyanine dyes with different arrangements and the results were compared to the values obtained by quantum mechanical calculations.[54] Accordingly, even at a small centre-to-centre distance of 3 Å the values were in good agreement with quantum mechanical calculations, while the point-dipole approximation overestimated the exciton coupling energy dramatically.

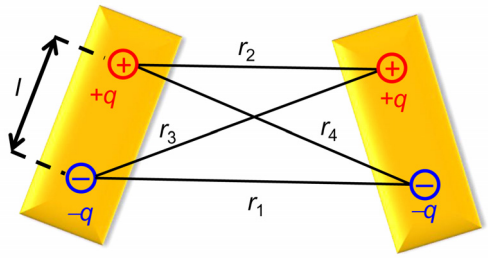

Figure 4. Determination of the exciton coupling energy between two chromophores according to the extended dipole approximation.[54] The exciton coupling energy corresponds to the Coulomb interaction energy between the respective charges of the different chromophores.

Higher accuracy is obtained by increasing the amount of transition charges for each chromophore using atomic partial charges. The transition charges have to adequately describe the transition dipole moment $\boldsymbol{\mu}_{eg}$ of the chromophores:[55, 56]

$$\boldsymbol{\mu}_{eg} = \sum_i q_i \mathbf{r}_i \tag{15}$$

with q_i being the transition charge on atom i and $\mathbf{r}_i$ the position vector of the respective atom. The transition charges nowadays can be obtained quite easily from the transition density provided by quantum mechanical calculations by fitting atomic charges to reproduce the transition density.[57]

Like in the case of the extended dipole approximation, in this approach the exciton coupling is determined by calculating the Coulomb interaction energy between the transition charges of the chromophores 1 and 2:

$$J = \frac{1}{4\pi\varepsilon_0} \sum_i \sum_j \frac{q_i^{(1)} \cdot q_j^{(2)}}{|\mathbf{r}_i^{(1)} - \mathbf{r}_j^{(2)}|}. \tag{16}$$

In this way, the exciton coupling energy between chromophores with short distance can be calculated with significantly higher accuracy compared to the point-dipole approximation.[19, 57, 58]

2.2.2 Exciton-Vibrational Coupling

The spectral changes upon aggregation can provide insight into the arrangement of chromophores in dye assemblies, which allows the elucidation of structure-property relationships. However, this is much more difficult for chromophores exhibiting pronounced vibronic progressions in the monomeric absorption spectra. Due to the coupling between electronic and vibrational transitions, the spectral changes upon aggregation of these dyes are more complex. In this case, the Born-Oppenheimer approximation breaks down and one has to take into account the vibrational degrees of freedom of the chromophores to adequately describe the absorption spectra of dye assemblies.[59, 60] Accordingly, the monomer can be described as

$$H_g = |g\rangle \hat{H}_g \langle g| + |e\rangle \hat{H}_e \langle e|, \tag{17}$$

where $\hat{H}_g$ is the vibrational Hamiltonian for the electronic ground state $|g\rangle$ (in Dirac notation) within the harmonic approximation:

$$\hat{H}_g = -\frac{1}{2}\frac{d^2}{dx^2} + \frac{1}{2}\omega^2 x^2 \tag{18}$$

with x being a scaled coordinate and ω the oscillator frequency of the vibration that induces the vibronic progression in the absorption spectrum.

The vibrational Hamiltonian for the electronic excited state |e> of the monomer can be written as

$$\hat{H}_e = -\frac{1}{2}\frac{d^2}{dx^2} + \frac{1}{2}\omega^2 (x - x_e)^2 + \Delta E_m \tag{19}$$

assuming the same vibrational frequency ω in the excited and ground state. The excited state potential is shifted by the equilibrium distance x_e and by the excitation energy ΔE_m with respect to the ground state potential. The equilibrium distance is related to the so-called Huang-Rhys factor ξ as $x_e = \xi\sqrt{\frac{2}{\omega}}$. The absorption spectrum is obtained by a Fourier transform of the calculated time-dependent function[61]:

$$\sigma(E) \sim \int dt\, e^{iEt} \langle \hat{\mu}_{eg} \Psi_0 | e^{-i\hat{H}_e t}\, \hat{\mu}_{eg}\, \Psi_0 \rangle\, w(t) \tag{20}$$

with Ψ_0 being the wave function of the vibronic ground state, $\hat{\mu}_{eg}$ is the transition dipole moment operator and $\hat{H}_e$ the excited state Hamiltonian. Furthermore, E is the photon energy and w(t) a Gaussian window function which leads to a finite width of the spectral lines.

With this model the vibronic progression of chromophores can be simulated as shown in Figure 5b for a perylene-3,4:9,10-bis(dicarboximide) (in short perylene bisimide, PBI) dye.[40] An oscillator frequency of $\omega = 1411$ cm^{-1} was used to describe the vibronic progression, which arises from the coupling of the electronic transition to the stretching mode of the perylene core. The dimer can be described as

$$\begin{aligned} H_d = {} & |g,g\rangle \hat{H}_{g,g} \langle g,g| + |e,g\rangle \hat{H}_{e,g} \langle e,g| + |g,e\rangle \hat{H}_{g,e} \langle g,e| \\ & + |e,g\rangle J \langle g,e| + |g,e\rangle J \langle e,g|, \end{aligned} \tag{21}$$

where energy contributions due to van-der-Waals interactions are neglected.

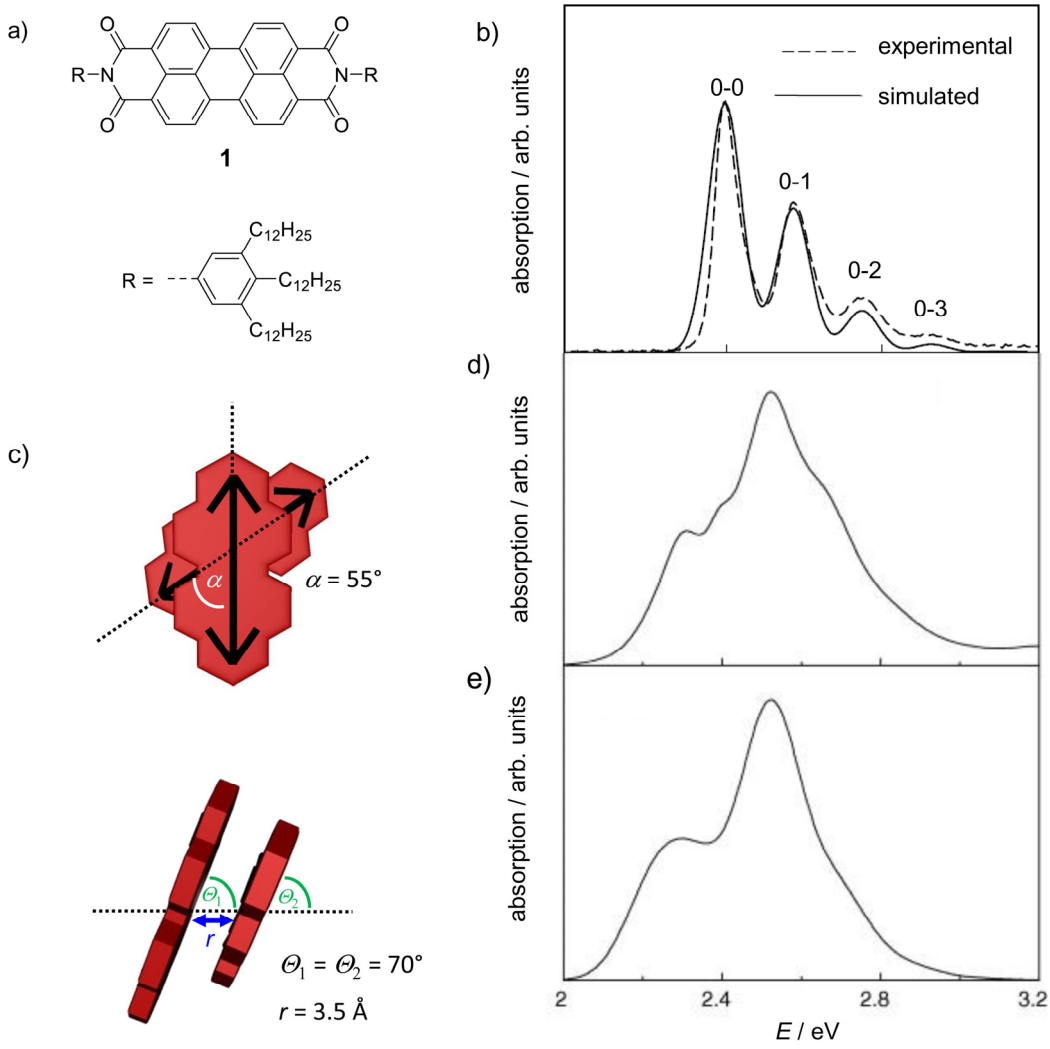

Figure 5. a) Chemical structure of PBI **1**. b) Measured monomer absorption spectrum (c = 2.1 x 10^{-7} M) in methylcyclohexane (dashed line) and calculated absorption spectrum (solid line) of PBI **1**. c) Top and side view in a graphical illustration of the chromophore arrangement in a PBI dimer, which shows the best agreement of the simulated absorption spectrum with the measured one. The black double-arrows indicate the orientation of the transition dipole moments. d) Measured absorption spectrum of PBI **1** in methylcyclohexane at c = 2.2 x 10^{-4} M and e) simulated absorption spectrum of the PBI dimer with the arrangement shown in Figure 5c.[40] Adapted with permission from Ref. [40]. Copyright 2006 Elsevier.

The state |e,g> corresponds to an electronic excitation of one monomer while the second monomer is in the ground state. Analogously, |g,e> represents a state in which the second chromophore is electronically excited while the first chromophore is in its ground state.These two states are coupled by J, which represents the exciton coupling energy.

The corresponding vibrational Hamiltonians are:

$$\hat{H}_{g,g} = -\frac{1}{2}\frac{d^2}{dx_1^2} - \frac{1}{2}\frac{d^2}{dx_2^2} + \frac{1}{2}\omega_1^2 x_1^2 + \frac{1}{2}\omega_2^2 x_2^2 \tag{22}$$

$$\hat{H}_{e,g} = -\frac{1}{2}\frac{d^2}{dx_1^2} - \frac{1}{2}\frac{d^2}{dx_2^2} + \frac{1}{2}\omega_1^2 (x_1 - x_{e,1})^2 + \frac{1}{2}x^2\omega_2^2 + \Delta E_m \tag{23}$$

and

$$\hat{H}_{g,e} = -\frac{1}{2}\frac{d^2}{dx_1^2} - \frac{1}{2}\frac{d^2}{dx_2^2} + \frac{1}{2}\omega_1^2 x_1^2 + \frac{1}{2}\omega_2^2 (x_2 - x_{e,2})^2 + \Delta E_m. \tag{24}$$

Here, $\hat{H}_{g,g}$ describes a state where both chromophores are in the vibrational ground state, while in the case of $\hat{H}_{e,g}$ and $\hat{H}_{g,e}$ one chromophore is vibrationally excited and the other one is in the vibrational ground state.

For a PBI H-dimer like the one studied by Engel and Würthner (Figure 5c) the simulated absorption spectrum is in good agreement with the experimental spectrum in methylcyclohexane at high concentration (c = 2.2 x 10^{-4} M) where almost only aggregated species are present.[62] While H-aggregates of chromophores without vibrational contribution exhibit a hypsochromic shift of the absorption band, the PBI **1** aggregate spectrum shows a reversal of the band intensities of the 0–0 and 0–1 transition band. This redistribution of oscillator strengths is due to vibrational broadening of the electronic transitions and is typically observed for H-aggregates whose vibrational frequency ω is comparable to the exciton coupling energy J (so-called intermediate coupling regime).[41]

For the investigation of larger dye aggregates in terms of exciton-vibrational coupling the employment of approximations, like the two-particle approximation, is useful to reduce computational effort.[63, 64] In general, the excitation in aggregates is described in terms of excitonic polarons, where a polaron corresponds to a vibronically excited molecule surrounded by vibrationally excited molecules in the electronic ground state. This can be illustrated according to Spano by a ball on a mattress where the compressed spring directly underneath the ball represents a vibronically excited molecule and all other surrounding springs correspond to vibrationally excited molecules in the electronic ground state (Figure 6a). A vibronically excited chromophore n with quantum number $\tilde{\nu}$ in the S_1 state is denoted by $|n, \tilde{\nu}>$. If all other chromophores are electronically and vibrationally unexcited this state corresponds to a single-particle excitation (Figure 6b, top). In contrast,

a two-particle excitation denoted by $|n, \tilde{\nu}; n', \nu'>$ describes a state in which chromophore n is vibronically excited and a second chromophore n' ($\neq n$) is vibrationally excited with quantum number ν' (≥ 1) in the electronic ground state (Figure 6b, bottom).

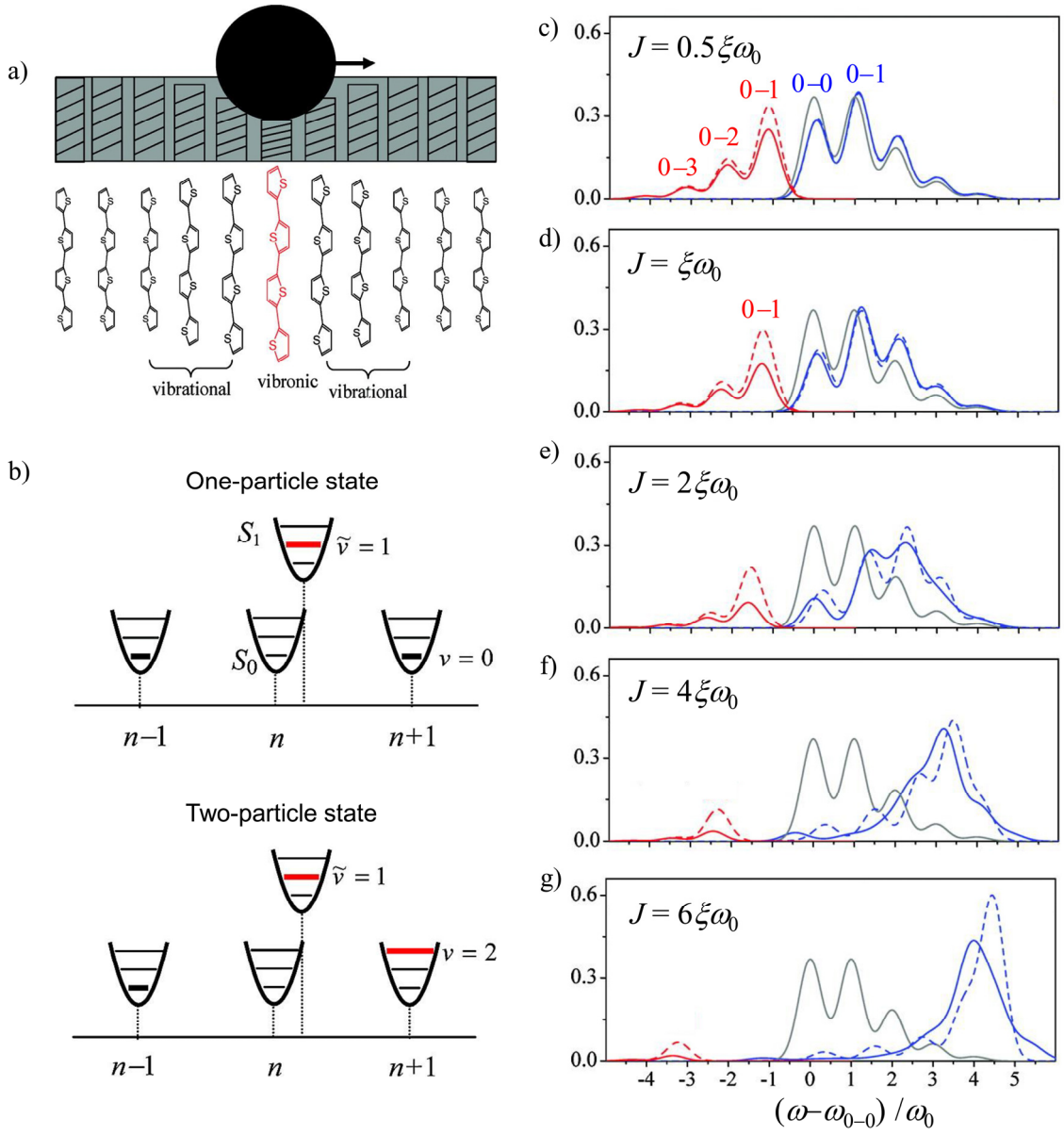

Figure 6. a) Illustration of a ball on a mattress describing the situation of an excitonic polaron in dye aggregates. b) Representation of a one-particle state (top) and a two-particle state (bottom) that are used within the two-particle approximation to describe excited states in aggregates. c)-g) Calculated absorption (blue) and fluorescence (red) spectra for an ideal H-aggregate ($\alpha = 0°$, $\Theta = 90°$) comprising 20 molecules with increasing exciton coupling energy. The vibrational frequency ω_0 is set to 1400 cm^{-1} and J and ξ represent the exciton coupling energy and the Huang-Rhys factor, respectively. For the simulation of the absorption spectra both the one-particle (dashed lines) and two-particle approximation (solid lines) have been used. The grey lines show the monomeric absorption spectra.[60] Adapted with permission from Ref. [60]. Copyright 2010 American Chemical Society.

Within the two-particle approximation only one- and two-particle states are considered and the αth eigenstate is described as a linear combination of these states:

$$|\Psi^{(\alpha)}\rangle = \sum_{n,\tilde{\nu}} c_{n,\tilde{\nu}}^{(\alpha)} |n, \tilde{\nu}\rangle + \sum_{n,\tilde{\nu}} \sum_{n',\nu'} c_{n,\tilde{\nu};n',\nu'}^{(\alpha)} |n, \tilde{\nu}; n', \nu'\rangle, \quad (25)$$

where $c_{n,\tilde{\nu}}^{(\alpha)}$ and $c_{n,\tilde{\nu};n',\nu'}^{(\alpha)}$ are the coefficients of the one- and two-particle excited states, respectively. This model was used by Spano *et al.* to investigate the influence of the exciton coupling strength on the optical properties of aggregates showing exciton-vibrational coupling.[60] Figure 6c-g shows the simulated absorption spectra (blue lines) of an ideal H-aggregate comprising 20 chromophores with increasing exciton coupling strength using both one- and two-particle states (solid lines) and only one-particle states (dashed lines).[60] The vibrational frequency ω_0 is set to 1400 cm^{-1} and only coupling between next-neighbored molecules is assumed. One can clearly see that with increasing exciton coupling strength the absorption spectrum is shifted more to higher energies. In the weak and intermediate coupling regime (Figure 6c,d) only a small hypsochromic shift is observed, while the ratio of the 0–0 and 0–1 absorption intensity changes significantly with respect to the monomer spectra (grey line) as in the case of the dimer of PBI **1** shown before (Figure 5). In contrast to the intermediate coupling regime of the PBI dimer, the redistribution of oscillator strengths for weak coupling is mainly due to an interband coupling between the optically allowed exciton states of different vibrational levels.[65-67] In the strong coupling regime (Figure 6f,g) the absorption shows a large hypsochromic shift and merges into one absorption band without pronounced vibronic progression which can be assigned to the transition to the highest exciton state. A comparison of the absorption spectra simulated based on one-particle (dashed lines) and two-particle approximation (solid lines) reveals large deviations in the strong coupling regime, while in the case of weak coupling no significant differences are observed. Thus, single-particle states are sufficient to describe the situation in the weak coupling regime revealing small polaron radii in the aggregate. In contrast, for strong couplings two-particle states also have to be considered, which indicates larger dimensions of the polarons.

As discussed before, perfect H-aggregates without pronounced vibrational coupling usually exhibit low fluorescence since the lowest exciton state is a dark state.[8] However, for H-aggregates with exciton-vibrational coupling only the 0-0 emission is forbidden, while sideband emission is allowed (Figure 6c-g, red lines). The reason is that required momentum conservation is maintained for sideband emission because here the final states

exhibit one or more vibrational phonons.[68] It is, however, rather difficult to distinguish this situation from the one provided by dye stacks with small rotational offsets where the lower exciton state also becomes partially allowed.[52]

2.3 Exciton Coupling in Heteroaggregates

While dye aggregates comprising the same type of chromophores, *i.e.* homoaggregates, have been intensively studied, relatively little is known about the exciton coupling in heteroaggregates containing different types of chromophores. One reason might be the synthetic challenge to construct such aggregates in a reliable manner, in particular due to the tendency of many dyes to undergo narcissistic self-sorting, resulting in the formation of homoaggregates.[22] Thus, the number of reported heteroaggregates is limited and the size of the aggregates as well as the exact arrangement of the constituent chromophores are unknown, which complicated detailed studies on the exciton coupling.[69-75]

In 1969 Kuhn *et al.* reported the design of heteroaggregates prepared from two monolayers of different cyanine dyes using the Langmuir-Blodgett method.[76] In this way, sandwich-type dimers comprising two different chromophores were obtained, which exhibited significant differences of the absorption properties with respect to the corresponding homoaggregates of the dyes. The absorption properties were explained in a qualitative and quantitative manner by applying the electron-gas model. A coupling of 700 cm^{-1} between the different types of chromophores was estimated by calculating the electron repulsion integrals. This value is comparable to the coupling in the respective homoaggregates. Nevertheless, the exact arrangements of the chromophores within the heterodimers was unknown and the aggregate structure was just estimated on the basis of CPK models. This shows the difficulty of the preparation and characterization of well-defined dye heteroaggregates.

An approach towards heterodimers with distinct orientations of the chromophores was achieved by using DNA-dye conjugates.[20] Hybridization of a series of two complementary DNA strands each comprising one particular type of chromophore resulted in double hetero dye stacks. For one double-strand aggregate the structure could be verified by nuclear Overhauser effect spectroscopy (NOESY), which revealed a π-stack of the employed chromophores. The absorption spectrum was explained by exciton theory in a qualitative manner assuming a coupling between the two chromophores exhibiting different excited state energies. While the intensity of the absorption band of

the chromophore with higher excited state energy was increased in the aggregate spectrum, a decrease in the intensity was observed for the low energy band. This was explained by an in-phase/out-of-phase coupling of the transition dipole moments for the higher/lower exciton state as in the case of a homoaggregate (Figure 2). In contrast to an H-aggregate comprising two identical chromophores, the transition to the lower exciton state is partially allowed, which was explained by the different magnitudes of the two transition dipole moments. In contrast to the predictions derived by exciton theory, both absorption bands showed a bathochromic shift with respect to the absorption bands of the monomeric chromophores. This might be caused by a change of the chromophore environment upon aggregation, which may affect the spectral shift due to solvent effects. Comparison between the different heterodimers suggested that the optical changes were the most significant for small excited state energy differences of the chromophores, whereas for the largest energy difference of 8900 cm^{-1} only slight changes were observed. Therefore, the authors have drawn the conclusion that exciton coupling is weakened when the excited state energy difference is increasing.[20]

Furthermore, a DNA-guided assembly resulting in alternating stacks of PBI and pyrene chromophores has recently been reported.[27] The authors concluded based on quantum chemical analysis that exciton coupling only occurs between the same type of chromophores leading to a co-existence of exciton states. However, their theoretical investigations did not consider vibrational coupling of the chromophores, which is necessary to adequately describe the absorption properties of dye aggregates comprising chromophores with pronounced vibronic progression as it is the case for pyrene and PBI dyes.[40, 41, 60] Hence, these results have to be handled carefully and point at the uncertainty concerning exciton coupling between different types of chromophores.

2.4 Exciton Coupling in Dye Heteroconjugates

Albeit not for aggregates but for covalently connected dyes, clear evidence for exciton coupling between different types of chromophores was recently reported by Lambert *et al.* showing that squaraine-boron-dipyrromethene (BODIPY) conjugates[77] and alternating squaraine-squaraine copolymers[30] exhibit considerably different absorption properties compared to the constituent monomeric chromophores. By extending Kasha`s exciton theory to hetero dye systems the absorption spectra of the heteroconjugates could be properly described in a qualitative and quantitative way, revealing strong exciton coupling

between the different types of chromophores. The absorption spectrum of squaraine-BODIPY conjugate **4** (for the chemical structures see Figure 7a) exhibits two absorption bands of different intensity at 667 and 526 nm (Figure 7b).[77]

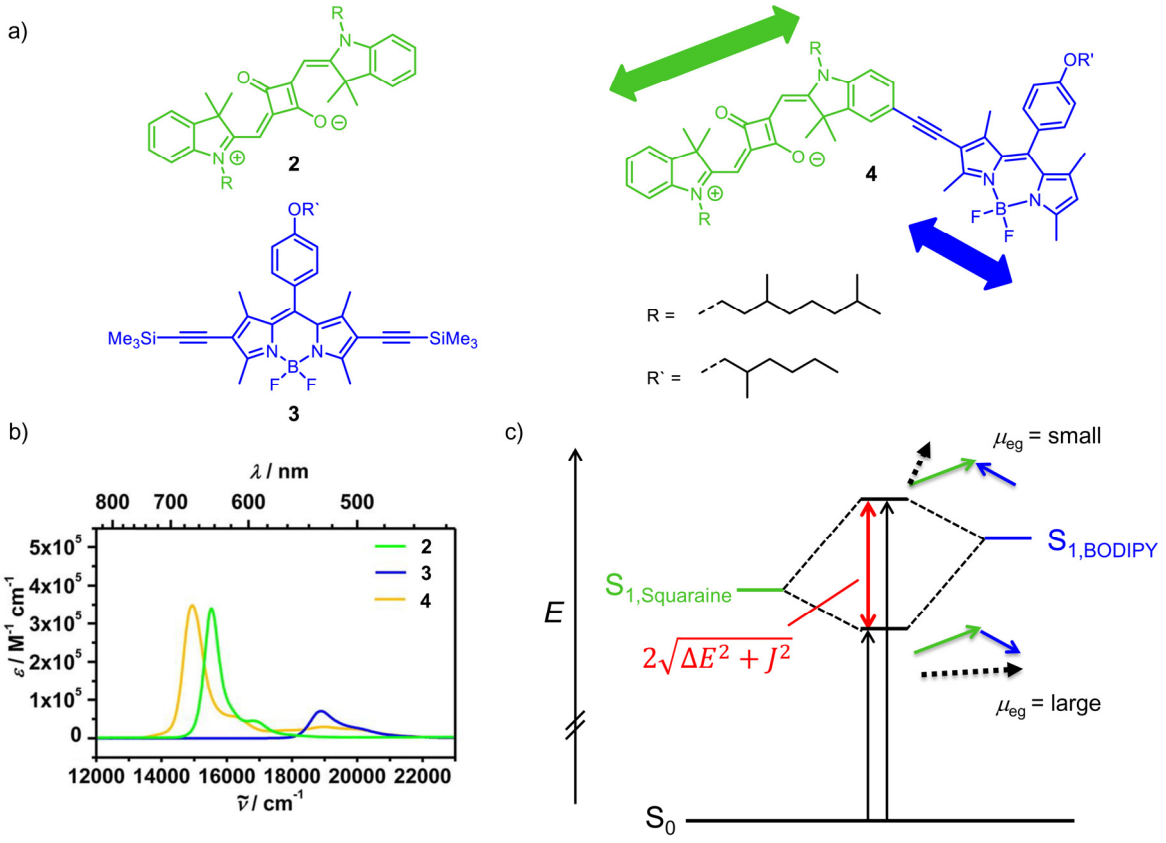

Figure 7. a) Chemical structures of squaraine **2** and BODIPY **3** (left) as well as of squaraine-BODIPY conjugate **4** (right). The bold arrows indicate the orientation of the transition dipole moments of the chromophores in **4**. b) UV/Vis absorption spectra of **2** (green line), **3** (blue line) and **4** (orange line) measured in toluene. c) Exciton state diagram for squaraine-BODIPY conjugate **4**. The green and blue arrows indicate the phase relations between the coupled transition dipole moments and the black dashed arrows represents the overall transition dipole moment obtained by vector addition. J denotes the exciton coupling energy and ΔE is half the energy difference between the excited states $S_{1,\mathrm{BODIPY}}$ and $S_{1,\mathrm{Squaraine}}$.[77] Adapted with permission from Ref. [77]. Copyright 2015 American Chemical Society.

While the absorption band of the squaraine chromophore in the conjugate **4** (Figure 7b, orange line) is very intense and exhibits a bathochromic shift with respect to the monomeric dye **2** (Figure 7b, green line), the absorption band of the BODIPY chromophore is weak and shows a small hypsochromic shift compared to monomeric BODIPY **3** (Figure 7b, blue line). The changes of the optical absorption properties can be explained by assuming an exciton coupling between the two different types of

chromophores. Hence, like for a homodimer the exciton wave function is written as a linear combination of the states where one of the chromophores is excited:

$$\Phi_e = c_1\varphi_1^*\varphi_2 + c_2\varphi_1\varphi_2^*, \tag{26}$$

where φ_1 and φ_2 are the ground state wave functions of the monomeric chromophores and φ_1^* and φ_2^* the respective wave functions of the excited states. When van-der-Waals terms are neglected, the eigenvalue equation for the heterodimer can be written in the following way:[30]

$$\begin{pmatrix} \Delta E & J \\ J & -\Delta E \end{pmatrix} \begin{pmatrix} c_1 \\ c_2 \end{pmatrix} = E_e \begin{pmatrix} c_1 \\ c_2 \end{pmatrix}, \tag{27}$$

where ΔE is half the energy difference between the excited states of the monomeric chromophores and the midpoint between the two excited states is set as zero level. Furthermore, J is the exciton coupling energy between the chromophores. Thus, two exciton state energies for the dimer are obtained:

$$E_e = \pm\sqrt{\Delta E^2 + J^2} \tag{28}$$

and the Davydov splitting amounts to

$$\Delta E_{DS} = 2\sqrt{\Delta E^2 + J^2}. \tag{29}$$

Since squaraine-BODIPY conjugate **4** represents a J-type ‘aggregate’, the excitation to the lower exciton state is highly allowed (Figure 7c) resulting in an intense absorption band at longer wavelengths. In addition, the excitation to the higher exciton state is partially allowed, which is attributed to the oblique alignment of the transition dipole moments in the conjugate as well as to the different magnitudes of the transition dipole moments of the chromophores.[77] Thus, even for a perfect J-aggregate with parallel alignment of the transition dipole moments the highest exciton state remains partially allowed in a heterodimer since the out-of-phase coupling of the transition dipole moments does not result in an overall transition dipole moment of 0 D. The exciton coupling energy determined according to equation (29) results in a value of -1050 cm^{-1}, hence revealing strong coupling between the different types of chromophores in the conjugate.

Exciton coupling between next-neighbored chromophores of different types was also observed for the copolymer **5** (Figure 8) of $[A\text{-}B]_N$ type comprising two different

squaraine chromophores SQA (chromophore A) and SQB (chromophore B).[30] Exciton theory applied for this system explained the unexpected absorption properties of the copolymer.

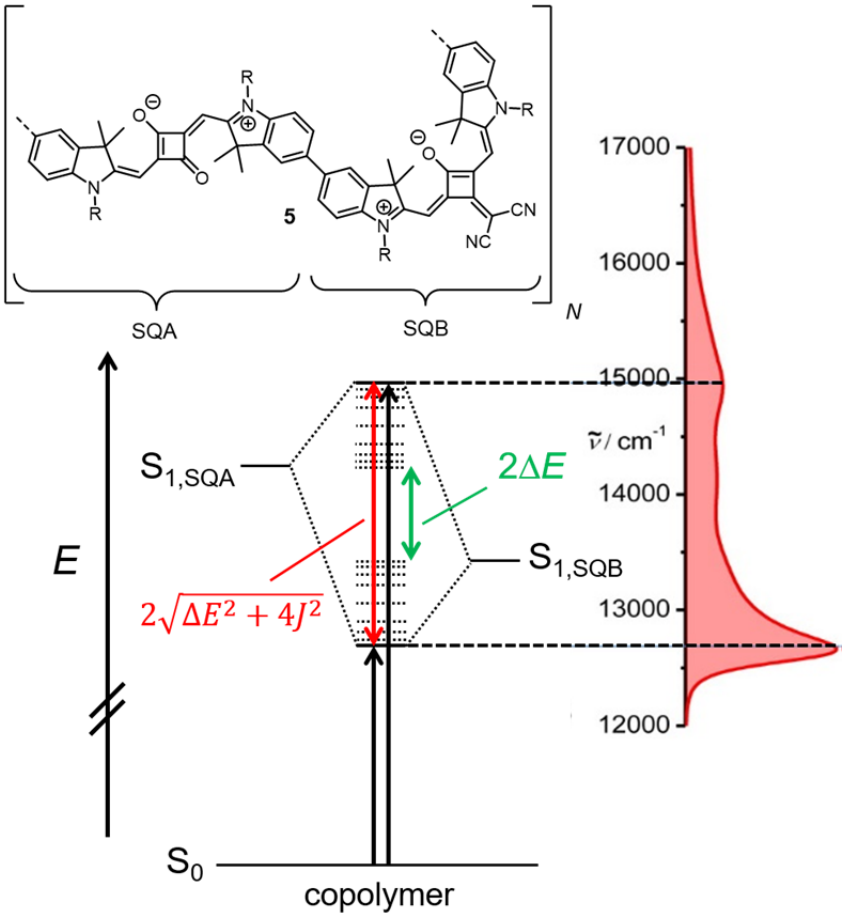

Figure 8. Chemical structure and exciton state diagram of [SQA-SQB]$_N$ copolymer **5** along with the UV/Vis absorption spectrum of **5** in toluene. ΔE is half the energy difference between the excited states of the two monomeric squaraine chromophores $S_{1,SQA}$ and $S_{1,SQB}$ and J denotes the exciton coupling energy between next-neighbored chromophores.[30] Adapted with permission from Ref. [30]. Copyright 2014 American Chemical Society.

The ground state is given as a product of the ground state wave functions of the monomeric chromophores:

$$\Phi_g = \Phi_g^{(A)}\, \Phi_g^{(B)} \tag{30}$$

with

$$\Phi_g^{(A)} = \prod_{n=1}^{N} \varphi_n^{(A)}. \tag{31}$$

Here, $\varphi_n^{(A)}$ represents the ground state wave function of monomeric chromophore n of type A (the same is true for the chromophores of type B). The exciton wave function can be described using Bloch-type functions[78, 79] with Born-von Karman boundary conditions:[80]

$$\Phi_{e,k}^{(A)} = \frac{1}{\sqrt{N}} \sum_{a=1}^{N} \exp(i\frac{2\pi}{N}ka)\phi_a^{(A)}, \quad k = 0, \pm1, \pm2, \ldots, \frac{N}{2}. \tag{32}$$

Here, k is a quantum number and $\phi_a^{(A)}$ is defined as

$$\phi_a^{(A)} = \varphi_a^{*(A)} \prod_{\substack{n=1 \\ n\neq a}}^{N} \varphi_n^{(A)}, \tag{33}$$

which describes the state in which chromophore a of type A is in the excited state (φ_a^*), while all other chromophores are in the ground state. Thus, the exciton wave functions of the entire copolymer can be written as linear combinations of the respective wave functions of both types of chromophores:

$$\Phi_{e,k,1} = c_1^{(A)} \Phi_{e,k}^{(A)} \Phi_g^{(B)} + c_1^{(B)} \Phi_{e,k}^{(B)} \Phi_g^{(A)} \tag{34}$$

$$\Phi_{e,k,2} = c_2^{(A)} \Phi_{e,k}^{(A)} \Phi_g^{(B)} + c_2^{(B)} \Phi_{e,k}^{(B)} \Phi_g^{(A)}. \tag{35}$$

The corresponding Hamiltonian has the form:

$$\hat{H}_{tot} = \sum_{a=1}^{N} \hat{H}_a^{(A)} + \sum_{b=1}^{N} \hat{H}_b^{(B)} + \frac{1}{2} \sum_{a\neq b}^{N} \hat{V}_{ab}, \tag{36}$$

where $\hat{H}_a^{(A)}$ and $\hat{H}_b^{(B)}$ are the Hamiltonians of the monomeric chromophores of type A and B, respectively, while $\hat{V}_{ab}$ represents the Coulomb interaction operator describing the exciton coupling between next-neighbored chromophores. With this, the excited state energies are obtained:

$$E_{e,k} = \bar{E} \pm \sqrt{\Delta E^2 + \left(2J\cos\left(\frac{\pi k}{N}\right)\right)^2}, \qquad k = 0, \pm1, \pm2, \ldots, \frac{N}{2}, \tag{37}$$

where $\bar{E}$ is the midpoint of the excited state energies of both types of chromophores and J represents the exciton coupling energy between next-neighbored chromophores of type A and B. The exciton bandwidth of the copolymer amounts to $2\sqrt{\Delta E^2 + 4J^2}$ (Figure 8), whereas it is $4J$ in the case of a homopolymer ($\Delta E = 0$).[7] In addition, for a perfect head-to-tail arrangement of the chromophores only the transition to the lowest exciton state is

allowed in a homopolymer, while for the copolymer also the transition to the highest exciton state is partially allowed. All further transitions are forbidden, which results in the appearance of two absorption bands for the copolymer (Figure 8). Based on the exciton bandwidth an exciton coupling energy of $J = 480\ \mathrm{cm}^{-1}$ was determined, which is comparable to the exciton coupling energy of the homopolymer of SQA ($J = 640\ \mathrm{cm}^{-1}$).[81] Furthermore, the absorption band at longer wavelengths is striking narrow, which is characteristic of J-aggregates and arises from a coherent excitation of multiple chromophores that leads to an averaging of the quasistatistic disorder in the aggregate.[82-84] The bandwidth allows the determination of the effective coherence length,[82, 85] resulting in a value of $N_{\mathrm{eff}} = 3.7$ for the copolymer, which means that the exciton is on average delocalized over a $[\mathrm{SQA\text{-}SQB}]_{3.7}$ unit.[30]

2.5 Conclusion

As discussed in this chapter, the knowledge on exciton coupling in dye heteroaggregates is still rather limited. Therefore, the major goal of this thesis was to achieve a better understanding on the exciton coupling between different types of chromophores. The main focus was on the optical absorption properties of dye heteroaggregates studied by UV/Vis spectroscopy. In addition, the respective homoaggregates were included in these studies for comparison. Quantum chemical analysis was intended to rationalize the absorption properties of the investigated heteroaggregates. In the following three chapters the results obtained towards this approach are discussed.

Chapter 3

Exciton Coupling in Homo- and Heteroaggregate Double Stacks of Merocyanine Dyes[1]

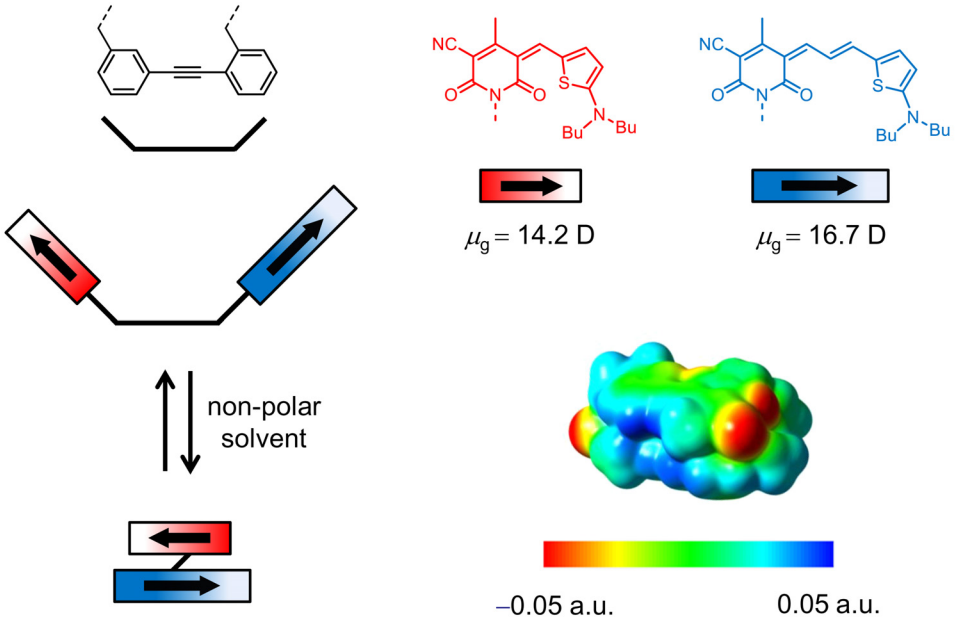

Abstract: Two identical or different merocyanine dyes, respectively, were tethered by a rigid diphenylacetylene spacer unit that enables the folding of the two dyes into cofacially π-stacked structures in solvents of low polarity. Pronounced spectral changes are observed upon folding and our quantum chemical analysis reveals strong exciton coupling also between the different types of chromophores of the hetero-π-stack. Thus, strong exciton coupling is not limited to the situation of two equal chromophores as often assumed.

[1] Part of this chapter was published in: D. Bialas, E. Kirchner, F. Würthner, *Chem. Commun.* **2016**, *52*, 3777–3780 (http://pubs.rsc.org/en/content/articlehtml/2016/cc/c6cc00221h). Reproduced with permission. Copyright 2016 Royal Society of Chemistry.

3.1 Introduction

In-depth studies on exciton coupling require distinct orientations of the chromophores, which is difficult to realize for supramolecular dye aggregates based on π-π-interactions since the prevailing dispersion interactions allow multiple arrangements of the chromophores with similar energies.[31, 32] In this regard, merocyanines represent a privileged class of dyes which form well-defined aggregates in solution.[34] Due to their strong dipolar character the chromophores dimerize in non-polar solvents resulting in centrosymmetric π-stacks with antiparallel orientation of the ground state dipole moments. However, it is difficult to derive heteroaggregate systems by co-self-assembly of these dyes because the dipolar interaction energies favor the formation of homoaggregates leading to narcissistic self-sorting.[86]

For these reasons and by taking inspiration from earlier work on spacer-directed organization of dipolar merocyanine dyes,[35, 87-89] molecule **7** comprising two merocyanine chromophores with different conjugation length was designed (Figure 9), whose folding into pleated heterodimer structure was predicted by density functional theory (DFT) calculations.

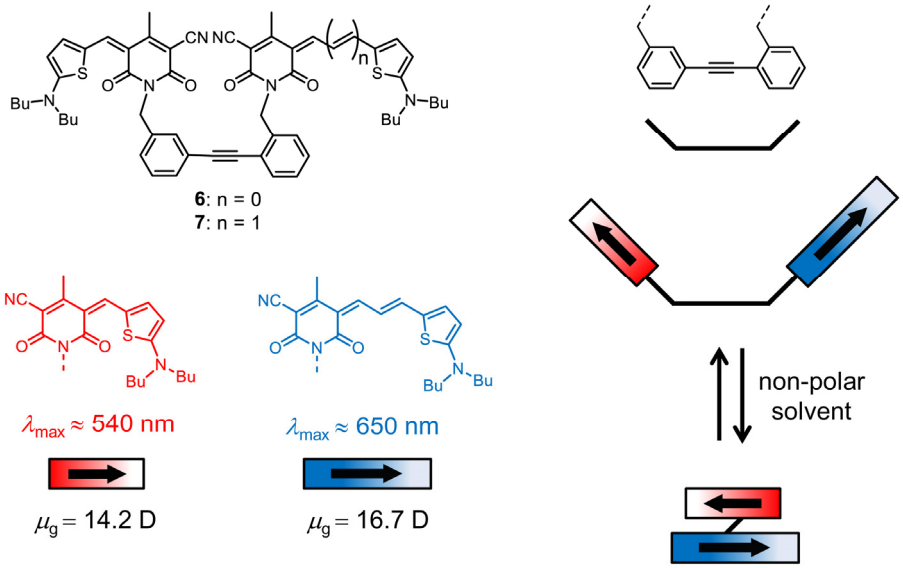

Figure 9. Chemical structure of bis(merocyanine) dyes **6** and **7** and schematic illustration of the folding process of **7** in non-polar solvents resulting in the heterodimer stack.

It was already shown in earlier work that bis(merocyanine) **6** (Figure 9) with two equal chromophores folds in non-polar solvents resulting in the respective homodimer π-stack, which was confirmed by 2D NMR spectroscopy.[90] Therefore, bis(merocyanine) **6** was included in the following studies for comparison.

3.2 Results and Discussion

3.2.1 Synthesis

Bis(merocyanine) dyes **6**[90] and **7** were synthesized according to the routes shown in Scheme 1.[2] The respective amines **8** and **15** were reacted with methyl cyanoacetate to afford cyanoacetamides **9** and **16**, respectively. While amine **15** is commercially available, compound **8** was prepared according to literature known procedures.[91]

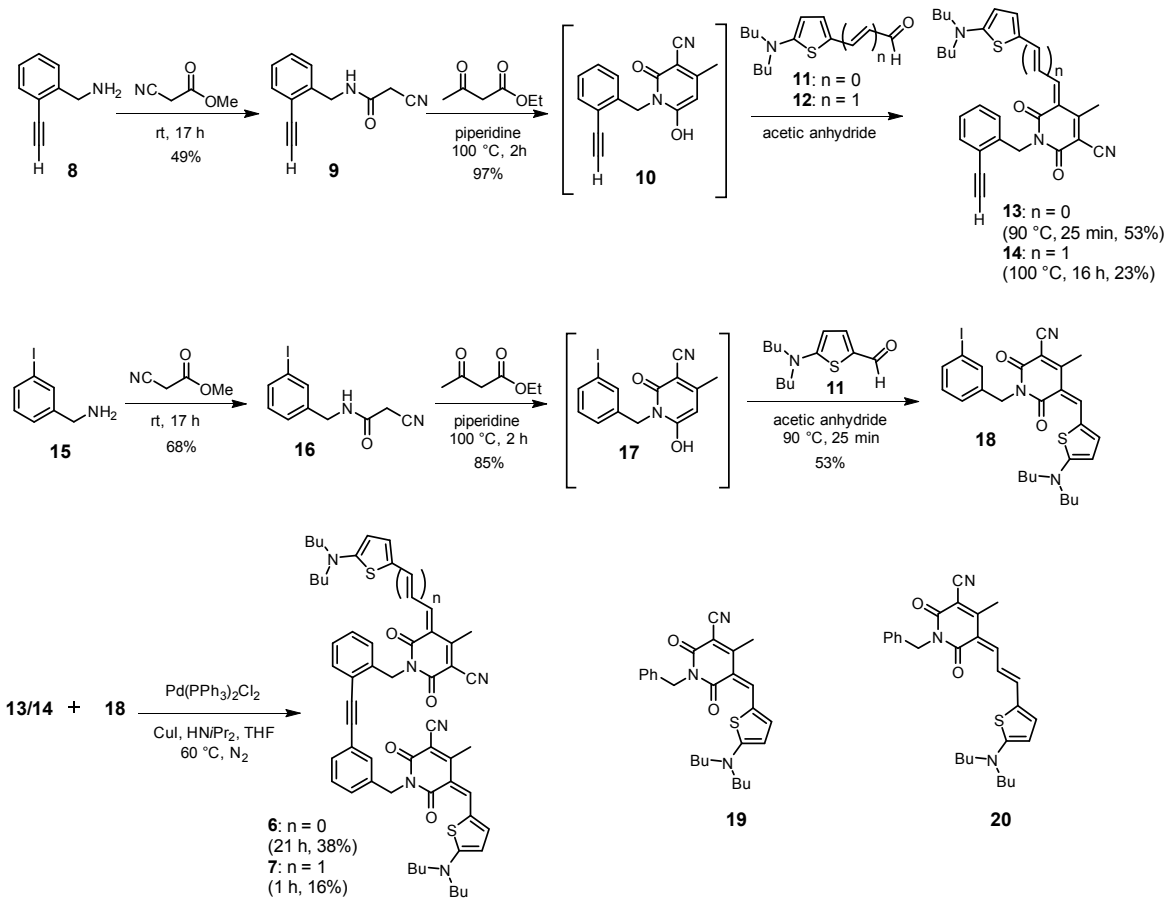

Scheme 1. Synthetic route to bis(merocyanine) dyes **6** and **7** and chemical structure of reference compounds **19** and **20**.

The hydroxypyridone intermediates **10** and **17** were synthesized by reacting the respective cyanoacetamide with ethyl acetoacetate in piperidine and subjected to a Knoevenagel condensation with aminothiophene aldehyde **11** and **12**, respectively, which were prepared according to literature,[92-94] to give the desired mono(merocyanine) dyes **13**, **14** and **18**. Finally, the target bis(merocyanine) dyes **6** and **7** were obtained *via* Sonogashira coupling

[2] Bis(merocyanine) **6** was synthesized by Eva Kirchner.

of **18** with the respective acetylene compound **13** and **14** under palladium catalysis in the presence of copper iodide and diisopropylamine in THF. The reference compounds **19** and **20** (Scheme 1) were available in the group from previous research on organic photovoltaics.[94]

3.2.2 UV/Vis Spectroscopy

The highest driving force for the folding of molecules **6** and **7** into only weakly dipolar pleated structures was expected for low polarity solvents, whereas more dipolar solvents are supposed to favor open conformations due to the better interaction of the solvent with the dipolar merocyanine dyes.[35, 95] Accordingly, the folding process of bis(merocyanine) dyes **6** and **7** was investigated in dichloromethane/methylcyclohexane (DCM/MCH) mixtures and monitored by UV/Vis spectroscopy. The spectra for bis(merocyanine) **6** are shown in Figure 10b.

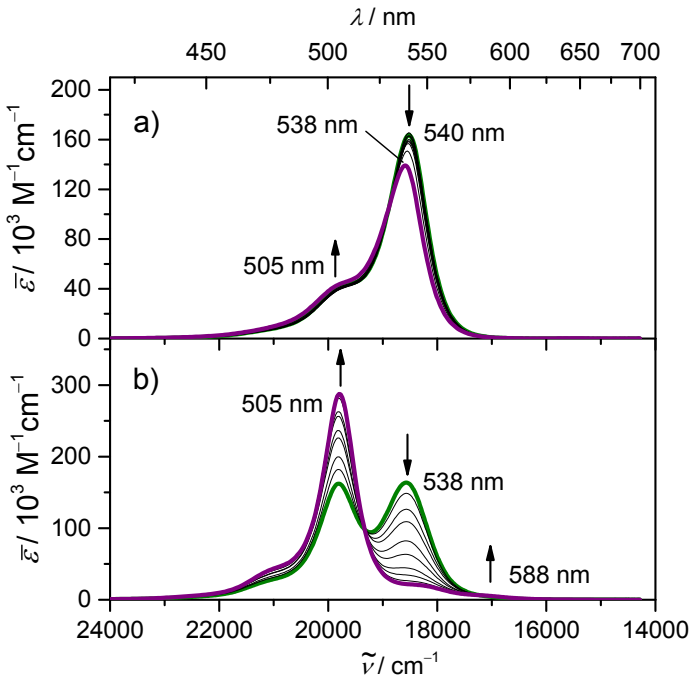

Figure 10. Solvent-dependent UV/Vis spectra of a) reference **19** and b) bis(merocyanine) dye **6** in DCM/MCH mixtures (c = 5 x 10^{-6} M) at 298 K starting in DCM (green line) and successively increasing the volume fraction of MCH in steps of 10 vol% up to 90 vol% (purple line). The arrows indicate the spectral changes upon increasing the volume fraction of MCH.

Remarkably, even for the more polar solvent DCM two absorption bands at 505 and 538 nm can be observed for bis(merocyanine) **6** (Figure 10b, green line), whereas the spectrum of reference compound **19** exhibits only one absorption maximum at 540 nm

(Figure 10a, green line). Hence, the absorption at 538 nm in the spectrum of bis(merocyanine) **6** can be assigned to non-interacting chromophores (open conformation), while the hypsochromically shifted absorption band at 505 nm indicates the presence of a stack of two merocyanine chromophores with H-type coupling (folded conformation).[95] The shape of the spectrum of **6** in dichloromethane shows no dependence on concentration (Figure 11a), thus, confirming an intramolecular aggregation process. The existence of folded species already in pure DCM (high permittivity $\varepsilon_r \approx 9.0$) denotes an excellent preorganization of the chromophores by the rigid diphenylacetylene spacer unit.

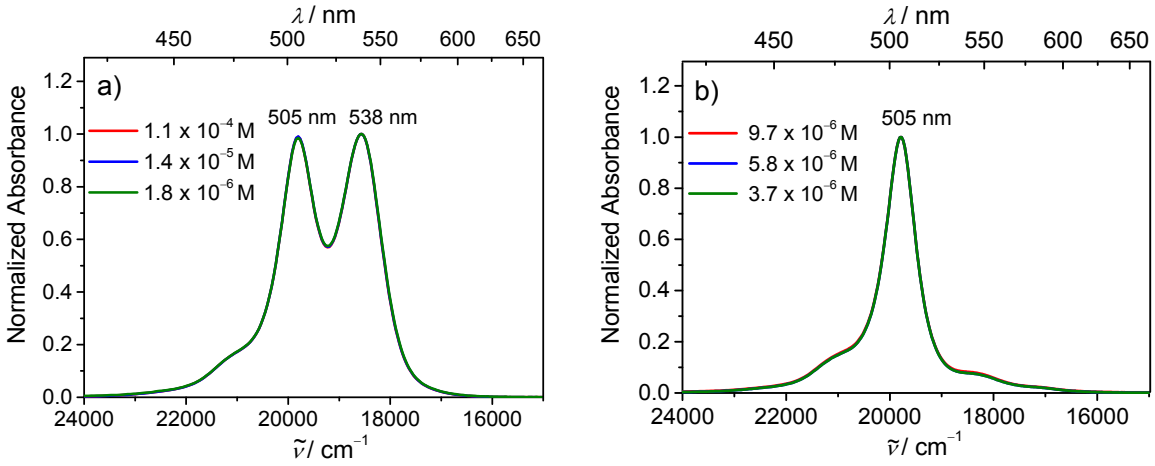

Figure 11. Normalized UV/Vis absorption spectra of bis(merocyanine) **6** in a) dichloromethane and b) DCM/MCH 10:90 at different concentrations at 298 K.

Upon increasing the amount of the low polarity solvent MCH (permittivity $\varepsilon_r \approx 2.0$) the intensity of the monomeric absorption band at 538 nm decreases (Figure 10b) with a concurrent increase of the intensity at 505 nm revealing that the folding process is favored in the non-polar solvent. The spectrum in DCM/MCH 10:90 (Figure 10b, purple line) displays an intense absorption band at 505 nm and a new very weak absorption at 588 nm, indicating that almost only folded species are present. The weak absorbance at longer wavelength is attributed to a weakly allowed J-band, which originates from the not perfectly coplanar transition dipole moments of the two merocyanines in the pleated conformation.[35, 40] In comparison, the solvent-dependent UV/Vis spectra of reference compound **19** (Figure 10a) exhibit only minor changes caused by solvatochromism effects.[96-98] Like in dichloromethane the shape of the spectra of bis(merocyanine) **6** in

DCM/MCH 10:90 are independent from concentration so that intermolecular processes can be ruled out also in non-polar solvent mixtures (Figure 11b.)

In the case of bis(merocyanine) **7** with two different types of chromophores, the spectrum in dichloromethane (Figure 12c, green line) exhibits two absorption bands at 540 nm and 657 nm, which closely resemble the spectra of the individual chromophores (Figure 12a,b, green lines) indicating the absence of exciton coupling between the chromophores.

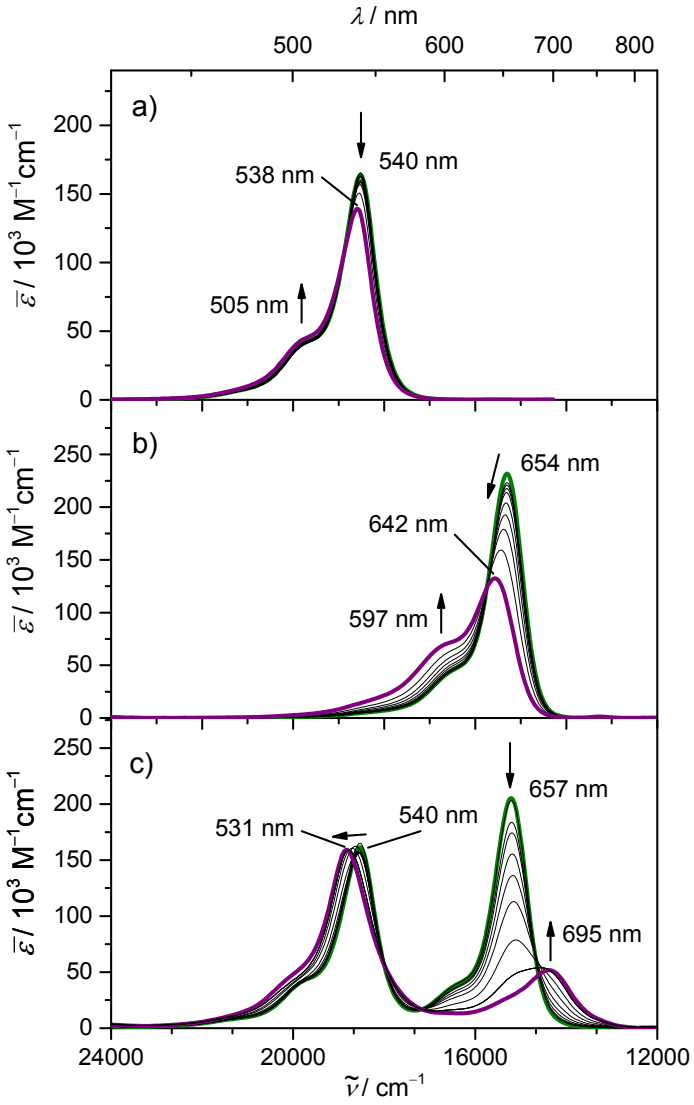

Figure 12. Solvent-dependent UV/Vis spectra of reference compounds a) **19** and b) **20** as well as of c) bis(merocyanine) **7** in DCM/MCH mixtures at 298 K ($c = 5 \times 10^{-6}$ M) starting in DCM (green line) and successively increasing the volume fraction of MCH in steps of 10 vol% up to 90 vol% (purple line). The arrows indicate the spectral changes upon increasing the volume fraction of MCH.

Upon increasing the amount of methylcyclohexane the absorption band of the short chromophore at 540 nm shows a slight hypsochromic shift (Figure 12c), whereas the absorption band of the long chromophore at 657 nm decreases remarkably with a concomitant bathochromic shift. In contrast to **19**, solvent-dependent studies for reference compound **20** show a pronounced hypsochromic shift of the absorption band upon increasing the amount of MCH (Figure 12b). The formation of H-dimers at higher MCH amount can be ruled out because the shape of the spectra in DCM/MCH 10:90 are independent from concentration (Figure 21 in the appendix). Thus, the changes observed in the solvent-dependent absorption spectra of **20** can be attributed to solvatochromism. As in the case of bis(merocyanine) **6** with two identical chromophores, the shape of the spectrum of **7** in DCM/MCH 10:90 shows no dependence on concentration (Figure 13). This observation corroborates a folding process like illustrated in Figure 9.

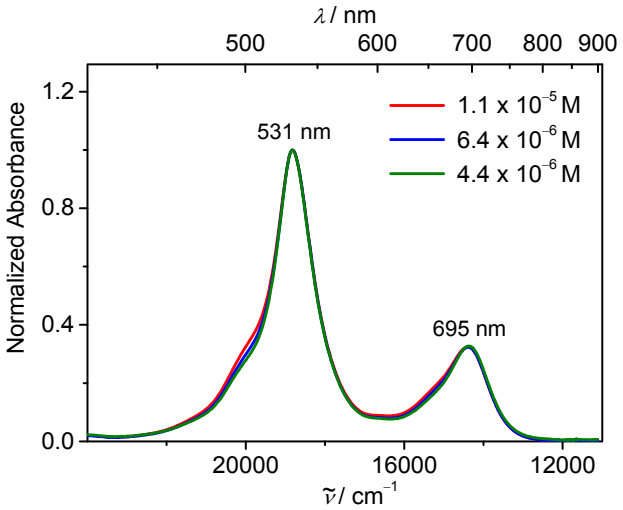

Figure 13. Normalized UV/Vis absorption spectra of bis(merocyanine) **7** in DCM/MCH 10:90 at different concentrations (298 K).

3.2.3 NMR Spectroscopy[3]

To unambiguously verify the folding of bis(merocyanine) dye **6** into antiparallel co-facially π-stacked chromophores, NMR spectroscopic studies were performed in 1,4-dioxane-d_8, a solvent of low polarity ($\varepsilon_r \approx 2.2$), in which predominantly the folded conformation is given according to UV/Vis spectroscopy (Figure 14).[90] For comparison,

[3] NMR studies were perfomed by Eva Kirchner.

the experiments have also been carried out in the highly polar solvent DMF-d_7 in which folding should be negligible.

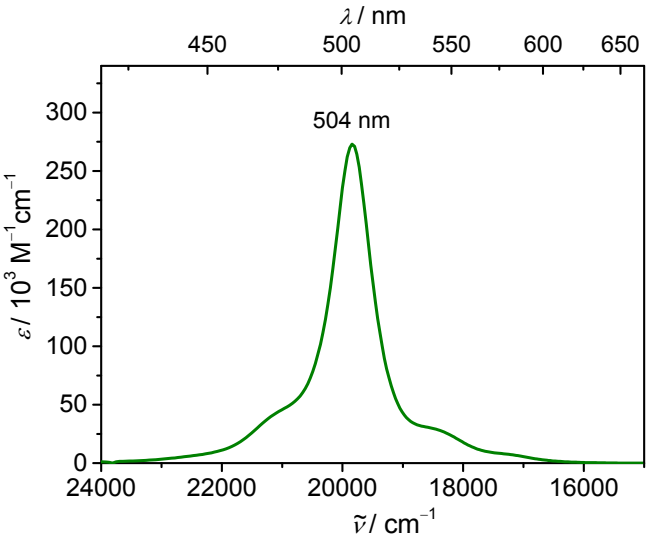

Figure 14. UV/Vis absorption spectrum of bis(merocyanine) **6** in 1,4-dioxane at 298 K (c = 5.0 x 10^{-6} M).[90]

Due to the unsymmetrical structure of the diphenylacetylene spacer unit, the two chromophores are chemically not equivalent and thus, show two different sets of resonances in the ^{1}H NMR spectrum (numbered with and without prime), for which pronounced upfield shifts are observed in 1,4-dioxane-d_8 (Figure 15a). These findings can be attributed to a shielding of the protons by the aromatic units of the adjacent dye in the folded conformation. In contrast, proton H4 of the diphenylacetylene spacer (Figure 15d) shows a downfield shift in the low polarity solvent upon folding. Close spatial proximity between protons of π-stacked chromophores was further confirmed by rotating-frame Overhauser enhancement spectroscopy (ROESY). Thus, in 1,4-dioxane-d_8 highly indicative cross-peaks between the methyl group (CH_3) and the protons H2' and H3' as well as between CH_3' and H2 and H3, respectively, were found (Figure 15b,d). Since these signals are lacking in DMF-d_7 (Figure 15c), they can thus definitely be related to interchromophoric through-space couplings between protons in the folded state.

Unfortunately, it was not possible to confirm the aggregate structure of bis(merocyanine) **7** due to the overlap of the proton signals in the NMR spectra so that the signals could not be assigned to the individual protons. Nevertheless, a π-stacked arrangement of the chromophores in the folded conformation driven by dipolar aggregation like for bis(merocyanine) **6** seems reasonable.

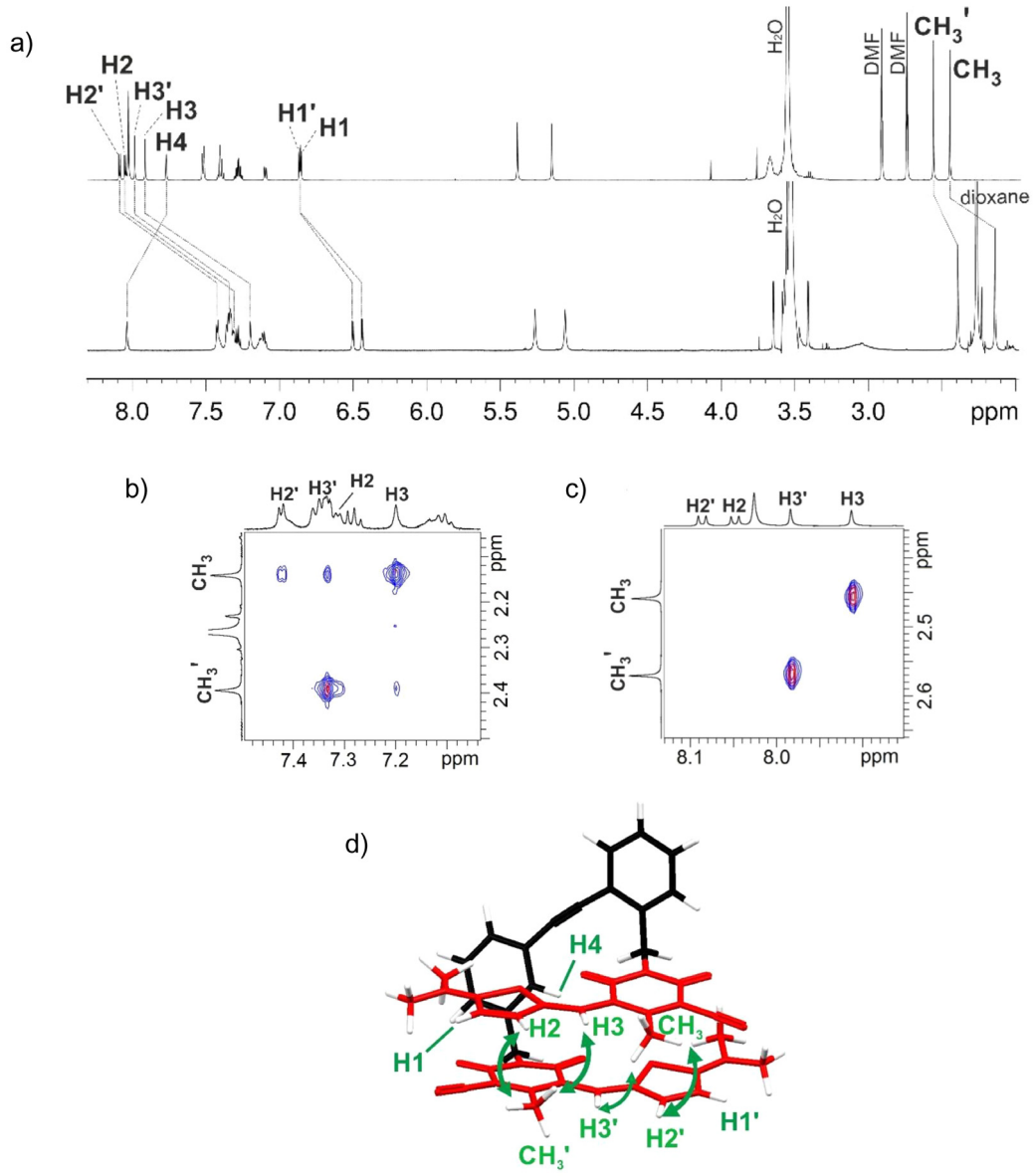

Figure 15. a) ^{1}H NMR (600 MHz) spectra of **6** in DMF-d_7 (top, c = 5 x 10^{-6} M, 298 K) and 1,4-dioxane-d_8 (bottom, c = 5 x 10^{-6} M, 333 K). Relevant section of 2D (600 MHz) ROESY (blue signals) and 2D correlation spectroscopy (COSY, red signals) spectra of **6** in b) 1,4-dioxane-d_8 (c = 5 x 10^{-6} M, 333 K) and c) DMF-d_7 (c = 5 x 10^{-6} M, 298 K). d) Structural model of **6** in the folded conformation. Green double arrows indicate close spatial proximity between the protons of different chromophores according to ROESY cross peaks in 1,4-dioxane-d_8.[90]

3.2.4 Quantum Chemical Calculations

Geometry optimizations were performed for bis(merocyanine) dyes **6** and **7** as well as for reference compounds **19** and **20** (benzyl and butyl groups were replaced by methyl groups) on the DFT level using the B97D3[99] functional including dispersion correction and def2-SVP[100] as basis set. The geometry optimized structures of bis(merocyanine)

dyes **6** and **7** exhibit a stack of two merocyanine chromophores with distances of 3.5 Å for the homostack (Figure 16a) and 3.4 Å for the heterostack (Figure 16b) representing values that are in accordance with crystallographic data for π-stacked molecules **6** and **7**.[94] The small dipole moment of 1.1 D for folded bis(merocyanine) **6** with two identical chromophores reveals an almost perfect antiparallel alignment of the dipole moments (14.2 D) of the chromophores. For the heteroaggregate of bis(merocyanine) **7** a larger value of 4.2 D is obtained. This is attributed to the different magnitudes of the dipole moments of the individual chromophores so that the antiparallel alignment of the π-systems does not result in an annihilation of the overall dipole moment of the stack.

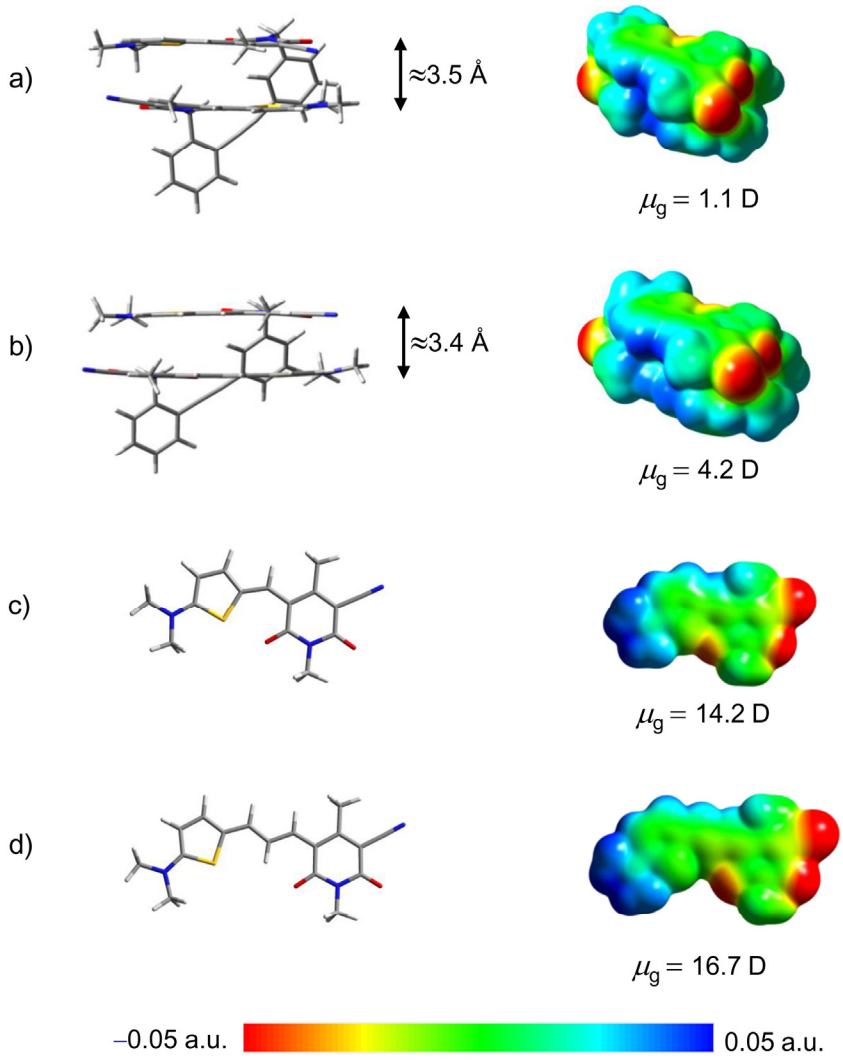

Figure 16. Geometry optimized structures (B97D3, def2-SVP) and electrostatic potential surfaces (isovalue = 0.001 a.u.) of bis(merocyanine) dyes a) **6** and b) **7** as well as of reference compounds c) **19** and d) **20**. Butyl and benzyl groups were replaced by methyl groups.

To rationalize the absorption properties of the dye stacks, time-dependent DFT (TDDFT) calculations were performed on the geometry optimized structures employing the long-range corrected ωB97 functional.[101] The simulated absorption spectra of bis(merocyanine) dyes **6** and **7** (Figure 17a) resemble the experimental spectra in DCM/MCH 10:90.

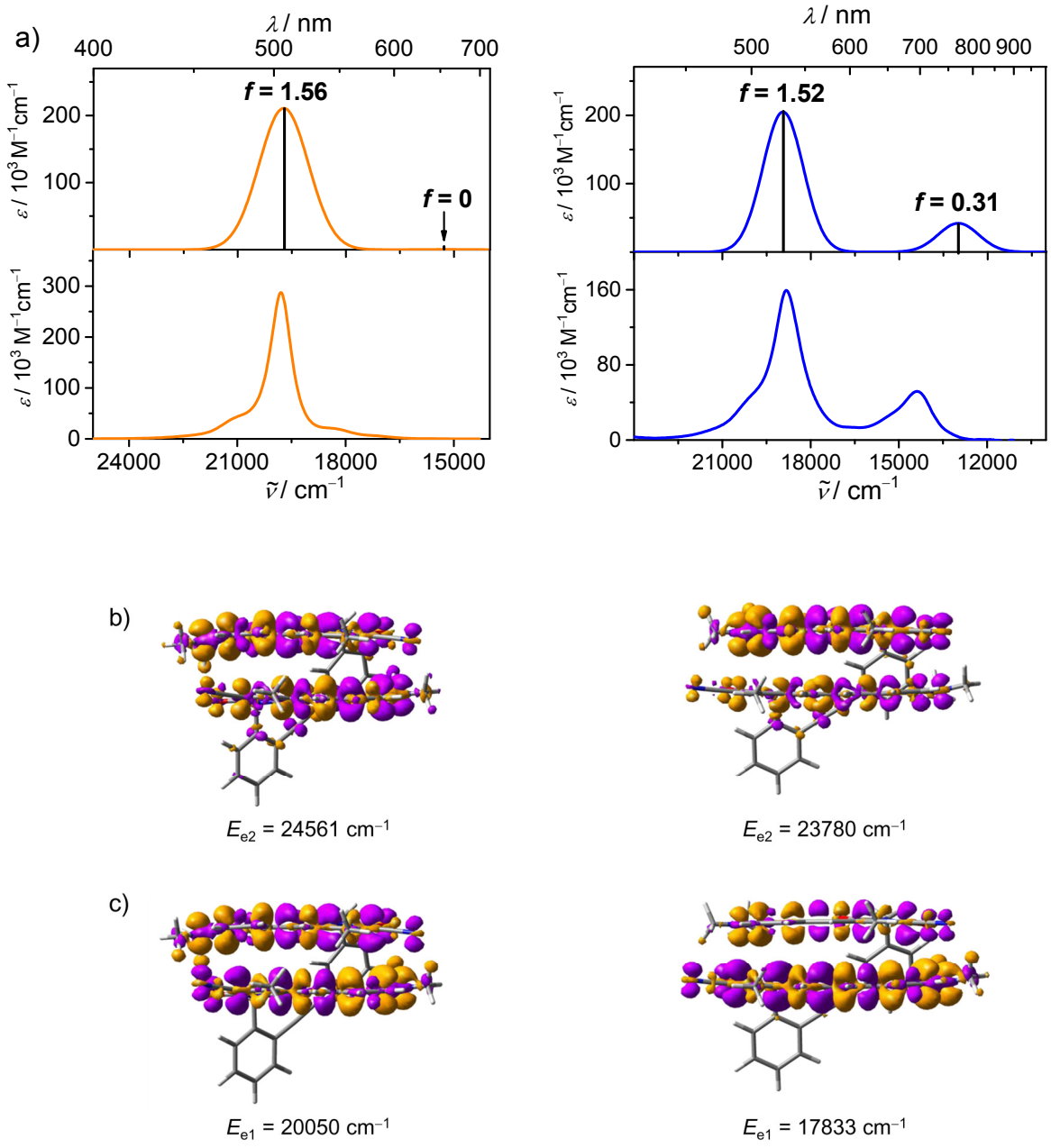

Figure 17. a) Calculated absorption spectra obtained by TDDFT calculations (ωB97/def2-SVP, top) and experimental spectra in DCM/MCH 10:90 (c = 5 x 10^{-6} M, bottom) of bis(merocyanine) dyes **6** (left) and **7** (right). The calculated spectra were shifted by 0.6 eV towards lower energies. In addition, the transition densities (isovalue = 0.0012 a.u.) and energies of the b) higher and c) lower excited state of bis(merocyanine) dyes **6** (left) and **7** (right) obtained by TDDFT calculations (ωB97/def2-SVP) are shown.

Both bichromophoric stacks exhibit two non-degenerated excited states (Table 1) with a strongly allowed transition to the highest excited state (large value of oscillator strength *f*), resulting in an intense absorption band. Since the excitation to the lowest excited state is forbidden in the case of the homoagggregate, the spectrum (Figure 17a, left) exhibits only one absorption band of appreciable intensity. In contrast, the transition to the lowest excited state is partially allowed for the heteroaggregate so that the spectrum of **7** (Figure 17a, right) displays, in addition to the intense absorption band at shorter wavelengths, a second absorption maximum with lower intensity at longer wavelengths.

Table 1. Excited state energies and corresponding oscillator strengths (*f*) for bis(merocyanine) dyes **6** and **7** obtained by TDDFT calculations (ωB97/def2-SVP).

	bis(merocyanine) **6**	bis(merocyanine) **7**
excited state energy	20050 cm^{-1} (f = 0.0019)	17833 cm^{-1} (f = 0.3116)
(oscillator strength)	24561 cm^{-1} (f = 1.5630)	23780 cm^{-1} (f = 1.5196)

For both dye stacks the overall transition density for the excitation to the higher excited state is a positive linear combination of the transition densities of the individual chromophores (Figure 17b). This is in accordance to Kasha's exciton theory where the highest exciton state of an H-aggregate is described by an in-phase coupling of the transition dipole moments. On the contrary, the transition density for the excitation to the lower excited state represents the negative linear combination (Figure 17c). In the case of the homoaggregate the transition density of the dye stack is equally distributed over the two equal chromophores for both excited states (Figure 17b,c, left). This is different for the heteroaggregate of bis(merocyanine) **7** where the transition density of the higher excited state is more localized on the short chromophore (Figure 17b, right). In contrast, the long chromophore has higher contribution to the overall transition density of the lower excited state (Figure 17c, right). In conclusion, exciton coupling in both dye stacks seems reasonable and the excited states obtained by TDDFT calculations are supposed to represent exciton states. Therefore, the molecular exciton theory is applied in the following to explain the optical absorption properties of the homo- and heteroaggregate of bis(merocyanine) **6** and **7**, respectively.

3.2.5 Quantum Chemical Investigations

As pointed out in the introduction, the impact of non-identical closely stacked chromophores on each other has so far received little attention.[20, 21, 24, 27] Nevertheless, the experimental results (Figure 12) and the outcome of the TDDFT calculations reveal significant interactions between non-identical dyes. Their mutual interactions can indeed be rationalized by exciton theory[8] considering also an exciton coupling between unequal chromophores, as recently demonstrated by Lambert and co-workers for head-to-tail connected squaraine dye co-polymers.[30]

Within exciton theory the exciton wave function Φ_e of a dimer of two chromophores 1 and 2 is described by the following linear combination:[5, 8, 30]

$$\Phi_e = c_1 \varphi_1^* \varphi_2 + c_2 \varphi_1 \varphi_2^*, \tag{38}$$

where φ_1, φ_2 are the ground state wave functions of chromophores 1, 2 and φ_1^*, φ_2^* the excited state wave functions. Furthermore, c_1 and c_2 represent coefficients that have to be determined. The Hamiltonian of the dimer is

$$\hat{H} = \hat{H}_1 + \hat{H}_2 + \hat{V}_{12}, \tag{39}$$

with $\hat{H}_1$ and $\hat{H}_2$ being the Hamiltonians of the isolated chromophores 1 and 2, and $\hat{V}_{12}$ is a perturbation between both molecules. The exciton state energy E_e of the dimer is obtained by applying the Hamiltonian operator $\hat{H}$ on the exciton wave function Φ_e:

$$\hat{H}\Phi_e = E_e\Phi_e . \tag{40}$$

Multiplying both sides of equation (40) by $\varphi_1^*\varphi_2$ followed by integration over the coordinates of both chromophores we obtain with equation (38):

$$c_1 H_{11} + c_2 H_{12} = E_e (c_1 S_{11} + c_2 S_{12}) \tag{41}$$

with

$H_{11} = \iint \varphi_1^* \varphi_2 \hat{H} \varphi_1^* \varphi_2 \, d\tau_1 d\tau_2$,

$H_{12} = \iint \varphi_1^* \varphi_2 \hat{H} \varphi_1 \varphi_2^* \, d\tau_1 d\tau_2$

and

$S_{11} = \iint \varphi_1^* \varphi_2 \varphi_1^* \varphi_2 d\tau_1 d\tau_2$,

$S_{12} = \iint \varphi_1^* \varphi_2 \varphi_1 \varphi_2^* d\tau_1 d\tau_2$.

If we neglect electronic overlap between the two chromophores, the integrals S simplify to $S_{11} = 1$ and $S_{12} = 0$. Thus, equation (41) becomes

$$c_1 H_{11} + c_2 H_{12} = E_e c_1. \tag{42}$$

Repeating the same procedure with equation (40) and multiplying it with $\varphi_1 \varphi_2^*$ we get

$$c_1 H_{21} + c_2 H_{22} = E_e c_2. \tag{43}$$

We can summarize equations (42) and (43) in a matrix notation:

$$\begin{pmatrix} H_{11} & H_{12} \\ H_{21} & H_{22} \end{pmatrix} \begin{pmatrix} c_1 \\ c_2 \end{pmatrix} = E_e \begin{pmatrix} c_1 \\ c_2 \end{pmatrix}. \tag{44}$$

The matrix elements can be simplified (for further details see the appendix) and we obtain the following eigenvalue equation for a heterodimer:

$$\begin{pmatrix} E_1^* + E_2 & J \\ J & E_2^* + E_1 \end{pmatrix} \begin{pmatrix} c_1 \\ c_2 \end{pmatrix} = E_e \begin{pmatrix} c_1 \\ c_2 \end{pmatrix}. \tag{45}$$

The eigenvalues of the Hamiltonian matrix represent the two exciton state energies of the dimer:

$$E_{e1} = -0.5 \cdot (\sqrt{(\Delta E_1 - \Delta E_2)^2 + 4J^2} - \Delta E_1 - \Delta E_2) \tag{46}$$

and

$$E_{e2} = 0.5 \cdot (\sqrt{(\Delta E_1 - \Delta E_2)^2 + 4J^2} + \Delta E_1 + \Delta E_2), \tag{47}$$

where $\Delta E_1 = E_1^* - E_1$ and $\Delta E_2 = E_2^* - E_2$ are the energy differences between the excited states and the ground states of the monomeric chromophores 1 and 2, respectively, *i.e.* the transition energies.

In the following, half the difference of the transition energies of the two monomeric chromophores is denoted by ΔE for simplicity:

$$\Delta E = \frac{\Delta E_1 - \Delta E_2}{2}, \qquad \text{with } \Delta E_1 > \Delta E_2. \tag{48}$$

The energy difference of the exciton states in the dimer (Davydov splitting) is:

$$\Delta E_{DS} = 2\sqrt{\Delta E^2 + J^2}. \tag{49}$$

For the homodimer ($\Delta E = 0$) equation (49) simplifies to:

$$\Delta E_{DS} = 2J. \tag{50}$$

Thus, in order to calculate the exciton state energies of the dye stacks one has to determine the exciton coupling energies between the two chromophores and additionally, the transition energies of both chromophores in the case of the hetero dye stack. The latter can be obtained from the corresponding absorption maxima of reference chromophores **19** and **20** in DCM/MCH 10:90. In this way, an excited state energy of 18600 cm^{-1} for the short chromophore and 15600 cm^{-1} for the long chromophore is obtained.

Turning to the calculation of the exciton coupling energy the point-dipole approximation is not applicable due to the small distance between the chromophores.[53] Thus, the more sophisticated transition charge method was applied.[55, 57] For this, TDDFT calculations (ωB97/def2-SVP) have been performed on the geometry optimized structures (B97D3/def2-SVP) of reference compounds **19** and **20** (benzyl and butyl groups were replaced by methyl groups) to obtain the transition densities of the individual chromophores (Figure 18a). The resulting magnitudes of the transition dipole moments of 9.9 D for **19** (Figure 18a, left) and 12.3 D for **20** (Figure 18a, right) are in excellent agreement with experimental values (9.8 D for the short chromophore and 12.3 D for the long chromophore, respectively).[94] To obtain the transition charges the density was then fitted to atomic charges derived by Mulliken population analysis of the transition densities using the Multiwfn software package[102] (Figure 18b and Table 2 and Table 3 in the appendix). In order to verify the accuracy of the Mulliken population analysis, the transition dipole moments of the chromophores were calculated by

$$\boldsymbol{\mu}_{eg} = \sum_i q_i \mathbf{r}_i \,, \tag{51}$$

where q_i represents the transition charge localized on atom i and $\mathbf{r}_i$ is the position vector of the respective atom. The magnitude of the transition dipole moment is obtained by

$$\mu_{eg} = \sqrt{\mu_{eg,x}^2 + \mu_{eg,y}^2 + \mu_{eg,z}^2}, \tag{52}$$

where $\mu_{eg,x}$, $\mu_{eg,y}$ and $\mu_{eg,z}$ are the components of the transition dipole moment vector $\boldsymbol{\mu}_{eg}$. The magnitudes of the transition dipole moments calculated by transition charges (9.7 D for the short chromophore and 12.2 D for the long chromophore, respectively, Figure 18b) are in very good agreement with the magnitudes of the transition dipole moments obtained directly by TDDFT calculations. In addition, the orientations of the transition dipole moments calculated from transition charges match with the orientations of the transition dipole moments calculated by TDDFT calculations.

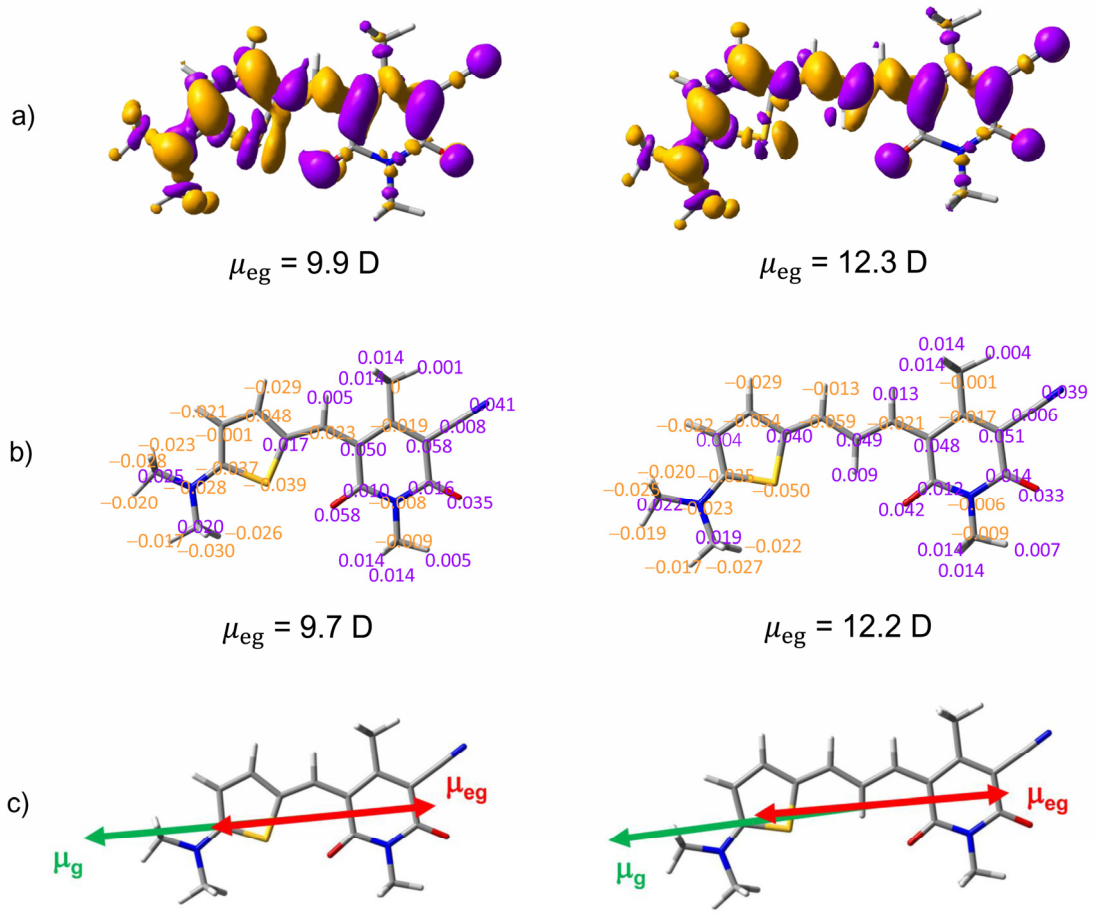

Figure 18. a) Transition density (isovalue = 0.0012 a.u.) and magnitude of transition dipole moment of reference compound **19** (left) and **20** (right) obtained by TDDFT calculations (ωB97/def2-SVP). Benzyl and butyl groups were replaced by methyl groups. b) Transition charges in atomic units of **19** (left) and **20** (right) derived by Mulliken population analysis of the transition density. In addition, the magnitudes of the transition dipole moments calculated from transition charges by equation (51)–(52) is displayed. c) Geometry optimized structures (B97D3/def2-SVP) of **19** (left) and **20** (right). The green arrow indicates the ground state dipole moment $\boldsymbol{\mu}_g$ (DFT, B97D3/def2-SVP) and the red arrow the transition dipole moment $\boldsymbol{\mu}_{eg}$ (TDDFT, ωB97/def2-SVP), respectively.

Thus, the transition charges obtained by Mulliken population analysis of the transition densities are suitable to calculate the exciton coupling energy (J) between the merocyanine chromophores, which is defined as the Coulomb interaction between the transition charges of the respective chromophores 1 and 2:[55, 57]

$$J = \frac{1}{4\pi\varepsilon_0} \sum_i \sum_j \frac{q_i^{(1)} \cdot q_j^{(2)}}{|\mathbf{r}_i^{(1)} - \mathbf{r}_j^{(2)}|}. \tag{53}$$

Here, $q_i^{(1)}$ is the transition charge on atom i of chromophore 1 and $q_j^{(2)}$ the transition charge on atom j at chromophore 2. $\mathbf{r}_i$ and $\mathbf{r}_j$ are the position vectors of the respective atoms.

Using the geometry optimized structures of both dimer stacks we obtain an exciton coupling energy of 1668 cm^{-1} for the homoaggregate and 1824 cm^{-1} for the heteroaggregate, respectively. Hence, both dye stacks exhibit strong exciton coupling with a larger coupling in the heteroaggregate. With the exciton coupling energies one can calculate the exciton state energies of the dye stacks of bis(merocyanine) dyes **6** and **7** according to equations (46)–(47) . In this way, we obtain for the homoaggregate a value of 20268 cm^{-1} (493 nm) for the higher exciton and 16932 cm^{-1} (591 nm) for the lower exciton, respectively, which is in good agreement with experimental values found for the absorption bands of folded **6** (Figure 10b, purple line). In the case of the heteroaggregate the higher exciton has an energy of 19462 cm^{-1} (514 nm) and the lower exciton of 14739 cm^{-1} (678 nm), again in good agreement with experimental values (Figure 12c, purple line).

We calculate the overall transition dipole moment ($\boldsymbol{\mu}_{eg}$) for both dye stacks to explain the shape of the absorption spectra of folded bis(merocyanine) dyes **6** (Figure 10b, purple line) and **7** (Figure 12c, purple line). The overall transition dipole moment can be described as linear combination of the transition dipole moments of the individual chromophores:

$$\boldsymbol{\mu}_{eg} = c_1\boldsymbol{\mu}_{eg,1} + c_2\boldsymbol{\mu}_{eg,2}, \tag{54}$$

with the coefficients c_1 and c_2 that can be determined by calculating the normed eigenvectors of the corresponding Hamiltonian matrix (Table 4 in the appendix). The ground state dipole moments of the chromophores are aligned in antiparallel fashion

within the stacks. Thus, it seems reasonable that the transition dipole moments of the chromophores have the same orientation because the ground state dipole moment and the transition dipole moment of a merocyanine chromophore are aligned along the same axis (Figure 18c). Consequently, the magnitude of the overall transition dipole moment μ_{eg} of the dye stacks can be calculated from equation (54) using the magnitudes of the transition dipole moments of the individual chromophores. With this, we can create an exciton state diagram for the homo- and heteroaggregate of bis(merocyanine) dyes **6** and **7** like shown in Figure 19. In the homodimer a Davydov splitting 2*J* of the excited states of the short chromophores ($S_{1,s}$) into two non-degenerated exciton states (S_1' and S_1'') is present (Figure 19a) due to the coupling. These two exciton states differ in the phase relationship of the transition dipole moments. In the case of the lower exciton state S_1', the transition dipole moments of the chromophores are coupled out of phase resulting in an overall transition dipole moments of 0 D for a perfect H-dimer comprising two equal chromophores. Thus, the corresponding transition is forbidden, whereas the transition to the higher exciton state S_1'' is strongly allowed because the transition dipole moments of the chromophores couple in phase. This in-phase coupling results in a large magnitude of the overall transition dipole moment so that the absorption spectrum of folded **6** displays one intense absorption band with a hypsochromic shift compared to the absorption maximum of the monomeric merocyanine chromophore (Figure 10). Having a closer look at the absorption spectrum of the dye stack, one can also notice three shoulders. One exhibits a hypsochromic shift and the other two a bathochromic shift with respect to the intense absorption band of the dye stack. This spectral pattern may originate from a combination of vibrational and exciton couplings and the presence of slightly twisted transition dipole moments, so that even the excitation to the lowest excited J-state gets partially allowed.[35] We assign the absorption band at 588 nm to the J-band, which is in very good agreement with the value calculated for the transition energy of the lower exciton state (591 nm). The presence of this J-band is useful since it enables us to calculate the magnitude of the exciton coupling energy $J = 0.5 \cdot (\tilde{\nu}_H - \tilde{\nu}_J) = 1400\ cm^{-1}$, where $\tilde{\nu}_H$ and $\tilde{\nu}_J$ are the energies of the H- and J-band, respectively. This exciton coupling energy is in compliance with the value calculated by transition charge method ($1668\ cm^{-1}$) revealing strong coupling between the chromophores.

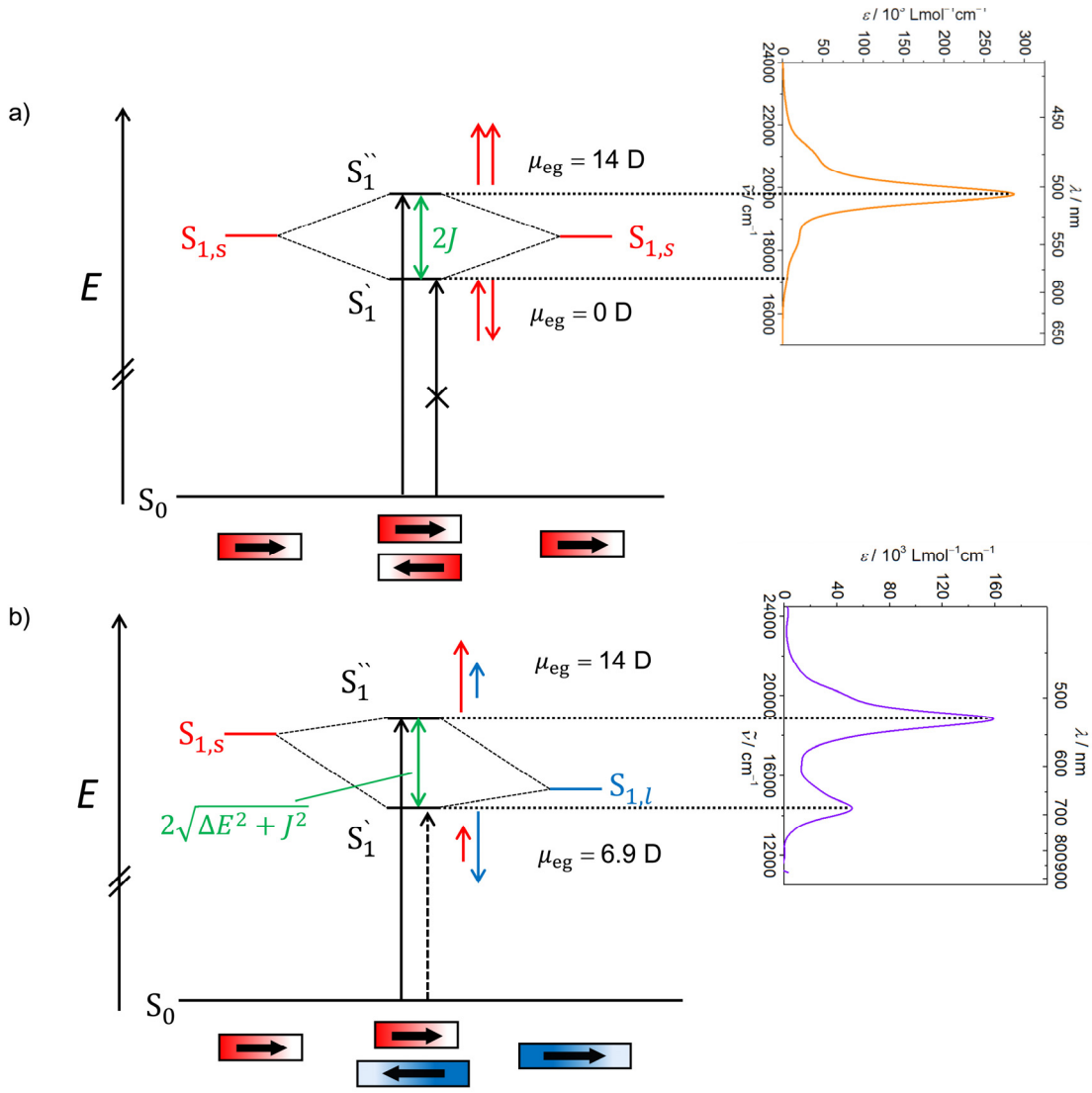

Figure 19. Exciton state diagram of the a) homoaggregate of bis(merocyanine) **6** and b) heteroaggregate of **7**. The arrows (red for short chromophore and blue for long chromophore, respectively) indicate the phase relations between the transition dipole moments. The lengths of the arrows reflect the magnitude of the coefficients of the transition dipole moments. $S_{1,s}$ represents the first excited state of the short chromophore and $S_{1,l}$ of the long chromophore, respectively, while J denotes the exciton coupling energy and ΔE is half the energy difference between the excited states $S_{1,s}$ and $S_{1,l}$. In addition, the corresponding UV/Vis spectra of **6** and **7** in DCM/MCH 10:90 (c = 5 x 10^{-6} M) are displayed.

For the stack of two different chromophores (Figure 19b) we assume again an exciton coupling resulting in a splitting of the excited states, whereby the transition to the higher exciton state $S_1^{''}$ is allowed due to the in-phase coupling of the transition dipole moments of the individual chromophores. Most interestingly, and in contrast to the homodimer of bis(merocyanine) **6**, the lower exciton state $S_1^{'}$ is now partially allowed in the heterodimer, even for a perfect H-aggregate. One reason is the different magnitude of the transition

dipole moments of the two chromophores so that the out-of-phase coupling does not result in an overall transition dipole moment of 0 D. In addition, for a heterodimer the coefficients c_1 and c_2 depend on the energy difference ΔE of the two chromophores leading to different magnitudes of c_1 and c_2 (Table 4 in the appendix) as illustrated in Figure 20.

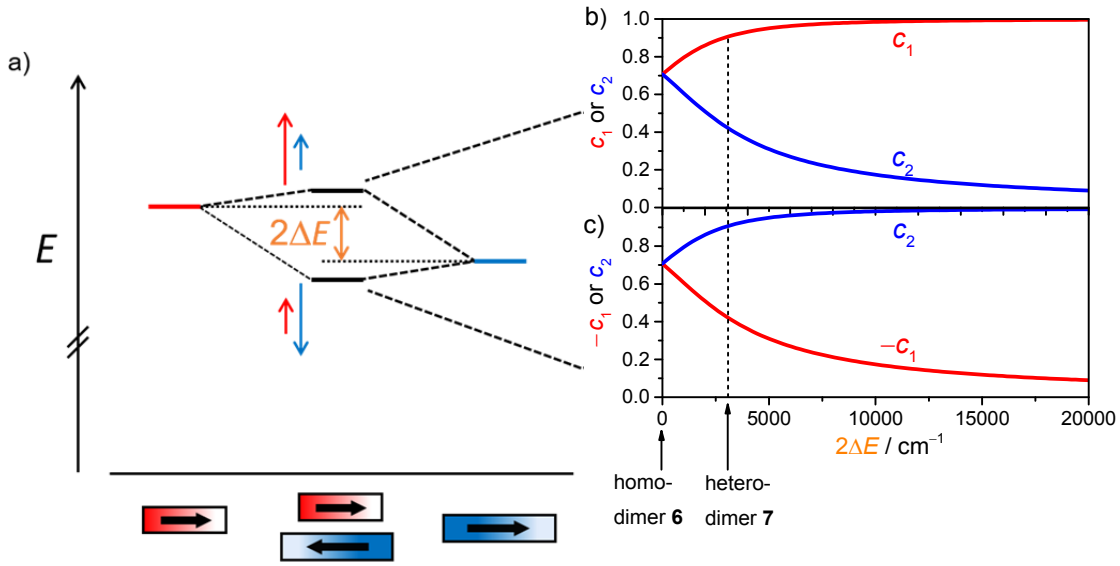

Figure 20. a) Exciton state diagram for a dimer comprising two chromophores with different excited state energies (the energy difference amounts to $2\Delta E$). Also shown are the coefficients b) c_1 and c_2 for the higher exciton and c) $-c_1$ and c_2 for the lower exciton as a function of $2\Delta E$. An exciton coupling energy of J = 1824 cm^{-1} is assumed for the calculation. c_1 denotes the coefficient of the chromophore with higher excited state energy and c_2 of the chromophore with lower excited state energy, respectively.

Figure 20b,c shows how the coefficients change upon increasing the energy difference between the excited states of the monomeric chromophores ($2\Delta E$) starting with a homodimer ($2\Delta E = 0$). The exciton coupling energy is kept fixed at a value of 1824 cm^{-1} as calculated for the heterodimer of bis(merocyanine) **7** by transition charge method (note: c_1 is the coefficient of the chromophore with higher excited state energy). In the case of a homodimer both coefficients have the same magnitude ($\frac{1}{\sqrt{2}}$), which is in agreement with the results obtained by TDDFT calculations where the transition density is equally distributed over the two chromophores (Figure 17b,c, left). Whereas for the higher exciton (Figure 20b) the coefficients are both positive, they have a different sign for the lower exciton (Figure 20c). On increasing the energy difference between the excited states of the

two chromophores, c_1 is increasing for the higher exciton while c_2 is decreasing (Figure 20b). This is vice versa in the case of the lower exciton. Here, the magnitude of c_1 is decreasing upon increasing the energy difference whereas c_2 is increasing. For an energy difference of $2\Delta E = 3000$ cm^{-1}, as it is the case for the two chromophores of bis(merocyanine) **7**, the coefficients amount to $c_1 = 0.90$ and $c_2 = 0.43$ for the higher exciton and $c_1 = -0.43$ and $c_2 = 0.90$ for the lower exciton, respectively. Again, this is in agreement with the transition densities obtained for the dye stack of bis(merocyanine) **7** showing that for the lower/higher exciton the transition density is more localized on the long/short chromophore (Figure 17b,c, left). Therefore, the out-of-phase coupling does not lead to an overall transition dipole moment of 0 D for the lower exciton, even if the magnitudes of the individual transition dipole moments were equal. However, the different magnitudes of the transition dipole moments lead to an additional increase of the value of the overall transition dipole moment for the lower exciton. Thus, the absorption spectrum of folded **7** (Figure 12c, purple line) exhibits an absorption band of substantial intensity with a bathochromic shift compared to the absorption maximum of the long chromophore. As in the case of the homoaggregate, one can furthermore observe a vibronic progression of the absorption band at 531 nm leading to an absorption shoulder at shorter wavelengths. The exciton coupling energy J for the heterodimer of bis(merocyanine) **7** can be calculated from the two respective band maxima by $J = \sqrt{(0.25 \cdot \Delta\tilde{\nu}^2 - \Delta E^2)} = 1609$ cm^{-1}. $\Delta\tilde{\nu}$ is the energy difference between the maxima of the J- and the H- band and ΔE is half the energy difference between the absorption maxima of the two respective monomeric chromophores. This value is in good agreement with the exciton coupling energy of 1824 cm^{-1} estimated by transition charge method. Hence, the analysis of the UV/Vis spectra as well as the transition charge method reveal a stronger exciton coupling in the case of the heterodimer. We attribute this mainly to the larger transition dipole moment of the long chromophore resulting in a stronger Coulomb coupling of the transition dipole moments.

It is apparent from Figure 20b that for large energy differences $2\Delta E$ the coefficient c_1 approaches unity while c_2 converges to zero for the higher exciton revealing that only the chromophore with higher excited state contributes to this transition. This is vice versa for the lower exciton and thus, the corresponding heterodimer will have similar optical absorption properties compared to the respective isolated chromophores, even if a strong

coupling is present. Furthermore, it is evident from equation (49) that for an increase of ΔE the influence of the exciton coupling energy J on the Davydov splitting is decreasing as pointed out by Lambert *et al*.[77] Hence, the fact that the UV/Vis spectrum of a heteroaggregate exhibits only small differences compared to the spectrum of the individual chromophores does not necessarily indicate a weak coupling between the dyes. This wrong conclusion might be the reason for the common perception[26] that exciton coupling is weak between chromophores with different absorption maxima.

3.3 Conclusion

In summary, a new bis(merocyanine) dye **7** composed of two different merocyanine chromophores tethered by a rigid diphenylacetylene spacer unit has been synthesized. This bichromophoric system undergoes folding in non-polar solvents resulting in a hetero-π-stack of two chromophores, in an analogous manner to the folding of bis(merocyanine) **6** with two equal chromophores that had been synthesized in earlier work. The insights derived from both systems are quite remarkable: not only for the homoaggregate but also for the heteroaggregate pronounced changes of the absorption spectra are observed upon folding. The absorption spectra obtained by TDDFT calculations resemble the experimental spectra of the folded species and our quantum chemical analysis reveals strong exciton coupling for the homo- and heterodimer. The most interesting outcome of the study is that dyes with different excited state energies strongly couple with each other. The coupling induces a pronounced redistribution of the oscillator strength, which in turn leads to a strong decrease of the lower energy absorption band. Further, our theoretical analyses based on exciton coupling theory suggest that the exciton coupling energy is even larger for the hetero- than for the homoaggregate despite of the significant difference in the excited state energies of the two chromophores. These interesting results, in particular the surprisingly large exciton coupling strength in the heteroaggregate, clearly motivate future experimental and theoretical investigation.

3.4 Experimental Section

3.4.1 Materials and Methods

All solvents and reagents were purchased from commercial sources and used as received without further purification. Column chromatography was performed using silica gel 60M (0.04–0.063 mm). NMR spectra were recorded on an Bruker Avance III HD spectrometer at 295 K. The spectra were calibrated to the residual solvent peak and the chemical shifts δ are in ppm. Multiplicities are denoted as follows: s = singlet, d = doublet, t = triplet, m = multiplet, br = broad. High-resolution mass spectra (ESI) were recorded on an ESI MicrOTOF Focus spectrometer. Melting points were determined on Olympus BX41 optical microscope with heating stage and are uncorrected. Solvents for spectroscopic studies were of spectroscopic grade and used as received. UV/Vis spectra were measured on a Lambda 950 or 35 spectrometer at 298 K in conventional quartz cell cuvettes with path lengths of 1–20 mm. The scan rate were 1 nm and 120 nm min^{-1}, respectively. For concentration-dependent studies freshly prepared stock solutions were subsequently diluted to adjust the desired concentration.

3.4.2 Synthesis and Characterization

(*Z*)-5-(*E*)-3-{[5-(Dibutylamino)thiophene-2-yl]allylidene}-1-(2-ethynylbenzyl)-4-methyl-2,6-dioxo-1,2,5,6-tetrahydropyridine-3-carbonitrile 14:

A suspension of hydroxyl pyridine **10** (445 mg, 1.68 mmol) and aminothiophene aldehyde **12** (406 mg, 1.53 mmol) in acetic anhydride (5 mL) was stirred for 16 h at 100 °C. The solvent was removed under reduced pressure and the crude product was purified by column chromatography (silica gel, CH_2Cl_2/ethyl acetate 10:1) to give merocyanine dye **14** as a green solid.

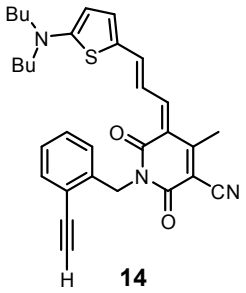

14

$C_{31}H_{33}N_3O_2S$ (511.68)

Yield: 180 mg (352 μmol, 23%), green solid.

Mp. 195 °C. ^{1}H NMR (400 MHz, CD_2Cl_2): δ = 8.00 (br, 1H), 7.57–7.34 (m, 4H), 7.29–7.16 (m, 2H), 6.89 (m, 1H), 6.25 (d, ^{3}J = 4.8 Hz, 4H), 5.33 (s, 2H, overlapped with solvent signal), 3.48 (s, 1H), 3.46 (t, ^{3}J = 7.8 Hz, 1H), 2.51 (s, 3H), 1.78–1.63 (m, 4H), 1.43–1.33 (m, 4H), 0.96 (t, ^{3}J = 7.3 Hz, 6H). ^{13}C NMR (101 MHz, CD_2Cl_2): δ = 171.8, 163.6, 162.6, 158.4, 152.1, 149.6, 145.2, 140.6, 133.1, 129.4, 127.5, 126.8, 125.1, 120.6, 118.8, 117.7, 111.5, 110.6, 94.8, 83.0, 81.5, 55.1, 42.0, 29.5, 20.5, 19.0, 13.9. HRMS (ESI, positive, acetonitrile/chloroform): *m/z* 511.22872 $[M]^{+}$, calculated for $C_{31}H_{33}N_3O_2S^{+}$: 511.22880. UV/Vis (CH_2Cl_2): λ_{max}/nm (ε/M^{-1} cm^{-1}) = 656 (223000).

Bis(merocyanine) 7:

Merocyanine **18** (150 mg, 256 µmol), bis(triphenylphosphine)-palladium(II) dichloride (3.70 mg, 5.29 µmol) and copper(I) iodide (1.01 mg, 5.26 µmol) were suspended in diisopropylamine (20 mL) and THF (60 mL) and the mixture was degassed by applying the freeze-pump-thaw method. A degassed solution of compound **14** (87.4 mg, 171 µmol) in THF (40 mL) was added dropwise under nitrogen atmosphere. After stirring for 1 h at 60 °C, the solvent was removed under reduced pressure and the crude product was then purified by column chromatography (silica, CH_2Cl_2/ethyl acetate 10:1) to give **7** as dark green solid.

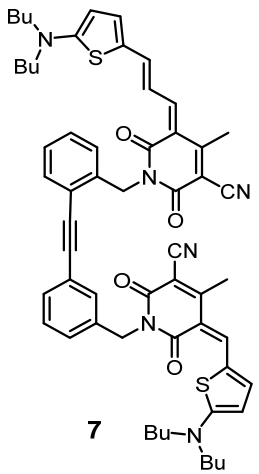

7

$C_{58}H_{62}N_6O_4S_2$ (971.29)

Yield: 26.6 mg (27.4 µmol, 16%), dark green solid.

Mp. 157 °C. ^{1}H NMR (400 MHz, CD_2Cl_2): δ = 8.00 (br, 1H), 7.60 (m, 1H), 7.57 (s, 1H), 7.56–7.51 (m, 2H), 7.46 (m, 2H), 7.43 (m, 1H), 7.40–7.36 (m, 2H), 7.29 (m, 1H), 7.25–7.18 (m, 2H), 6.93 (m, 1H), 6.41 (d, ^{3}J = 5.2 Hz, 1H), 6.24 (d, ^{3}J = 4.7 Hz, 1H), 5.36 (s,

2H), 5.17 (s, 2H), 3.53 (t, ^3J = 7.8 Hz, 4H), 3.44 (t, ^3J = 7.8 Hz, 4H), 2.48 (s, 3H), 2.47 (s, 3H), 1.75–1.63 (m, 8H), 1.44–1.32 (m, 8H), 0.99–0.93 (m, 12H). ^{13}C NMR (101 MHz, CD_2Cl_2): δ = 176.7, 172.0, 163.6, 163.4, 162.63, 162.61, 158.8, 158.2, 152.7, 151.7, 149.4, 145.2, 142.1, 139.9, 138.8, 132.5, 131.4, 130.7, 128.80, 128.77, 128.6, 127.7, 126.8, 125.4, 125.0, 123.6, 121.7, 118.9, 117.9, 117.8, 111.7, 111.5, 110.7, 107.0, 95.2, 94.6, 94.3, 87.4, 55.1, 42.8, 42.2, 29.5, 20.5, 19.1, 19.0, 13.9. HRMS (ESI, positive, acetonitrile/chloroform): *m/z* 971.43384 $[M+H]^+$, calculated for $C_{58}H_{63}N_6O_4S_2^+$: 971.43467. UV/Vis (CH_2Cl_2): λ_{max}/nm (ε/M^{-1} cm^{-1}) = 540 (151000), 657 (192000).

3.4.3 Computational Calculations

All calculations were performed using the Gaussian 09 program package.[103] The structures were geometry optimized, followed by frequency calculations on the optimized structures. One very small imaginary frequency of 11i cm^{-1} was obtained for bis(merocyanine) dye **7**. Small imaginary frequencies (<100i cm^{-1}) are considered most likely to be an artefact of the calculation,[104] thus, the resulting geometries can be seen as real minima.

UV/Vis spectra were simulated with the help of the GaussView 5[105] visualization software package using the results obtained by TDDFT calculations with a half-width at half-height of 0.10 eV.

3.5 Appendix

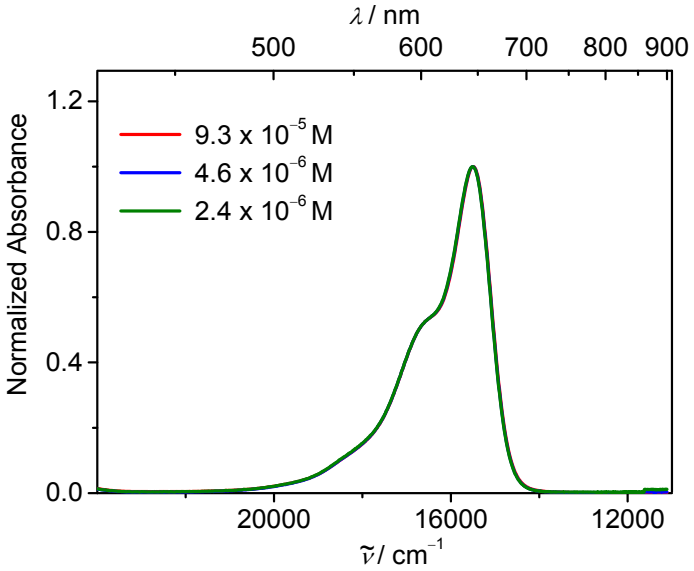

Figure 21. Normalized UV/Vis absorption spectra of bis(merocyanine) **20** in DCM/MCH 10:90 at different concentrations (298 K).

Additional Theoretical Investigations

The matrix elements of equation (44) in the main text can be simplified and we will first discuss the non-diagonal matrix elements.

With equation (39) we can write for H_{12}:

$$H_{12} = \iint \varphi_1^* \varphi_2 \hat{\mathrm{H}}_1 \varphi_1 \varphi_2^* \, \mathrm{d}\tau_1 \mathrm{d}\tau_2 + \iint \varphi_1^* \varphi_2 \hat{\mathrm{H}}_2 \, \varphi_1 \varphi_2^* \, \mathrm{d}\tau_1 \mathrm{d}\tau_2 + \iint \varphi_1^* \varphi_2 \hat{\mathrm{V}}_{12} \, \varphi_1 \varphi_2^* \, \mathrm{d}\tau_1 \mathrm{d}\tau_2. \tag{55}$$

Due to orthonormalization of the wave functions we can simplify the first two terms:

$$\iint \varphi_1^* \varphi_2 \hat{\mathrm{H}}_1 \varphi_1 \varphi_2^* \, \mathrm{d}\tau_1 \mathrm{d}\tau_2 = \int \varphi_2 \varphi_2^* \, \mathrm{d}\tau_2 \int \varphi_1^* \hat{\mathrm{H}}_1 \varphi_1 \, \mathrm{d}\tau_1 = 0$$

and

$$\iint \varphi_1^* \varphi_2 \hat{\mathrm{H}}_2 \, \varphi_1 \varphi_2^* \mathrm{d}\tau_1 \mathrm{d}\tau_2 = \int \varphi_1^* \varphi_1 \, \mathrm{d}\tau_1 \int \varphi_2 \hat{\mathrm{H}}_2 \, \varphi_2^* \, \mathrm{d}\tau_2 = 0.$$

Thus, only the last term $\iint \varphi_1^* \varphi_2 \hat{\mathrm{V}}_{12} \, \varphi_1 \varphi_2^* \, \mathrm{d}\tau_1 \mathrm{d}\tau_2$ remains, which is the exciton coupling energy J. The same is valid for H_{21} and we obtain for eigenvalue equation (44):

$$\begin{pmatrix} H_{11} & J \\ J & H_{22} \end{pmatrix} \begin{pmatrix} c_1 \\ c_2 \end{pmatrix} = E_\mathrm{e} \begin{pmatrix} c_1 \\ c_2 \end{pmatrix}. \tag{56}$$

In addition, also the diagonal matrix elements can be simplified if we neglect van-der-Waals energy contributions. For H_{11} we write:

$$H_{11} = \iint \varphi_1^* \varphi_2 \hat{H}_1 \varphi_1^* \varphi_2 \, d\tau_1 d\tau_2 + \iint \varphi_1^* \varphi_2 \hat{H}_2 \, \varphi_1^* \varphi_2 d\tau_1 d\tau_2 + \iint \varphi_1^* \varphi_2 \hat{V}_{12} \, \varphi_1^* \varphi_2 \, d\tau_1 d\tau_2. \quad (57)$$

The last term describes the van-der-Waals interaction between chromophore 1 in the excited state and chromophore 2 in the ground state, which will be ignored. In addition, the first term can be simplified due to orthonormalization of the wave functions:

$$\iint \varphi_1^* \varphi_2 \hat{H}_1 \varphi_1^* \varphi_2 \, d\tau_1 d\tau_2 = \int \varphi_2 \varphi_2 \, d\tau_2 \int \varphi_1^* \hat{H}_1 \varphi_1^* d\tau_1 = \int \varphi_1^* \hat{H}_1 \varphi_1^* d\tau_1 = E_1^*, \quad (58)$$

where E_1^* is the excited state energy of monomeric chromophore 1. The second integral in equation (57) represents the ground state energy of chromophore 2:

$$\iint \varphi_1^* \varphi_2 \hat{H}_2 \, \varphi_1^* \varphi_2 \, d\tau_1 d\tau_2 = \int \varphi_1^* \varphi_1^* \, d\tau_1 \int \varphi_2 \hat{H}_2 \, \varphi_2 d\tau_2 = \int \varphi_2 \hat{H}_2 \, \varphi_2 d\tau_2 = E_2. \quad (59)$$

Hence, the diagonal matrix element H_{11} is

$$H_{11} = E_1^* + E_2. \quad (60)$$

The same holds true for H_{22} and we can write:

$$H_{22} = E_2^* + E_1. \quad (61)$$

Table 2. Cartesian coordinates of the geometry optimized structure (B97D3/def-2SVP) of **19** and transition charges derived from Mulliken population analysis of the transition density obtained by TDDFT calculations (ωB97/def2-SVP).

	x	y	z	transition charges
C	3.77493	–0.33666	–0.03340	–0.03717
C	3.62867	–1.74358	–0.01579	–0.00131
C	2.28565	–2.12202	–0.00724	–0.04826
C	1.35256	–1.05516	–0.00554	0.01729
S	2.22376	0.49426	–0.01089	–0.03900
N	4.93693	0.36561	–0.06159	–0.02846
C	6.20091	–0.35028	0.04026	0.02470
C	4.90879	1.81896	0.03031	0.02014
C	–0.03750	–1.30055	0.00251	–0.02255
C	–1.21235	–0.53444	0.00413	0.04969
C	–2.49860	–1.19618	0.00616	–0.01850
C	–3.65940	–0.43258	0.00283	0.05807
C	–3.64949	1.04376	–0.00266	0.01565
N	–2.36755	1.63814	–0.00180	–0.00750
C	–1.15869	0.93866	0.00399	0.01046
O	–0.10191	1.57938	0.00938	0.05791
C	–2.28036	3.09972	–0.00375	–0.00898
O	–4.66913	1.72142	–0.00703	0.03466
C	–2.59061	–2.70191	0.01082	0.00036
C	–4.95384	–1.03821	0.00396	0.00826
N	–5.99935	–1.56823	0.00510	0.04140
H	4.46361	–2.44712	–0.01034	–0.02142
H	1.95108	–3.16493	–0.00021	–0.02890
H	7.03167	0.35955	–0.08894	–0.01999
H	6.27914	–1.11957	–0.74978	–0.02303
H	6.31393	–0.85084	1.02311	–0.02787
H	4.61016	2.16494	1.04112	–0.02983
H	5.90608	2.22141	–0.20378	–0.01680
H	–0.21542	–2.38199	0.00721	0.00525
H	–3.30537	3.49270	–0.01038	0.00517
H	–1.72528	3.44255	–0.89276	0.01419
H	–1.73587	3.44587	0.89056	0.01409
H	–3.63769	–3.03805	0.01463	0.00084
H	–2.09712	–3.13193	–0.87975	0.01375
H	–2.09207	–3.12678	0.90102	0.01369
H	4.18720	2.23386	–0.69769	–0.02599

Table 3. Cartesian coordinates of the geometry optimized structure (B97D3/def-2SVP) of **20** and transition charges derived from Mulliken population analysis of the transition density obtained by TDDFT calculations (ωB97/def2-SVP).

	x	y	z	transition charges
C	4.99540	–0.13305	–0.03564	0.03473
C	5.11274	–1.53791	–0.02397	–0.00434
C	3.86204	–2.18061	–0.02329	0.05378
C	2.75770	–1.31429	–0.02112	–0.04032
S	3.31178	0.36976	–0.01624	0.05005
N	5.99484	0.79056	–0.05877	0.02302
C	7.37109	0.33204	0.06161	–0.02185
C	5.68276	2.20526	0.07924	–0.01917
C	1.38242	–1.65110	–0.01527	0.05935
C	–2.20969	–0.46645	–0.00317	–0.04768
C	–3.48966	–1.13852	0.01098	0.01670
C	–4.65824	–0.38828	0.01287	–0.05147
C	–4.66472	1.08961	0.00074	–0.01415
N	–3.39445	1.69999	–0.01262	0.00605
C	–2.16484	1.02222	–0.01537	–0.01160
O	–1.12665	1.68430	–0.02769	–0.04218
O	–5.69674	1.74979	0.00219	–0.03255
C	–3.56356	–2.64541	0.02386	0.00094
C	–5.94587	–1.00790	0.02682	–0.00645
N	–6.98511	–1.55017	0.03851	–0.03947
H	6.06938	–2.06342	–0.01581	0.02211
H	3.73706	–3.26840	–0.02111	0.02930
H	8.05054	1.18713	–0.07248	0.01935
H	7.60113	–0.41594	–0.71896	0.01974
H	7.57019	–0.12735	1.05140	0.02488
H	5.35328	2.46341	1.10717	0.02688
H	6.57281	2.80356	–0.16901	0.01735
H	1.17148	–2.73151	–0.00735	0.01283
H	–4.60632	–2.99460	0.03361	–0.00439
H	–3.06667	–3.07315	–0.86572	–0.01356
H	–3.05478	–3.05835	0.91370	–0.01358
H	4.87431	2.48733	–0.62064	0.02201
C	–3.32918	3.16252	–0.02502	0.00936
H	–2.77743	3.52229	0.85943	–0.01415
H	–4.35941	3.54145	–0.02093	–0.00747
H	0.49273	0.31761	–0.02713	–0.00899
C	0.31686	–0.76252	–0.01692	–0.04938
H	–1.13981	–2.30422	0.00397	–0.01283
C	–1.02307	–1.21314	–0.00522	0.02123
H	–2.78989	3.50771	–0.92287	–0.01405

Table 4. Components of the normed eigenvectors of the Hamiltonian matrix for the dye stacks of bis(merocyanine) dyes **6** and **7**.

	Exciton state 1:	Exciton state 2:
Bis(merocyanine) **6**	$c_1 = \frac{1}{\sqrt{2}}$ $c_2 = -\frac{1}{\sqrt{2}}$	$c_1 = \frac{1}{\sqrt{2}}$ $c_2 = \frac{1}{\sqrt{2}}$
Bis(merocyanine) **7**	$c_1 = \frac{1}{\sqrt{1+\frac{\left(\sqrt{\Delta E^2+J^2}+\Delta E\right)^2}{J^2}}}$ $c_2 = -\frac{\left(\sqrt{\Delta E^2+J^2}+\Delta E\right)}{J\sqrt{1+\frac{\left(\sqrt{\Delta E^2+J^2}+\Delta E\right)^2}{J^2}}}$	$c_1 = \frac{1}{\sqrt{1+\frac{\left(\sqrt{\Delta E^2+J^2}-\Delta E\right)^2}{J^2}}}$ $c_2 = -\frac{\left(\sqrt{\Delta E^2+J^2}-\Delta E\right)}{J\sqrt{1+\frac{\left(\sqrt{\Delta E^2+J^2}-\Delta E\right)^2}{J^2}}}$

Chapter 4

Exciton Coupling in Homo- and Heteroaggregate Quadruple Stacks of Merocyanine Dyes[4]

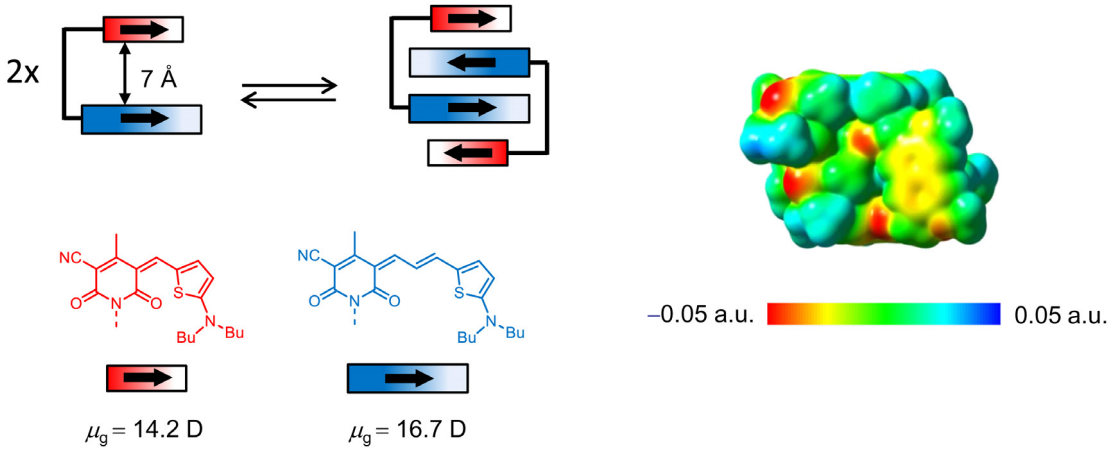

Abstract: Quadruple dye stacks were obtained from two bis(merocyanine) dyes with same or different chromophores, respectively, which dimerize in less-polar solvents resulting in the respective homo- and heteroaggregates. The structures of the quadruple dye stacks were assigned by NMR techniques and unambiguously confirmed by single-crystal X-ray analysis. The heteroaggregate stack formed from the bis(merocyanine) bearing two different chromophores exhibits remarkably different UV/Vis absorption bands compared to those of the homoaggregate of the bis(merocyanine) comprising two identical chromophores. Quantum chemical analysis based on an extension of Kasha's exciton theory appropriately describes the absorption properties of both types of stacks revealing strong exciton coupling also between different chromophores within the heteroaggregate.

---

[4]This chapter was published in: D. Bialas, A. Zitzler-Kunkel, E. Kirchner, D. Schmidt, F. Würthner, *Nat. Commun.* **2016**, *7*, 12949 (http://www.nature.com/articles/ncomms12949). Reproduced and adopted with permission. Copyright 2016 Nature Publishing Group.

4.1 Introduction

The unexpected optical absorption properties of the hetero-π-stack of bis(merocyanine) **7** (see Chapter 3) caused by strong exciton coupling between the different types of chromophores motivated us to elucidate exciton coupling in larger heteroaggregates. It was known from earlier work that bis(merocyanine) **21** bearing the same type of chromophores linked by a rigid naphthalene spacer self-assembles in less-polar solvents resulting in quadruple dye stacks (Figure 22a)[106]

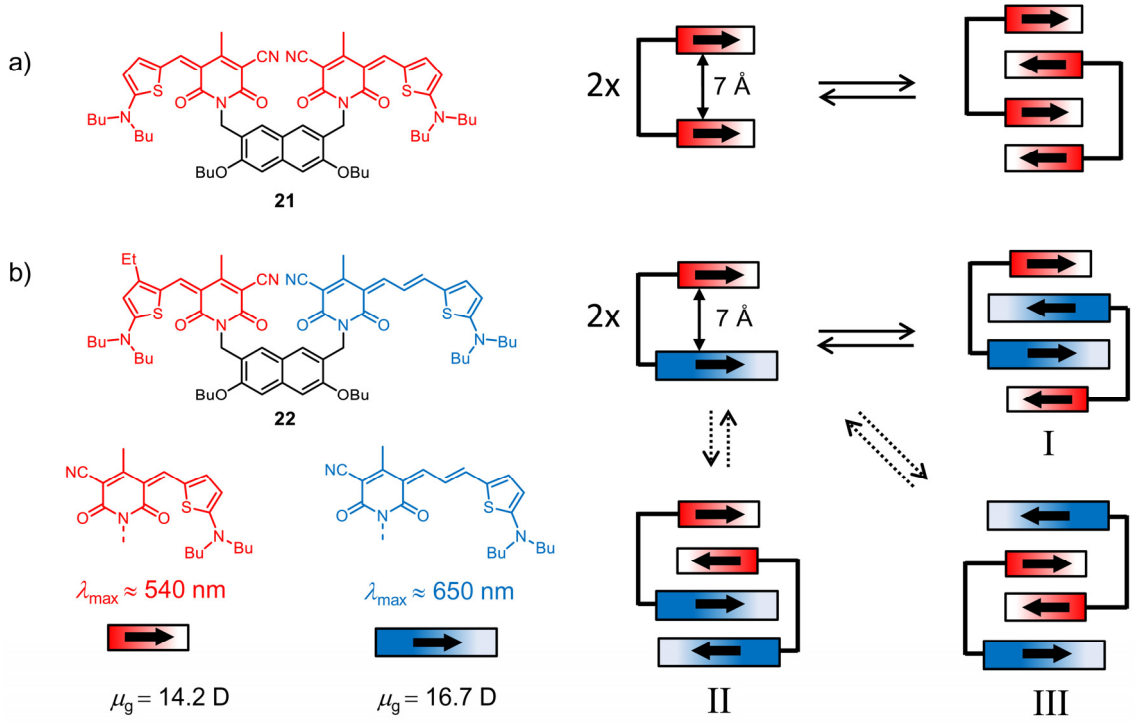

Figure 22. Chemical structure of bis(merocyanine) **21** with two identical chromophores and its self-aggregation into homodimer stack. b) Chemical structure of bis(merocyanine) **22** with two different chromophores and its self-aggregation into three possible dimer structures. The bold arrows illustrate ground state dipole moments of the chromophore units.

Keeping this in mind, we have designed bis(merocyanine) dye **22** comprising two merocyanine chromophores of different conjugation lengths, respectively (Figure 22b). For this unsymmetric bis(merocyanine) in principle three different types of dimer aggregate structures are possible. Hence, 2D NMR spectroscopy was provided to elucidate which dimer structures are formed upon self-assembly of **22**. For this purpose, an ethyl group was attached to the short chromophore which should act as a probe. In the following studies, bis(merocyanine) **21** containing two equal chromophores serves as reference compound.

4.2 Results and Discussion

4.2.1 Synthesis

Bis(merocyanine) dye **21**[5] was synthesized *via* Knoevenagel condensation reaction of literature known napthalenedimethylene-bridged bis(pyridone) **23**[107] and aminothiophene **11**[92, 93] (Scheme 2). The synthesis of the unsymmetrical bis(merocyanine) **22** bearing two different merocyanine chromophores that are tethered by the same spacer unit as in **21** could also be accomplished by condensation of bis(pyridone) **23** with the aminothiophenes **24** and **12** in a one-pot reaction.

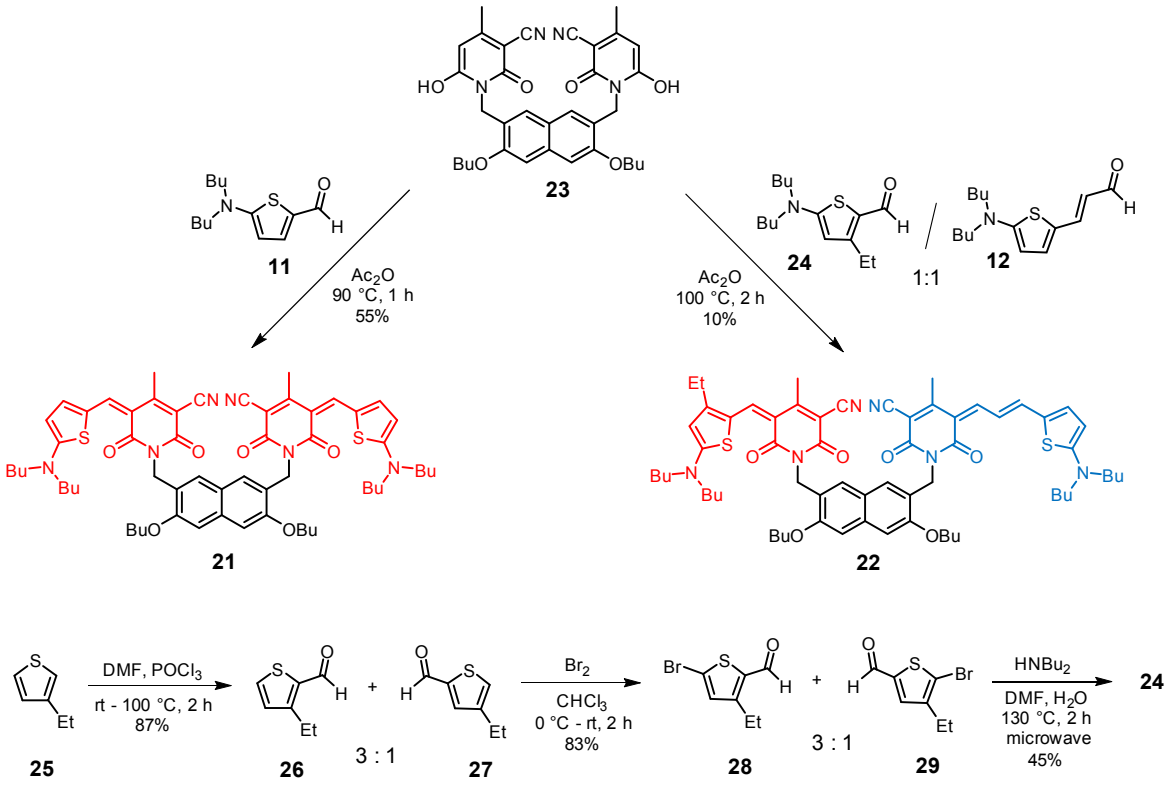

Scheme 2. Synthesis of symmetric bis(merocyanine) **21**[106] and unsysmmetric bis(merocyanine) **22**, and the precursor aminothiophene **24**.

While aminothiophene **12** is literature known,[94] the unknown derivative **24** was synthesized in three steps starting with the commercially available 3-ethylthiophene **25** as outlined in Scheme 2 (bottom). In the first step, Vilsmaier-Haack formylation of **25** according to a literature known procedure[108] led to the formation of a 3:1 regioisomeric mixture of 3-ethylthiophene-2-carboxaldehyde **26** and 4-ethylthiophene-2-carboxaldehyde

[5] Bis(merocyanine) **21** was synthesized by Dr. André Zitzler-Kunkel.

27. The undesired regioisomer **27** could not be separated by column chromatography due to similar polarity of both isomers. Thus, the obtained mixture was brominated to give the corresponding regioisomeric bromo-thiophene derivatives **28** and **29** again in a 3:1 mixture, which was then subjected to a microwave reaction with dibutylamine resulting in exclusive formation of aminothiophene **24** by selective amination of the major bromo-thiophene isomer **28**, where the bromine substituent is sterically less encumbered.

4.2.2 Concentration-dependent UV/Vis Spectroscopy

The aggregation properties of bis(merocyanine) dyes **21** and **22** have been explored by concentration-dependent UV/Vis studies in chlorobenzene. At a low concentration ($c = 4.4 \times 10^{-7}$ M), bis(merocyanine) **21** shows a typical absorption spectrum with a maximum at 541 nm for the utilized monomeric merocyanine chromophore (Figure 23a).[94]

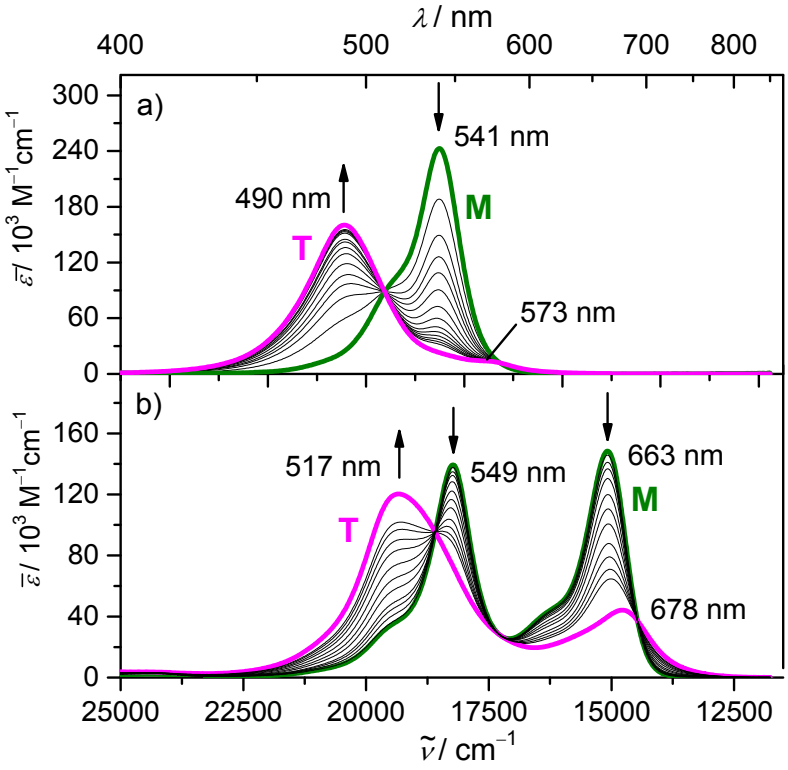

Figure 23. Concentration-dependent UV/Vis spectra of a) bis(merocyanine) **21** ($c = 4.4 \times 10^{-7} - 6.0 \times 10^{-4}$ M) and b) bis(merocyanine) **22** ($c = 5.0 \times 10^{-7} - 3.4 \times 10^{-4}$ M) in chlorobenzene at 298 K. The arrows indicate the spectral changes upon increasing the concentration. The green (denoted with M) and the purple lines (denoted with T) represent the calculated spectra of the monomers and the tetrachromophoric (dimer) stacks, respectively, by extrapolation of the spectral data towards most diluted and most concentrated solutions.

Upon increasing the concentration (up to 6.0 x 10^{-4} M), the absorption band at 541 nm decreases with concomitant appearance of a new, hypsochromically shifted absorption band at 490 nm, which is an indication for the formation of strongly exciton coupled H-type aggregates.[8] In contrast to the symmetrical bis(merocyanine) **21**, the monomer solution of unsymmetrical bis(merocyanine) **22** in chlorobenzene at a low concentration (c = 5.0 x 10^{-7} M) displays two absorption bands with maxima at 549 and 663 nm (Figure 23b), which closely resemble those of the individual merocyanine chromophores.[94] Upon increasing the concentration (up to 3.4 x 10^{-4} M), both bands decrease in an analogous manner while a new broad band at 517 nm appears concurrently. This hypsochromically shifted band signifies the formation of excitonically coupled H-type aggregates. For the concentration-dependent spectra of both bis(merocyanine) dyes clear isosbestic points at 510 and 579 nm (for **21**) and at 538, 580 and 691 nm (for **22**) were observed, revealing an equilibrium between two species, respectively, these are the monomer and the corresponding dimer. Indeed, the concentration-dependent UV/Vis absorption data of bis(merocyanine) dyes **21** and **22** could be properly fitted to the dimer model[95] (fitting curves are shown in Figure 24), corroborating the formation of bimolecular complexes in both cases. Thus, a dimerization constant (K_D) of 5.04 x 10^5 M^{-1} (for **21**) and 2.24 x 10^4 M^{-1} (for **22**) in chlorobenzene and Gibbs free energies (ΔG_D^0) of –32.5 kJ mol^{-1} and –24.8 kJ mol^{-1}, respectively, were calculated based on the dimer model.

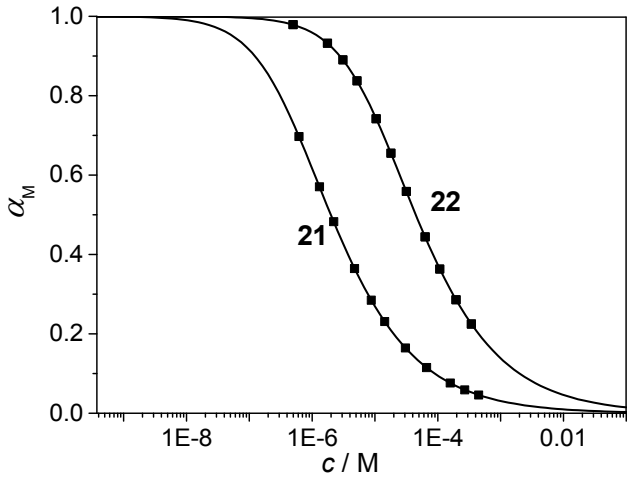

Figure 24. Plot of the fraction of monomeric species α_M against the total concentration calculated from the UV/Vis data at 298 K and results of the non-linear regression analysis based on the dimerization model for bis(merocyanine) dyes **21** and **22** in chlorobenzene (■). Also shown are the respective fitting curves (solid lines) according to the dimer model.

With this, the ideal monomer (green line) and dimer (magenta line) spectra could be calculated (Figure 23). The calculated dimer spectra of bis(merocyanine) **21** (Figure 23a, magenta line) exhibits an intense absorption band at 490 nm with a very weak transition at 573 nm, whereas the calculated dimer spectrum of **22** (Figure 23b, magenta line) shows two absorption bands at 517 and 678 nm, the latter being of considerably strong intensity. Whilst the dimer spectrum of **21** can easily be rationalized based on Kasha's exciton theory, the situation for **22** is obviously more complicated and does not enable us to relate the UV/Vis spectra to one of the structural models I, II or III shown in Figure 22.

4.2.3 NMR Spectroscopy

To elucidate the structural features of bis(merocyanines) **21**[6] and **22** aggregates, in-depth one- and two-dimensional (2D) NMR studies were performed. The ^{1}H NMR spectrum of **21** in high-polarity solvent CD_2Cl_2 (c = 1 x 10^{-3} M), where this dye does not aggregate, displays a single set of nicely resolved proton signals as expected for the monomer of this C_{2v} symmetric molecule, whose both halves are chemically equivalent on the NMR time scale (Figure 25c). The signals could be clearly assigned to the chromophore and backbone protons of this dye by 2D correlation spectroscopy (COSY) (data are listed in Table 7 in the appendix). In contrast to the spectrum in CD_2Cl_2, ^{1}H NMR spectrum of **21** in less-polar C_6D_5Cl (c = 1 x 10^{-3} M), where almost only aggregated species are present (Figure 24), shows a complex signal pattern with significantly higher number of proton resonances (Figure 25d). As the proton signals are well separated, they can be reliably assigned to the chromophore and spacer protons of dye **21** by 2D COSY and rotating frame Overhauser effect spectroscopy (ROESY) experiments, revealing a splitting of the monomer proton signals into two sets of signals (for the detailed assignment see Table 7 in the appendix), with the exception for the protons 5 of the two methylene groups in backbone which, instead of one singlet in monomer spectrum, show four doublets (protons 5α/β and 5`α/β) with a coupling constant of about 16 Hz each that is typical for a geminal coupling.[109] These spectral features are in compliance with a centrosymmetric dimer structure as shown in Figure 25b. In this dimer structure with antiparallel stacking of the chromophores the two halves of each monomer are no more chemically equivalent, and thus splitting of the monomer proton signals is observed. As the methylene protons of the

[6] NMR studies for bis(merocyanine) **21** were performed by Dr. André Zitzler-Kunkel and Eva Kirchner.

spacer unit are no more chemically equivalent in this dimer structure, four sets of doublets with geminal coupling are observed.

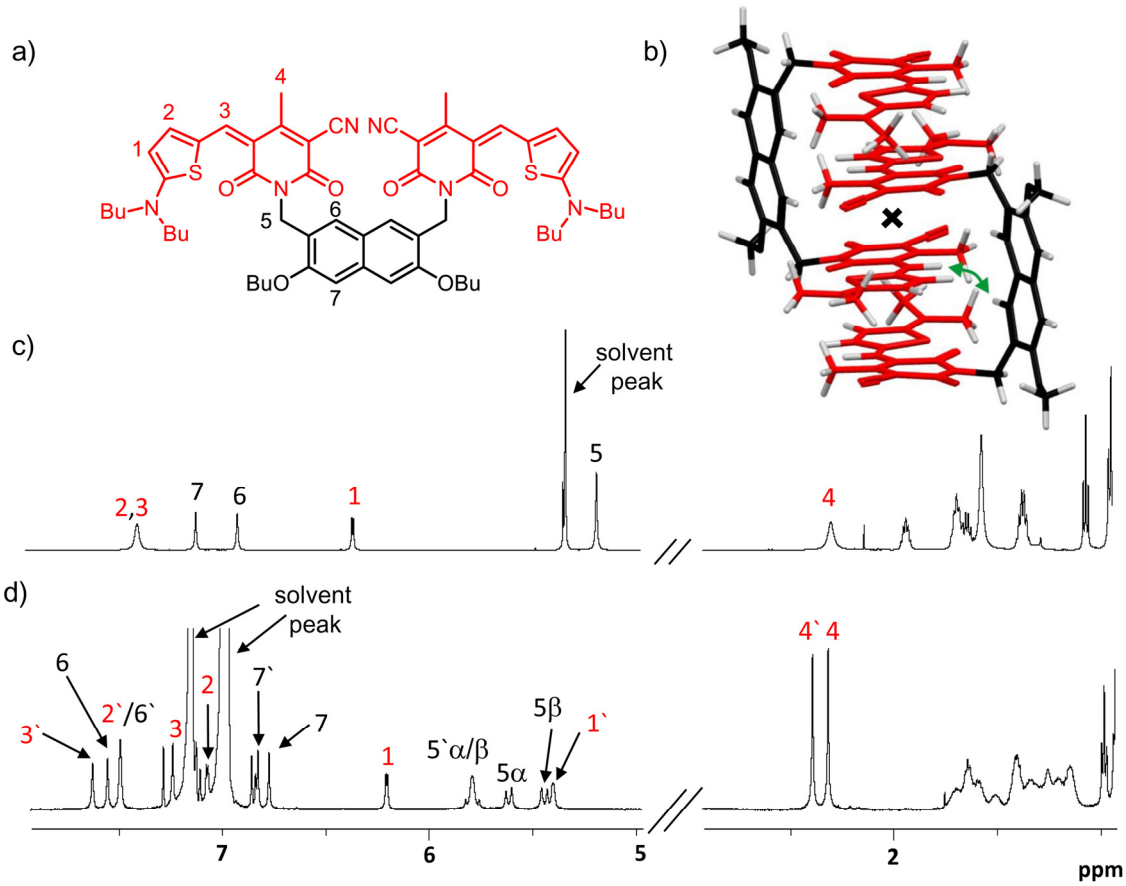

Figure 25. a) Chemical structure of **21** with the significant protons numbered. b) Geometry optimized structure (B97D3/def2-SVP, butyl chains were replaced by methyl groups) of dimer aggregate. The inversion center of the dimer is indicated with a cross, and the green curved arrow indicates the close proximity of chromophore and backbone protons in the dimer. c) Relevant sections of ^{1}H NMR (600 MHz) spectrum of **21** monomer in CD_2Cl_2 (c = 1 x 10^{-3} M) at 295 K. d) Spectrum of aggregate in C_6D_5Cl (c = 1 x 10^{-3} M) at 233 K with the assignment of significant proton signals. The two sets of signals for the aggregate chromophore protons are denoted with and without prime of the respective signals.

The 2D NMR spectrum obtained by ROESY measurements of dye **21** aggregate in C_6D_5Cl (c = 1 x 10^{-3} M) shows cross-peaks between the resonances of chromophore proton 3` of one monomer and backbone proton 6 of the other monomer (as indicated with double arrow in Figure 25b) revealing intermolecular close spatial proximity between these protons (Figure 26). Thus, the results of ROESY experiments are highly supportive for a dimer structure of the aggregate.

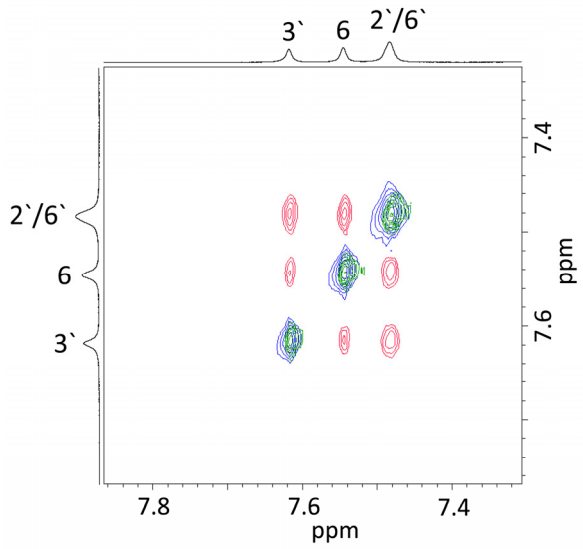

Figure 26. Selected region of superposed ROESY NMR (600 MHz; negative signals marked in blue and positive signals in red, respectively) and COSY NMR (600 MHz; marked in green) spectra of bis(merocyanine) **21** in C_6D_5Cl (c = 1 x 10^{-3} M) at 233 K.

For the unsymmetrical bis(merocyanine) **22**, in principle three different types of dimer aggregates are possible (Figure 22b). To clarify which of these aggregates are formed, NMR studies of **22** were performed in a 1:1 mixture of 1,1,2,2-tetrachloroethane-d_2/tetrachloromethane (c = 8 x 10^{-3} M), where almost only aggregated species are present as confirmed by UV/Vis absorption spectroscopy (Figure 34 in the appendix). As in the case of symmetric bis(merocyanine) **21**, sharp and well resolved signals are observed in ^{1}H NMR spectrum of bis(merocyanine) **22** in above-mentioned solvent mixture, indicating the formation of well-defined aggregates with definite size (Figure 27d). Relevant proton signals could be assigned with the help of COSY and heteronuclear single quantum coherence (HSQC) experiments (for the detailed assignment see Table 8 in the appendix). No splitting of the proton signals occurs upon aggregation, while some of the signals of significant protons are up- or down-field shifted compared to those in the monomer spectrum in polar CD_2Cl_2 (Figure 27c). Based on these observations, the presence of aggregate type II dimer, which should exhibit two sets of proton signals due to the lack of symmetry, could be excluded. On the basis of ^{1}H NMR spectrum type I and III dimers cannot be differentiated because both of them should show only one set of signals due to the presence of an inversion center in the dimer structure.

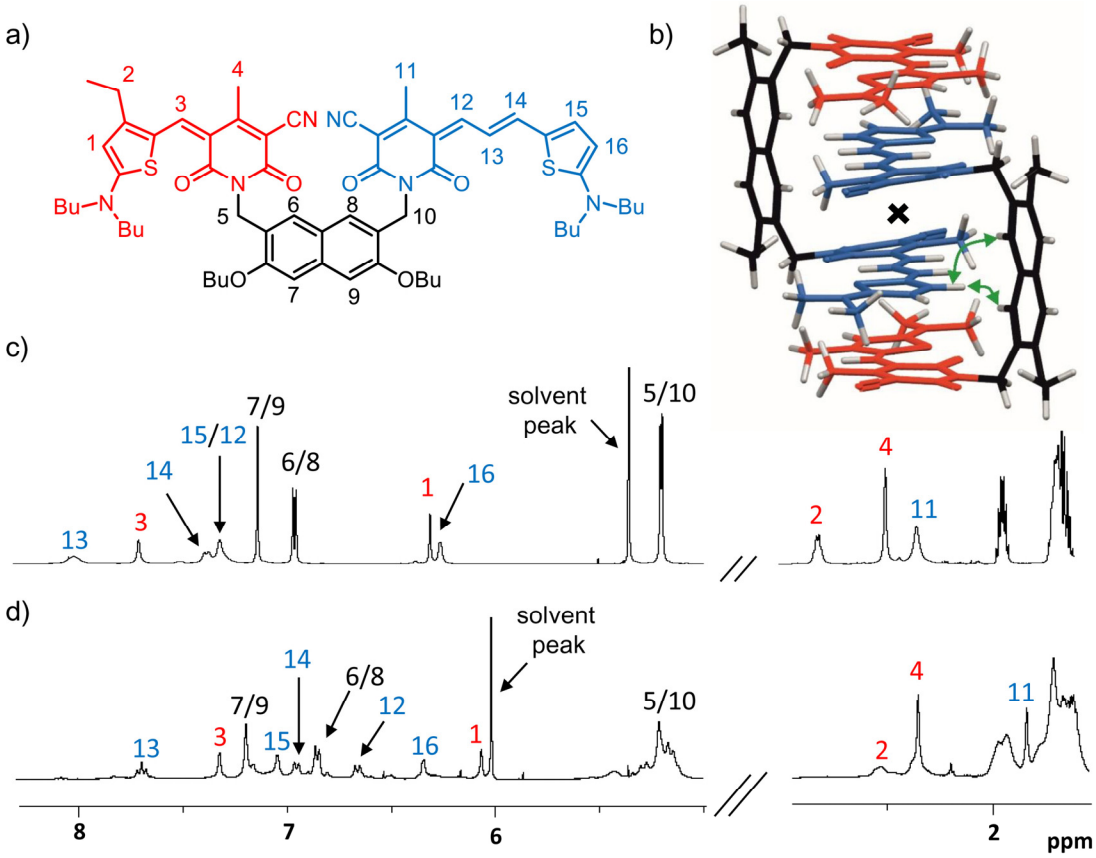

Figure 27. a) Chemical structure of **22** with the significant protons numbered. b) Geometry optimized structure (B97D3/def2-SVP, alkyl chains were replaced by methyl groups) of dimer aggregate. The inversion center of the dimer is indicated with a cross, and the green curved arrows indicate the close proximity of chromophore and backbone protons in the dimer. c) Relevant sections of ^{1}H NMR (600 MHz) spectrum of **22** monomer in CD_2Cl_2 (c = 5 x 10^{-3} M) at 295 K. d) Spectrum of aggregate in a 1:1 mixture of 1,1,2,2-tetrachloroethane-d_2/tetrachloromethane (c = 8 x 10^{-3} M) at 253 K with the assignment of significant proton signals.

Therefore, ROESY NMR studies were performed. In the corresponding ROESY spectrum of aggregated **22** (Figure 28a) a cross-peak between protons 6 and 8 of the naphthalene spacer and 15 of the long merocyanine chromophore can be observed, which indicates an intercalation of the long chromophore in the stack. Moreover, no cross-peaks are observed between protons 6 and 8 of the spacer unit and protons 2, 3 and 4 of the short chromophore (Figure 28a,b). Therefore, an intercalation of the short chromophore (as in type III dimer) can be ruled out and hence the formation of type I dimer with the structure shown in Figure 27b, where the long chromophores are located at the inner part of the tetrachromophoric stack, is most reasonable.

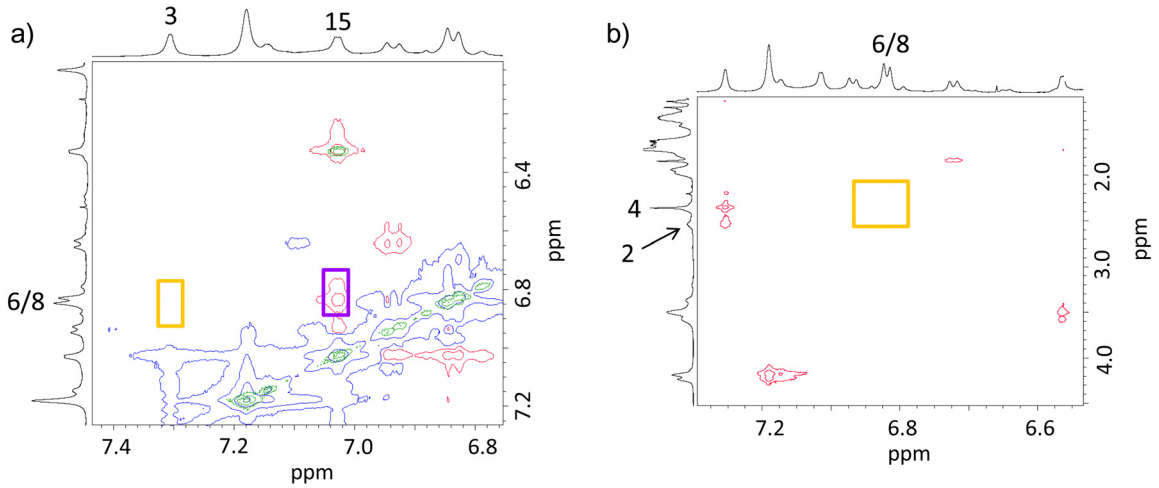

Figure 28. a) and b): Selected regions of superposed ROESY NMR (600 MHz; negative signals marked in blue and positive signals in red, respectively) and COSY NMR (600 MHz; marked in green) spectra of bis(merocyanine) **22** in a 1:1 mixture of 1,1,2,2-tetrachloroethane-d_2/tetrachloromethane (c = 8 x 10^{-3} M) at 253 K. The orange rectangles indicate the missing cross-signals that should be present if the short chromophores were located in the inner part of the tetrachromophoric stack, whereas the violet rectangle highlights the cross-peak between the protons of the naphthalene spacer (protons 6 and 8) and the long chromophore (proton 15).

4.2.4 Structural Elucidation by X-Ray Analysis

Single crystals of bis(merocyanine) **21** suitable for X-ray analysis could be grown by slow diffusion of methanol into a chloroform solution of **21** at room temperature,[106] while crystals of bis(merocyanine) **22** were obtained from a saturated solution in 1,4-dioxane at room temperature.[7] As shown in Figure 29 (solvent molecules are omitted for clarity), the dimer structures proposed for **21** and **22** based on spectroscopic studies in solution can be confirmed in the solid state by single-crystal X-ray analysis. In the solid state, bis(merocyanine) **21** bears a triclinic space group $P\bar{1}$ with two dye molecules amongst six molecules of chloroform and two molecules of methanol in one unit cell (Figure 29a and Figure 35 in the appendix). The packing motif is described by dimeric units of the tweezer-like dyes that are arranged in one-dimensional columnar stacks, surrounded by a hydrogen-bonded network of solvent molecules. A closer look on the dimer units reveals a centrosymmetric stack comprising four antiparallel oriented chromophore units (Figure

[7] Crystals of bis(merocyanine) **21** were grown by Dr. André Zitzler-Kunkel and the crystal structure was solved by Dr. Christian Burschka. The crystal structure of bis(merocyanine) **22** was solved by Dr. David Schmidt.

29a). The crystal structure of unsymmetric bis(merocyanine) **22** also shows a triclinic space group $P\bar{1}$ with two dye molecules and two molecules of dioxane in the unit cell (Figure 29b and Figure 36 in the appendix).

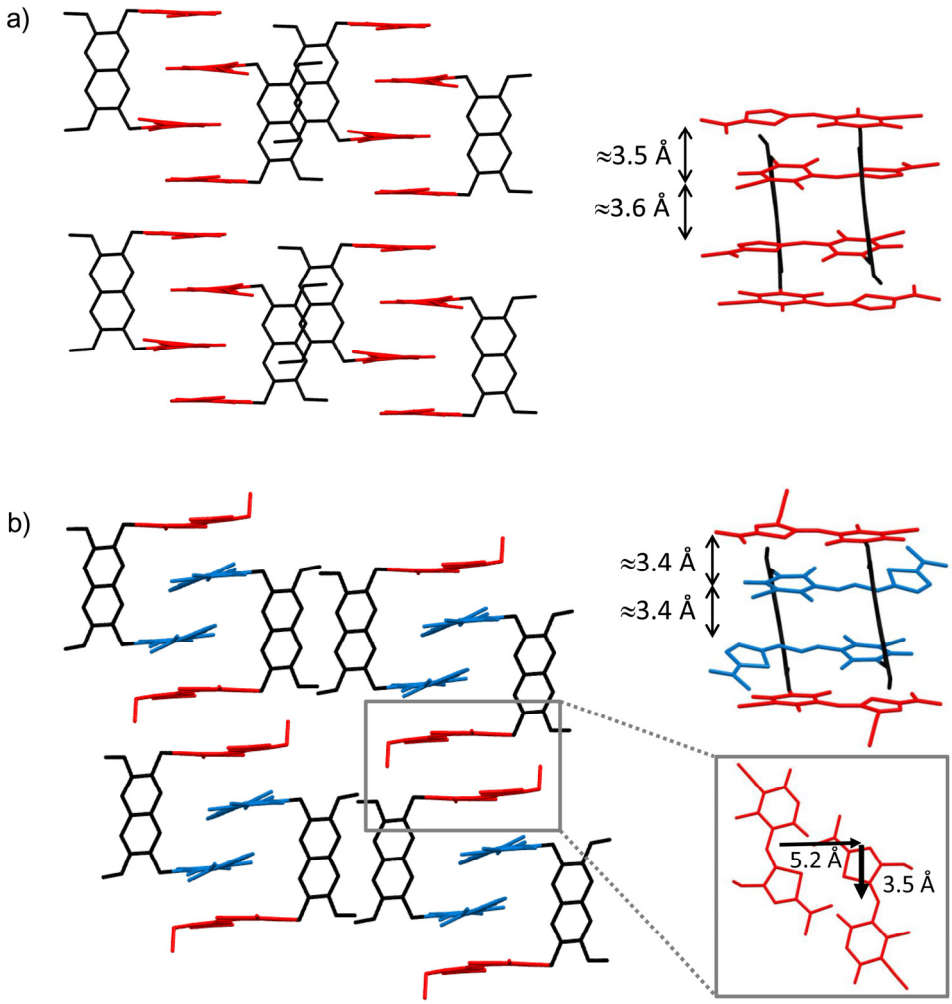

Figure 29. Molecular packing of a) bis(merocyanine) **21**[106] and b) **22** in the solid state (side view) with enlargement of the dimer structure motif (front view). Solvent molecules and hydrogen atoms are omitted for clarity and butyl chains were replaced by methyl groups. A section of the crystal structure (top view) of **22** is shown (b, right) illustrating the lateral and transversal shift of two chromophores of next-neighbored quadruple dye stacks.

As our NMR studies suggested, the long chromophores of two dye molecules are located in the interior and the short chromophores in the exterior of the quadruple dye stack. In contrast to bis(merocyanine) **21**, the packing motif of **22** displays no extended π-stack in the crystal since the next-neighbored bimolecular stack of four dyes is laterally shifted by 5.2 Å and transversally shifted by 3.5 Å (Figure 29b). The distances between the chromophores within one dimer of 3.5 and 3.6 Å for bis(merocyanine) **21** and 3.4 Å for

bis(merocyanine) **22** confirm a tight packing at van-der-Waals distance, which explains the strong aggregation tendency of both bis(merocyanine) dyes in less-polar solvents. Supported by the in-depth NMR and UV/Vis spectroscopic studies, we can conclude that similar stacks as observed in the solid state are present in solution.

4.2.5 Quantum Chemical Calculations

Geometry optimizations of dimer structures of **21** and **22** were performed on the DFT level using the B97D3[99] functional including dispersion correction and def2-SVP[100] as basis set. For both dimer structures an overall ground state dipole moment of zero Debye is obtained, revealing a centrosymmetric geometry with an antiparallel alignment of the ground state dipole moments of the chromophores (Figure 30a).

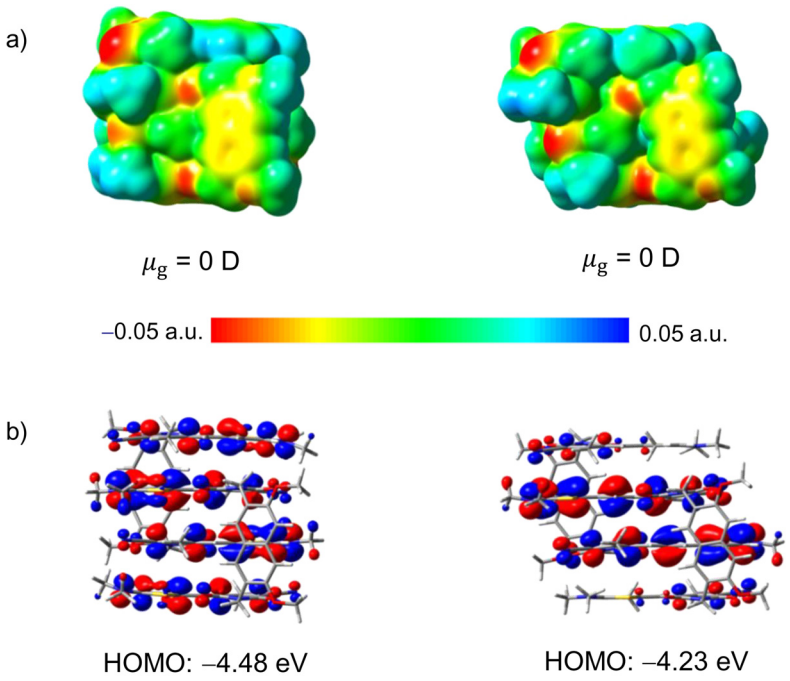

Figure 30. a) Electrostatic potential surface (isovalue = 0.001 a.u.) and b) HOMO distribution (isovalue = 0.02 a.u.) of the geometry optimized structures (B97D3, def2-SVP) of the dimers of bis(merocyanine) dyes **21** (left) and **22** (right).

On the basis of the electrostatic potential surfaces one can clearly see that the strong dipolar character of the individual merocyanine chromophores (Figure 16c,d in Chapter 3) is much less pronounced within the aggregate stack (Figure 30a) as it is expected for the antiparallel alignment of the dipolar chromophores. Furthermore, the highest occupied molecular orbital (HOMO) of bis(merocyanine) **21** dimer has large coefficients on all four

merocyanine chromophores (Figure 30b, left), while the HOMO of aggregated **22** is mostly localized in the inner part of the dye stack, *i.e.* on the long chromophores (Figure 30b, right). This is in accordance with the observation that the long chromophore shows a lower oxidation potential than the short one and thus, the former is easier to oxidize.[94] Hence, due to the same reason, the HOMO energy level of the heteroaggregate (dimer of **22**) is higher compared to that of the homoaggregate (dimer of **21**).

In order to get deeper insight into the absorption properties of the quadruple merocyanine dye stacks, TDDFT calculations were performed on the geometry optimized structures employing the long-range corrected ωB97[101] functional (the results are listed in Table 5). The simulated absorption spectra together with the corresponding experimental spectra, are shown in Figure 31. Obviously, the shape of the experimental dimer spectra derived from UV/Vis experiments are well reproduced by the TDDFT calculations and one can easily recognize that for both aggregate structures the transition to the lowest and third excited state is forbidden (oscillator strength *f* is equal to zero for both states).

Table 5. Excited state energies and corresponding oscillator strengths (*f*) of the dimers of bis(merocyanine) dyes **21** and **22** obtained by TDDFT calculations (ωB97/def2-SVP).

	bis(merocyanine) **21**	bis(merocyanine) **22**
excited state energy	20615 cm^{-1} ($f = 0$)	17202 cm^{-1} ($f = 0$)
(oscillator strength)	21226 cm^{-1} ($f = 0.0614$)	17811 cm^{-1} ($f = 0.3213$)
	23130 cm^{-1} ($f = 0$)	22619 cm^{-1} ($f = 0$)
	25579 cm^{-1} ($f = 2.4697$)	23856 cm^{-1} ($f = 2.6982$)

On the other hand, the fourth excited state transition is strongly allowed for both quadruple dye stacks as reflected by a very intense absorption band. The experimental dimer spectrum of the homoaggregate exhibits an additional weak absorption shoulder at longer wavelength (573 nm), which can be attributed to the partially allowed transition to the second excited state (Figure 31a). This transition is significantly more allowed in the heteroaggregate dye stack that shows a stronger absorption at the longer wavelength of 678 nm (Figure 31b).

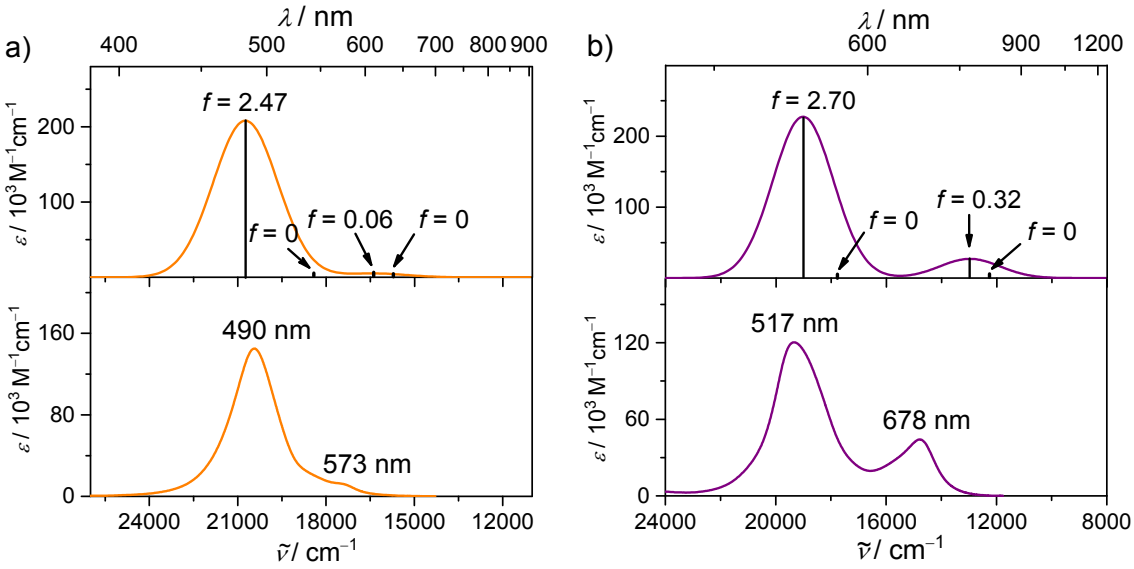

Figure 31. Time-dependent DFT (ωB97/def2-SVP) calculated (top) and experimental dimer spectra (bottom) of a) bis(merocyanine) **21** and b) **22**. The calculated spectra were shifted by 0.6 eV towards lower energies. The experimental dimer spectra were calculated from the data obtained by concentration-dependent UV/Vis studies in chlorobenzene at 298 K.

The transition densities obtained by TDDFT calculations are shown in Figure 32. For both dye stacks the transition density for the fourth excited state shows an in-phase coupling of the transition densities of the individual chromophores, whereas an out-of phase coupling is present for the lowest excited state. The other two states show a partially out-of phase coupling of the transition densities with increasing amount of nodes going from higher to lower energies. However, significant differences of the transition density distribution can be observed for both dye stacks. In the homoaggregate the transition density is slightly more localized on the inner chromophores for the first and fourth excited state (Figure 32a). For the other two excited states the outer chromophores have larger contributions to the overall transition density. In the case of the heteroaggregate the transition density is more localized on the inner (*i.e.* longer) chromophores for the two lowest excited states, whereas it is more localized on the outer (*i.e.* shorter) chromophores for the other two excited states. The results of the TDDFT calculations are highly indicative for an exciton coupling in both aggregates. Hence, the excited states of the quadruple dye stacks are supposed to represent exciton states.

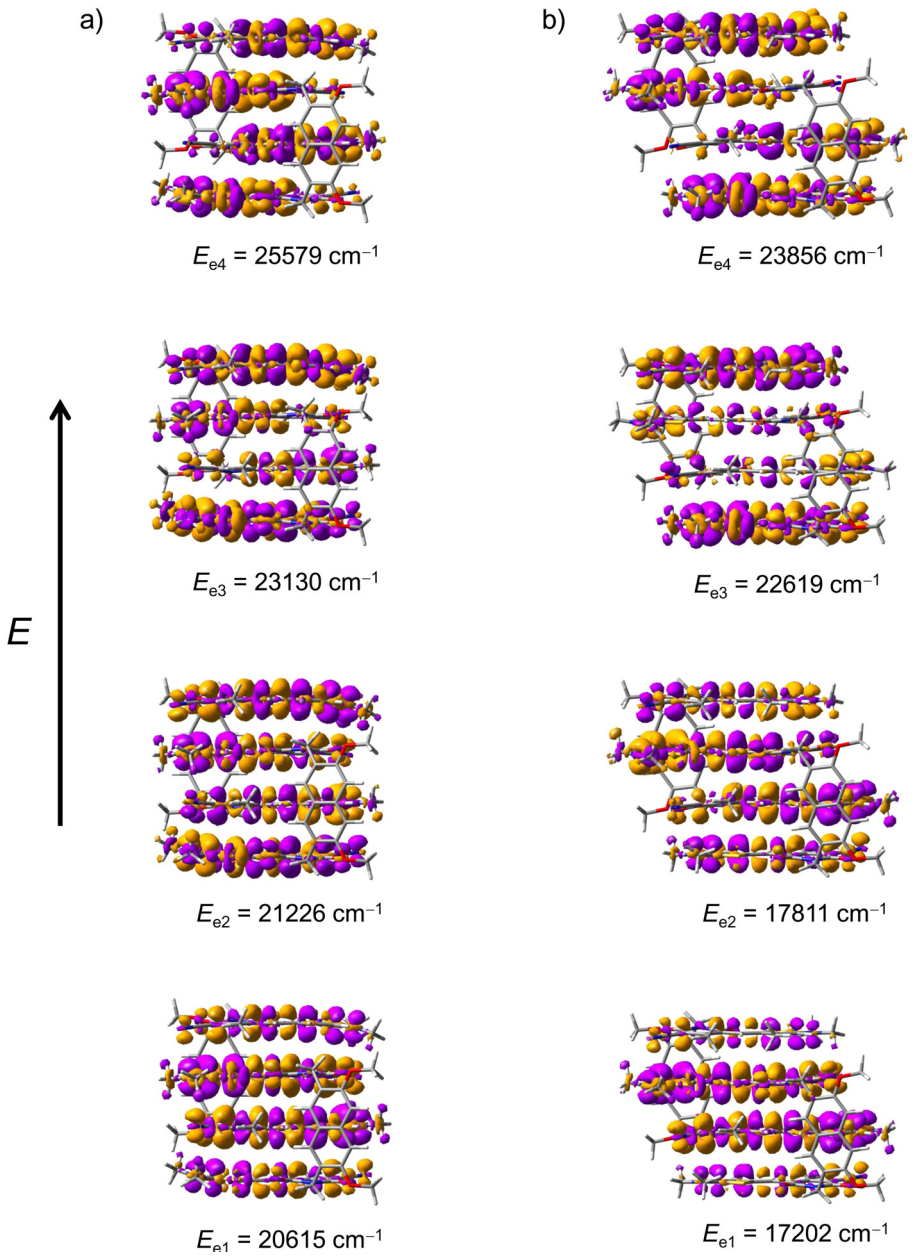

Figure 32. Transition densities (isovalue = 0.0007 a.u.) and energies of the four excited states of the dimer aggregates of bis(merocyanine) dyes a) **21** and b) **22** obtained by TDDFT calculations (ωB97/def2-SVP).

4.2.6 Quantum Chemical Investigations

To analyze the absorption properties of the dimer structures of bis(merocyanine) dyes **21** and **22**, Kasha's exciton theory[8] is applied to homo- and heteroaggregates consisting of four chromophore units. In particular, the aim is to elucidate whether the spectral changes of **22** upon aggregation are caused by exciton coupling not only between the same types of chromophores but also between the chromophores of different types, *i.e.* chromophores with different excitation energies.

The exciton wave function Φ_e of an aggregate consisting of four chromophores can be described as follows:

$$\Phi_e = c_1 \cdot \varphi_1^* \varphi_2 \varphi_3 \varphi_4 + c_2 \cdot \varphi_1 \varphi_2^* \varphi_3 \varphi_4 + c_3 \cdot \varphi_1 \varphi_2 \varphi_3^* \varphi_4 + c_4 \cdot \varphi_1 \varphi_2 \varphi_3 \varphi_4^* , \quad (62)$$

where φ_x (x = 1, 2, 3 or 4) is the ground state wave function of chromophore x and φ_x^* the excited state wave function of the corresponding chromophore and c_1, c_2, c_3 and c_4 represent coefficients of the linear combination. If we assume only interaction between next-neighboring chromophores within the dye stack, the Hamiltonian has the form:

$$\hat{H} = \hat{H}_1 + \hat{H}_2 + \hat{H}_3 + \hat{H}_4 + \hat{V}_{12} + \hat{V}_{23} + \hat{V}_{34}. \quad (63)$$

Here, $\hat{H}_x$ is the Hamiltonian of monomeric chromophore x and $\hat{V}_{xy}$ describes the perturbation between next-neighbored chromophores x and y. We obtain the exciton state energy E_e by applying the Hamiltonian operator $\hat{H}$ on the exciton wave function Φ_e:

$$\hat{H}\Phi_e = E_e \Phi_e. \quad (64)$$

Multiplying both sides of equation (64) by $\varphi_1^* \varphi_2 \varphi_3 \varphi_4$ and integration over the coordinates of the chromophores 1, 2, 3 and 4 (*i.e.* τ_1, τ_2, τ_3 and τ_4), we obtain with equation (62):

$$c_1 H_{11} + c_2 H_{12} + c_3 H_{13} + c_4 H_{14} = E_e (c_1 S_{11} + c_2 S_{12} + c_3 S_{13} + c_4 S_{14}), \quad (65)$$

with

$H_{11} = \iiiint \varphi_1^* \varphi_2 \varphi_3 \varphi_4 \hat{H} \varphi_1^* \varphi_2 \varphi_3 \varphi_4 d\tau_1 d\tau_2 d\tau_3 d\tau_4$,

$H_{12} = \iiiint \varphi_1^* \varphi_2 \varphi_3 \varphi_4 \hat{H} \varphi_1 \varphi_2^* \varphi_3 \varphi_4 d\tau_1 d\tau_2 d\tau_3 d\tau_4$ etc.

and

$S_{11} = \iiiint \varphi_1^* \varphi_2 \varphi_3 \varphi_4 \varphi_1^* \varphi_2 \varphi_3 \varphi_4 d\tau_1 d\tau_2 d\tau_3 d\tau_4$,

$S_{12} = \iiiint \varphi_1^* \varphi_2 \varphi_3 \varphi_4 \varphi_1 \varphi_2^* \varphi_3 \varphi_4 d\tau_1 d\tau_2 d\tau_3 d\tau_4$ etc.

By neglecting the electronic overlap between the chromophores, the integrals S can be simplified due to orthonormalization of the wave functions:

$$S_{xy} = 1 \text{ for } x = y, \text{ and } S_{xy} = 0 \text{ for } x \neq y.$$

Thus, one obtains for equation (65):

$$c_1 H_{11} + c_2 H_{12} + c_3 H_{13} + c_4 H_{14} = E_e c_1. \quad (66)$$

Repeating the same procedure starting from equation (64) and multiplication with $\varphi_1\varphi_2^*\varphi_3\varphi_4$, $\varphi_1\varphi_2\varphi_3^*\varphi_4$ and $\varphi_1\varphi_2\varphi_3\varphi_4^*$, respectively, gives the following equations:

$$c_1 H_{21} + c_2 H_{22} + c_3 H_{23} + c_4 H_{24} = E_e c_2 \tag{67}$$

$$c_1 H_{31} + c_2 H_{32} + c_3 H_{33} + c_4 H_{34} = E_e c_3 \tag{68}$$

$$c_1 H_{41} + c_2 H_{42} + c_3 H_{43} + c_4 H_{44} = E_e c_4. \tag{69}$$

This leads to the following eigenvalue equation in matrix notation which summarizes equations (66)–(69):

$$\begin{pmatrix} H_{11} & H_{12} & H_{13} & H_{14} \\ H_{21} & H_{22} & H_{23} & H_{24} \\ H_{31} & H_{32} & H_{33} & H_{34} \\ H_{41} & H_{42} & H_{43} & H_{44} \end{pmatrix} \begin{pmatrix} c_1 \\ c_2 \\ c_3 \\ c_4 \end{pmatrix} = E_e \begin{pmatrix} c_1 \\ c_2 \\ c_3 \\ c_4 \end{pmatrix}. \tag{70}$$

The Hamiltonian matrix for the homoaggregate of **21** simplifies to

$$\begin{pmatrix} 0 & J_{12} & 0 & 0 \\ J_{12} & 0 & J_{23} & 0 \\ 0 & J_{23} & 0 & J_{12} \\ 0 & 0 & J_{12} & 0 \end{pmatrix}$$

within the next-neighbor approximation (for further details see the appendix), where the non-diagonal matrix elements J_{xy} represent the exciton coupling energy between next-neighbored chromophores x and y. The diagonal matrix elements represent the excited state energy of the short chromophore and are set as zero level.

In an analogous manner the Hamiltonian matrix for the dimer of bis(merocyanine) **22** can be written as

$$\begin{pmatrix} \Delta E & J_{12} & 0 & 0 \\ J_{12} & -\Delta E & J_{23} & 0 \\ 0 & J_{23} & -\Delta E & J_{12} \\ 0 & 0 & J_{12} & \Delta E \end{pmatrix},$$

where ΔE is half the energy difference between the first excited states of the monomeric long and short chromophore, respectively (for further details see the appendix). In addition, the midpoint of the excited state energies of both chromophores is set as zero level.

The exciton state energies of the quadruple dye stacks correspond to the eigenvalues of the Hamiltonian matrices. For the dye stack of bis(merocyanine) **21** we obtain:

$$E_{e1} = \frac{1}{2}\left(-\sqrt{4J_{12}^2 + J_{23}^2} - J_{23}\right) \tag{71}$$

$$E_{e2} = \frac{1}{2}\left(-\sqrt{4J_{12}^2 + J_{23}^2} + J_{23}\right) \tag{72}$$

$$E_{e3} = \frac{1}{2}\left(\sqrt{4J_{12}^2 + J_{23}^2} - J_{23}\right) \tag{73}$$

$$E_{e4} = \frac{1}{2}\left(\sqrt{4J_{12}^2 + J_{23}^2} + J_{23}\right) \tag{74}$$

and for bis(merocyanine) **22**:

$$E_{e1} = \frac{1}{2}\left(-J_{23} - K\right) \tag{75}$$

$$E_{e2} = \frac{1}{2}\left(J_{23} - L\right) \tag{76}$$

$$E_{e3} = \frac{1}{2}\left(-J_{23} + K\right) \tag{77}$$

$$E_{e4} = \frac{1}{2}\left(J_{23} + L\right) \tag{78}$$

with $L = \sqrt{4J_{12}^2 + 4\Delta E^2 - 4\Delta E J_{23} + J_{23}^2}$

and $K = \sqrt{4J_{12}^2 + 4\Delta E^2 + 4\Delta E J_{23} + J_{23}^2}$.

Thus, in order to calculate the exciton state energies one has to determine the exciton coupling energies of two next-neighbored chromophores in the stacks as well as the excited state energies of the isolated chromophores. The latter can be obtained from the corresponding absorption maxima of the ideal monomer spectrum of the corresponding bis(merocyanine) dyes **21** and **22** obtained by concentration-dependent UV/Vis spectroscopy in chlorobenzene. In this way, we obtain an excited state energy of 18505 cm^{-1} for the chromophore of bis(merocyanine) **21** and 18229 cm^{-1} for the short chromophore and 15084 cm^{-1} for the long chromophore of bis(merocyanine) **22**, respectively.

The exciton coupling energy between two next-neighbored chromophores of the quadruple dye stacks was determined by applying the transition charge method as

discussed in Chapter 3.[55, 57] Using the geometry optimized structures of both dimer aggregates (B97D3/def2-SVP) we obtain $J_{12} = 1576\ cm^{-1}$ and $J_{23} = 1452\ cm^{-1}$ for the homoaggregate, where J_{12} and J_{23} denote the coupling energies for the chromophore pair in the exterior and in the interior of the stack, respectively (Table 6). In the case of the heteroaggregate the exciton coupling energies amount to $J_{12} = 1861\ cm^{-1}$ and $J_{23} = 1108\ cm^{-1}$, respectively (Table 6). Accordingly, the largest coupling is indeed given for the heteropair despite of the significantly different excitation energies of the given chromophores. With the exciton coupling energies, we can calculate the exciton state energies of the dye stacks of bis(merocyanine) dyes **21** and **22** according to equations (71)–(74) and (75) –(78), respectively (Table 9 in the appendix).

Table 6. Exciton coupling energies J of the relevant chromophore pairs in the dye stacks of bis(merocyanine) dyes **21** and **22** determined by transition charge method.

	bis(merocyanine) **21**	bis(merocyanine) **22**
J_{12}	$1576\ cm^{-1}$	$1861\ cm^{-1}$
J_{23}	$1452\ cm^{-1}$	$1108\ cm^{-1}$

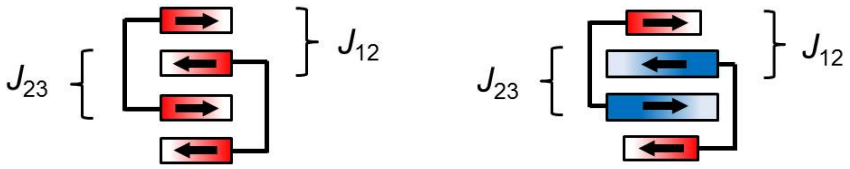

The overall transition dipole moment (μ_{eg}) of the quadruple stacks can be written as a linear combination of the transition dipole moments of the four individual chromophores:

$$\mu_{eg} = c_1\mu_{eg,1} + c_2\mu_{eg,2} + c_3\mu_{eg,3} + c_4\mu_{eg,4}. \quad (79)$$

The coefficients c_1–c_4 can be determined by calculating the normed eigenvectors of the Hamiltonian matrix of the corresponding dye stacks (see appendix). The calculated values are listed in Table 10 and Table 11 in the appendix. Like in Chapter 3 discussed for the double merocyanine stacks, the magnitude of the overall transition dipole moment (μ_{eg}) of the quadruple stacks can be calculated from equation (79) by using the magnitudes of the transition dipole moments of the individual chromophores since the transition dipole moments of the chromophores are aligned along the same axis within the stacks.

Based on these data, exciton state diagrams for the homo- and heteroaggregate dye stacks can be elucidated as shown in Figure 33. Accordingly, four non-degenerated exciton states can be observed as predicted by TDDFT calculations. The amount of nodes of the coupled transition dipole moments of the chromophores is decreasing from three for the lowest exciton state to zero for the highest exciton state. For both aggregate structures, the transition to the highest exciton state is strongly allowed since all the transition dipole moments of the chromophores are coupled in phase resulting in a large magnitude of the overall transition dipole moment (μ_{eg}). Furthermore, the excitation to the lowest and third exciton state is forbidden since the overall transition dipole moment amounts to zero. This is due to the fact that the transition dipole moments of the chromophores that have the same coefficients (note: the magnitude of the coefficient is indicated by the length of the arrows that represent the transition dipole moments) couple out of phase. On the other hand, the transition to the second lowest exciton state is partially allowed for both aggregate structures since the outer chromophores have different coefficients than the transition dipole moments of the inner chromophores resulting in overall transition dipole moments of 4.2 D (for **21**) and 7.8 D (for **22**). This value is higher for the heteroaggregate of bis(merocyanine) **22** since the differences of the coefficients of the inner and outer chromophores are slightly larger compared to those of the homoaggregate (Table 10 and Table 11 in the appendix). In addition, the long chromophore exhibits a larger transition dipole moment (12.3 D**)** than the short chromophore (9.9 D, Figure 18a in Chapter 3). Thus, the dimer spectrum of bis(merocyanine) **21** shows only a weak absorption shoulder at longer wavelength (573 nm), whereas the corresponding absorption band (678 nm) is more intense for bis(merocyanine) **22** dimer. The energy splittings $\Delta\tilde{\nu}$ between the two absorption bands of the quadruple dye stacks depend on the exciton coupling energies J between next-neighboring chromophores within the dye stacks and, in the case of the heteroaggregate, additionally on the energy difference ΔE as depicted in Figure 33. The position of the calculated absorption maxima (477 and 572 nm for **21** and 517 and 663 nm for **22**, respectively) are in good agreement with the ones of the experimental dimer spectra obtained by concentration-dependent UV/Vis measurements in chlorobenzene (Figure 23). Furthermore, the transition dipole moments shown in Figure 33 reasonably describe the transition densities of the exciton states obtained by TDDFT calculations (Figure 32).

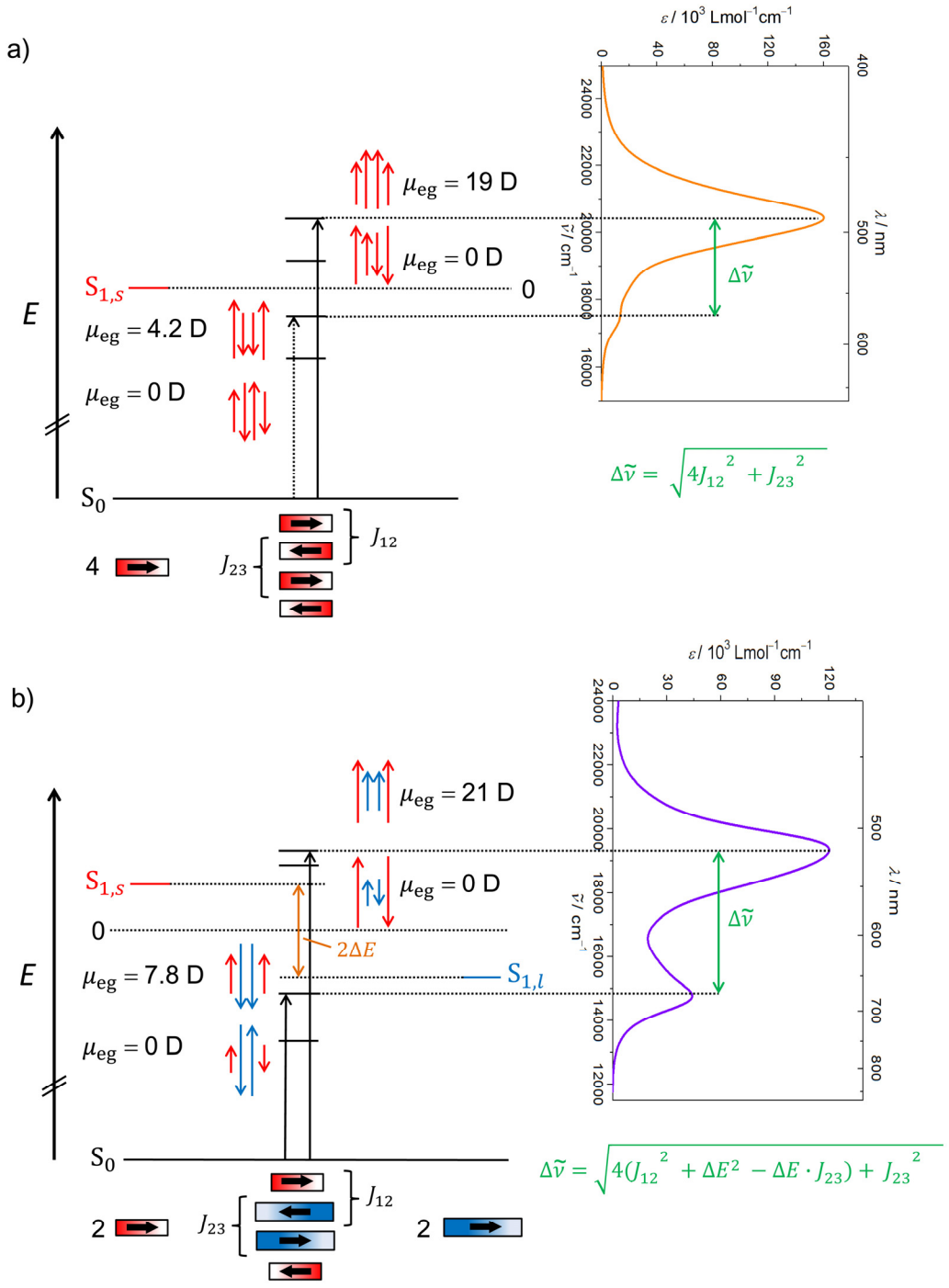

Figure 33. Exciton state diagram of the quadruple dye stacks of a) bis(merocyanine) **21** and b) bis(merocyanine) **22**. The arrows (red for the short chromophore and blue for the long chromophore, respectively) indicate the phase relations between the corresponding transition dipole moments. The lengths of the arrows reflect the magnitude of the coefficients of the transition dipole moments. The corresponding experimental dimer spectrum obtained from concentration-dependent UV/Vis spectroscopy in chlorobenzene is depicted to indicate the allowed transitions. J_{12} and J_{23} denote the exciton coupling energies for the chromophore pairs in the exterior and in the interior of the dye stack, respectively, whereas $S_{1,s}$ and $S_{1,l}$ are the energies of the first excited states of the short and long chromophore, respectively.

4.3 Conclusion

A new bis(merocyanine) dye comprising two chromophores with different conjugation length tethered by a rigid naphthalene spacer unit has been synthesized. In-depth aggregation studies including concentration-dependent UV/Vis spectroscopy and 2D NMR spectroscopy revealed that this bis(merocyanine) exclusively forms quadruple dye stacks upon dimerization in low polar solvents with the long chromophores located in the interior of the stack. The structure of the aggregate could be unambiguously confirmed in the solid state by X-ray analysis.

The UV/Vis absorption properties of the heteroaggregate were compared to the ones of the respective homoaggregate of bis(merocyanine) **21** comprising two short chromophores, which can be classified as H-type aggregate exhibiting a hypsochromic shift of the absorption with respect to the monomeric chromophore. In contrast, the absorption spectrum of the quadruple π-stack heteroaggregate of bis(merocyanine) **22** is more complex. It shows a hypsochromically shifted main absorption band of high intensity and a second band of considerably strong intensity and a bathochromic shift. This observation cannot be rationalized by presuming an exciton coupling only between the same types of chromophores, which should result in two hypsochromically shifted absorption bands with respect to the absorption bands of the corresponding monomeric chromophores. Our extension of the molecular exciton theory to heteroaggregates adequately describes the absorption spectrum of the aggregate of bis(merocyanine) **22** and is in accordance with the results obtained by TDDFT calculations. Remrkably, the largest coupling was estimated between the different types of chromophores. Thus, exciton coupling in heteroaggregates is not only present between the same type of chromophores and significantly influences the optical absorption properties of the dye aggregate.

4.4 Experimental Section

4.4.1 Materials and Methods

All solvents and reagents were purchased from commercial sources and used as received without further purification. Microwave reactions were performed in Discover® CEM Microwave Reactor. Column chromatography was performed using silica gel 60M (0.04–0.063 mm). NMR spectra were recorded on an Bruker Avance III HD 400 or Bruker Avance III HD 600 spectrometer at 295 K, unless otherwise stated. The spectra were calibrated to the residual solvent peak and the chemical shifts δ are given in ppm. Multiplicities are denoted as follows: s = singlet, d = doublet, t = triplet, q = quartet, dd = doublet of doublets, m = multiplet, br = broad. High-resolution mass spectra (ESI) were recorded on an ESI MicrOTOF Focus spectrometer. Elemental analysis were performed on a CHNS 932 analyzer. Solvents for spectroscopic studies were of spectroscopic grade and used as received. Concentration-dependent UV/Vis spectra were recorded on UV/Vis spectrometers Lambda 950 or 35. The spectral band width and the scan rate were 1 nm and 120 nm min^{-1}, respectively. Stock solutions of the studied compounds in chlorobenzene were accurately prepared, and continuously diluted for absorption measurements at different concentrations by taking into account the solubility and the absorbance of the respective compound. The UV/Vis measurements were performed in conventional quartz cell cuvettes with path lengths of 0.2 – 50 mm. The spectra were fitted according to the dimer model[95] by applying a global analysis.

4.4.2 Synthesis and Characterization

3-Ethylthiophene-2-carboxaldehyde 26[108]

A mixture of dimethylformamide (520 µL, ρ = 0.948 g/mL, 493 mg, 6.74 mmol) and phosphorus oxychloride (624 µL, ρ = 1.65 g/mL, 1.03 g, 6.73 mmol) was stirred until the heat evolution was ceased. Afterwards, 3-ethylthiophene (500 mg, 4.46 mmol) was added dropwise over a period of 1 h. The mixture was stirred for 1 h at room temperature and for additional 1 h at 100 °C. After cooling down to room temperature, dichloromethane (50 mL) and a saturated aqueous solution of $NaHCO_3$ (50 mL) were added and the layers were separated. The aqueous layer was extracted with dichloromethane (3 x 30 mL) and the organic layers were combined and washed with brine (50 mL). The solvent was removed under reduced pressure and the crude product was purified by column chromatography (silica gel, hexane/ethyl acetate 9:1) to afford a bright yellow oil

consisting of a 3:1 mixture of the regioisomers 3-ethylthiophene-2-carboxaldehyde **26** and 4-ethylthiophene-2-carboxaldehyde **27**. The regioisomeric ratio was determined by ^{1}H NMR spectroscopy of the mixture.

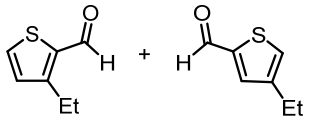

26 3 : 1 **27**

C_7H_8OS (140.20)

Yield: 543 mg (3.87 mmol, 87%), bright yellow oil.

^{1}H NMR of **26** (400 MHz, $CDCl_3$): δ = 10.0 (d, ^5J = 1.1 Hz, 1H), 7.64 (dd, ^3J = 5.0 Hz, ^5J = 1.1 Hz, 1H), 7.03 (d, ^3J = 5.0 Hz, 1H), 3.00 (q, ^3J = 7.6 Hz, 2H), 1.31 (t, J = 7.6 Hz, 3H). ^{1}H NMR of **27**: ^{1}H NMR (400 MHz, $CDCl_3$): δ = 9.87 (d, ^5J = 1.2 Hz, 1H), 7.62 (m, 1H), 7.38 (m, 1H), 2.68 (m, 2H), 1.27 (t, ^3J = 7.5 Hz, 3H).

5-Bromo-3-ethylthiophene-2-carboxaldehyde 28

A portion of 400 mg (2.86 mmol) of a 3:1 mixture of 3-ethylthiophene-2-carboxaldehyde **26** and 4-ethylthiophene-2-carboxaldehyde **27**, as obtained from the previous reaction, was dissolved in chloroform (15 mL) and cooled to 0 °C. Bromine (150 µL, ρ = 3.10 g/mL, 465 mg, 2.91 mmol) was added dropwise over a period of 15 min and the mixture stirred for 2 h at room temperature. A saturated aqueous solution of $Na_2S_2O_3$ (5 mL) and dichloromethane (100 mL) were added and the layers were separated. The organic layer was washed successively with distilled water (50 mL), aqueous solution of K_2CO_3 (50 mL), and brine (50 mL). The solvent was removed under reduced pressure and the crude product was purified by column chromatography (silica gel, hexane/ethyl acetate 19:1) to afford a bright yellow oil consisting of a 3:1 mixture of the regioisomers 5-bromo-3-ethylthiophene-2-carboxaldehyde **28** and 5-bromo-4-ethylthiophene-2-carboxaldehyde **29**. The regioisomeric ratio was determined by ^{1}H NMR spectroscopy of the mixture.

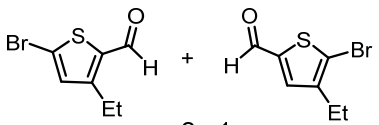

28 3 : 1 **29**

C_7H_7BrOS (219.10)

Yield: 519 mg (2.37 mmol, 83%), bright yellow oil.

^{1}H NMR of **28** (400 MHz, $CDCl_3$): δ = 9.91 (s, 1H), 7.02 (s, 1H), 2.95 (q, ^3J = 7.6 Hz, 2H), 1.30 (t, ^3J = 7.6 Hz, 3H). ^{1}H NMR of **29** (400 MHz, $CDCl_3$): δ = 9.76 (s, 1H), 7.48 (s, 1H), 2.63 (q, ^3J = 7.6 Hz, 2H), 1.24 (t, ^3J = 7.6 Hz, 3H). CHN (%) calculated for C_7H_7BrOS: C, 38.37; H, 3.22; S, 14.63. Found: C, 38.46; H, 3.28; S, 14.76 (for regioisomeric mixture). HRMS (ESI, positive, acetonitrile/chloroform): *m/z* 218.94743 $[M+H]^+$, calculated for $C_7H_8BrOS^+$: 218.94737 (for regioisomeric mixture).

5-(Dibutylamino)-3-ethylthiophene-2-carboxaldehyde 24

To a portion of 490 mg (2.24 mmol) of a 3:1 mixture of 5-bromo-3-ethylthiophene-2-carboxaldehyde **28** and 5-bromo-4-ethylthiophene-2-carboxaldehyde **29**, as obtained from the previous reaction, and dibutylamine (700 mg, 5.43 mmol) was added dimethylformamide (3 mL) and distilled water (1 mL). The mixture was then stirred for 2 h at 130 °C in the microwave. Distilled water (100 mL) and dichloromethane (100 mL) were added and the organic phase was separated. The aqueous layer was extracted with dichloromethane (2 x 70 mL) and the organic phases were combined. The solvent was removed under reduced pressure and the crude product was purified by column chromatography (silica gel, dichloromethane/ethyl acetate 8:1) yielding compound **24** as the only product as a brown oil.

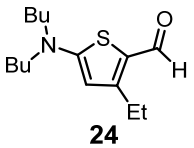

24

$C_{15}H_{25}NOS$ (267.43)

Yield: 204 mg, (763 µmol, 45% referring to corresponding major regioisomer **28**), brown oil.

^{1}H NMR (400 MHz, CD_2Cl_2): δ = 9.60 (s, 1H), 5.77 (s, 1H), 3.31 (t, ^3J = 7.7 Hz, 4H), 2.80 (q, ^3J = 7.5 Hz, 2H), 1.63 (m, 4H), 1.36 (m, 4H), 1.26 (t, ^3J = 7.5 Hz, 3H), 0.96 (t, ^3J = 7.4 Hz, 6H). HRMS (ESI, positive, acetonitrile/chloroform): *m/z* 268.17272 $[M+H]^+$, calculated for $C_{15}H_{26}NOS$: 268.17296. CHN (%) calculated for $C_{15}H_{25}NOS$: C, 67.37; H, 9.42; N, 5.24; S, 11.99. Found: C, 67.63; H, 9.50; N, 5.30; S, 11.79.

Bis(merocyanine) 22

Bis(pyridone) **23**[107] (78.0 mg, 131 μmol), 5-(dibutylamino)-3-ethylthiophene-2-carboxaldehyde **24** (42.0 mg, 157 μmol) and aminothiophene **12**[94] (41.0 mg, 155 μmol) were stirred for 2 h in acetic anhydride (1 mL) at 100 °C. The solvent was removed under reduced pressure and the crude product was purified by column chromatography (silica gel, dichloromethane/ethyl acetate 8:1) yielding a purple solid.

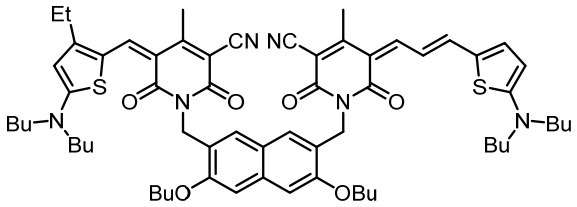

22

$C_{64}H_{80}N_6O_6S_2$ (1093.50)

Yield: 14.3 mg (13.1 μmol 10%), purple solid.

Mp: 182–184 °C. ^{1}H NMR (400 MHz, CD_2Cl_2): δ = 7.99 (br, 1H), 7.70 (s, 1H), 7.38-7.30 (m, 3H), 7.07 (s, 2H), 6.93 (s, 1H), 6.91 (s, 1H), 6.28 (s, 1H), 6.20 (d, ^3J = 4.4 Hz, 1H), 5.17 (s, 4H), 4.15 (t, ^3J = 6.3 Hz, 4H), 3.43 (m, 8H), 2.80 (q, ^3J = 7.6 Hz, 2H), 2.49 (s, 3H), 2.37 (s, 3H), 1.93-1.87 (m, 4H), 1.70-1.58 (m, 11H), 1.37-1.27 (m, 12H), 1.04 (t, ^3J = 7.3 Hz, 3H), 1.03 (t, ^3J = 7.3 Hz, 3H), 0.95-0.96 (m, 12H). ^{13}C NMR (151 MHz, CD_2Cl_2): δ = 176.8, 175.1, 171.9, 167.9, 163.6, 163.4, 162.7, 162.6, 158.7, 158.2, 155.6, 155.5, 151.6, 148.9, 145.0, 136.8. 134.1, 129.4, 128.5, 127.8, 125.6, 124.9, 124.8, 123.3, 123.0, 121.3, 119.0, 118.2, 117.9, 112.7, 111.5, 110.9, 105.8, 105.0, 94.6, 93.2, 68.07, 68.06, 55.1, 39.4, 39.2, 31.82, 31.81, 29.5, 24.0, 20.5, 20.4, 19.91, 19.89, 19.2, 19.0, 14.8, 14.18, 14.16, 13.9. HRMS (ESI, positive, acetonitrile/chloroform): *m/z* 1093.56763 $[M+H]^+$, calculated for $C_{64}H_{81}N_6O_6S_2^+$: 1093.56535. UV/Vis (CH_2Cl_2): λ_{max}/nm (ε/M^{-1} cm^{-1}) = 541 (126000), 678 (135000).

4.4.3 Single-Crystal X-Ray Analysis

Single-crystal X-ray diffraction data for bis(merocyanine) **22** were collected at 100 K on a Bruker D8 Quest Kappa Diffractometer with a Photon100 CMOS detector and multi-layered mirror monochromated $Cu_{K\alpha}$ radiation. The structures were solved using direct methods, expanded with Fourier techniques and refined with the Shelx software package.[110] All non-hydrogen atoms were refined anisotropically. Hydrogen atoms were included in the structure factor calculation on geometrically idealized positions.

Crystallographic data have been deposited with the Cambridge Crystallographic Data Centre as supplementary publication no. CCDC 1476633. These data can be obtained free of charge from The Cambridge Crystallographic Data Centre *via* www.ccdc.ac.uk/data.request/cif.

Crystal data for bis(merocyanine) **22** ($C_{64}H_{80}N_6O_6S_2 \cdot C_4H_8O_2$): M_r = 1181.56, blue block, 0.32 x 0.16 x 0.12 mm^3, triclinic space group $P\bar{1}$, a = 13.9822(3) Å, α = 74.6400(11)°, b = 15.9375(4) Å, β = 65.1290(10)°, c = 16.5230(4) Å, γ = 69.0340(10)°, V = 3090.79(13) $Å^3$, Z = 2, $\rho(calcd.)$ = 1.270 $g \cdot cm^{-3}$, μ = 1.267 mm^{-1}, $F(000)$ = 1268, $GooF(F^2)$ = 1.087, R_1 = 0.0584, wR^2 = 0.1515 for $I>2\sigma(I)$, R_1 = 0.0693, wR^2 = 0.1583 for all data, 12419 unique reflections [$\theta \leq 74.643°$] with a completeness of 98.9% and 800 parameters, 12 restraints.

4.4.4 Computational Details

Computational calculations were performed using the Gaussian 09 program package.[103] Geometry optimizations were carried out at the DFT level for the dimer aggregates of bis(merocyanine) dyes **21** and **22** (butyl and ethyl chains were replaced by methyl groups) with B97D3[99] as functional and def2-SVP[100] as basis set. The structures were geometry optimized, followed by frequency calculations on the optimized structures. One very small imaginary frequency of 13i cm^{-1} was obtained for the dimers of each of the bis(merocyanine) dyes **21** and **22**. Small imaginary frequencies (<100i cm^{-1}) are considered most likely to be an artefact of the calculation[104], thus the resulting geometries can be seen as real minima.

TDDFT calculations were performed on the geometry optimized structures using the long-range corrected ωB97 functional[101] and def2-SVP[100] as basis set. UV/Vis spectra of the dimer aggregates of bis(merocyanine) dyes **21** and **22** were simulated with the help of the GaussView 5[105] visualization software package using the results obtained by TDDFT calculations with a half-width at half-height of 0.16 eV.

For the determination of the exciton coupling energies we used the transition charges obtained for reference compounds **19** and **20** of Chapter 2.

4.5 Appendix

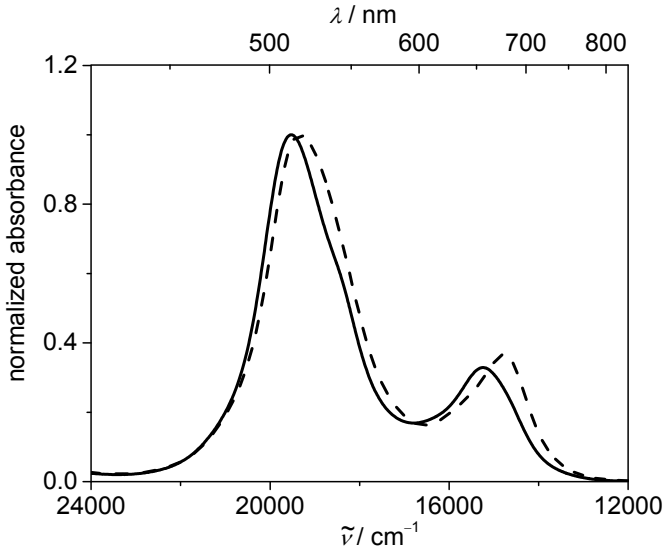

Figure 34. UV/Vis absorption spectrum of bis(merocyanine) **22** in a 1:1 mixture of 1,1,2,2-tetrachloroethane-d_2/tetrachloromethane (c = 8 x 10^{-3} M, solid line) at 298 K. The ideal dimer spectrum obtained by extrapolation of the data from concentration-dependent UV/Vis spectroscopy in chlorobenzene is shown (dashed line) for comparison.

Table 7. Summary of ^{1}H NMR (600 MHz) data for bis(merocyanine) **21**: Chemical shifts δ (ppm) and coupling constants J (Hz), and assignment of the significant chromophore and backbone proton signals of bis(merocyanine) dye **21** monomer (CD_2Cl_2 at 295 K) and aggregate (C_6D_5Cl at 233 K). The two sets of signals for the aggregate protons are denoted with (outer part of dye stack) and without prime (inner part of dye stack), respectively.

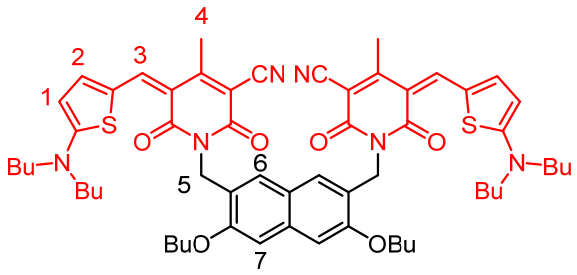

21

proton	δ_H [ppm] in CD_2Cl_2	δ_H [ppm] in C_6D_5Cl
1	6.36 (d, ^3J = 5.2 Hz, 2H)	6.19 (d, ^3J = 5.0 Hz, 1H)
1`		5.39 (d, ^3J = 4.2 Hz, 1H)
2	7.41 (2H, overlapped with proton 3)	7.06 (d, ^3J = 5.0 Hz, 1H)
2`		7.48 (2H, overlapped with proton 6`)
3	7.41 (2H, overlapped with proton 2)	7.22 (s, 1H)
3`		7.61 (s, 1H)
4	2.28 (br, 6H)	2.30 (s, 3H)
4`		2.38 (s, 3H)
5α	5.17 (s, 4H)	5.60 (d, ^2J = 16.9 Hz, 1H)
5β		5.43 (d, ^2J = 15.5 Hz, 1H)
5`α		5.79/5.76 (d, ^2J = 15.5 Hz, 1H)
5`β		5.79/5.76 (d, ^2J = 15.5 Hz, 1H)
6	6.92 (s, 2H)	7.54 (s, 1H)
6`		7.48 (overlapped with proton 2`, 1H)
7	7.12 (s, 2H)	6.76 (s, 1H)
7`		6.81 (s, 1H)

Table 8. Summary of ^{1}H NMR (600 MHz) data for bis(merocyanine) **22**: Chemical shifts δ (ppm) and coupling constants J (Hz), and assignment of the significant chromophore and backbone proton signals of bis(merocyanine) dye **22** monomer (CD_2Cl_2 at 295 K) and aggregate (1:1 mixture of 1,1,2,2-tetrachloroethane-d_2/tetrachloromethane at 253 K).

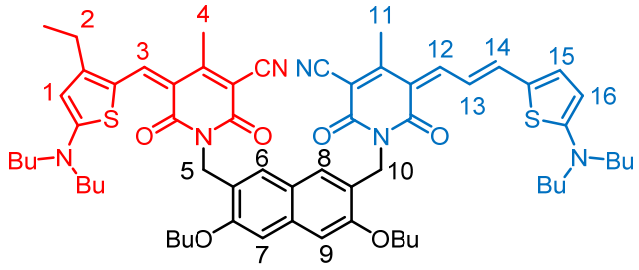

22

proton	δ_H [ppm] in CD_2Cl_2	δ_H [ppm] in 1,1,2,2-tetrachloroethane-d_2/CCl_4 1:1
1	6.27 (s, 1H)	6.05 (s, 1H)
2	2.77 (q, ^{3}J = 7.1 Hz, 2H)	2.53 (br 2H)
3	7.69 (s, 1H)	7.31 (s, 1H)
4	2.46 (s, 3H)	2.35 (s, 3H)
5	5.17/5.16 (s, 2H, could not be distinguished from protons 10)	5.33-5.08 (br, 2H, overlapped with protons 10)
6	6.91/6.90 (s, 1H, could not be distinguished from proton 8)	6.85/6.83 (s, 1H, could not be distinguished from proton 8)
7	7.08 (s, 1H, overlapped with proton 9)	7.18/7.15 (s, 1H, could not be distinguished from proton 9)
8	6.91/6.90 (s, 1H, could not be distinguished from proton 6)	6.85/6.83 (s, 1H, could not be distinguished from proton)
9	7.08 (s, 1H, overlapped with proton 7)	7.18/7.15 (s, 1H, could not be distinguished from proton 7)
10	5.17/5.16 (s, 2H, could not be distinguished from proton 5)	5.33-5.08 (br, 2H, overlapped with protons 5)
11	2.32 (s, 3H)	1.84 (s, 3H)
12	7.27 (1H, overlapped with proton 15)	6.64 (d, ^{3}J = 13.0 Hz, 1H)
13	7.96 (br, 1H)	7.68 (dd, ^{3}J = 13.0 Hz, ^{3}J = 12.0 Hz, 1H)
14	7.34 (d, ^{3}J = 12.5 Hz, 1H)	6.94 (d, ^{3}J = 12.0 Hz, 1H)
15	7.27 (1H, overlap with proton 12)	7.03 (d, ^{3}J = 4.1 Hz, 1H)
16	6.21 (d, ^{3}J = 3.3 Hz, 1H)	6.33 (d, ^{3}J = 4.1 Hz, 1H)

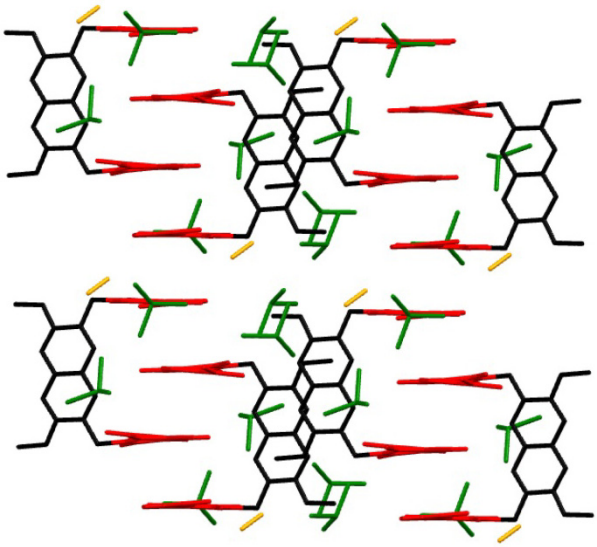

Figure 35. Molecular packing of bis(merocyanine) **21** in the solid state (hydrogen atoms are omitted for clarity and butyl chains were replaced by methyl groups).[106] The chromophores are colored in red and the naphthalene spacer unit in black. Chloroform and methanol solvent molecules are visualized in green and orange, respectively.

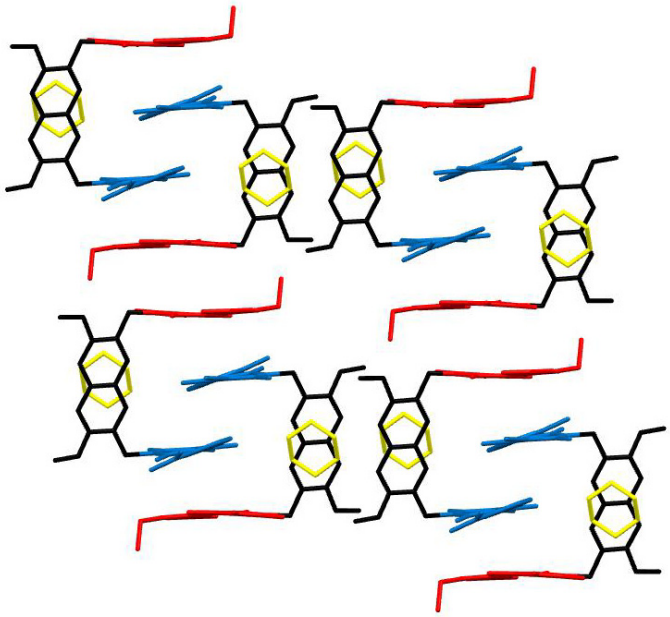

Figure 36. Molecular packing of bis(merocyanine) **22** in the solid state (hydrogen atoms are omitted for clarity and butyl chains were replaced by methyl groups). The chromophores are colored in red (short chromophore) and blue (long chromophore), respectively, while the naphthalene spacer unit is colored in black. Solvent (1,4-dioxane) molecules are colored in yellow.

Additional Theoretical Investigations

Like shown in Chapter 3 for the Hamiltonian of the dimers, the diagonal matrix elements represent the excited state energies of the monomeric chromophores, whereas the non-diagonal matrix elements correspond to the exciton coupling energy. Hence, the Hamiltonian for the quadruple dye stacks can be written as

$$\begin{pmatrix} E_1^* & J_{12} & 0 & 0 \\ J_{12} & E_2^* & J_{23} & 0 \\ 0 & J_{23} & E_3^* & J_{34} \\ 0 & 0 & J_{34} & E_4^* \end{pmatrix},$$

where the next-neighbor approximation is applied, which means that only the exciton coupling between next-neighbored chromophores are considered. Due to the symmetry of the dye stack, the exciton coupling energy between chromophore 1 and 2 is the same like between chromophores 3 and 4 and we obtain:

$$\begin{pmatrix} E_1^* & J_{12} & 0 & 0 \\ J_{12} & E_2^* & J_{23} & 0 \\ 0 & J_{23} & E_3^* & J_{12} \\ 0 & 0 & J_{12} & E_4^* \end{pmatrix}.$$

For the homoaggregate of bis(merocyanine) **21** the Hamiltonian simplifies to:

$$\begin{pmatrix} 0 & J_{12} & 0 & 0 \\ J_{12} & 0 & J_{23} & 0 \\ 0 & J_{23} & 0 & J_{12} \\ 0 & 0 & J_{12} & 0 \end{pmatrix},$$

where the excited state energy of the short chromophore is set as zero level. We write for the Hamiltonian matrix of the heteroaggregate of **22**:

$$\begin{pmatrix} \Delta E & J_{12} & 0 & 0 \\ J_{12} & -\Delta E & J_{23} & 0 \\ 0 & J_{23} & -\Delta E & J_{12} \\ 0 & 0 & J_{12} & \Delta E \end{pmatrix}.$$

Here, ΔE is half the energy difference between the excited state energies of the long and short chromophore, respectively, and the midpoint of both excited state energies is set as zero level.

Table 9. Exciton state energies of the dimers of bis(merocyanine) **21** and **22** determined on the basis of the eigenvalues of the corresponding Hamiltonian matrix.

bis(merocyanine) **21**[a]	bis(merocyanine) **22**[b]
16044 cm^{-1}	13277 cm^{-1}
17496 cm^{-1}	15090 cm^{-1}
19514 cm^{-1}	18929 cm^{-1}
20966 cm^{-1}	19333 cm^{-1}

[a]Calculated by $E_e + 18505\ cm^{-1}$. [b]Calculated by $E_e + 16657\ cm^{-1}$. E_e represents the corresponding eigenvalue of the Hamiltonian matrix. The translation is necessary due to the definition of the zero level.

Table 10. Calculated coefficients of the normed eigenvectors of the Hamiltonian matrix of the quadruple dye stack of bis(merocyanine) **21**.

	c_1	c_2	c_3	c_4
E_{e1}	–0.3813	0.5954	–0.5954	0.3813
E_{e2}	0.5955	–0.3813	–0.3813	0.5955
E_{e3}	–0.5955	–0.3813	0.3813	0.5955
E_{e4}	0.3813	0.5954	0.5954	0.3813

Table 11. Calculated coefficients of the normed eigenvectors of the Hamiltonian matrix of the quadruple dye stack of bis(merocyanine) **22**.

	c_1	c_2	c_3	c_4
E_{e1}	–0.2487	0.6619	–0.6619	0.2487
E_{e2}	0.3605	–0.6084	–0.6084	0.3605
E_{e3}	–0.6619	–0.2486	0.2486	0.6619
E_{e4}	0.6083	0.3604	0.3604	0.6083

Components of the normed eigenvectors of the Hamiltonian matrix for the dye stack of bis(merocyanine) **21**.

Exciton state 1:

$$c_1 = -\frac{1}{\sqrt{2+\frac{\left(J_{23}+\sqrt{4J_{12}^2+J_{23}^2}\right)^2}{2J_{12}^2}}}$$

$$c_2 = \frac{J_{23}+\sqrt{4J_{12}^2+J_{23}^2}}{2J_{12}\sqrt{2+\frac{\left(J_{23}+\sqrt{4J_{12}^2+J_{23}^2}\right)^2}{2J_{12}^2}}}$$

$$c_3 = -\frac{J_{23}+\sqrt{4J_{12}^2+J_{23}^2}}{2J_{12}\sqrt{2+\frac{\left(J_{23}+\sqrt{4J_{12}^2+J_{23}^2}\right)^2}{2J_{12}^2}}}$$

$$c_4 = \frac{1}{\sqrt{2+\frac{\left(J_{23}+\sqrt{4J_{12}^2+J_{23}^2}\right)^2}{2J_{12}^2}}}$$

Exciton state 2:

$$c_1 = \frac{1}{\sqrt{2+\frac{\left(J_{23}-\sqrt{4J_{12}^2+J_{23}^2}\right)^2}{2J_{12}^2}}}$$

$$c_2 = \frac{J_{23}-\sqrt{4J_{12}^2+J_{23}^2}}{2J_{12}\sqrt{2+\frac{\left(J_{23}-\sqrt{4J_{12}^2+J_{23}^2}\right)^2}{2J_{12}^2}}}$$

$$c_3 = \frac{J_{23}-\sqrt{4J_{12}^2+J_{23}^2}}{2J_{12}\sqrt{2+\frac{\left(J_{23}-\sqrt{4J_{12}^2+J_{23}^2}\right)^2}{2J_{12}^2}}}$$

$$c_4 = \frac{1}{\sqrt{2+\frac{\left(J_{23}-\sqrt{4J_{12}^2+J_{23}^2}\right)^2}{2J_{12}^2}}}$$

Exciton state 3:

$$c_1 = -\frac{1}{\sqrt{2+\frac{\left(J_{23}-\sqrt{4J_{12}^2+J_{23}^2}\right)^2}{2J_{12}^2}}}$$

$$c_2 = \frac{J_{23}-\sqrt{4J_{12}^2+J_{23}^2}}{2J_{12}\sqrt{2+\frac{\left(J_{23}-\sqrt{4J_{12}^2+J_{23}^2}\right)^2}{2J_{12}^2}}}$$

Exciton state 4:

$$c_1 = \frac{1}{\sqrt{2+\frac{\left(J_{23}+\sqrt{4J_{12}^2+J_{23}^2}\right)^2}{2J_{12}^2}}}$$

$$c_2 = \frac{J_{23}+\sqrt{4J_{12}^2+J_{23}^2}}{2J_{12}\sqrt{2+\frac{\left(J_{23}+\sqrt{4J_{12}^2+J_{23}^2}\right)^2}{2J_{12}^2}}}$$

$$c_3 = -\frac{J_{23} - \sqrt{4J_{12}^2 + J_{23}^2}}{2J_{12}\sqrt{2 + \frac{\left(J_{23} - \sqrt{4J_{12}^2 + J_{23}^2}\right)^2}{2J_{12}^2}}} \qquad c_3 = \frac{J_{23} + \sqrt{4J_{12}^2 + J_{23}^2}}{2J_{12}\sqrt{2 + \frac{\left(J_{23} + \sqrt{4J_{12}^2 + J_{23}^2}\right)^2}{2J_{12}^2}}}$$

$$c_4 = \frac{1}{\sqrt{2 + \frac{\left(J_{23} - \sqrt{4J_{12}^2 + J_{23}^2}\right)^2}{2J_{12}^2}}} \qquad c_4 = \frac{1}{\sqrt{2 + \frac{\left(J_{23} + \sqrt{4J_{12}^2 + J_{23}^2}\right)^2}{2J_{12}^2}}}$$

Components of the normed eigenvectors of the Hamiltonian matrix for the dye stack of bis(merocyanine) **22**.

Exciton state 1:

$$c_1 = -\frac{1}{\sqrt{2 + \frac{\left(2\Delta E + J_{23} + \sqrt{4\Delta E^2 + 4J_{12}^2 + 4\Delta E J_{23} + J_{23}^2}\right)^2}{2J_{12}^2}}}$$

$$c_2 = \frac{2\Delta E + J_{23} + \sqrt{4\Delta E^2 + 4J_{12}^2 + 4\Delta E J_{23} + J_{23}^2}}{2J_{12}\sqrt{2 + \frac{\left(2\Delta E + J_{23} + \sqrt{4\Delta E^2 + 4J_{12}^2 + 4\Delta E J_{23} + J_{23}^2}\right)^2}{2J_{12}^2}}}$$

$$c_3 = -\frac{2\Delta E + J_{23} + \sqrt{4\Delta E^2 + 4J_{12}^2 + 4\Delta E J_{23} + J_{23}^2}}{2J_{12}\sqrt{2 + \frac{\left(2\Delta E + J_{23} + \sqrt{4\Delta E^2 + 4J_{12}^2 + 4\Delta E J_{23} + J_{23}^2}\right)^2}{2J_{12}^2}}}$$

$$c_4 = \frac{1}{\sqrt{2 + \frac{\left(2\Delta E + J_{23} + \sqrt{4\Delta E^2 + 4J_{12}^2 + 4\Delta E J_{23} + J_{23}^2}\right)^2}{2J_{12}^2}}}$$

Exciton state 2:

$$c_1 = \frac{1}{\sqrt{2 + \frac{\left(2\Delta E - J_{23} + \sqrt{4\Delta E^2 + 4J_{12}^2 - 4\Delta E J_{23} + J_{23}^2}\right)^2}{2J_{12}^2}}}$$

$$c_2 = -\frac{2\Delta E - J_{23} + \sqrt{4\Delta E^2 + 4J_{12}^2 - 4\Delta E J_{23} + J_{23}^2}}{2J_{12}\sqrt{2 + \frac{\left(2\Delta E - J_{23} + \sqrt{4\Delta E^2 + 4J_{12}^2 - 4\Delta E J_{23} + J_{23}^2}\right)^2}{2J_{12}^2}}}$$

$$c_3 = -\frac{2\Delta E - J_{23} + \sqrt{4\Delta E^2 + 4J_{12}^2 - 4\Delta E J_{23} + J_{23}^2}}{2J_{12}\sqrt{2 + \frac{\left(2\Delta E - J_{23} + \sqrt{4\Delta E^2 + 4J_{12}^2 - 4\Delta E J_{23} + J_{23}^2}\right)^2}{2J_{12}^2}}}$$

$$c_4 = \frac{1}{\sqrt{2 + \frac{\left(2\Delta E - J_{23} + \sqrt{4\Delta E^2 + 4J_{12}^2 - 4\Delta E J_{23} + J_{23}^2}\right)^2}{2J_{12}^2}}}$$

Exciton state 3:

$$c_1 = -\frac{1}{\sqrt{2 + \frac{\left(2\Delta E - J_{23} + \sqrt{4\Delta E^2 + 4J_{12}^2 - 4\Delta E J_{23} + J_{23}^2}\right)^2}{2J_{12}^2}}}$$

$$c_2 = \frac{2\Delta E + J_{23} - \sqrt{4\Delta E^2 + 4J_{12}^2 + 4\Delta E J_{23} + J_{23}^2}}{2J_{12}\sqrt{2 + \frac{\left(2\Delta E + J_{23} - \sqrt{4\Delta E^2 + 4J_{12}^2 + 4\Delta E J_{23} + J_{23}^2}\right)^2}{2J_{12}^2}}}$$

$$c_3 = -\frac{2\Delta E + J_{23} - \sqrt{4\Delta E^2 + 4J_{12}^2 + 4\Delta E J_{23} + J_{23}^2}}{2J_{12}\sqrt{2 + \frac{\left(2\Delta E + J_{23} - \sqrt{4\Delta E^2 + 4J_{12}^2 + 4\Delta E J_{23} + J_{23}^2}\right)^2}{2J_{12}^2}}}$$

$$c_4 = \frac{1}{\sqrt{2 + \frac{\left(2\Delta E + J_{23} - \sqrt{4\Delta E^2 + 4J_{12}^2 + 4\Delta E J_{23} + J_{23}^2}\right)^2}{2J_{12}^2}}}$$

Exciton state 4:

$$c_1 = \frac{1}{\sqrt{2 + \frac{\left(2\Delta E - J_{23} - \sqrt{4\Delta E^2 + 4J_{12}^2 - 4\Delta E J_{23} + J_{23}^2}\right)^2}{2J_{12}^2}}}$$

$$c_2 = -\frac{2\Delta E - J_{23} - \sqrt{4\Delta E^2 + 4J_{12}^2 - 4\Delta E J_{23} + J_{23}^2}}{2J_{12}\sqrt{2 + \frac{\left(2\Delta E - J_{23} - \sqrt{4\Delta E^2 + 4J_{12}^2 - 4\Delta E J_{23} + J_{23}^2}\right)^2}{2J_{12}^2}}}$$

$$c_3 = -\frac{2\Delta E - J_{23} - \sqrt{4\Delta E^2 + 4J_{12}^2 - 4\Delta E J_{23} + J_{23}^2}}{2J_{12}\sqrt{2 + \frac{\left(2\Delta E - J_{23} - \sqrt{4\Delta E^2 + 4J_{12}^2 - 4\Delta E J_{23} + J_{23}^2}\right)^2}{2J_{12}^2}}}$$

$$c_4 = \frac{1}{\sqrt{2 + \frac{\left(2\Delta E - J_{23} - \sqrt{4\Delta E^2 + 4J_{12}^2 - 4\Delta E J_{23} + J_{23}^2}\right)^2}{2J_{12}^2}}}$$

Chapter 5

Exciton-Vibrational Coupling in Homo- and Heteroaggregate Stacks of Perylene Bisimide Dyes Within Cyclophanes[8]

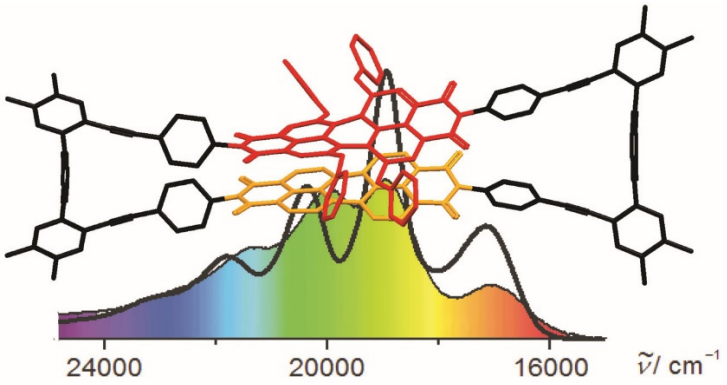

Abstract: The optical properties of a series of three cyclophanes comprising either identical or different perylene bisimide (PBI) chromophores were studied by UV/Vis absorption spectroscopy and their distinctive spectral features were analyzed. All the investigated cyclophanes show significantly different absorption features with respect to the corresponding constituent PBI monomers indicating strong coupling interactions between the PBI units within the cyclophanes. DFT calculations suggest a π-stacked arrangement of the PBI units at a close van-der-Waals distance in the cyclophanes with a rotational displacement. Simulations of the absorption spectra based on time-dependent quantum mechanics properly reproduced the experimental spectra, revealing exciton-vibrational coupling between the chromophores both in homo- and heterodimer stacks. The PBI cyclophane comprising two different PBI chromophores represents the first example of a PBI heterodimer stack for which the exciton coupling has been investigated. The quantum dynamics analysis reveals that exciton coupling in heteroaggregates is indeed of similar strength as in homoaggregates.

[8] This chapter was published in: D. Bialas, C. Brüning, F. Schlosser, B. Fimmel, J. Thein, V. Engel, F. Würthner, *Chem. Eur. J.* **2016**, *22,* 15011–15018 (http://onlinelibrary.wiley.com/doi/10.1002/chem.201603205/full).

5.1 Introduction

The studies on merocyanine hetero-π-stacks[111, 112] revealed strong exciton coupling between different types of chromophores with distinct absorption maxima at ≈540 and ≈650 nm despite an energetic offset of >3000 cm^{-1} between the absorption energies of the two dyes. Consequently, significantly different absorption spectra were recorded for the heteroaggregate systems compared to the addition of the spectra of the individual monomeric dyes as well as to the spectra of the respective homoaggregates.

These results constituted the starting point for the studies on the exciton coupling in perylene bisimide-based homo- and heteroaggregates. Perylene-3,4:9,10-bis(dicarboximides) (in short perylene bisimides; PBIs) represent a privileged class of chromophores for various applications owing to their outstanding optical and electronic features. They exhibit high photostability,[113] easily tunable absorption, fluorescence and redox properties,[114, 115] and thus comply with the basic requirements for applications in organic electronics[36, 37] and photovoltaics.[38, 39] In addition, their unique self-assembly behavior based on π-π-stacking and hydrogen-bonding interactions makes them highly versatile building blocks for the construction of functional supramolecular assemblies.[116]

The optical properties of PBI assemblies depend not only on the structural features of the constituent monomeric chromophores but also very decisively on the molecular arrangement in the assembly, leading to exciton coupling regimes that cover the whole range from H- to J-type.[116, 117] For PBIs the situation is, however, more challenging than for the above-mentioned merocyanine dyes because the optical excitation of PBIs is accompanied by a strong coupling to aromatic carbon-carbon stretching vibrations. The resultant complex exciton-vibrational coupling in PBI aggregates requires accordingly a more elaborate quantum dynamical treatment that we and others have pursued in work on PBI π-stacks of various size but always comprised of the same type of PBI chromophores.[40, 41, 118-121]

Since supramolecular aggregates consisting of different types of chromophores can provide functionalities that cannot be realized for homoaggregates,[20, 21, 24, 25, 27, 122-124] gaining insight into the exciton coupling of PBI hetero-π-stacks should be a rewarding task.

Detailed studies of interchromophore interactions require model systems with distinct orientations of the chromophores.[125, 126] For this purpose, PBI cyclophanes[127, 128] bearing two PBI chromophores with a fixed geometry imposed by a spacer are properly suited.

Accordingly, the absorption properties of a first example of a structurally well-defined PBI heterodimer π-stack was elucidated by quantum dynamical analysis, along with two homodimer π-stacks for comparison (Chart 1).

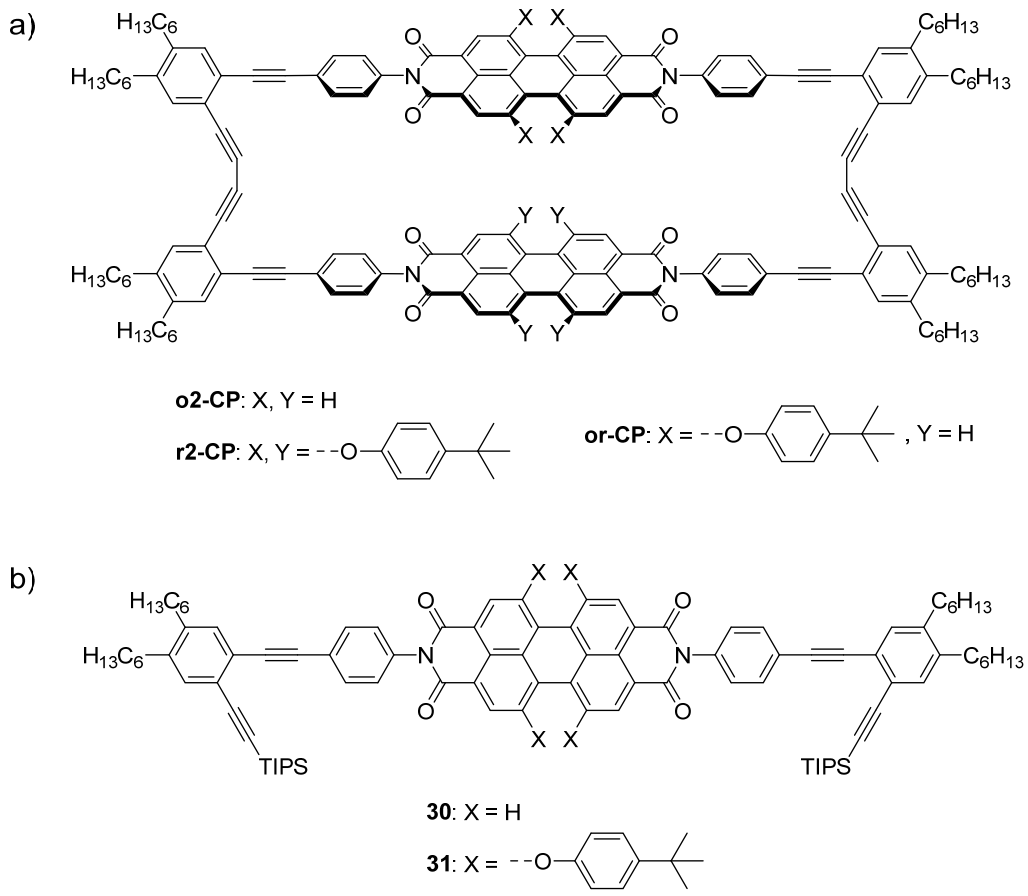

Chart 1. a) Chemical structures of homo PBI cyclophanes **o2-CP** and **r2-CP** containing two identical chromophores and hetero PBI cyclophane **or-CP** comprising two different ones. In the notation of the cyclophanes (CP) 'o' and 'r' indicate the parent orange-colored and the tetraphenoxy-substituted red-colored PBI chromophores, respectively. b) Chemical structure of reference PBI dyes **30** and **31**.[129]

Cyclophane **r2-CP** comprising two identical PBI chromophores bearing *tert*-butylphenoxy substituents at the bay positions ('red PBI') affords cofacially stacked PBI chromophores, as already reported.[130] A perfect preorganization of the PBI chromophores in these molecules in a π-stacked arrangement is provided by the phenylene butadiynylene spacer unit. To study exciton coupling in PBI heterodimer stacks, cyclophane **or-CP**[129] consisting of two different PBI units, one bearing *tert*-butylphenoxy groups at the bay positions and a non-substituted PBI unit ('orange PBI') has been selected. For

comparison, cyclophane **o2-CP**[129] containing two bay-unsubstituted PBI chromophores was also included in these studies (Chart 1).[9]

5.2 Results and Discussion

5.2.1 UV/Vis Absorption Spectroscopy[10]

Exciton-vibrational couplings manifest in the UV/Vis absorption bands of the respective optical transitions. Accordingly, the PBI cyclophanes **o2-CP**, **r2-CP** and **or-CP** were studied in comparison with the corresponding mono-chromophoric PBI references by UV/Vis spectroscopy in high permittivity ($\varepsilon_r \approx 9.0$) solvent dichloromethane under high dilution to ensure the absence of any intermolecular aggregates formed by self-association. The mono-chromophoric reference PBI **30** shows typical absorption bands of a core-unsubstituted PBI chromophore with a pronounced vibronic fine structure (Figure 37a, orange line).[116] The 0-0 transition of the highest intensity is located at 528 nm and is accompanied by vibronic progressions at 491, 459 and 431 nm. In contrast, the spectrum of cyclophane **o2-CP** containing two identical core-unsubstituted PBI chromophores shows a reversal of the band intensities compared to the reference PBI **30** at around 530 and 490 nm (Figure 37a, black line). This phenomenon is characteristic of helically π-stacked orange PBI chromophores and arises from exciton-vibrational coupling.[40, 41] The spectra indeed resemble those of self-assembled closely stacked orange PBI dyes[131, 132] for which our analysis yielded an exciton coupling strength of 524 cm^{-1} for the exciton coupling strength, *i.e.* a situation called the intermediate coupling regime.[40, 41] A similar situation is given for the red cyclophane **r2-CP** (Figure 37b, black line). Here, the mono-chromophoric red PBI reference **31** bearing four *tert*-butylphenoxy substituents at bay positions shows a bathochromic shift to 583 nm compared to the core-unsubstituted orange PBI reference **30** with broader absorption bands and a loss of vibronic fine structure (Figure 37b, red line). These less defined vibronic progressions are caused by the bulky *tert*-butylphenoxy substituents, which induce a rotational twist of the two naphthalene-imide subunits, thereby reducing the rigidity of the scaffold and enabling a broader conformational distribution.[133-136] The absorption band at 541 nm corresponds to

[9] The PBI cyclophanes were synthesized by Dr. Felix Schlosser, Dr. Benjamin Fimmel and Johannes Thein.
[10] UV/Vis measurements were performed by Dr. Felix Schlosser and Dr. Benjamin Fimmel.

the vibronic progression of the S_0-S_1 absorption band, while the weak absorption band at 454 nm arises from the S_0-S_2 transition.[137]

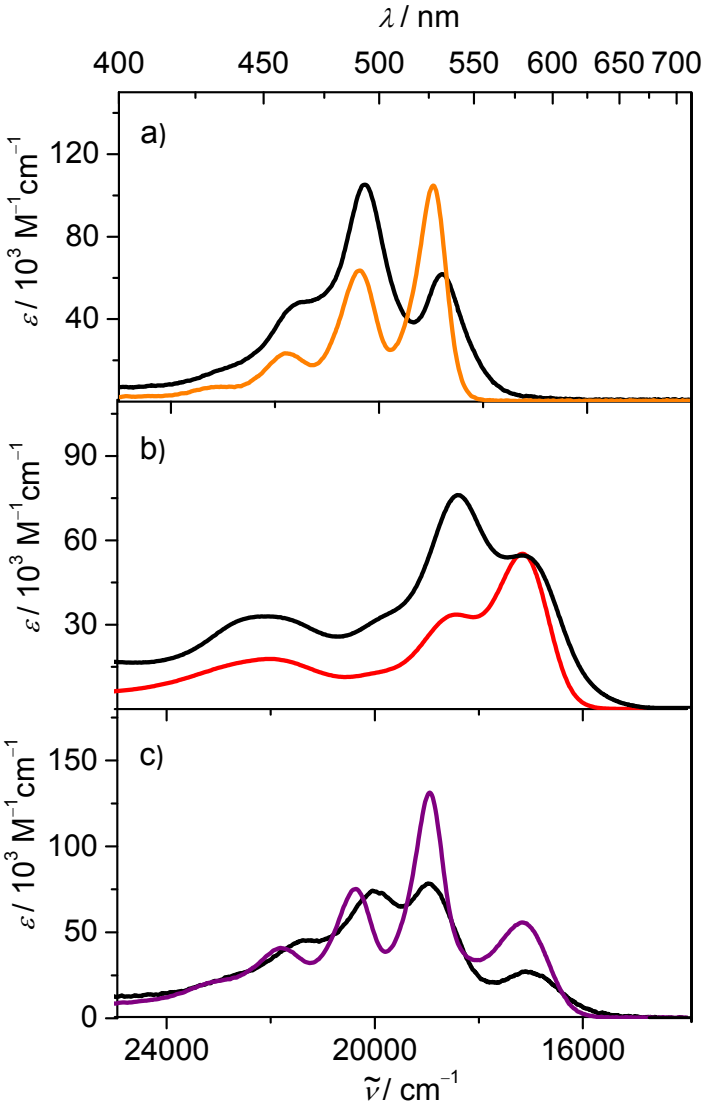

Figure 37. UV/Vis absorption spectra of a) reference **30** (orange line) and cyclophane **o2-CP** (black line), b) reference **31** (red line) and cyclophane **r2-CP** (black line) and c) sum of the spectra of **30** and **31** (purple line) as well as the spectrum of cyclophane **or-CP** (black line) in dichloromethane ($c \approx 10^{-5}$ M) at 298 K.

Like in the case of cyclophane **o2-CP**, the absorption spectrum of cyclophane **r2-CP** bearing two identical core-tetraphenoxy-substituted red PBI chromophores shows a reversal of the band intensities at around 580 and 540 nm with respect to the corresponding reference PBI derivative **31**. This spectral feature of **r2-CP** indicates a π-stacked arrangement with exciton-vibrational coupling of the red PBI chromophores in this cyclophane as well (Figure 37b, black line),[130] similarly to **o2-CP**.

As evident from Figure 37c, the situation for cyclophane **or-CP** bearing one core-unsubstituted and one core-tetraphenoxy-substituted PBI chromophore is more complex. Thus, the absorption spectrum of **or-CP** (black line) does neither equal the sum of the spectra of the respective reference compounds **30** and **31** (situation without exciton coupling, purple line), nor does it resemble the spectra of **o2-CP** and **r2-CP**. However, a clearly visible redistribution of oscillator strength among the dyes is indicative of an exciton coupling interaction between the different types of chromophores within this cyclophane. The shift of the 0-0 absorption band of the constituent PBIs are, however, very modest for cyclophane **or-CP** when compared with **o2-CP**. Accordingly, in the spectrum of **or-CP** a small bathochromic shift of the absorption band of the core-tetraphenoxy-substituted PBI chromophore from 583 to 586 nm and a smaller modulation of the absorption of the core-unsubstituted PBI were observed compared to **o2-CP**. As for the homodimers **o2-CP** and **r2-CP** additional bands at 500 and 469 nm are observed, which are of higher intensity and show a bathochromic shift compared to the absorption bands of the vibronic progression of reference PBI **30**. Taken together, these spectroscopic observations clearly indicate an exciton coupling between the two different PBI chromophores within cyclophane **or-CP** leading to distinctive changes in the optical absorption properties.

The absorption spectra of all three cyclophanes in less polar solvent toluene (Figure 38) are very similar to the ones measured in dichloromethane. Besides a hypsochromic shift for cyclophanes **r2-CP** and **or-CP**, which is known as positive solvatochromism of PBI chromophores,[138, 139] the shape of the spectra is not affected by the solvent polarity. This indicates similar coupling strengths in toluene and dichloromethane for all three cyclophanes and hence, same arrangements of the chromophores in both solvents.

The subsequent theoretical studies were devoted to establish a proper understanding of this exciton coupling in heterodimers in the presence of strong vibrational coupling observed for PBI dyes and the majority of other common chromophores.

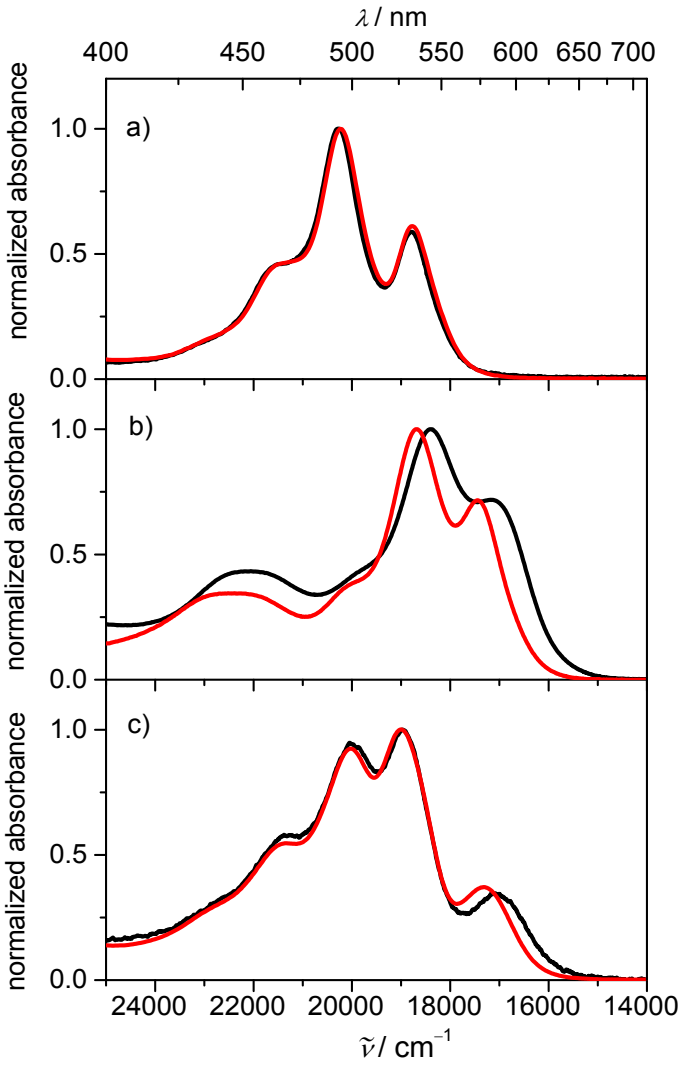

Figure 38. UV/Vis absorption spectra of PBI cyclophanes a) **o2-CP**, b) **r2-CP** and c) **or-CP** measured in dichloromethane (black lines) and toluene (red lines) at 298 K ($c \approx 10^{-5}$ M).

5.2.2 Quantum Chemical Studies

According to CPK models, the π-conjugated phenylene butadiynylene tethers are supposed to preorganize the PBI units in a rather stiff or even compressed cofacial π-stacking arrangement. Nevertheless, due to the different geometries of the two utilized PBI cores – orange PBI being planar and red PBI having a twisted π-core (rotational twist of 25-30° between the two naphthalene imide subunits)[133-135] – and the sterical demands of the tetraphenoxy substituents, a deeper insight into the specific molecular arrangement of the PBI chromophores within the cyclophanes is required. Therefore, DFT calculations were performed by employing B97D3[99] as functional and def2-SVP[100] as basis set. The

functional includes dispersion correction which is required to describe π-π-interactions between the PBI chromophores in an adequate way.[32] The geometry optimized structures of the PBI cyclophanes are shown in Figure 39. All three cyclophanes show π-π-stacking between the PBI chromophores with distances (r) of 3.24 – 3.84 Å and rotational displacements (α) of 10.6 – 28.6° between the chromophores. The molecular arrangement of the chromophores in cyclophane **o2-CP** (r = 3.24 Å, α = 28.6°) represents the ideal ground state geometry of two cofacially stacked core-unsubstituted orange PBI chromophores.[32] This corroborates validity of our molecular design of a spacer unit for supporting the desired preorganization of these chromophores in the cyclophanes.

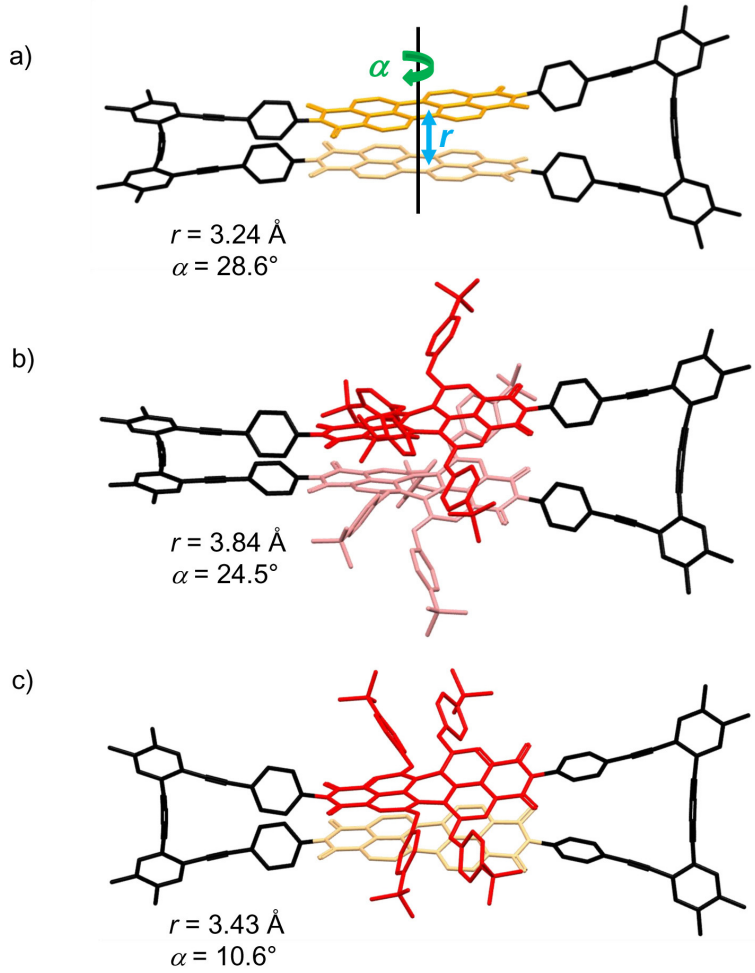

Figure 39. Geometry optimized structures of PBI cyclophanes a) **o2-CP**, b) **r2-CP** and c) **or-CP** (B97D3, def2-SVP, hexyl groups were replaced by methyl groups). Hydrogen atoms were omitted for clarity. α represents the rotational displacement and r the distance between the chromophores in the respective cyclophanes as depicted in Figure 39a.

While the core-unsubstituted orange PBI chromophores in **o2-CP** are almost perfectly planar, the naphthalene imide units of the core-tetraphenoxy-substituted red PBI in **r2-CP** are twisted by 27° due to the steric constraints in the bay area imposed by the bulky *tert*-butylphenoxy substituents.[33, 133-135] Notably, this value is also in accordance with crystallographic data for monomeric tetraphenoxy-substituted PBIs.[133-135, 140] The phenoxy substituents prevent, however, a close contact of the PBI chromophores in twisted conformation, which results in a larger distance of 3.84 Å between the π-scaffolds in **r2-CP**. As our calculation shows, the phenylene butadiynylene tether enforced helical displacement of 24.5° enables all eight phenoxy substituents to accommodate without sterical congestions as a homochiral dye pair (both dyes exhibit the same planar chirality, *i.e. PP* or *MM*). For **or-CP** the situation is obviously more demanding because a planar and a non-planar dye have to interact by cofacial π–π-stacking. According to our calculations, the interchromophore distance in **or-CP** is smaller compared to that of **r2-CP** and indeed close to **o2-CP** despite the fact that one PBI contains bulky substituents and a twisted π-core. Remarkably, to enable such a close contact the planarity of the core-unsubstituted orange PBI chromophore is lost in cyclophane **or-CP** leading to a rotational twist of ca. 11° caused by a templating effect of the core-twisted (26°) red PBI chromophore bearing four bay substituents. Accordingly, the utilized phenylene butadiynylene bridging units indeed act as brackets which compress the two dyes on top of each other.

5.2.3 Quantum Dynamics Studies

For a dimer stack of two identical chromophores in a hypothetical perfectly collinear arrangement we should expect a hypsochromically shifted absorption band with respect to the monomer absorption band according to molecular exciton theory (Figure 40a).[5, 8] As shown in Chapter 3 on the merocyanine heterodimer composed of two chromophores with different excited state energies, an exciton coupling also occurs between two different types of chromophores.[111] Based on these insights, we can expect two absorption bands for a perfect heterodimer with a hypsochromic and a bathochromic shift with regard to the absorption bands of the involved monomeric chromophores and a redistribution of oscillator strength, *i.e.* an increase in absorbance of the higher and a decrease in absorbance of the lower exciton state, should be observed (Figure 40b).

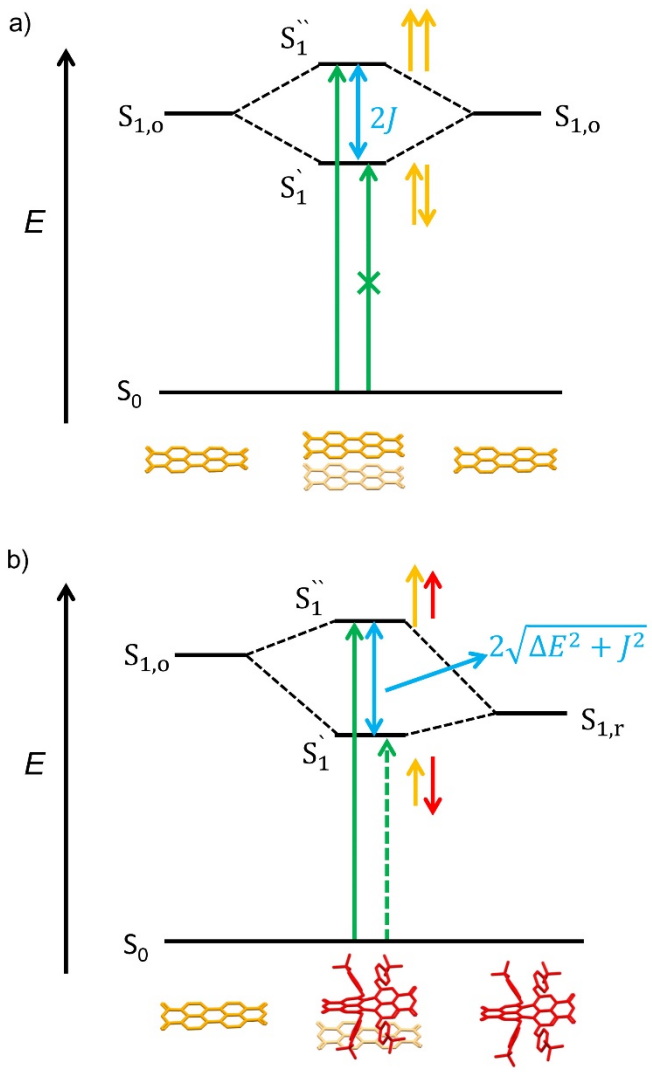

Figure 40. Schematic exciton state diagram for H-type PBI dimer stack composed of a) identical and b) different chromophores in a hypothetical collinear arrangement and neglecting vibrational coupling. The orange and red arrows illustrate the relationship between the transition dipole moments. $S_{1,o}$ and $S_{1,r}$ denote the excited states of orange and red PBI, respectively. ΔE is half the energy difference between the excited states $S_{1,o}$ and $S_{1,r}$, and J represents the exciton coupling energy.

For the given PBI cyclophanes the situation is, however, more complex due to the strong coupling of the PBI $S_0 \rightarrow S_1$ transition to aromatic CC-stretching modes and a rotational displacement of the chromophores. In the case of a rotational displacement of the chromophores, the transition to the lower exciton state becomes partially allowed,[8] which is manifested by the presence of a second less intense absorption band with a bathochromic shift ('J-band') even for identical chromophores. Due to the fact that for the PBI $S_0 \rightarrow S_1$ transition the vibrational coupling of about 1400 cm^{-1} is stronger than the exciton coupling of about 500 cm^{-1} (so-called intermediate coupling regime) the main

signature of the exciton coupling is indeed not a pronounced shift of the absorption band but the reversal of the intensity of the two lowest energy bands[40, 41, 118-121] as observed for **o2-CP** and **r2-CP** homodimers in Figure 37a,b. Accordingly, the simple model described above has to be extended by considering rotational displacements as well as vibrational coupling between the chromophores. Following our earlier work on homoaggregates of PBIs[40, 41] we can be confident to obtain a conclusive understanding of the absorption bands of **o2-CP** and **r2-CP** homodimers and novel insights into the hitherto unexplored impact of exciton-vibrational couplings on the spectra of hetero PBI cyclophane **or-CP**.

Towards this goal time-dependent quantum mechanical simulations have been performed in the group of Prof. Engel.[11] More specifically, the time-dependent Schrödinger equation for a Hamiltonian of Holstein-type[59, 141] is solved, which gives excellent description of vibronic spectra[60, 142] and has been applied to self-assembled PBI aggregates before.[40, 41]

To set up the models for the monomers, a typically employed approach was used which includes the electronic ground state |g> and the excited state |e> with vibrational Hamiltonians

$$\hat{H}_g = -\frac{1}{2}\frac{d^2}{dx^2} + \frac{1}{2}\omega^2 x^2 \tag{80}$$

and

$$\hat{H}_e = -\frac{1}{2}\frac{d^2}{dx^2} + \frac{1}{2}\,\omega^2\,(x - x_e)^2 + \Delta E_m. \tag{81}$$

The Hamiltonians are those of harmonic oscillators with a scaled vibrational coordinate x and the vibrational frequency ω. The excited state potential is shifted by the equilibrium distance x_e and the excitation energy ΔE_m. The value of the equilibrium distance is related to the Huang-Rhys factor ξ as $x_e = \xi\sqrt{\frac{2}{\omega}}$.

The dimer Hamiltonian is constructed from Hamiltonians of the monomers as follows:

$$H_d = |g,g\rangle\hat{H}_{g,g}\langle g,g| + |e,g\rangle\hat{H}_{e,g}\langle e,g| + |g,e\rangle\hat{H}_{g,e}\langle g,e|$$
$$+ |e,g\rangle J\langle g,e| + |g,e\rangle J\langle e,g|. \tag{82}$$

[11] Time-dependent quantum mechanical simulations were performed by Dr. Christoph Brüning.

Here, we assume the Hamiltonian in the ground state |g,g> to be separable. The excited state |e,g> corresponds to a local excitation of monomer 1 and likewise, |g,e> represents excitation of the other monomer 2 whereas *J* corresponds to the exciton coupling energy. The vibrational Hamiltonians are:

$$\hat{H}_{g,g} = -\frac{1}{2}\frac{d^2}{dx_1^2} - \frac{1}{2}\frac{d^2}{dx_2^2} + \frac{1}{2}\omega_1^2 x_1^2 + \frac{1}{2}\omega_2^2 x_2^2 \tag{83}$$

$$\hat{H}_{e,g} = -\frac{1}{2}\frac{d^2}{dx_1^2} - \frac{1}{2}\frac{d^2}{dx_2^2} + \frac{1}{2}\omega_1^2 \left(x_1 - x_{e,1}\right)^2 + \frac{1}{2}x^2\omega_2^2 + \Delta E_1 \tag{84}$$

and

$$\hat{H}_{g,e} = -\frac{1}{2}\frac{d^2}{dx_1^2} - \frac{1}{2}\frac{d^2}{dx_2^2} + \frac{1}{2}\omega_1^2 x_1^2 + \frac{1}{2}\omega_2^2 \left(x_2 - x_{e,2}\right)^2 + \Delta E_2. \tag{85}$$

The absorption spectra are then obtained by a Fourier transform of the calculated time-dependent autocorrelation function:[61]

$$\sigma(E) \sim \int dt\ e^{iEt} \langle \hat{\mu}_{eg}\Psi_0 | e^{-i\hat{H}_e t}\ \hat{\mu}_{eg}\Psi_0 \rangle\, w(t). \tag{86}$$

Here, Ψ_0 is the vibronic ground state, $\hat{\mu}_{eg}$ the transition dipole moment operator and $\hat{H}_e$ is the excited state Hamiltonian of the monomer and dimer. In calculating the Fourier transform, we use a Gaussian window function w(*t*) which results in a finite width of the spectral lines.

Figure 41 displays a comparison between calculated and measured spectra for the mono-chromophoric reference PBIs **30** and **31** (panels a), c)) and the **o2-CP** and **r2-CP** homodimers (panels b), d)). We use the monomer spectra to fix the parameters which enter the model Hamiltonian. These are the frequencies ω, Huang-Rhys-factors ξ, and excitation energies ΔE_m. Best agreement with experiment is achieved for the sets: ω = 1411 cm^{-1}, ξ = 0.79, ΔE_1 = 18954 cm^{-1} for the orange PBI monomer and ω = 1331 cm^{-1}, ξ = 0.78 and ΔE_m = 17164 cm^{-1} for the red PBI monomer. The very similar values for the vibrational frequency and the Huang-Rhys factor indicate that the substituents attached to the red PBI monomer do not influence the vibrational motion significantly.

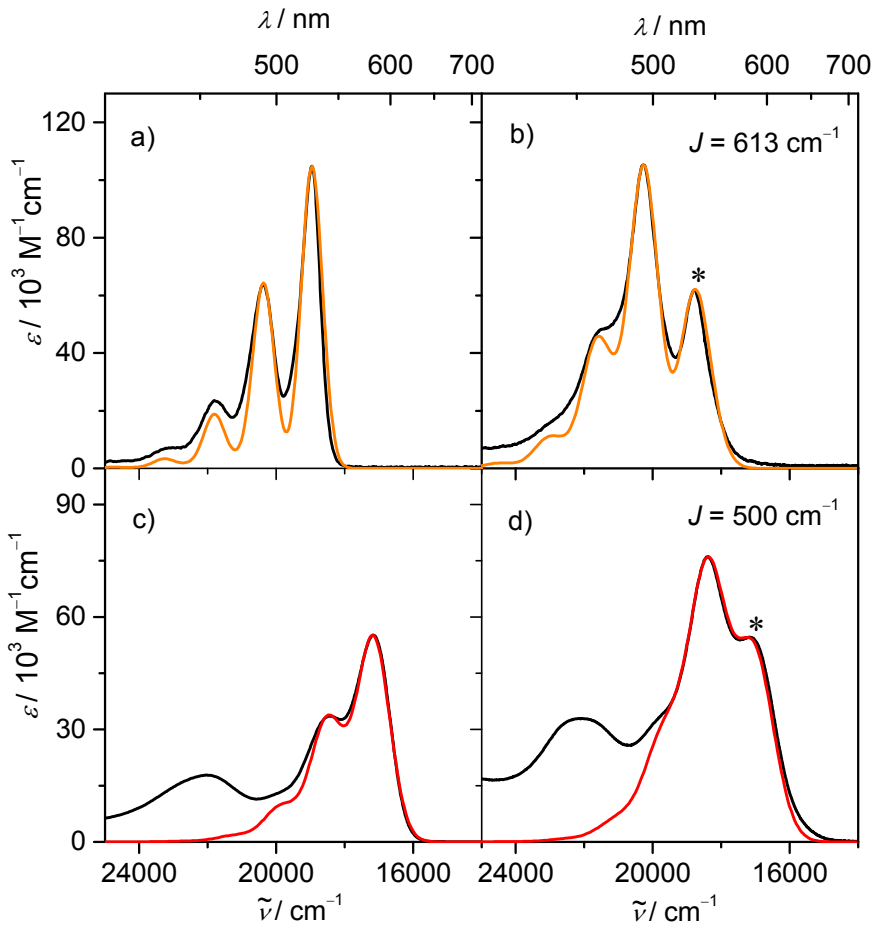

Figure 41. Comparison between experimental (black lines, measured in dichloromethane, $c \approx 10^{-5}$ M, 298 K) and calculated absorption spectra (colored lines) of a) reference PBI **30** (orange PBI), b) **o2-CP** homodimer, c) reference PBI **31** (red PBI) and d) **r2-CP** homodimer. The calculated spectra are normalized to match the measured peak of highest intensity in each case. The value of the exciton coupling energy J is given for the two dimers. It essentially influences the intensity of the low energy peaks (*), which are marked in panels b) and d). The model does not account for the $S_0 \rightarrow S_2$ transition seen around 22000 cm^{-1} in panels c) and d).

For the homodimers, the angle α between the transition dipole moments is kept fixed (28.6° for **o2-CP** and 24.5° for **r2-CP**, respectively, see Figure 39). The absolute values of the transition dipole moments result, at least in the case of homodimers, only in a global pre-factor in the spectrum, and is therefore set equal to one. Best agreement for the simulated spectra with experiment is obtained for an exciton coupling energy of J = 613 cm^{-1} for **o2-CP** and 500 cm^{-1} for **r2-CP**. These values are comparable to the coupling strength of 524 cm^{-1} found for self-assembled homodimers of core-unsubstituted PBI molecules.[40, 41]

The two exciton states illustrated in Figure 40a overlap because the coupling strength is small compared to the vibrational frequency. Since the $S_0 \rightarrow S_1^{`}$ transition is only weakly allowed for angles of roughly 25°, we attribute the line-shape mostly to vibrational levels in the $S_1^{``}$ exciton state. The intensities of the peaks marked with an asterisk in the figure are strongly dependent on the exciton coupling energy.[142, 143] The Huang-Rhys factors are increased to $\xi = 0.88$ (**o2-CP**) and 0.83 (**r2-CP**) to achieve a better agreement with the experiment. This may indicate that in the dimers a strain acts on the PBI scaffold, and thus changes the excited-state equilibrium geometry of the monomer units.

The same model is applied to the **or-CP** heterodimer. The calculated spectra for the sum of the monomers and the heterodimer are shown in Figure 42. In contrast to the homodimers, the relative strength of the transition dipole moments is important here. Their absolute values will, however, still result in a global factor. Therefore, the ratio

$$\bar{\mu}_{eg} = \frac{\mu_{eg}(r)}{\mu_{eg}(o)} \tag{87}$$

of the individual absolute values is given, where $\mu_{eg}(o)$ and $\mu_{eg}(r)$ are the transition dipole moments of the orange and red PBI chromophore, respectively. The sum of the monomer spectra is best matched by a model spectrum for an uncoupled dimer ($J = 0$) when the transition dipole moment ratio is set to $\bar{\mu}_{eg} = 0.69$. All other parameters have been kept at the values determined from the individual monomer spectra. For the spectrum of the **or-CP** heterodimer, the angle α between the transition dipole moments is kept fixed at a value of 10.6° as indicated in Figure 39c and the Huang-Rhys factors at the values determined from the homodimer spectra. From the comparison of calculated and measured spectra, a transition dipole moment ratio of $\bar{\mu}_{eg} = 0.81$ and an exciton coupling energy of $J = 427\ cm^{-1}$ is obtained. It is smaller than the value found for the homodimers, but still comparable in its numerical value. Again, the ratio of the transition dipole moments has a large effect on the intensity of the 0–0 transition peak of the orange PBI chromophore and additionally, on the intensity of the low-energy band originating mainly from the red PBI chromophore (marked with an asterisk in Figure 42b).

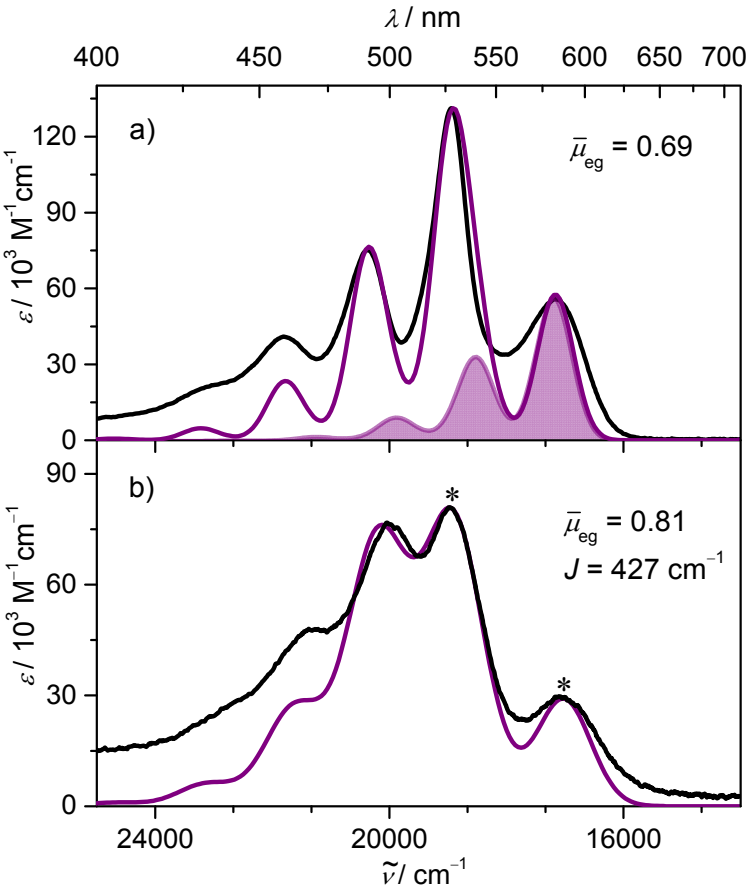

Figure 42. Comparison between experimental (black lines, measured in dichloromethane, $c \approx 10^{-5}$, 298 K) and calculated absorption spectra (purple lines): a) Sum of measured spectra of reference PBI dyes **30** (orange PBI) and **31** (red PBI) and calculated uncoupled **or-CP** heterodimer. Also shown is the theoretical spectrum of reference PBI **31** (filled curve). b) Coupled heterodimer. Values for the exciton coupling energy J and the ratio of the magnitudes of the dipole moments are indicated. The latter essentially influences the intensity of the energy peaks (*) marked in panel b).

Overall, the calculated absorption spectra of the studied monomers, homodimers and heterodimers are in very good agreement with the experimental ones, while the parameters which enter the model differ only little from those found for self-assembled PBI aggregates.[40, 41, 118-121] It is obvious that the simple model of exciton states as illustrated in Figure 40 is insufficient to explain the spectral lineshapes. Because of the rather weak exciton coupling, the appearance of the spectra is dominated by vibronic progressions for both homo- and hetero-PBI aggregates.

5.3 Conclusion

In a comparative study of two PBI cyclophanes each bearing two identical chromophores and one PBI cyclophane comprising two different chromophores, pronounced changes in the absorption properties with respect to the monomeric chromophores were observed. This could be assigned to substantial exciton coupling between the PBI units within the cyclophanes. Most importantly, by comparing calculated and measured absorption spectra, the exciton-vibrational coupling in these cyclophanes could be quantified. These couplings lead to the emergence of quite different absorption properties compared to the corresponding monomeric PBI chromophores, not only for homo- but also for heterodimer aggregates. To the best of our knowledge, our quantum mechanical analysis on the cyclophane bearing two different PBI chromophores represents the first example of PBI hetero-π-stacks for which exciton-vibrational coupling has been explored. The new insights derived from our work justify further efforts toward an understanding of optical properties of larger PBI hetero-π-stacks. Based on those studies tailored dye aggregate systems should become accessible for functional materials with desired properties.

Chapter 6

Supramolecular p/n-Heterojunctions Based on Bis(merocyanine)-C_{60} Conjugates

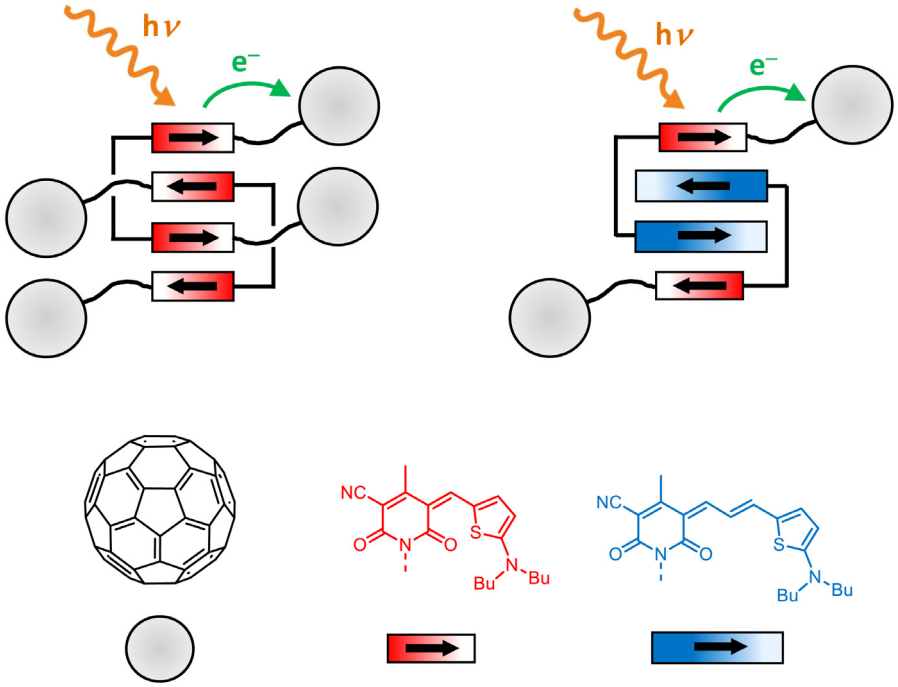

Abstract: Two bis(merocyanine)-C_{60} conjugates bearing same and different types of chromophores, respectively, have been synthesized. Both compounds self-assemble in non-polar solvents resulting in the formation of quadruple dye stacks with the fullerene moieties in the periphery. The aggregate structure of bis(merocyanine)-C_{60} conjugate comprising the same type of chromophores was confirmed by 2D NMR spectroscopy. Hence, well-defined supramolecular p/n-heterojunctions are formed in solution, which enable studies on the photoinduced electron transfer from the dye stack to the fullerene moieties for both bis(merocyanine)-C_{60} conjugates by femtosecond time-resolved transient absorption spectroscopy. Our studies suggest both electron and energy transfers from the excited dye stack to the fullerene moiety. The lifetime of the charge separated state is rather short (nanosecond timescale) indicating a fast charge recombination.

6.1 Introduction

Merocyanine dyes represent a priviliged class of dyes which enable the design of well-defined supramolecular dye aggregates as demonstrated in Chapters 3 and 4.[34] In addition to their outstanding self-assembly properties, these dyes show promising p-type semiconductor behavior in organic field-effect transistors[144, 145] and photovoltaics in combination with fullerene derivatives as n-type semiconductor.[86, 93, 146-149] However, the power conversion efficiencies of the solar cell devices based on merocyanine dyes are still moderate[94, 150] despite the successful improvement of the morphology of the active material.[89]

A key step for the generation of charge carriers in organic solar cells represents the charge separation at the p/n-heterointerface of the active material.[42] In order to gain insight into this process, we have designed bis(merocyanine)-C_{60} conjugate **32** comprising the same type of chromophores that are linked to a fullerene moiety by a flexible spacer unit (Figure 43a). The fullerene moieties in **32** resemble [6,6]-phenyl-C_{61}-butyric acid methyl ester (PCBM), a widely used acceptor material in organic photovoltaics.[151-153] The octyl chain attached at the phenyl ring of the fullerene units shall ensure enough solubility in organic solvents. Based on our results obtained for bis(merocyanine) **21** (Chapter 4) we expect a self-assembly of bis(merocyanine)-C_{60} conjugate **32** in non-polar solvents resulting in a quadruple dye stack with the four fullerene units in the periphery of the stack (Figure 43a). In this way, a well-defined supramolecular p/n-heterojunction is obtained, which allows studies on the photoinduced electron transfer from the dye stack to the fullerene moiety. In addition, we have envisioned bis(merocyanine)-C_{60} conjugate **33** comprising two different types of chromophores and one fullerene unit (Figure 43b). For this unsymmetric bis(merocyanine)-C_{60} we expect a self-assembly into a dimer stack like in the case of bis(merocyanine) **22** (Chapter 4) with the long chromophores located in the inner part of the dye stack (Figure 43b). DFT calculations revealed that the HOMO of the hetero dye stack is localized on the long chromophores (Figure 30b (right) in Chapter 4) whereas in the homoaggregate the HOMO is equally distributed over all four chromophores (Figure 30b (left) in Chapter 4). Hence, the positive charge of the oxidized stack should be more localized in the inner part of the stack of bis(merocyanine)-C_{60} conjugate **33**. The fullerene moieties in **33** are attached to the short chromophores in the periphery of the dye stack. Therefore, we expect a larger distance between the hole and electron formed upon photoinduced electron transfer compared to symmetric bis(merocyanine)-C_{60} conjugate **32**

bearing the same type of chromophores. This should result in a longer lifetime of the charge separated state compared to bis(merocyanine)-C_{60} conjugate **32**.

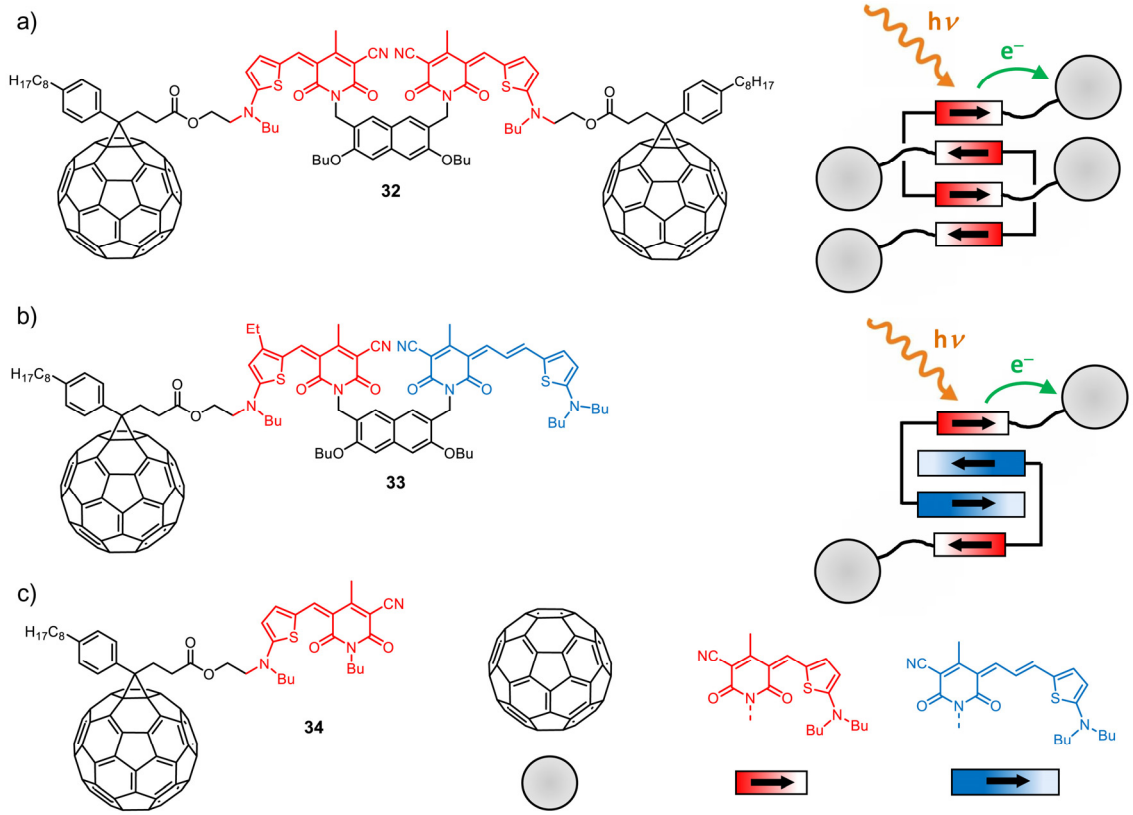

Figure 43. Chemical structure and schematic illustration of the dimer aggregate structure of a) symmetric bis(merocyanine)-C_{60} conjugate **32** comprising the same type of chromophores as well as of b) unsymmetric bis(merocyanine)-C_{60} conjugate **33** with two different types of chromophores. c) Chemical structure of merocyanine-C_{60} conjugate **34**.

To study the photoinduced charge separation femtosecond time-resolved transient absorption spectroscopy is applied. Merocyanine-C_{60} conjugate **34** consisting of one merocyanine chromophore and a fullerene unit (Figure 43c) serves as reference compound for bis(merocyanine)-C_{60} conjugates **32** and **33**.

6.2 Results and Discussion

6.2.1 Synthesis

The precursor **43** for the synthesis of merocyanine-C_{60} conjugate **34** and bis(merocyanine)-C_{60} conjugate **32** was synthesized according to the route shown in Scheme 3. In the first step, commercially available phenyloctane **35** was subjected to a Friedel-Crafts acylation reaction with 3-(carbomethoxy)propionyl chloride **36**. Subsequent condensation reaction with *p*-toluenesulfonyl hydrazide afforded hydrazone **38**, which was then reacted with C_{60} to obtain the [5,6]-cycloadduct **39**. The [5,6]-cycloadduct was then isomerized to the thermodynamically more stable [6,6]-cycloadduct **40** without further purification by heating under reflux in 1,2-dichlorobenzene.[154]

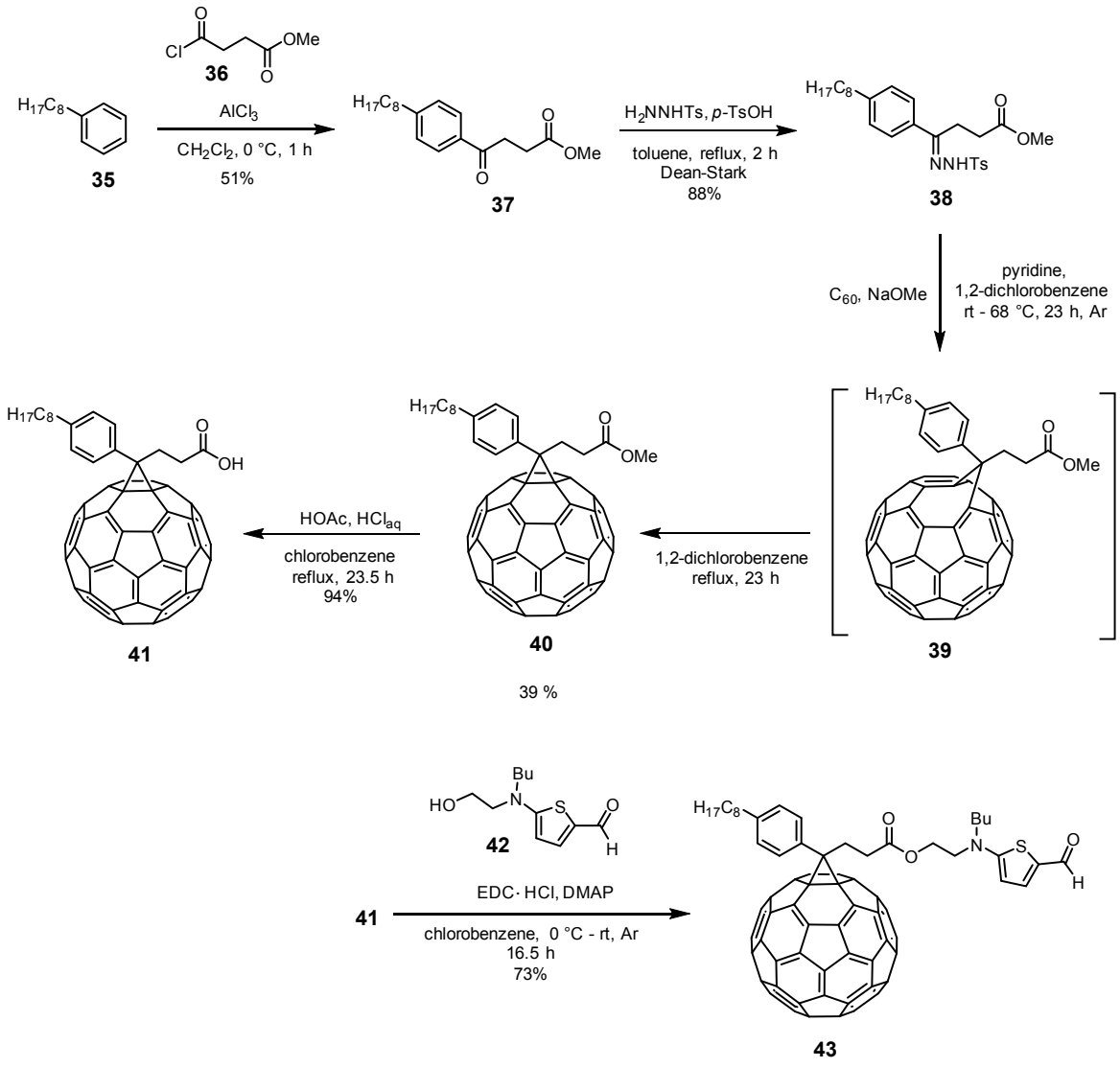

Scheme 3. Synthetic route to fullerene derivative **43**.

Hydrolysis of **40** followed by Steglich esterification with aminothiophene **42**[155] using *N*-(3-dimethylaminopropyl)-*N*'-ethylcarbodiimide hydrochloride as coupling reagent provided the desired fullerene derivative **43**.

Finally, merocyanine-C_{60} conjugate **34** and bis(merocyanine)-C_{60} conjugate **32** were obtained from fullerene derivative **43** by Knoevenagel condensation reaction with hydroxypyridone **44** and bis(pyridone) **23**,[107] respectively (Scheme 4). Whereas **34** could be synthesized in a good yield of 70% using acetic anhydride as solvent, the Verley-Doebner[156, 157] modification of the Knoevenagel condensation reaction had to be applied using β-alanine as catalyst and a 1:1 mixture of 1,2-dichloroethane/ethanol as solvent to obtain the symmetric bis(merocyanine)-C_{60} conjugate **32** in a moderate yield of 20%. Both compounds were purified by column chromatography followed by recycling GPC in the case of bis(merocyanine)-C_{60} conjugate **32**.

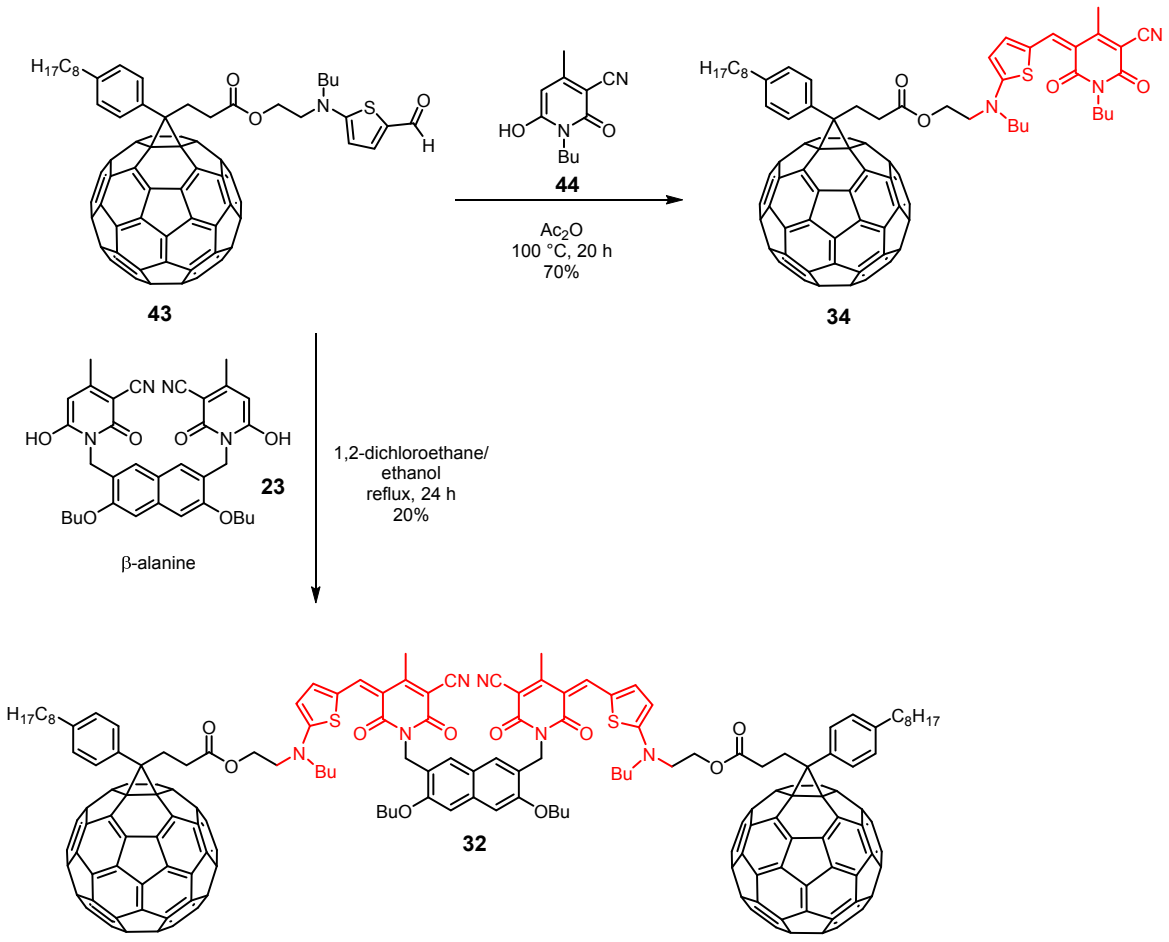

Scheme 4. Synthesis of merocyanine-C_{60} conjugate **34** and bis(merocyanine)-C_{60} conjugate **32**.

The synthesis of unsymmetric bis(merocyanine)-C_{60} conjugate **33** comprising two different types of chromophores is shown in Scheme 5. Aminothiophene **46** was synthesized using a similar procedure as for aminothiophene **24** (Chapter 4) starting from a 5:2 regioisomeric mixture of 3-ethylthiophene-2-carboxaldehyde **28** and 4-ethylthiophene-2-carboxaldehyde **29** by microwave reaction with 2-butylaminoethanol. Fullerene derivative **47** was then obtained by Steglich esterification of [6,6]-(4-octylphenyl)-C_{61}-propionic acid **41** with aminothiophene **46** with 65% yield.

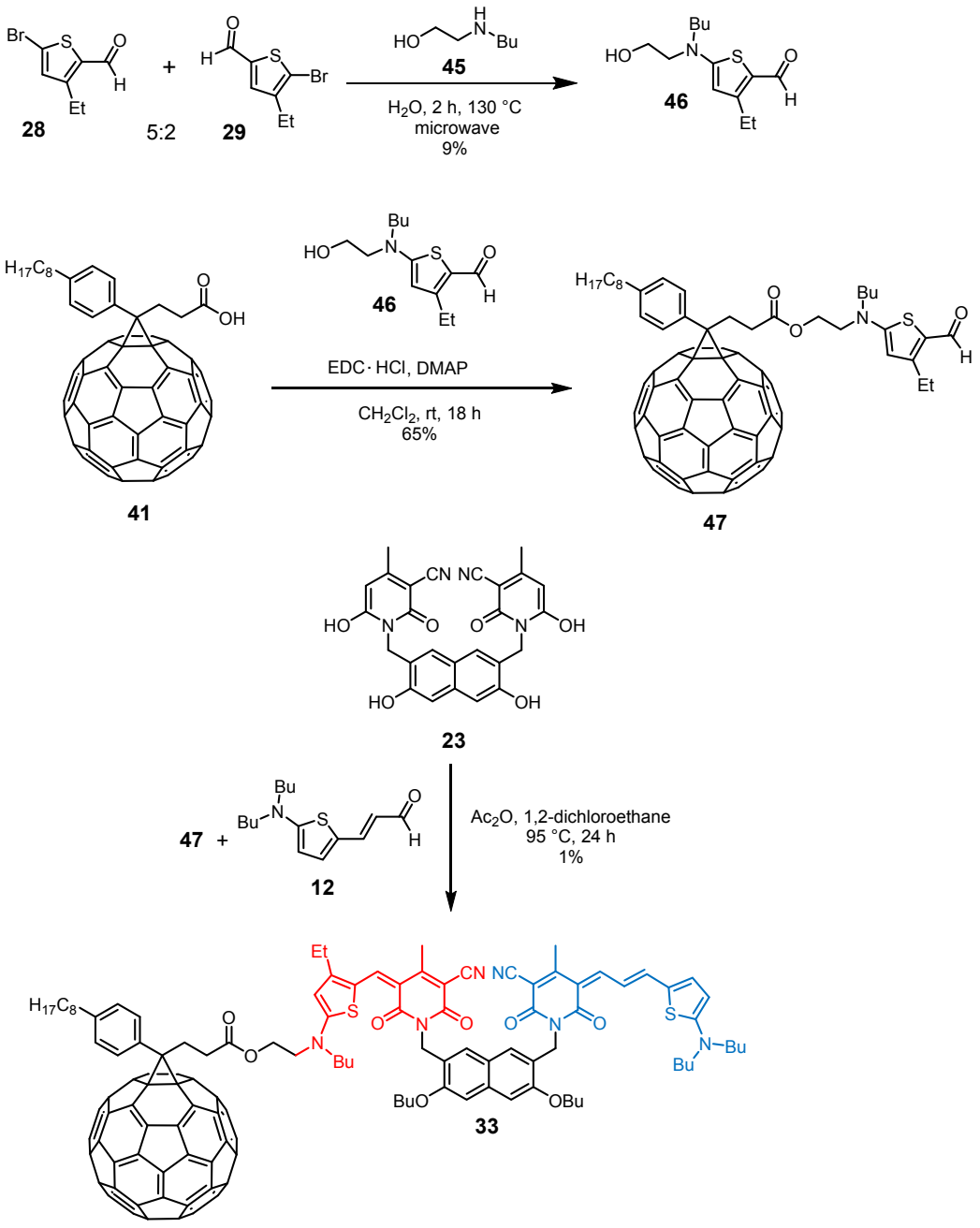

Scheme 5. Synthesis of bis(merocyanine)-C_{60} conjugate **33**.

Finally, bis(merocyanine)-C_{60} conjugate **33** was synthesized by Knoevenagel condensation reaction of bis(pyridone) **23**[107] with a mixture of aminothiophene **12**[94] and fullerene derivative **47** in a molar ratio of 1:2. The very low yield of 1% can be attributed to the challenging purification process due to the formation of the undesired symmetric byproducts. Hence, column chromatography as well as recycling-GPC had to be performed to obtain pure bis(merocyanine)-C_{60} conjugate **33**. In addition, the aldehyde group of fullerene derivative **47** is much less reactive compared to the one in aminothiophene **12** due to the sterical demand of the fullerene moiety, which leads to less favored formation of the desired unsymmetric bis(merocyanine)-C_{60} conjugate **33**.

6.2.2 UV/Vis Spectroscopy

UV/Vis Spectroscopy of merocyanine-C_{60} conjugate 34

The UV/Vis absorption spectrum of merocyanine-C_{60} conjugate **34** in toluene is shown in Figure 44. The absorption maximum at 537 nm can be assigned to the transition of the monomeric merocyanine chromophore, whereas the absorption band at 331 nm arises from the fullerene moiety.[158] In addition, a very weak absorption band at 434 nm can be observed, which is characteristic for C_{60} mono-adducts. However, the origin of this absorption is not clearly understood.[158, 159] Since no additional absorption band is present in the UV/Vis spectrum, we can exclude a pronounced charge-transfer interaction of the merocyanine chromophore and the fullerene moiety. This type of interaction usually manifests in the appearance of additional absorption bands at higher wavelengths.[160, 161]

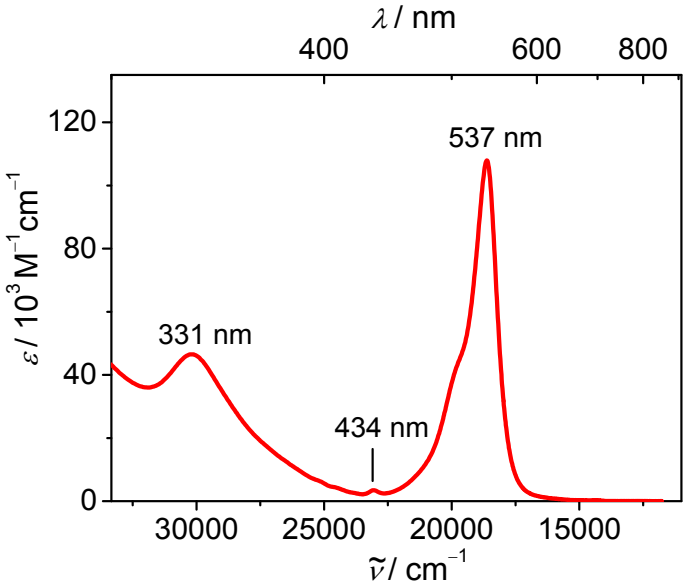

Figure 44. UV/Vis absorption spectrum of merocyanine-C_{60} conjugate **34** in toluene at 298 K ($c \approx 10^{-5}$ M).

UV/Vis Spectroscopy of bis(merocyanine)-C_{60} conjugate 32

To investigate the influence of the fullerene moiety on the aggregation behavior of the bis(merocyanine)-C_{60} conjugates, concentration-dependent UV/Vis spectroscopy was performed for **32** in chlorobenzene (Figure 45a). Spectral changes upon aggregation of dyes can be monitored in the visible region of the spectrum and thus, the UV region is not shown in Figure 45. The concentration-dependent absorption spectra of bis(merocyanine) **21** without fullerene moieties, for which the dimerization in solution was confirmed by 2D NMR spectroscopy (Chapter 4), are shown for comparison (Figure 45b).

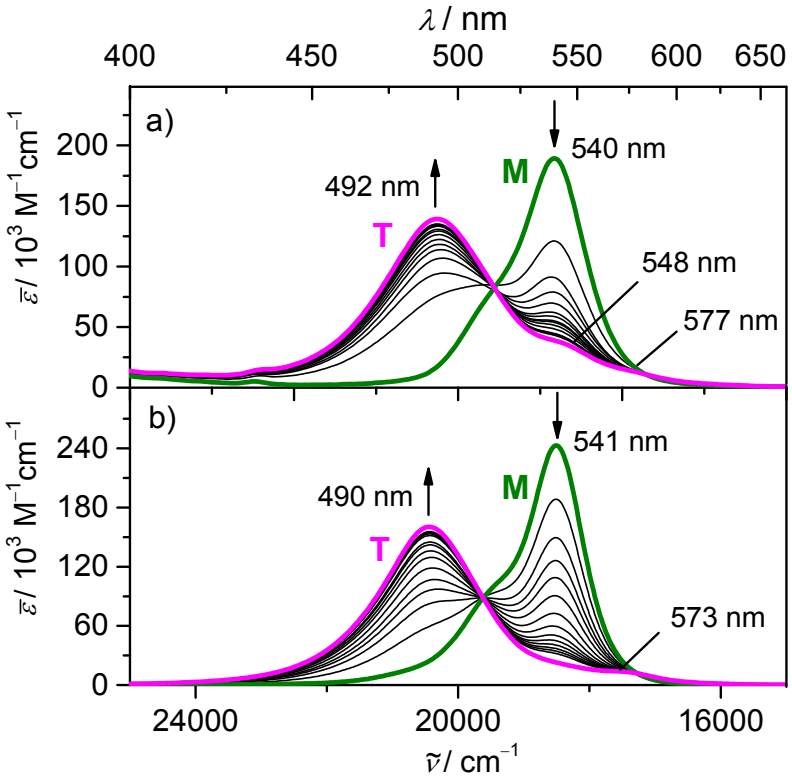

Figure 45. Concentration-dependent UV/Vis absorption spectra of a) bis(merocyanine)-C_{60} conjugate **32** (c = 8.6 x 10^{-7} – 5.2 x 10^{-4} M) and b) bis(merocyanine) **21** (c = 4.4 x 10^{-7} – 6.0 x 10^{-4} M) in chlorobenzene at 298 K. The arrows indicate the spectral changes upon increasing the concentration. The green (denoted with M) and magenta lines (denoted with T) represent the calculated spectra of the monomers and the tetrachromophoric (dimer) stacks, respectively, by extrapolation of the spectral data for most diluted and most concentrated solutions.

Both compounds show very similar spectral changes upon increasing the concentration. The monomeric absorption band located at ≈540 nm is decreasing with concomitant appearance of a hypsochromically shifted absorption band at 492 nm for bis(merocyanine)-C_{60} conjugate **32** (Figure 45a) and 490 nm for bis(merocyanine) **21**

(Figure 45b), respectively. These spectral changes are in accordance with the formation of quadruple merocyanine stacks with H-type coupling (Chapter 4). The data could be fitted to the dimer model[95] (the fitting curves are shown in Figure 46) resulting in a dimerization constant K_D of 5.04 x 10^5 M^{-1} for bis(merocyanine) **21** and 9.98 x 10^5 M^{-1} for bis(merocyanine)-C_{60} conjugate **32** in chlorobenzene at 298 K. The similar aggregation strength of both compounds indicate that the fullerene moieties do not significantly affect the self-assembly of bis(merocyanine)-C_{60} conjugate **32**.

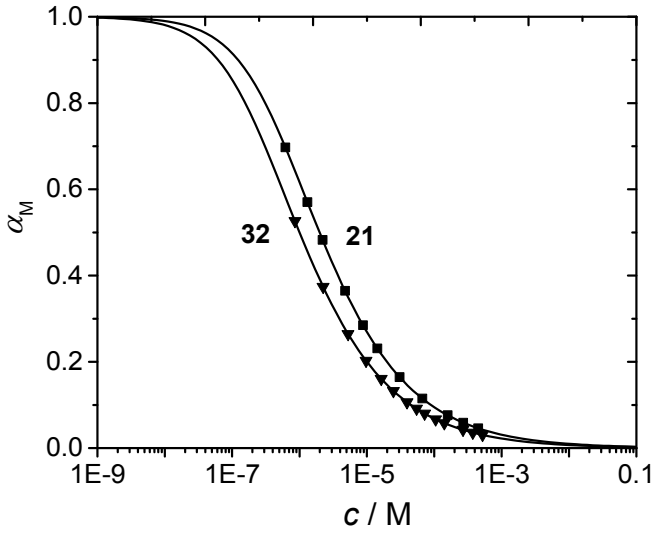

Figure 46. Plot of the fraction of monomeric species α_M against the total concentration calculated from the UV/Vis data at 298 K and results of the non-linear regression analysis based on the dimerization model for bis(merocyanine) **21** (■) and bis(merocyanine)-C_{60} conjugate **32** (▼) in chlorobenzene. Also shown are the respective fitting curves (solid lines) according to the dimer model.

With the calculated dimerization constants the ideal monomer (green line) and dimer (magenta line) spectra of **21** and **32** were calculated (Figure 45). A closer look at the calculated dimer spectra reveals an absorption band with high intensity at ≈490 nm for both compounds and a very weak absorption band at ≈573 nm. While the absorption band at shorter wavelengths arises from the transition to the highest exciton state, the absorption band at longer wavelengths can be attributed to the transition to the second exciton state of the dye stack (Figure 33a in Chapter 4). This transition is not fully forbidden, even for a perfect H-type aggregate, whereas all other transitions are forbidden. The ideal dimer spectrum of bis(merocyanine)-C_{60} conjugate **32** shows an additional weak absorption band at 548 nm (Figure 45a, magenta line), which is not present in the spectrum of bis(merocyanine) **21** (Figure 45b, magenta line). This could indicate a small twist of the

chromophores in the dye stacks of bis(merocyanine)-C_{60} conjugate **32** so that additional transitions become partially allowed. This rotational displacement of the chromophores in the dye stack of **32** may arise from the sterical hindrance of the fullerene moieties. Another reason for the absorption band at 548 nm might be a charge transfer interaction between the dye stack and the C_{60} unit.

The absorption spectrum of **32** in non-polar solvent toluene (Figure 47, red line) resembles the ideal dimer spectrum obtained by concentration-dependent UV/Vis spectroscopy in chlorobenzene (Figure 47, blue line). Thus, even at a low concentration of 3.2 x 10^{-5} M only dimeric species are present in toluene.

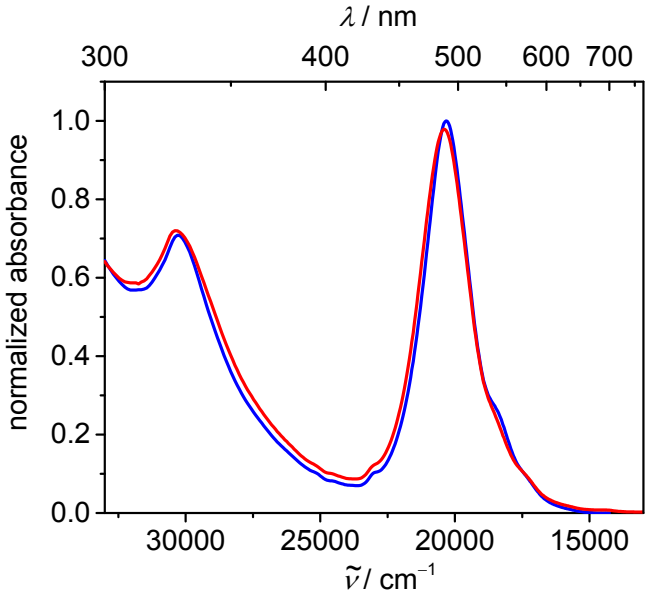

Figure 47. UV/Vis absorption spectrum of bis(merocyanine)-C_{60} conjugate **32** in toluene (c = 3.2 x 10^{-5} M, red line) at 298 K and calculated dimer spectrum obtained by analysis of the concentration-dependent UV/Vis spectroscopy in chlorobenzene (blue line) at 298 K.

UV/Vis Spectroscopy of bis(merocyanine)-C_{60} conjugate 33

Figure 48 shows the absorption spectrum of bis(merocyanine)-C_{60} conjugate **33** in toluene (red line) in comparison with the ideal dimer spectrum of bis(merocyanine) **22** (Chapter 4) obtained by concentration-dependent UV/Vis spectroscopy in chlorobenzene (blue line). The large differences in the UV region are caused by the fullerene units in bis(merocyanine)-C_{60} conjugate **33**, which show strong absorption in this spectral range.[158, 159] Small deviations can be observed in the visible region, which can mainly be attributed to the different solvents (toluene and chlorobenzene) used in these measurements. Hence, we can assume that nearly exclusively aggregated species are

present in toluene and that the structure of the aggregate is the same like for bis(merocyanine) **22** with the long chromophores in the interior of the dye stack like shown in Figure 43.

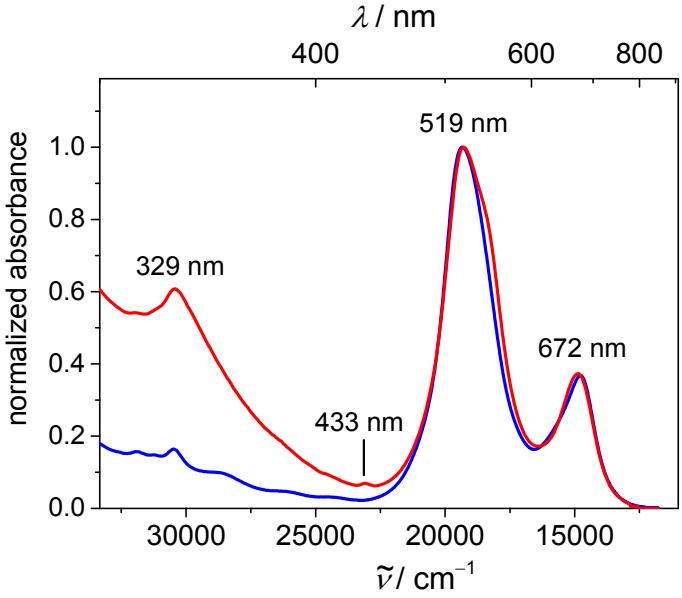

Figure 48. UV/Vis absorption spectrum of bis(merocyanine)-C_{60} conjugate **33** in toluene (c = 2.7 x 10^{-5} M, red line) at 293 K and ideal dimer spectrum of bis(merocyanine) **22** calculated based on the data obtained by concentration-dependent UV/Vis spectroscopy in chlorobenzene (blue line) at 298 K.

6.2.3 NMR spectroscopy

The results obtained by UV/Vis spectroscopy of bis(merocyanine)-C_{60} conjugates **32** and **33** are highly indicative for a self-assembly of both compounds in low polarity solvents resulting in aggregate structures like those schematically shown in Figure 43. Indeed, the quadruple dye stack of **32** with equal chromophores could be confirmed by NMR spectroscopy. The spectra were measured in chlorobenzene at a concentration of 4.0 x 10^{-3} M, where almost only aggregated species are present according to the analysis of the concentration-dependent UV/Vis studies (Figure 46). The ^{1}H NMR spectrum shows well resolved signals of the protons revealing a well-defined aggregate structure (Figure 49c). Compared to the monomer spectrum measured in 1,1,2,2-tetrachloroethane-d_2 (Figure 49b) a splitting of the signals of the chromophores into two sets can be observed. This is in agreement with the formation of a dimer structure like shown in Figure 49e, in which the C_{2v} symmetry of the molecule is lost.

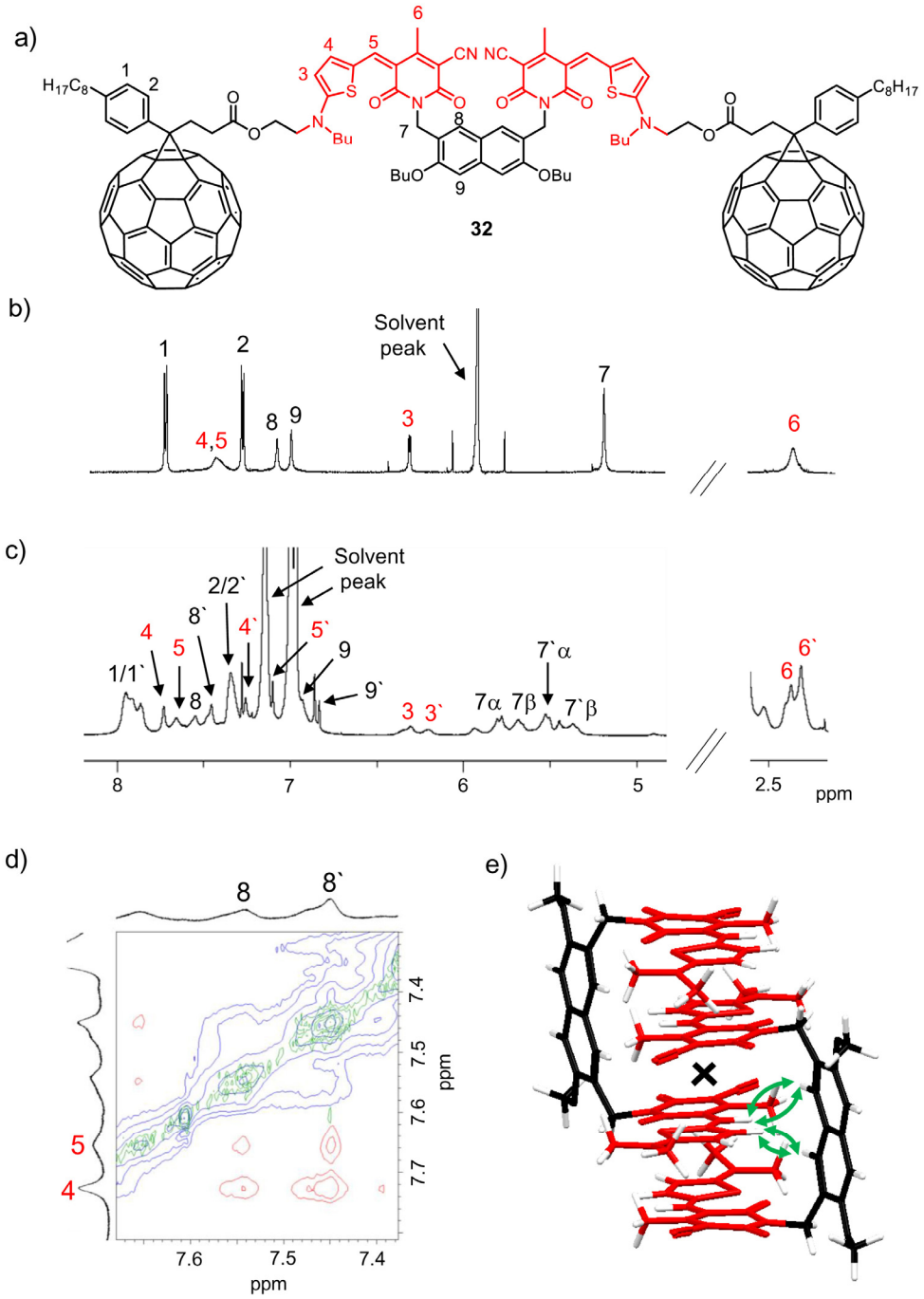

Figure 49. a) Chemical structure of bis(merocyanine)-C_{60} conjugate **32** with the significant protons numbered. Relevant sections of ^{1}H NMR (600 MHz) spectrum of **32** monomer (b) in 1,1,2,2-tetrachloroethane-d_2 (c = 2.8 x 10^{-3} M) at 343 K and aggregate (c) in C_6D_5Cl (c = 4.0 x 10^{-3} M) at 276 K. The two sets of signals for the aggregate are denoted with and without prime. d) Selected region of superposed ROESY NMR (600 MHz; negative signals marked in blue and positive signals in red, respectively) and COSY NMR (600 MHz; marked in green) spectra of **32** in C_6D_5Cl (c = 4 x 10^{-3} M) at 276 K. e) Geometry optimized structure (B97D3/def2-SVP, butyl chains and fullerene moieties were replaced by methyl groups) of dimer aggregate. The green arrows indicate close proximity of chromophore and backbone protons in the dimer and the cross represents the inversion center of the dye stack.

The signals could be assigned to the individual protons with the help of COSY and HSQC experiments (Table 12 in the appendix). Evidence for the aggregate structure was obtained by ROESY NMR spectroscopy. Cross peaks between protons 4 and 5 of the chromophore units and protons 8 and 8` of the naphthalene spacer can be observed, which are not present in the COSY spectrum (Figure 49d). Thus, these protons exhibit close spatial proximity corroborating the existence of the aggregate structure shown in Figure 49e.

6.2.4 Time-resolved Transient Absorption Spectroscopy

In order to investigate the photoinduced electron transfer from the dye stack to the fullerene moiety in the dimer aggregates of bis(merocyanine)-C_{60} conjugates **32** and **33** time-resolved transient absorption spectroscopy was performed in the laboratory of Prof. Lambert.[12] For comparison, the measurements were also done for monomeric merocyanine-C_{60} conjugate **34** and for the dye stack of bis(merocyanine) **21** (Chapter 4) without fullerene moieties. All measurements have been carried out in toluene as solvent to ensure the complete aggregation of bis(merocyanine) **21** and bis(merocyanine)-C_{60} conjugates **32** and **33**. The compounds were excited by means of a femtosecond laser pulse in the respective absorption band of the merocyanine chromophore and merocyanine dye stack, respectively, and then probed by a second broad band laser pulse with variable temporal delay with respect to the excitation pulse. Two different probe pulses were applied. On the one hand a UV/Vis probe to monitor the spectral response of the merocyanine units and on the other hand an NIR probe to identify the C_{60} radical anion. In both cases the transient spectra were corrected for chirp and scattered light.[13]

The UV/Vis transient absorption spectra of bis(merocyanine) **21** are shown in Figure 50a. An intense negative signal located at the absorption maximum of the dye stack (≈490 nm) can be observed. Hence, we can assign this signal to the bleaching of the ground state and the stimulated emission, whereas the positive signals at ≈420 and ≈530 nm represent excited state absorption. The transient absorption spectra of bis(merocyanine)-C_{60} conjugate **32** (Figure 50b) comprising four fullerene moieties shows similar signatures like bis(merocyanine) **21**.

[12] The measurements were carried out by Alexander Schmiedel.

[13] The data processing was done by Dr. Franziska Fennel and Dr. Marco Holzapfel. The interpretation of the data was done by Prof. Christoph Lambert, Dr. Franziska Fennel and David Bialas. Dr. Marco Holzapfel gave input in discussing the results.

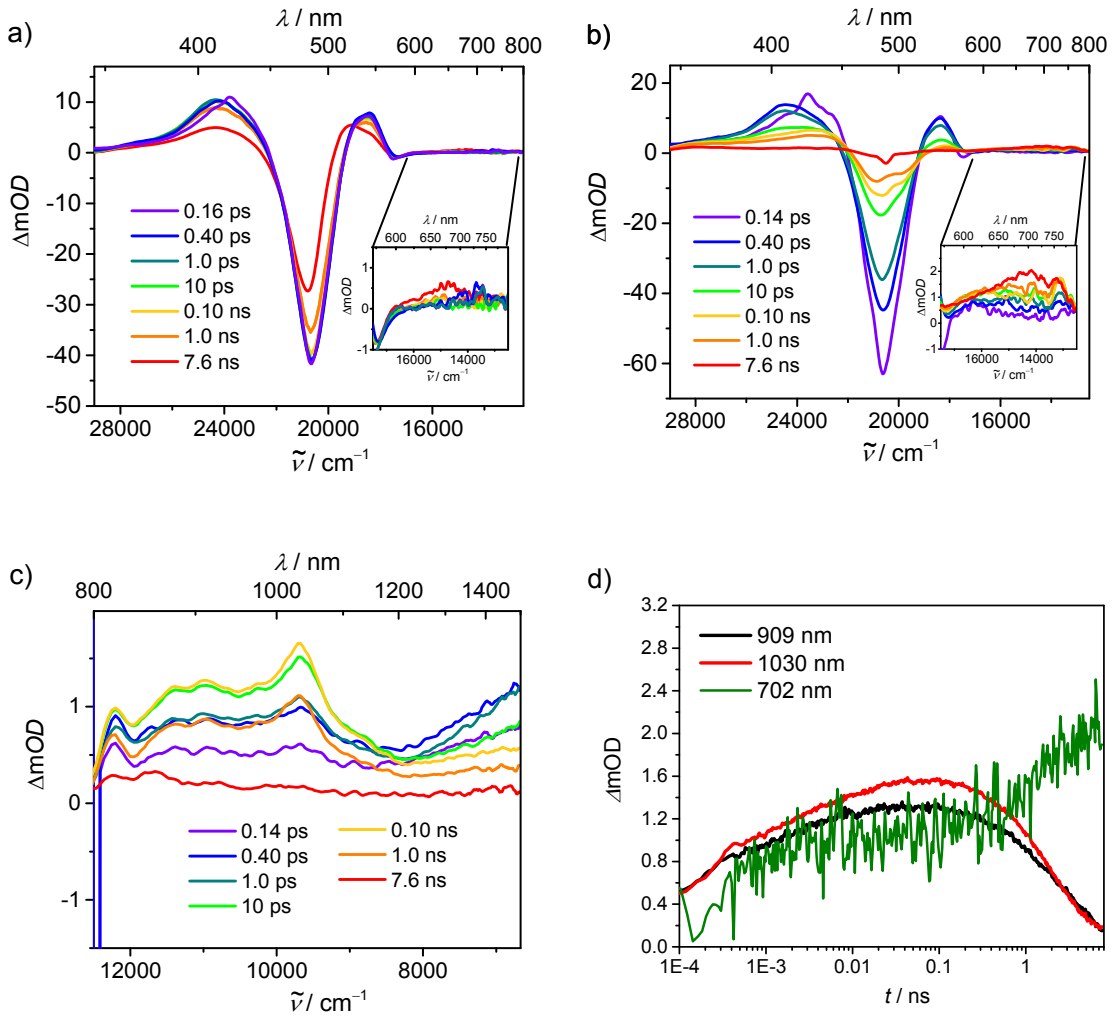

Figure 50. Transient absorption spectra of a) bis(merocyanine) **21** (λ_{exc} = 489 nm, 50 nJ/pulse) and bis(merocyanine)-C_{60} conjugate **32** (λ_{exc} = 490 nm, 50 nJ/pulse) in toluene probed in the b) UV/Vis and c) NIR region. The spectra were corrected for chirp, scattered light and smoothed with a Savitzky-Golay filter with 9 points. d) Time scans at selected wavenumbers for bis(merocyanine)-C_{60} conjugate **32**.

The characteristic features are slightly shifted in wavelength, positive signals are observed at ≈410 and ≈545 nm together with a pronounced ground state bleach at ≈485 nm. Both systems were excited in the high energy tail of the exciton manifold. We expect for both compounds a very fast internal conversion (IC) in the exciton manifold to the lowest exciton state after photoexcitation (Figure 51). This type of process is known to be ultrafast.[162-164] Therefore, the spectral changes of the excited state absorption observed at short delay times of < 1 ps may be attributed to this fast internal conversion process. The striking difference, when comparing the transient absorption spectra of the two systems, is the time scale for the ground state recovery manifested in the decay of the band at 485 nm respectively 490 nm. In the presence of C_{60} (bis(merocyanine)-C_{60} conjugate **32**) the

signal decay is very fast (picosecond time scale) and the ground state is almost completely repopulated after ≈7.6 ns (Figure 50b, red line), whereas for bis(merocyanine) **21** without fullerenes a very pronounced ground state bleach is still present at the maximal delay time of 7.6 ns (Figure 50a, red line).

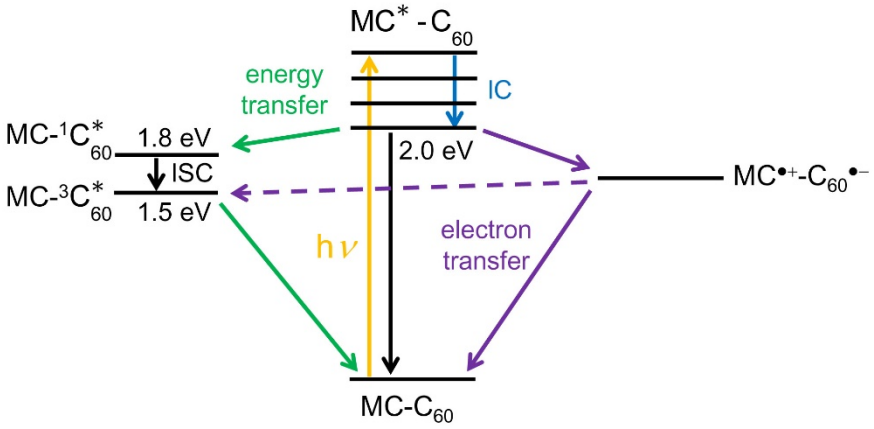

Figure 51. Proposed Jablonski diagram for the dimer aggregate of bis(merocyanine)-C_{60}conjugate **32** showing the potential competition between photoinduced electron transfer and energy transfer. The energy level of the lowest exciton state of the dye stack was estimated from Table 9 (Chapter 4 in the appendix), whereas the energy levels of the excited singlet and triplet PCBM was taken from literature.[165] Note that the exact energy level of the charge separated state is unknown. MC denotes the quadruple merocyanine dye stack and IC and ISC stand for internal conversion and intersystem crossing, respectively.

The different decay kinetics for the ground state bleach of bis(merocyanine) **21** and bis(merocyanine)-C_{60} conjugate **32** indicate a faster recovery of the ground state in the case of **32**. We attribute the faster decay times to the presence of C_{60}, which enables two possible additional relaxation pathways (Figure 51). In the case of bis(merocyanine)-C_{60} **32** we expect an electron transfer from the excited stack to the C_{60} based on a Weller analysis (see appendix). Indeed, a weak excited state absorption band in the spectral region of the C_{60} radical anion (around 1000 nm)[166] is observed in the NIR transient absorption measurement (Figure 50c). The signal increases within ≈100 ps and decays on a nanosecond time scale (Figure 50d, red line).

The presence of the oxidized dye stack cannot be confirmed in the transient spectra since no clear additional signature is visible in case of bis(merocyanine)-C_{60} conjugate **32**. It might be that the shift of the excited state absorption to longer wavelengths and the changes of the band shape of the ground state bleach is caused by the oxidized stack. However, this guess cannot be confirmed experimentally as the absorption spectrum of the radical cation of the stack cannot be measured. This is due to the disassembly of the stack

into monomeric species of **32** in polar solvents, which are required for spectroelectrochemistry measurements in order to solve the electrolyte.

Based on the extinction coefficient of the dye stack of **32** (ε_{490} = 1.2 x 10^5 M^{-1} cm^{-1} in toluene, Figure 55 in the appendix) and the one of methanofullerene radical anion (ε_{1050} = 1.0 x 10^4 M^{-1} cm^{-1} in toluene/acetone/2-propanol 8:1:1)[166] we would expect an intensity ratio of about 12:1 for the intensity of the ground state bleach and the signal of the radical anion if the efficiency of the charge separation was 100%. However, we observe a ratio of 37:1 indicating that less amount of fullerene radical anion is formed.[14] In general, energy transfer from the excited stack to C_{60} can be a competing process to the charge separation. In our case energy transfer would lead to an excitation of the fullerene to the first singlet state, which is known to undergo efficient intersystem crossing (ISC) to the long-lived triplet state (Figure 51).[167, 168]

The life-time of singlet excited PCBM is 1.4 ns in chlorobenzene and is characterized by an absorption maximum at ≈900 nm.[169] A respective positive signal can be observed in the transient absorption spectra of aggregated bis(merocyanine)-C_{60} conjugate **32** (Figure 50c and Figure 50d, black line) indicating the presence of the excited singlet fullerene. In addition, a very weak positive signal at ≈700 nm is present (inset of Figure 50b), which is increasing with time (Figure 50d, green line). This spectral signature can be assigned to the excited state absorption of triplet excited fullerene having a lifetime of 40 μs.[169] In case of the plain merocyanine stack we only observe a much weaker signal on the noise level at 700 nm (Figure 50a). This gives further indication that the positive signal observed at ≈700 nm for bis(merocyanine)-C_{60} conjugate **32** is a fullerene signature of the excited triplet state and not a contribution from the stack. However, at the current point we cannot clearly attribute the triplet signature unambiguously to energy transfer from the stack to the C_{60} moiety. The signal might be also caused by a direct photoexcitation of C_{60} having a weak extinction (ε_{490} = 1.6 x 10^3 M^{-1} cm^{-1} in toluene)[170] compared to the merocyanine dye stack (ε_{490} = 1.2 x 10^5 M^{-1} cm^{-1} in toluene, Figure 55 in the appendix). In addition, the fullerene excited triplet state might be also populated upon charge recombination (Figure 51). In order to clarify the origin of the fullerene excitation further measurements and a global analysis are required.

[14] We are aware that the comparison of the signal intensities in the UV/Vis and NIR region exhibits a certain inaccuracy since the spectra are obtained by two different measurements. However, the comparison is done as an estimation.

For comparison, time-resolved transient absorption spectroscopy was also performed for monomeric merocyanine-C_{60} conjugate **34** (Figure 52). The negative signal at 541 nm can be assigned to the bleaching of the ground state, while the positive signal at 444 nm may mainly arise from excited state absorption (Figure 52a).

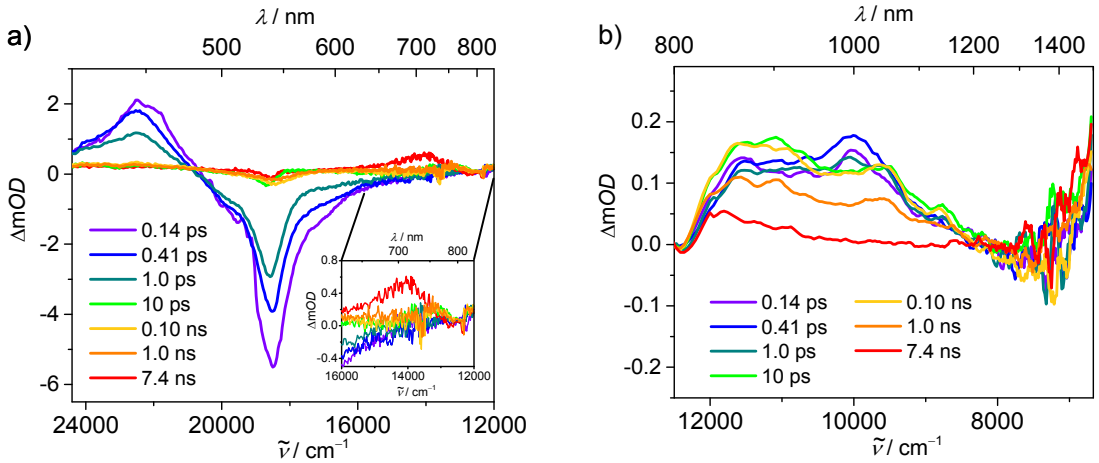

Figure 52. Transient absorption spectra of merocyanine-C_{60} conjugate **34** (λ_{exc} = 538 nm, 50 nJ/pulse) in toluene probed in the a) UV/Vis and b) NIR region. The spectra were corrected for chirp, scattered light and smoothed with a Savitzky-Golay filter with 9 points.

Like for bis(merocyanine)-C_{60} conjugate **32**, a weak positive signal is observed at ≈1000 nm (Figure 52b) indicating the presence of a fullerene radical anion.[166] In addition, a positive signal is observed at ≈900 nm indicating a possible energy transfer from the merocyanine chromophore to the fullerene unit. This is in accordance with the appearance of an absorption band at ≈700 nm (inset of Figure 52a) showing the formation of triplet excited fullerene. The radical cation of the merocyanine chromophore has an absorption maximum at ≈400 nm in dichloromethane.[155] Thus, the positive signal at 444 nm (Figure 52a) may correspond to an overlap of the signals arising from excited state absorption of the merocyanine as well as from the absorption of the radical cation formed upon charge separation. However, to get further insight into the possible energy transfer, additional measurements are required in order to identify the origin of the C_{60} triplet population. Furthermore, a kinetic model has to be developed in the future to determine the rate constants for possible energy transfer and to quantify the rates for charge separation and recombination.

Most likely, electron transfer also happens in the case of bis(merocyanine)-C_{60} conjugate **33** comprising two different types of chromophores (Figure 53). The respective positive signal for the fullerene radical anion can be observed at ≈1030 nm chromophores (Figure 53b).

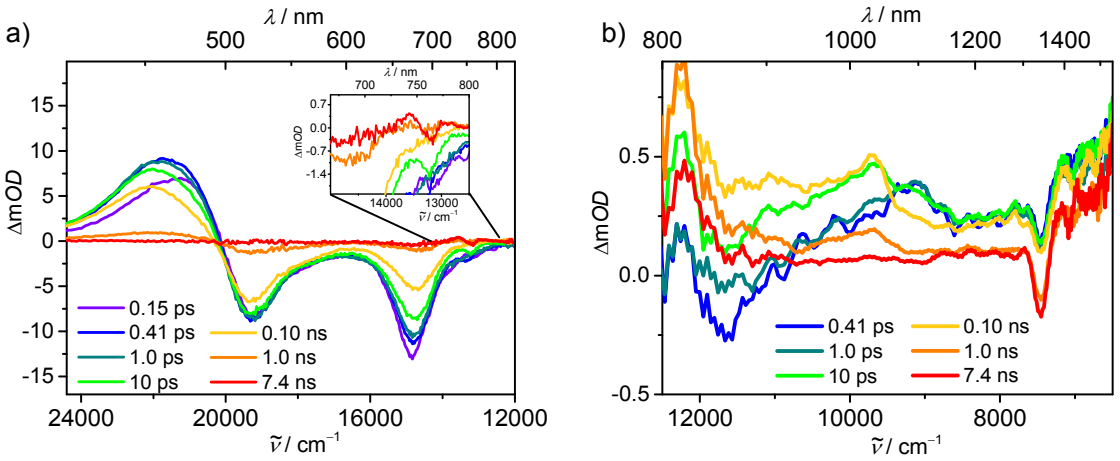

Figure 53. Transient absorption spectra of bis(merocyanine)-C_{60} conjugate **33** (λ_{exc} = 674 nm) in toluene probed in the a) UV/Vis (200 nJ/pulse for excitation) and b) NIR region (500 nJ/pulse for excitation). The spectra were corrected for chirp, scattered light and smoothed with a Savitzky-Golay filter with 9 points.

The comparison of the ground state bleach of **33** (Figure 53a) with the steady-state absorption spectrum in toluene (Figure 48) shows a reversal of the band intensities of the two absorption maxima in the visible spectral range. This may arise from an overlap of excited state absorption and ground state bleach at ≈520 nm in the transient absorption spectra. In addition, the absorption of the oxidized dye stack, which is unknown due to the same reasons as discussed for the dye stack of **32**, may also influence the spectral signature in this wavelength region.

Figure 54 shows the decay of the ground state bleach as a function of time for all investigated compounds for comparison. Accordingly, bis(merocyanine) **21** without fullerene moieties shows the slowest decay of the signal (Figure 54, orange line) revealing a slow recovery of the ground state. In contrast, symmetric bis(merocyanine)-C_{60} conjugate **32** (Figure 54, red line) as well as merocyanine-C_{60} conjugate **34** (Figure 54, blue line) exhibit a much faster decay. Thus, the presence of the fullerene moieties strongly affects the relaxation of the excited dye stack to the ground state as discussed before.

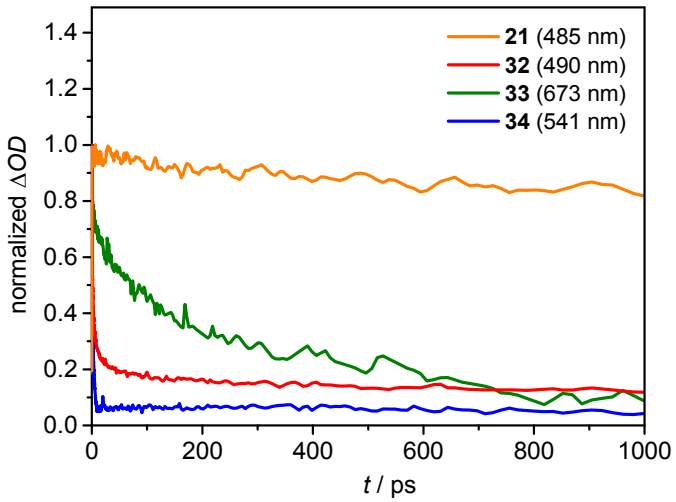

Figure 54. Decay of the ground state bleach of all investigated compounds as a function of time (the curves were normalized so that ΔOD = 1 for t = 0).

In addition, unsymmetric bis(merocyanine)-C_{60} conjugate **33** (Figure 54, green line) shows a slower decay compared to bis(merocyanine)-C_{60} conjugate **32** and merocyanine-C_{60} conjugate **34**. Hence, the recovery of the ground state in unsymmetric bis(merocyanine)-C_{60} conjugate **33** is slower compared to symmetric bis(merocyanine)-C_{60} conjugate **32** and merocyanine-C_{60} conjugate **34** indicating that the total process of charge separation and recombination is slower in the case of **33**.

6.3 Conclusion

In summary, one merocyanine-C_{60} conjugate and two bis(merocyanine)-C_{60} conjugates with same and different types of chromophores, respectively, have been synthesized. Concentration-dependent UV/Vis studies reveal a dimerization process for both bis(merocyanine)-C_{60} conjugates in less-polar solvents resulting in the formation of quadruple dye stacks with the fullerene moieties in the periphery. The structure of the supramolecular p/n-heterojunction formed upon self-assembly of bis(merocyanine)-C_{60} conjugate **32** was confirmed by 2D NMR spectroscopy in solution. Time-resolved transient absorption spectroscopy was performed for all three compounds as well as for bis(merocyanine) **21** without fullerene units. A significantly faster relaxation to the ground state of the dye stack after photoexcitation was observed for bis(merocyanine)-C_{60} conjugate **32** compared to bis(merocyanine) **21** revealing additional deactivation pathways. Indeed, the transient absorption spectra of both bis(merocyanine)-C_{60} conjugates **32** and **33** as well as of merocyanine-C_{60} conjugate **34** exhibit spectral signatures that can be assigned to the presence of a fullerene radical anion indicating a photoinduced electron transfer from the respective dye stack or monomeric chromophore to the fullerene unit. The C_{60} radical anion has a short lifetime (nanosecond timescale) for all compounds and presumably recombines with the oxidized merocyanine species. Thus, a considerable stabilization of the charge separated state for long time scales in the case of the dye stack of unsymmetric bis(merocyanine)-C_{60} conjugate **33** could not be observed. This might be due to the flexible spacer unit between the merocyanine chromophore and the fullerene unit, which allows a folding of the C_{60} towards the merocyanine units resulting in a short distance between the electron and the hole. In addition, weak spectral features of singlet and triplet excited fullerene were observed, which might originate from energy transfer as competing process to charge separation. To get further insight additional investigations have to be done including the establishment of a kinetic model to determine the rate constants for all processes and a global analysis of the transient absorption spectra.

In conclusion, an electron transfer and possibly also an energy transfer process from the dye stack to the fullerene moiety takes place at the p/n-heterointerface. The short lifetime of the charge separated state observed in the transient spectra indicates a fast charge recombination of the electron and the hole, which is an undesired process in organic solar cell devices.

6.4 Experimental Section

6.4.1 Materials and Methods

All solvents and reagents were purchased from commercial sources and used as received without further purification. Microwave reactions were performed in Discover® CEM Microwave Reactor. Column chromatography was performed using silica gel 60M (0.04–0.063 mm). Gel permeation chromatography was performed on a Shimadzu Recycling GPC system (LC-20AD prominence pump; SPDMA20A, prominence diode array detector) using two preparative columns (JAIGEL-1H, JAIGEL-2H und JAIGEL-2.5H) from Japan Analytical Industries Co., Ltd. and chloroform was used as eluent. NMR spectra were recorded on a Bruker Avance III HD 400 or Bruker Avance III HD 600 spectrometer at 295 K, unless otherwise stated. The spectra were calibrated to the residual solvent peak and the chemical shifts δ are given in ppm. Multiplicities are denoted as follows: s = singlet, d = doublet, t = triplet, q = quartet, m = multiplet, br = broad. High-resolution mass spectra (ESI) were recorded on an ESI MicrOTOF Focus spectrometer. Solvents for spectroscopic studies were of spectroscopic grade and used as received. Concentration-dependent UV/Vis spectra were recorded on UV/Vis spectrometers Lambda 950 or 35. The spectral band width and the scan rate were 1 nm and 120 nm min^{-1}, respectively. Stock solutions of the studied compounds were accurately prepared and continuously diluted for absorption measurements at different concentrations by taking into account the solubility and the absorbance of the respective compound. The UV/Vis measurements were performed in conventional quartz cell cuvettes with path lengths of 0.2 – 50 mm. The spectra were fitted according to the dimer model[95] by applying a global analysis.

Computational Details

Computational calculations were performed using the Gaussian 09 program package.[103] Geometry optimization for merocyanine-C_{60} conjugate **34** (butyl groups were replaced by methyl groups and the octyl chain was replaced by a hydrogen atom) was carried out at the AM1 level[171] followed by frequency calculation to confirm the existence of a minimum. To calculate the radius of the radical cation of the short merocyanine chromophore a geometry optimization of the oxidized chromophore of **19** (Chapter 3, butyl groups were replaced by methyl groups) was performed at the DFT level with B97D3[99] as functional and def2-SVP[100] as basis set. The structure was geometry

optimized, followed by frequency calculations on the optimized structures. The recommended radius for the Onsager solvent reaction field model was then used as the radius of the radical cation.

Femtosecond transient absorption spectroscopy:

The samples were dissolved in toluene and filled in 0.2 cm quartz cuvettes. Afterwards, the solution was purged with argon for 15 min prior to measurement. The measurements were performed with a Helios Transient Absorption Spectrometer using a Ti:sapphire laser as light source operating at 1 kHz. The laser beam was split into two parts. One part was used to pump an optical parametric amplifier (TOPAS-C) from Light Conversion to generate the pump pulse with duration of 140 fs and appropriate wavelength. The second part was focused onto a vertically oscillating CaF_2 crystal (UV/Vis) or Ti:sapphire crystal (NIR) to generate a white light continuum as probe pulse.

6.4.2 Synthesis and Characterization

4-Oxo-4-(4-octylphenyl)butyric acid methyl ester 37

A suspension of aluminium chloride (2.63 g, 19.7 mmol) in dry dichloromethane (15 mL) was cooled down to 0 °C and phenyloctane (2.84 g, 14.9 mmol) was added under nitrogen atmosphere. Then 3-(carbomethoxy)propionyl chloride (2.20 g, 14.6 mmol) was added dropwise within 20 min and the mixture was stirred for 60 min at 0 °C. Distilled water (20 mL) and dichloromethane (10 mL) were added and the aqueous layer was separated. The organic layer was washed with hydrochloric acid (7%, 10 mL) and distilled water (10 mL) and the solvent was removed under reduced pressure. Finally, the crude product was purified by column chromatography (silica gel, CH_2Cl_2/*n*-pentane 3:1) to give the desired product.

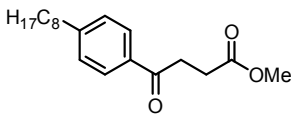

37

$C_{19}H_{28}O_3$ (304.43)

Yield: 2.33 g (7.65 mmol, 51%), colorless solid.

Mp. 37-40 °C. ^{1}H NMR (400 MHz, $CDCl_3$): δ = 7.90 (m, 2H), 7.26 (m, 2H), 3.71 (s, 3H), 3.30 (t, ^3J = 6.7 Hz, 2H), 2.76 (t, ^3J = 6.7 Hz, 2H), 2.66 (m, 2H), 1.63 (m, 2H), 1.35–1.23 (m, 10H), 0.88 (t, ^3J = 6.8 Hz, 3H). ^{13}C NMR (101 MHz, $CDCl_3$): δ = 197.8, 173.6, 149.1, 134.4, 128.8, 128.3, 51.9, 36.1, 33.4, 32.0, 31.2, 29.5, 29.4, 29.3, 28.2, 22.8, 14.2. HRMS (ESI, positive, acetonitrile/chloroform): *m*/*z* 327.19302 $[M+Na]^+$, calculated for $C_{19}H_{28}NaO_3^+$: 327.19307.

Methyl-4-(4-Octylphenyl)-butanoat-*p*-tosylhydrazone 38

4-Oxo-4-(4-octylphenyl)butyric acid methyl ester **37** (5.14 g, 16.9 mmol), *p*-toluenesulfonyl hydrazide (3.93 g, 21.1 mmol) and *p*-toluenesulfonic acid monohydrate (160 mg, 842 µmol) were dissolved in toluene (150 mL) and the mixture stirred for 2 h under reflux using a Dean-Stark apparatus. The solvent was removed under reduced pressure and the crude product purified by column chromatography (silica gel, *n*-pentane/EtOAc 6:1). The desired product was obtained as a 10:1 mixture of the *E*- and *Z*-isomer.

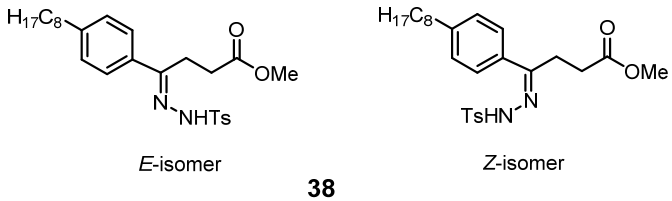

38

$C_{26}H_{36}N_2O_4S$ (472.64)

Yield: 7.02 g (14.9 mmol, 88%).

Mp. 66–69 °C. ^{1}H NMR of *E*-isomer (400 MHz, CD_2Cl_2): δ = 9.71 (s, 1H, overlap with signal of *Z*-isomer), 7.90–7.86 (m, 2H), 7.46–7.42 (m, 2H), 7.35–7.31 (m, 2H, overlap with signal of *Z*-isomer), 7.17–7.14 (m, 2H), 3.59 (s, 3H), 2.92 (m, 2H), 2.63–2.56 (m, 4H), 2.41 (m, 3H), 1.56 (m, 2H, overlap with signal of *Z*-isomer), 1.32–1.23 (m, 10H, overlap with signal of *Z*-isomer), 0.87 (t, ^3J(H,H) = 6.9 Hz, 3H). ^{1}H NMR of *Z*-isomer (400 MHz, CD_2Cl_2): δ = 9.71 (s, 1H, overlap with signal of E-isomer), 7.79–7.69 (m, 2H), 7.38 (m, 2H), 7.34 (m, 2H, overlap with signal of *E*-isomer), 7.29 (m, 2H), 3.67 (s, 3H), 3.28 (t, ^3J = 6.5 Hz, 2H), 2.74–2.65 (m, 4H), 2.45 (m, 3H), 1.56 (m, 2H, overlap with signal of *E*-isomer), 1.32–1.23 (m, 10H, overlap with signal of *E*-isomer), 0.88 (m, 3H, overlap with signal of E-isomer). HRMS (ESI, positive, acetonitrile/chloroform): *m*/*z* 473.24654 $[M+H]^+$, calculated for $C_{26}H_{37}N_2O_4S^+$: 473.24685.

5-[Butyl(2-hydroxyethyl)amino]-3-ethylthiophene-2-carboxaldehyde 46

To a portion of 3.01 g (13.7 mmol) of a 5:2 mixture of 5-bromo-3-ethylthiophene-2-carboxaldehyde **28** and 5-bromo-4-ethylthiophene-2-carboxaldehyde **29**[112] was added 2-butylaminoethanol (3.48 g, 29.7 mmol) and distilled water (8 mL). The mixture was then stirred for 2 h at 130 °C in the microwave. Distilled water (100 mL) and dichloromethane (100 mL) were added and the organic phase was separated. The aqueous layer was extracted with dichloromethane (2 x 100 mL) and the organic phases were combined. The solvent was removed under reduced pressure and the crude product was purified by column chromatography (silica gel, dichloromethane/ethyl acetate 3:1) yielding compound **46** as the only product as a brown oil.

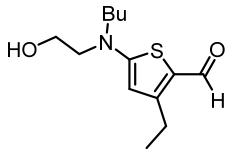

46

$C_{13}H_{21}NO_2S$ (255.38)

Yield: 220 mg (861 μmol, 9% referring to corresponding major regioisomer **28**), brown oil.

^{1}H NMR (400 MHz, CD_2Cl_2): δ = 9.63 (s, 1H), 5.84 (s, 1H), 3.84 (m, 2H), 3.51 (t, ^3J = 5.8 Hz, 2H), 3.40 (m, 2H), 2.81 (q, ^3J = 7.6 Hz, 2H), 1.73 (t, ^3J = 5.6 Hz, 1H), 1.69–1.62 (m, 2H), 1.42–1.31 (m, 2H), 1.26 (t, ^3J = 7.6 Hz, 3H), 0.96 (t, ^3J = 7.3 Hz, 3H). HRMS (ESI, positive, acetonitrile/chloroform): 256.13687 $[M+H]^+$, calculated for $C_{13}H_{22}NO_2S$: 256.13658.

[6,6]-(4-Octylphenyl)-C61-propionic acid methyl ester 40

Hydrazone **38** (542 mg, 1.15 mmol) and sodium methylate (64.2 mg, 1.19 mmol) were stirred for 15 min in dry pyridine (8 mL) at room temperature under argon atmosphere. A solution of C_{60} (405 mg, 562 μmol) in dry 1,2-dichlorobenzene (28 mL) was added and the mixture was stirred under argon atmosphere for 23 h at 68 °C. Pyridine was removed under reduced pressure and the solution was stirred for 23 h under reflux. The mixture was purified by column chromatography (silica gel, toluene) and the solid finally precipitated from CH_2Cl_2/MeOH to afford the desired fullerene derivative **40**.

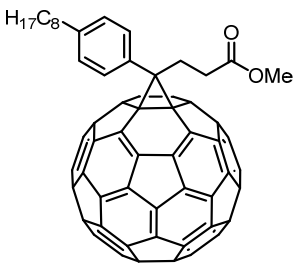

40

$C_{79}H_{28}O_2$ (1009.09)

Yield: 220 mg (218 μmol, 39%), brown solid.

Mp. 175–177 °C. ^{1}H NMR (400 MHz, $CDCl_3$): δ = 7.80 (m, 2H), 7.34 (m, 2H), 3.69 (s, 3H), 3.21 (m, 2H), 2.87 (m, 2H), 2.70 (m, 2H), 1.71 (m, 2H), 1.44–1.24 (m, 10H), 0.89 (t, ^3J = 7.0 Hz, 3H). ^{13}C NMR (101 MHz, 1,1,2,2-tetrachloroethane-d_2): δ = 173.3, 149.0, 147.8, 146.1, 145.39, 145.36, 145.34, 145.30, 145.2, 145.0, 144.9, 144.7, 144.6, 144.2, 143.9, 143.5, 143.3, 143.22, 143.18, 143.16, 143.12, 143.10, 142.5, 142.3, 141.2, 140.9, 138.4, 137.9, 133.2, 132.2, 128.8, 54.1, 52.3, 51.1, 36.1, 32.2, 32.0, 31.5, 29.89, 29.85, 29.82, 29.61, 23.1, 14.6. HRMS (ESI, positive, acetonitrile/chloroform): *m*/*z* 1009.21568 $[M+H]^+$, calculated for $C_{79}H_{29}O_2^+$: 1009.21621.

[6,6]-(4-Octylphenyl)-C_{61}-propionic acid 41

A mixture of [6,6]-(4-octylphenyl)-C_{61}-propionic acid methyl ester (1.68 g, 1.69 mmol), acetic acid (154 mL), concentrated hydrochloric acid (60 mL) and chlorobenzene (134 mL) was stirred for 23.5 h under reflux. The solvent was removed under reduced pressure and the residue dissolved in dichloromethane (150 mL). Methanol (200 mL) was added and the precipitate filtered off and dried under vacuum.

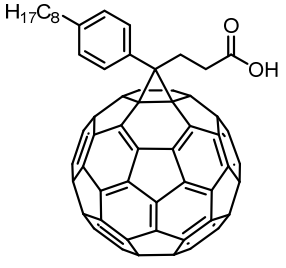

41

$C_{78}H_{26}O_2$ (995.06)

Yield: 1.58 g (1.59 mmol, 94%), dark brown solid.

Mp. 190–192 °C. ^{1}H NMR (400 MHz, $CDCl_3$): δ = 7.81 (m, 2H), 7.35 (m, 2H), 3.21 (m, 2H), 2.90 (m, 2H), 2.70 (m, 2H), 1.71 (m, 2H), 1.44–1.24 (m, 10H), 0.89 (t, ^3J = 7.0 Hz, 3H). ^{13}C NMR (101 MHz, 1,1,2,2-tetrachloroethane-d_2): δ = 177.2, 149.0, 147.7, 146.1, 145.40, 145.36, 145.34, 145.28, 145.23, 145.0, 144.9, 144.7, 144.6, 144.2, 143.9, 143.5, 143.3, 143.22, 143.18, 143.16, 143.10, 142.5, 142.3, 141.2, 140.9, 138.3, 137.9, 133.1, 132.1, 128.8, 99.8, 79.9, 54.1, 50.8, 36.1, 32.2, 31.6, 31.5, 29.9, 29.8, 29.6, 23.1, 14.6. HRMS (ESI, positive, acetonitrile/chloroform): *m*/*z* 995.20082 $[M+H]^+$, calculated for $C_{78}H_{27}O_2^+$: 995.20056.

Fullerene derivative 43

[6,6]-(4-Octylphenyl)-C_{61}-propionic acid (672 mg, 675 μmol), aminothiophene **42**[155] (243 mg, 1.07 mmol) and 4-dimetylaminopyridine (109 mg, 752 μmol) were dissolved in dry chlorobenzene (100 mL) under argon atmosphere. The solution was cooled down to 0 °C and *N*-(3-dimethylaminopropyl)-*N*'-ethylcarbodiimide hydrochloride (144 mg, 751 μmol) was added. The mixture was stirred for 1.5 h at 0 °C and for additional 15 h at room temperature. The solvent was removed under reduced pressure and the crude product purified by column chromatography (silica gel, CH_2Cl_2/EtOAc 350:6). The solid was finally precipitated from CH_2Cl_2/MeOH to afford the desired fullerene derivative **43**.

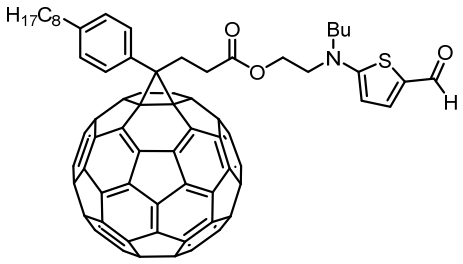

43

$C_{89}H_{41}NO_3S$ (1204.37)

Yield: 595 mg (494 mmol, 73%), brown solid.

Mp. 144–146 °C. ^{1}H NMR (400 MHz, CD_2Cl_2): δ = 9.46 (s, 1H), 7.83 (m, 2H), 7.42 (d, ^3J = 4.4 Hz, 1H), 7.36 (m, 2H), 5.99 (d, ^3J = 4.4 Hz, 1H), 4.28 (t, ^3J = 5.7 Hz, 2H), 3.63 (t, ^3J = 5.8 Hz, 2H), 3.40 (m, 2H), 3.18 (m, 2H), 2.84 (m, 2H), 2.71 (m, 2H), 1.75–1.61 (m, 4H), 1.44-1.26 (m, 12H), 0.96 (t, ^3J = 7.3 Hz, 3H), 0.89 (t, ^3J = 7.0 Hz, 3H). ^{13}C NMR (101 MHz, 1,1,2,2-tetrachloroethane-d_2): δ = 180.3, 172.6, 166.8, 148.9, 147.7, 146.0,

145.41, 145.38, 143.20, 143.12, 143.10, 142.4, 142.3, 141.2, 140.9, 138.2, 137.9, 133.1, 132.2, 128.8, 126.3, 120.6, 103.7, 80.0, 61.3, 54.7, 51.8, 50.9, 36.1, 32.2, 32.1, 31.5, 29.85, 29.80, 29.6, 29.1, 23.0, 20.4, 14.6, 14.3. HRMS (ESI, positive, acetonitrile/chloroform): *m*/*z* 1204.28903 $[M+H]^+$, calculated for $C_{89}H_{42}NO_3S^+$: 1204.28799.

Synthesis of fullerene derivative 47

[6,6]-(4-Octylphenyl)-C_{61}-propionic acid (708 mg, 712 μmol), aminothiophene **47** (220 mg, 861μmol) and 4-dimetylaminopyridine (103 mg, 843 μmol) were dissolved in dry dichloromethane (100 mL). A portion of *N*-(3-dimethylaminopropyl)-*N*'-ethylcarbodiimide hydrochloride (187 mg, 974 μmol) was added and the mixture was stirred for 18 h at room temperature. The mixture was concentrated to 50 mL and purified by column chromatography (silica gel, CH_2Cl_2/EtOAc 100:3).

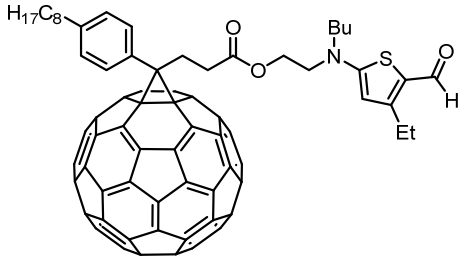

47

$C_{91}H_{45}NO_3S$ (1232.43)

Yield: 570 mg (463 μmol, 65%), brown solid.

^{1}H NMR (400 MHz, CD_2Cl_2): δ = 9.64 (s, 1H), 7.84 (m, 2H), 7.36 (m, 2H), 5.84 (s, 1H), 4.26 (t, ^3J = 5.8 Hz, 2H), 3.61 (t, ^3J = 5.8 Hz, 2H), 3.38 (m, 2H), 3.19 (m, 2H), 2.84 (m, 2H), 2.80 (q, ^3J = 7.6 Hz, 2H), 2.71 (m, 2H), 1.74–1.62 (m, 4H), 1.45–1.28 (m, 12H), 1.26 (t, ^3J = 7.6 Hz, 3H), 0.96 (t, ^3J = 7.3 Hz, 3H), 0.89 (t, ^3J = 6.9 Hz, 3H).

Merocyanine-C_{60} conjugate 34

Hydroxypyridone **44** (95.0 mg, 461 μmol) and fullerene derivative **43** (180 mg, 150 μmol) were stirred in acetic anhydride (3 mL) for 20 h at 100 °C. The solvent was removed under reduced pressure and the crude product was purified by column chromatography (silica gel, CH_2Cl_2, then CH_2Cl_2/EtOAc 100:1). The solid was precipitated from CH_2Cl_2/MeOH to give the desired merocyanine-C_{60} conjugate **34**.

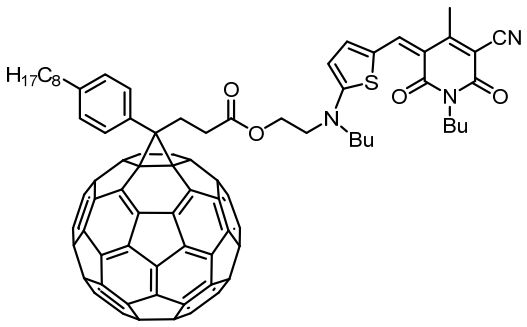

34

$C_{100}H_{53}N_3O_4S$ (1392.60)

Yield: 146 mg (105 μmol, 70%), red solid.

Mp. 159–161 °C. ^{1}H NMR (400 MHz, CD_2Cl_2): δ = 7.79 (m, 2H), 7.57 (m, 2H), 7.35 (m, 2H), 6.46 (d, ^3J = 5.1 Hz, 1H), 4.37 (t, ^3J = 5.3 Hz, 2H), 3.92 (m, 2H), 3.84 (t, ^3J = 5.3 Hz, 2H), 3.60 (m, 2H), 3.11 (m, 2H), 2.83 (m, 2H), 2.70 (m, 2H), 2.45 (s, 3H), 1.80–1.65 (m, 4H), 1.62–1.54 (m, 2H), 1.48–1.26 (m, 12H), 0.99 (t, ^3J = 7.3 Hz, 3H), 0.95 (t, ^3J = 7.3 Hz, 3H), 0.89 (t, ^3J = 7.0 Hz, 3H). ^{13}C NMR (101 MHz, 1,1,2,2-tetrachloroethane-d_2): δ = 175.9, 172.4, 163.4, 162.4, 158.4, 152.3, 148.7, 147.5, 145.9, 145.4, 145.3, 145.2, 145.1, 145.0, 144.78, 144.75, 144.7, 144.5, 144.2, 143.9, 143.8, 143.5, 143.21, 143.19, 143.1, 143.02, 142.95, 142.28, 142.25, 142.19, 141.0, 140.9, 138.1, 137.9, 133.0, 132.1, 128.8, 124.9, 117.8, 110.9, 108.3, 95.8, 79.9, 61.2, 50.7, 39.9, 36.1, 32.2, 32.1, 31.5, 30.4, 29.9, 29.81, 29.77, 29.6, 29.3, 23.0, 20.7, 20.4, 19.2, 14.6, 14.4, 14.2. HRMS (ESI, positive, acetonitrile/chloroform): m/z 1392.37890 $[M]^+$, calculated for $C_{100}H_{53}N_3O_4S^+$: 1392.37848. UV/Vis (toluene): λ_{max}/nm (ε/M^{-1} cm^{-1}) = 331 (47000), 433 (3000), 537 (108000).

Symmetric Bis(merocyanine)-C_{60} conjugate 32

Fullerene derivative **43** (70.0 mg, 58.2 μmol), bis(pyridone) **23**[107] (17.2 mg, 28.8 mmol) and β-alanine (300 μg, 3.37 μmol) were dissolved in a mixture of ethanol (0.5 mL) and 1,2-dichloroethane (0.5 mL). After stirring for 24 h under reflux the solvent was removed under reduced pressure and the crude product purified by column chromatography (siliga gel, CH_2Cl_2) followed by recycling GPC. The solid was precipitated from CH_2Cl_2/MeOH to give the desired bis(merocyanine)-C_{60} conjugate **32**.

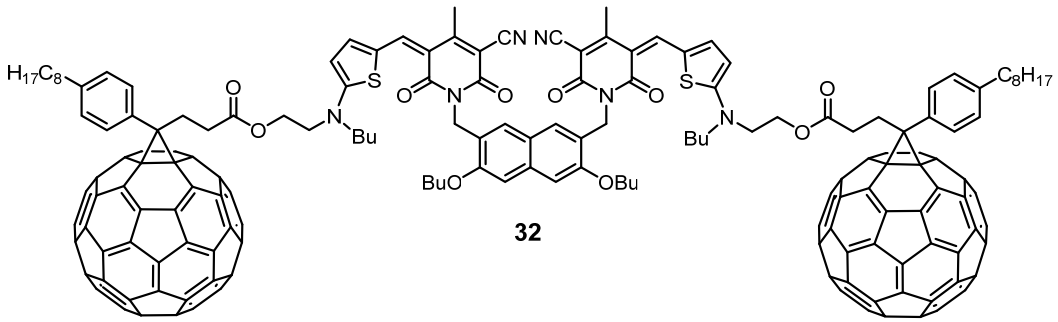

32

$C_{212}H_{114}N_6O_{10}S_2$ (2969.40)

Yield: 17.1 mg (5.76 μmol, 20%), red solid.

Mp. 231–234 °C. ^{1}H NMR (400 MHz, CD_2Cl_2): δ = 7.78 (m, 4H), 7.48 (br, 4H), 7.32 (m, 4H), 7.09 (s, 2H), 6.94 (s, 2H), 6.41 (d, ^3J = 4.7 Hz, 2H), 5.15 (s, 4H), 4.29 (t, ^3J = 5.4 Hz, 4H), 4.16 (t, ^3J = 6.0 Hz, 4H), 3.75 (br, 4H), 3.51 (m, 4H), 3.11 (m, 4H), 2.82 (m, 4H), 2.69 (t, ^3J = 7.8 Hz, 4H), 2.35 (br, 6H), 1.90 (m, 4H), 1.72–1.63 (m, 8H), 1.63–1.55 (m, 4H), 1.37–1.27 (m, 24H), 1.02 (t, ^3J = 7.4 Hz, 6H), 0.94–0.86 (m, 12H). ^{13}C NMR (101 MHz, 1,1,2,2-tetrachloroethane-d_2): δ = 177.6, 172.4, 163.3, 159.1, 155.6, 152.2, 148.9, 147.6, 146.0, 145.38, 145.36, 145.3, 145.2, 145.0, 144.8, 144.7, 144.5, 144.2, 143.92, 143.86, 143.46, 143.2, 143.1, 143.0, 142.3, 142.2, 142.1, 140.9, 138.2, 137.9, 134.0, 133.1, 132.1, 125.2, 124.7, 123.1, 120.6, 117.6, 105.3, 99.8, 94.7, 79.9, 68.3, 61.2, 50.8, 39.2, 36.1, 32.2, 32.0, 31.7, 31.5, 30.0, 29.9, 29.8, 29.6, 23.1, 20.4, 19.8, 14.6, 14.5, 14.2. HRMS (ESI, positive, chloroform/methanol): 2969.82270 $[M+H]^+$, calculated for $C_{212}H_{115}N_6O_{10}S_2$: 2969.81777. UV/Vis (toluene): λ_{max}/nm (ε/M^{-1} cm^{-1}) = 330 (88000), 434 (14000), 490 (121000).

Unsymmetric Bis(merocyanine)-C_{60} conjugate 33

Fullerene derivative **47** (604 mg, 490 μmol), bis(pyridone) **23**[107] (145 mg, 243 μmol) and aminothiophene **12**[94] (65.0 mg, 245 μmol) were dissolved in 1,2-dichloroethane (40 mL). Acetic anhydride (10 mL) was added and the mixture stirred for 24 h at 95 °C. The solvent was removed under reduced pressure and the crude product purified by column chromatography (silica gel, CH_2Cl_2/ethyl acetate 10:1) followed by recycling GPC. The solid was precipitated from CH_2Cl_2/MeOH.

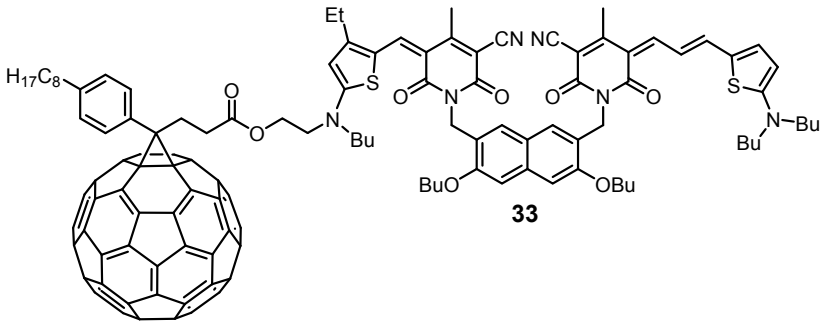

33

$C_{140}H_{100}N_6O_8S_2$ (2058.49)

Yield: 7.0 mg (3.4 μmol, 1%), blue solid.

^{1}H NMR (400 MHz, CD_2Cl_2): δ = 7.99 (br, 1H), 7.77 (m, 2H), 7.74 (s, 1H), 7.44–7.28 (m, 5H), 7.06 (s, 2H), 6.91 (s, 2H), 6.36 (s, 1H), 6.21 (d, ^3J(H,H) = 4.2 Hz, 1H), 5.17 (s, 2H), 5.13 (s, 2H), 4.28 (t, ^3J(H,H) = 5.5 Hz, 2H), 4.13 (t, ^3J(H,H) = 6.2 Hz, 4H), 3.75 (t, ^3J(H,H) = 5.8 Hz, 2H), 3.50 (m, 4H), 3.41 (m, 4H), 3.09 (m, 2H), 2.87–2.77 (m, 4H), 2.69 (m, 2H), 2.50 (s, 3H), 2.41 (s, 3H), 1.93–1.83 (m, 4H), 1.71–1.58 (m, 12H), 1.32 (m, 14H), 1.05–0.97 (m, 6H), 0.96–0.86 (m, 15 H). HRMS (ESI, positive, acetonitrile/chloroform): 2056.70237 $[M]^+$, calculated for 2056.70386 for $C_{140}H_{100}N_6O_8S_2^+$. UV/Vis (toluene): λ_{max}/nm (ε/M^{-1} cm^{-1}) = 329 (45000), 433 (5000), 519 (74000), 672 (28000).

6.5 Appendix

Table 12. Summary of ^{1}H NMR (600 MHz) data for bis(merocyanine)-C_{60} conjugate **32**: Chemical shifts δ (ppm) and coupling constants J (Hz), and assignment of the significant chromophore and backbone proton signals of bis(merocyanine)-C_{60} conjugate **32** monomer (1,1,2,2-tetrachloroethane-d_2 at 343 K) and aggregate (C_6D_5Cl at 276 K). The two sets of signals for the aggregate protons are denoted with (outer part of dye stack) and without prime (inner part of dye stack), respectively.

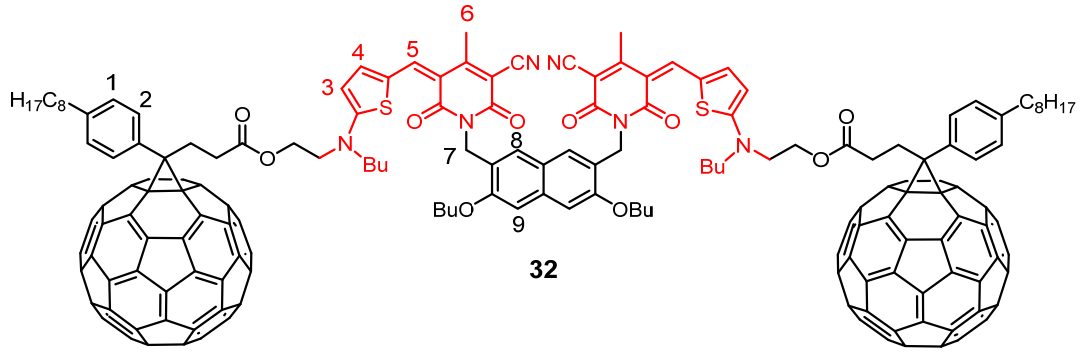

32

proton	δ_H [ppm] in 1,1,2,2-tetrachloroethane-d_2	δ_H [ppm] in C_6D_5Cl
1/1`	7.72 (m, 4H)	7.91 (m, 4H)
2/2`	7.27 (m, 4H)	7.34 (m, 4H)
3	6.31 (d, ^3J = 5.1 Hz, 2H)	6.30 (br, 2H)
3`		6.19 (br, 2H)
4	7.42 (br, 2H, overlapped with proton 5)	7.73 (br, 1H)
4`		7.10 (br, 1H)
5	7.42 (br, 2H, overlapped with proton 4)	7.65 (s, 1H)
5`		7.10 (s, 1H)
6	2.34 (s, 6H)	2.36 (s, 3H)
6`		2.30 (s, 3H)
7α	5.18 (s, 4H)	5.84 (br, 1H)
7β		5.68 (br, 1H)
7`α		5.51 (br, 1H)
7`β		5.37 (br, 1H)
8	7.07 (s, 2H)	7.54 (s, 1H)
8`		7.45 (s, 1H)
9	6.99 (s, 2H)	6.93 (s, 1H, overlapped with solvent signal)
9`		6.83 (s, 1H)

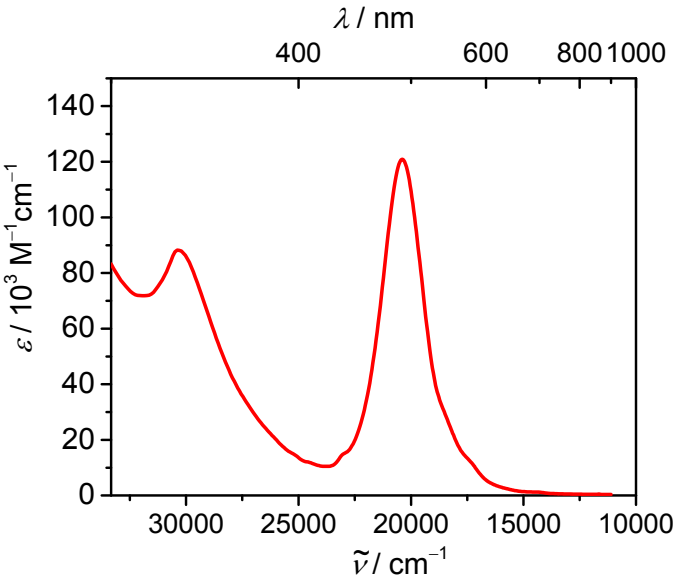

Figure 55. UV/Vis absorption spectrum of bis(merocyanine)-C_{60} conjugate **32** in toluene at 298 K (c = 1.43 x 10^{-4} M).

Weller analysis

The Gibbs free energy for a photoinduced charge separation can be estimated by Weller analysis:[172]

$$\Delta G_{CS} = e\,(E_{ox} - E_{red}) - E_{00} - \frac{e^2}{4\pi\varepsilon_0\varepsilon_s R_{CC}} - \frac{e^2}{8\pi\varepsilon_0}\left(\frac{1}{r_+} + \frac{1}{r_-}\right)\left(\frac{1}{\varepsilon_{ref}} - \frac{1}{\varepsilon_s}\right), \qquad (88)$$

where E_{ox} and E_{red} are the oxidation potential of the electron donor and the reduction potential of the electron acceptor, respectively, and E_{00} is the excited state energy of the donor. In addition, e is the charge of an electron and R_{CC} the center-to-center distance between the radical cation and the radical anion formed by charge separation. r_+ and r_- represent the radii of the radical cation and radical anion, respectively, while ε_0 stands for the vacuum permittivity. ε_{ref} is the permittivity of the solvent in which the redox potentials were determined, whereas ε_s is the permittivity of the solvent in which the charge separation occurs.

The half-wave reduction potential of methanofullerene is −1.11 V in dichloromethane (*versus* ferrocenium/ferrocene)[155] and the half-wave oxidation potential of the monomeric short merocyanine chromophore amounts to 0.52 V in dichloromethane (*versus* ferrocenium/ferrocene)[94]. For the stretched arrangement of the flexible spacer moiety in merocyanine-C_{60} conjugate **34** a center-to-center distance of R_{CC} = 17 Å was

determined based on the geometry optimized structure (AM1, Figure 56). The radius of the fullerene radical anion is set to $r_- = 5.6$ Å[173] and the radius of the radical cation of the merocyanine chromophore was estimated by DFT calculations (B97D3, def2-SVP) to be $r_+ = 5.3$ Å (for further details see the Experimental Section). The excited state energy E_{00} of 2.31 eV was determined from the absorption spectrum of merocyanine-C_{60} conjugate **34** in toluene. Thus, with the solvent permittivity of $\varepsilon_{ref} = 8.93$ (dichloromethane) and $\varepsilon_s = 2.38$ (toluene) we obtain for the Gibbs free energy of the photoinduced charge separation for **34** in toluene:

$$\Delta G_{CS} = -0.22 \text{ eV},$$

revealing an exergonic electron transfer process for the largest possible value of R_{CC} in merocyanine-C_{60} conjugate **34**. For smaller distances R_{CC} the driving force is further increased according to equation (88), which is reasonable due to flexibility of the spacer unit. Hence, we expect a photoinduced charge separation for merocyanine-C_{60} conjugate **34** in toluene.

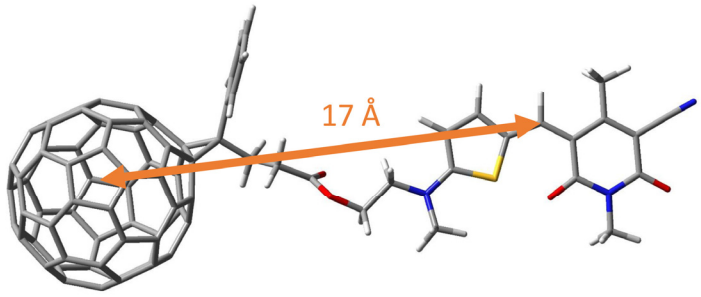

Figure 56. a) Geometry optimized structure of merocyanine-C_{60} conjugate **34** (AM1, butyl chains were replaced by methyl groups and the octyl group was replaced by a hydrogen atom).

To calculate the Gibbs free energy for the charge separation of the dimer aggregate of bis(merocyanine)-C_{60} conjugate **32** an excited state energy of $E_{00} = 1.99$ eV is supposed, which corresponds to the energy of the lowest exciton state (Table 9 in Chapter 4).
Under the assumption that the positive charge of the oxidized stack is localized on one chromophore we obtain for the corresponding Gibbs free energy:

$$\Delta G_{CS} = 0.10 \text{ eV},$$

which indicates a slightly endergonic charge separation process. For the calculation of ΔG_{CS} we supposed a center-to-center distance of R_{CC} = 17 Å like for merocyanine-C_{60} conjugate **34** and the same oxidation potential. However, the oxidation potential of the dye stack is supposed to be lower compared to the oxidation potential of the monomeric constituent chromophores based on the energies of the HOMO obtained by DFT calculations. The energy of the HOMO of the monomeric short chromophore is –4.93 eV, whereas it is –4.48 eV for the quadruple dye stack (Figure 30b (left) in Chapter 4). Hence, the dye stack is easier to oxidize, which should result in an exergonic charge separation process. Furthermore, the distance of R_{CC} = 17 Å represents the highest possible value and for smaller distances the charge separated state is more stabilized. Accordingly, a value of R_{CC} = 12 Å already results in an exergonic charge separation process with ΔG_{CS} = –0.05 eV. Additionally, it is reasonable that the hole in the dye stack of bis(merocyanine)-C_{60} conjugate **32** is delocalized over more than one chromophore unit. Hence, a larger radius of the radical cation r_+ can be expected resulting in a lower value of ΔG_{CS} according to equation (88).

Chapter 7

Summary

7.1 Summary

The electronic coupling between dyes leading to exciton states (exciton coupling) is of great importance for the functional properties of organic dyes and semiconductors as well as for their application in (opto-)electronics and organic photovoltaics. It significantly influences the absorption and emission properties of dye aggregates and enables coherent energy transfer between chromophores, like in the natural light-harvesting systems. Whereas exciton coupling between the same type of chromophores has been extensively explored in the last decades, there is an apparent lack of information on the coupling between different types of chromophores.

Thus, the main focus of this thesis was to gain a deeper understanding in the exciton coupling between different types of chromophores. Towards this goal, bis(merocyanine) **7** comprising two chromophores with different conjugation length (Figure 57a) was synthesized. The spacer unit in **7** assures a preorganization of the two chromophores, which enables folding of the two chromophores in non-polar solvents into double hetero dye stacks. Bis(merocyanine) **6** with the same type of chromophores (Figure 57a) was used as reference compound for comparison. Solvent-dependent UV/Vis studies revealed significant spectral changes upon increasing the amount of non-polar solvent for both compounds. The changes in the UV/Vis spectra observed for bis(merocyanine) **6** are in agreement with the formation of an H-type aggregate. Remarkably, the pronounced spectral changes observed for bis(merocyanine) **7** bearing two different chromophores could not be explained by solvatochromism indicating a strong interaction between the chromophoric units. Further, concentration-dependent UV/Vis measurements revealed no spectral changes for both compounds upon dilution confirming an intramolecular stacking of the π-systems (Figure 57a). The results obtained by DFT calculations indeed suggest a π-stacked arrangement of the two chromophores at a van-der-Waals distance for both bis(merocyanine) dyes with an antiparallel orientation of the ground state dipole moments. To gain insight into the excited state properties of the dye stacks time-dependent DFT

calculations were performed. The simulated absorption spectra were in good agreement with the experimental ones in low polarity solvent.

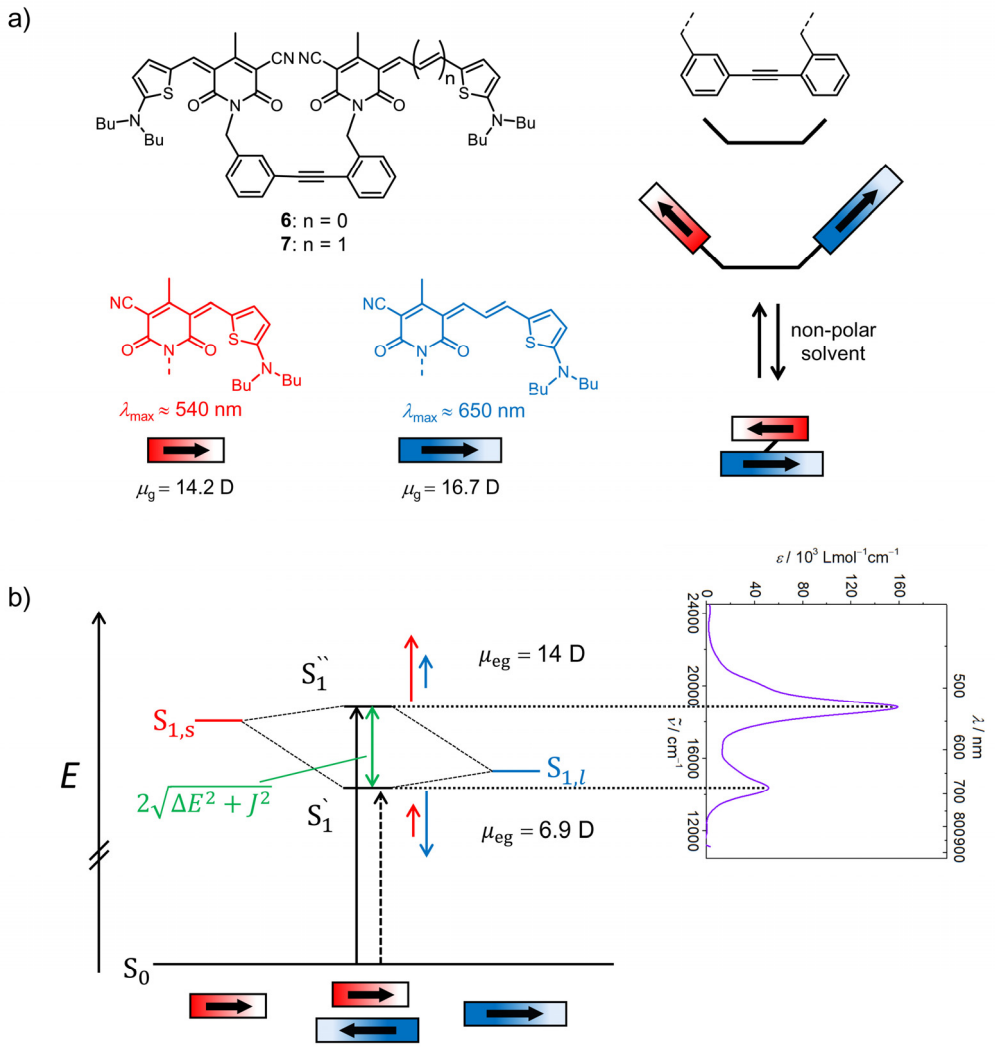

Figure 57. a) Chemical structure of bis(merocyanine) dyes **6** and **7** and schematic illustration of the folding process of **7** in non-polar solvents resulting in the heterodimer stack. b) Exciton state diagram for the heterodimer of **7**. The arrows (red for short chromophore and blue for long chromophore) indicate the phase relations between the transition dipole moments. The lengths of the arrows reflect the magnitude of the coefficients of the transition dipole moment. $S_{1,s}$ represents the first excited state of the short chromophore and $S_{1,l}$ of the long chromophore, respectively, while J denotes the exciton coupling energy and ΔE is half the energy difference between the excited states $S_{1,s}$ and $S_{1,l}$. In addition, the corresponding UV/Vis spectrum of **7** in DCM/MCH 10:90 (c = 5 x 10^{-6} M) is displayed.

In addition, the transition densities obtained for both dye stacks showed an in-phase and out-of-phase coupling of the transition densities of the individual chromophores for the higher and lower excited state, respectively. Thus, exciton theory was applied to the homo

and hetero dye stack assuming an exciton coupling also between the different types of chromophores. In this way, the absorption properties of the heterodimer stack could be explained in qualitative and quantitative manner (Figure 57b).

The exciton coupling energies calculated by transition charge method were in good agreement with the values determined from the UV/Vis data revealing even a larger coupling for the hetero-π-stack (1824 cm^{-1}) than for the homo-π-stack (1668 cm^{-1}). Thus, strong exciton coupling is not only present between the same but also different types of chromophores and significantly influences the absorption properties of the heterodimer stack of bis(merocyanine) **7**.

The second part of the thesis dealed with the exciton coupling in quadruple merocyanine dye stacks comprising the same or different types of chromophores. It is known from earlier work that symmetric bis(merocyanine) **21** containing two identical chromophores self-assembles in non-polar solvents resulting in dye stacks with four equal chromophores (Figure 58a). Therefore, unsymmetric bis(merocyanine) **22** with two different types of chromophores was synthesized and its aggregation behavior investigated by concentration-dependent UV/Vis spectroscopy in chlorobenzene. Pronounced spectral changes were observed upon increasing the concentration and the absorption data could be successfully fitted to the dimer model. While for the symmetric bis(merocyanine) **21** only one type of dimer structure is possible, in principle three different types of dimers can be formed by self-assembly of the unsymmetric bis(merocyanine) **22** (Figure 58b). The structure of the heteroaggregate dimers have been assigned by different NMR techniques and unambiguously confirmed in the solid state by X-ray analysis. These studies clearly confirmed that bis(merocyanine) **22** self-assembles exclusively into dimers with the long chromophores located in the interior and the shorter ones in the terminal of the quadruple stack (aggregate type I in Figure 58b). The heteroaggregate dye stacks exhibit unexpected absorption spectral features compared to those of the respective monomeric dyes and the homoaggregate stacks. The simulated absorption spectra of the homoaggregate of **21** and the heteroaggregate of **22** obtained by time-dependent DFT calculations resemble the respective experimental spectra. The absorption spectral features of the heteroaggregate could not be explained by assuming an exciton coupling only between the same type of chromophores within the stack.

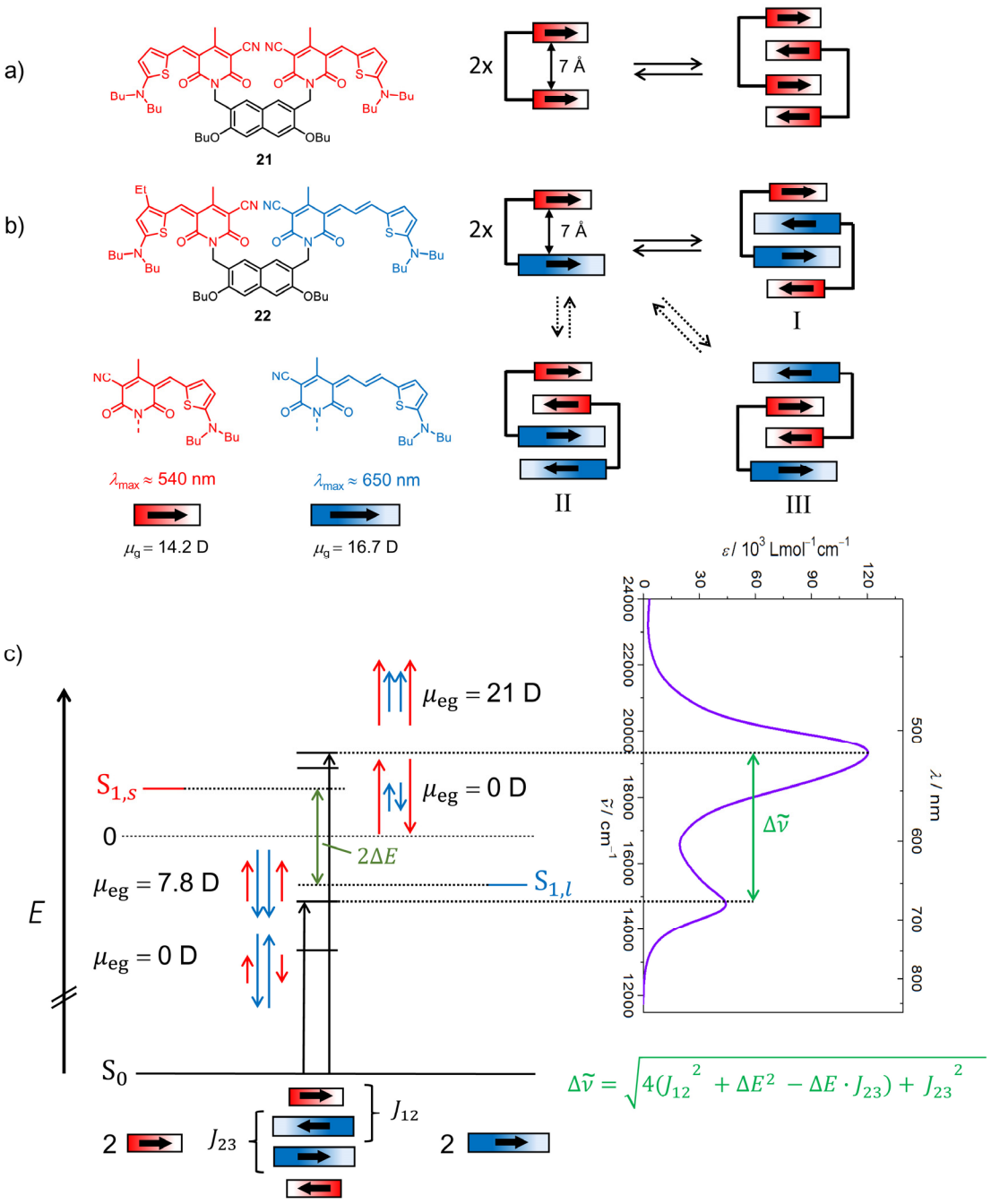

Figure 58. a) Chemical structure of bis(merocyanine) **21** with two identical chromophores and schematic representation of its self-assembly into homoaggregates. b) Chemical structure of bis(merocyanine) **22** with two different chromophores and schematically representation of its self-assembly into three possible dimer structures. c) Exciton state diagram for the quadruple dye stacks of bis(merocyanine) **22**. The arrows (red for the short chromophore and blue for the long chromophore) indicate the phase relations between the transition dipole moments. The lengths of the arrows reflect the magnitude of the coefficients of the transition dipole moments. The corresponding experimental dimer spectrum obtained from concentration-dependent UV/Vis spectroscopy in chlorobenzene is depicted to indicate the allowed transitions. $S_{1,s}$ and $S_{1,l}$ are the energies of the first excited states of the short and long chromophore, respectively.

Therefore, exciton theory was applied within the next-neighbor approximation assuming an exciton coupling also between the different types of chromophores in the stack. The resulting exciton state diagram is in agreement with the results obtained by time-dependent DFT calculations (Figure 58c). Indeed, the exciton coupling energies estimated by transition charge method reveal a stronger coupling between the different types of chromophores (J_{12} = 1861 cm^{-1}) compared to the coupling between the same types of chromophores (J_{23} = 1108 cm^{-1}) within the hetero dye stack.

Afterwards, exciton coupling between different perylene bisimide (PBI) dyes was analyzed. For this purpose, the optical absorption properties of cyclophane **or-CP** (Figure 59c) comprising one core-unsubstituted PBI chromophore ('orange PBI') and one *tert*-butylphenoxy-substituted PBI ('red PBI') was investigated. For comparison, PBI-cyclophanes **o2-CP** (Figure 59a) and **r2-CP** (Figure 59b) bearing two orange PBI and red PBI chromophores, respectively, were included in the studies.

All three cyclophanes showed significantly different absorption properties (Figure 59d-f, black solid lines) compared to the absorption spectra of the constituent monomeric PBI units (Figure 59d-f, black dotted lines) indicating strong interaction between the chromophores within the cyclophanes. Indeed, the geometry optimized structures obtained by DFT calculations indicate a π-stacked arrangement of the PBI chromophores at close van-der-Waals distance with rotational displacement (Figure 59a-c). However, the spectra of the PBI cyclophanes are much more complex than the ones of π-stacked merocyanine dyes due to vibrational contribution in the former case. Therefore, time-dependent quantum mechanical simulations were performed for the PBI cyclophanes employing the Holstein-type Hamiltonian, which is known to adequately describe the absorption properties of dye aggregates exhibiting exciton-vibrational coupling. In this way, the absorption spectra of all three cyclophanes were simulated (Figure 59d-f, colored lines) showing very good agreement with the experimental spectra. The resulting exciton coupling energies reveal similar coupling strength for the hetero PBI cyclophane **or-CP** (427 cm^{-1}) compared to the coupling strengths in homo PBI cyclophanes **o2-CP** (613 cm^{-1}) and **r2-CP** (500 cm^{-1}). This coupling strength is comparable to the stretching mode of the PBI cores (≈1400 cm^{-1}) that induces the vibronic progression in the absorption spectra. Thus, all three cyclophanes are in the so-called intermediate coupling regime. The most interesting outcome of this study is that exciton-vibrational coupling is

also present in hetero PBI cyclophane **or-CP** and significantly influences the absorption spectrum of the heterodimer PBI stack.

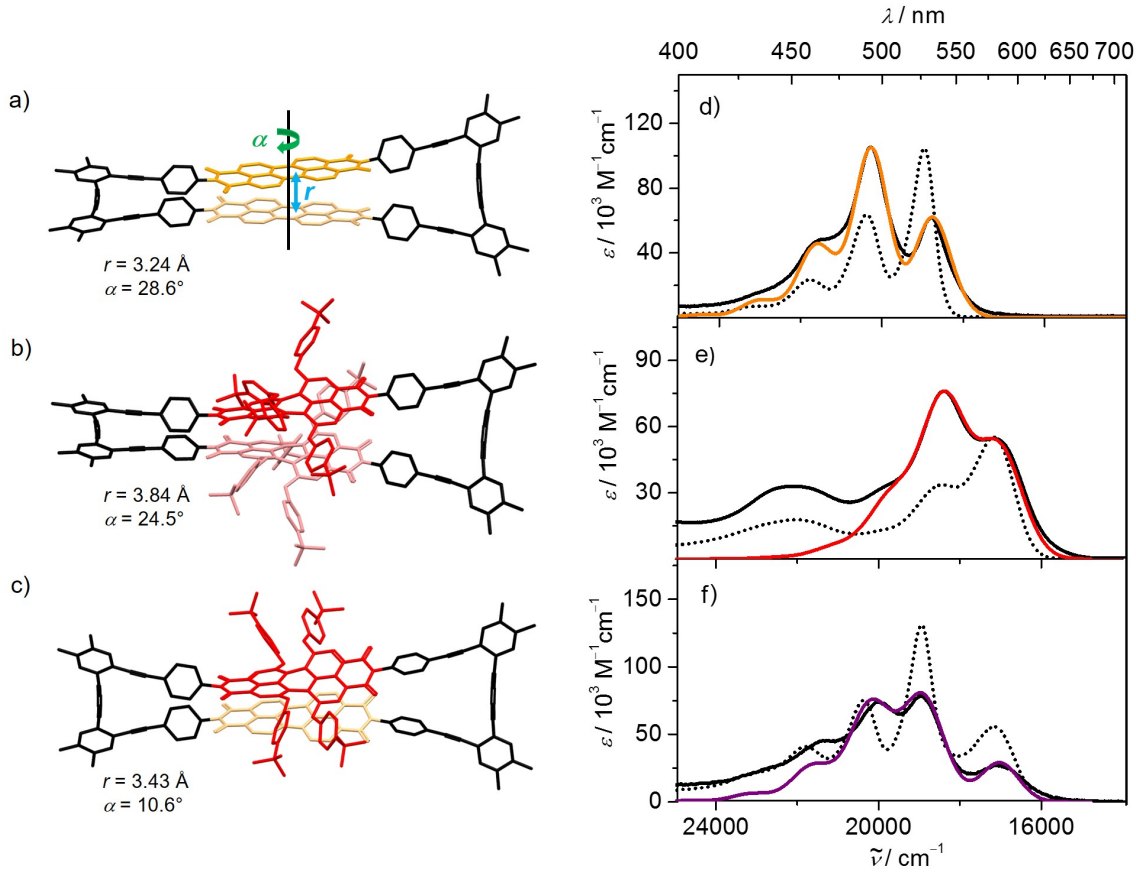

Figure 59. Geometry optimized structures of PBI cyclophanes a) **o2-CP**, b) **r2-CP** and c) **or-CP** (B97D3, def2-SVP, hexyl groups were replaced by methyl groups). Hydrogen atoms were omitted for clarity. α represents the rotational displacement and r the distance between the chromophores in the respective cyclophanes as depicted in Figure 59a. UV/Vis absorption spectra of d) monomeric orange PBI chromophore (black dotted line) and cyclophane **o2-CP** (black solid line), e) monomeric red PBI chromophore (black dotted line) and cyclophane **r2-CP** (black solid line) and f) sum of the spectra of monomeric red PBI and orange PBI chromophores (black dotted line) as well as the spectrum of cyclophane **or-CP** (black solid line) in dichloromethane ($c \approx 10^{-5}$ M) at 298 K. Also shown are the simulated absorption spectra of the respective cyclophanes (colored lines). The calculated spectra are normalized to match the measured peak of highest intensity in each case. The model does not account for the $S_0 \rightarrow S_2$ transition seen around 22000 cm^{-1} in Figure 59e,f.

In the last part of this thesis, the photoinduced electron transfer process in well-defined supramolecular p/n-heterojunctions was investigated. For this purpose, two bis(merocyanine)-C_{60} conjugates **32** and **33** (Figure 60a,b) comprising the same and different types of chromophores, respectively, were synthesized. We expected for both

compounds a self-assembly into quadruple dye stacks like for bis(merocyanine) dyes **21** and **22** (Figure 58a,b) with the fullerene moieties in the periphery of the stacks (Figure 60a,b).

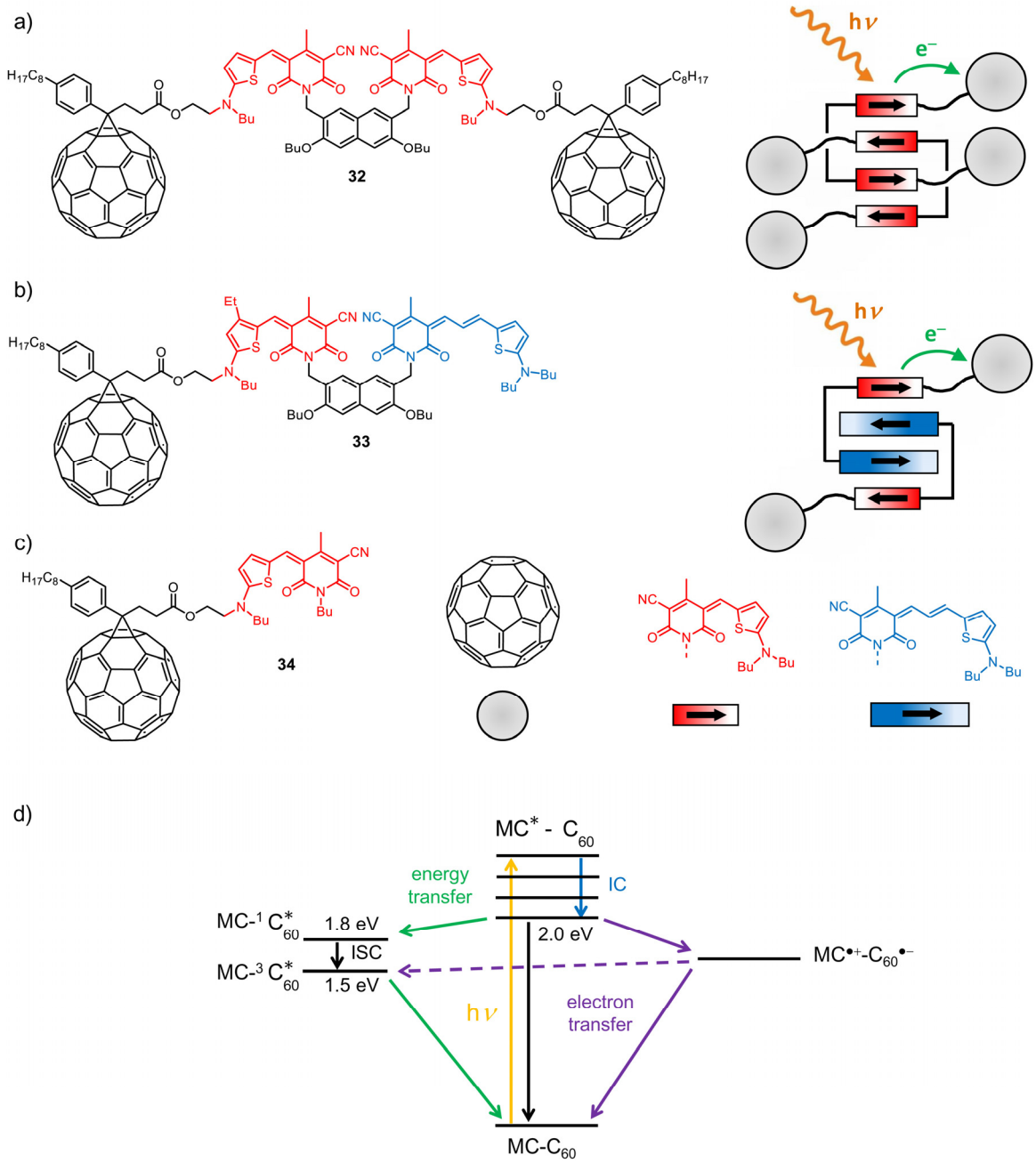

Figure 60. Chemical structure and schematic illustration of the dimer aggregate of a) symmetric bis(merocyanine)-C_{60} conjugate **32** and b) unsymmetric bis(merocyanine)-C_{60} conjugate **33**. c) Chemical structure of merocyanine-C_{60} conjugate **34**. d) Proposed Jablonski diagram for the dimer aggregate of bis(merocyanine)-C_{60} conjugate **32** showing the potential competition between photoinduced electron transfer and energy transfer. Note that the exact energy level of the charge separated state is unknown. MC denotes the quadruple merocyanine dye stack and IC and ISC stand for internal conversion and intersystem crossing, respectively.

After photoexcitation an electron transfer from the dye stack to the fullerene moiety might occur, which represents a key step for the formation of charge carriers in organic photovoltaics. Since the HOMO of the heteroaggregate of bis(merocyanine) **22** is localized at the long chromophores, the positive charge formed upon charge separation supposed to be mostly localized in the interior of the stack. Accordingly, the unsymmetric bis(merocyanine)-C_{60} conjugate **33** exhibits only one fullerene moiety compared to symmetric bis(merocyanine)-C_{60} conjugate **32** in order to increase the distance between the negatively charged fullerene and the positive charge of the dye stack. In this way, a charge separated state with long lifetime could be realized.

The self-assembly of symmetric bis(merocyanine)-C_{60} conjugate **32** was investigated by concentration-dependet UV/Vis studies revealing a dimerization process. Indeed, the structure of the quadruple dye stack could be confirmed by 2D NMR spectroscopy. Further, the absorption spectra of both bis(merocyanine)-C_{60} conjugates **32** and **33** in toluene resemble the ideal dimer spectra of bis(merocyanine) dyes **21** and **22** revealing the presence of almost only aggregated species, even at low concentrations.

To investigate the photoinduced electron transfer from the dye stacks of both aggregated bis(merocyanine)-C_{60} conjugates to the fullerene moieties, femtosecond time-resolved transient absorption spectroscopy was performed in toluene. For comparison, the measurements were also conducted for the newly synthesized monomeric merocyanine-C_{60} conjugate **34** (Figure 60c) and the dimer aggregate of bis(merocyanine) **21**. The comparison of the transient spectra of bis(merocyanine) **21** and bis(merocyanine)-C_{60} conjugate **32** revealed a significantly faster recovery of the ground state of the dye stack for the latter after photoexcitation. Thus, the presence of the fullerene moieties in **32** leads to an additional relaxation pathway. Indeed, a spectral signature in the transient absorption spectra could be observed, which can be assigned to the fullerene radical anion indicating an electron transfer from the excited dye stack to the fullerene unit (Figure 60d). The signal decays on a nanosecond timescale revealing a lifetime of the charge separated state of < 7 ns. In addition, spectral signatures for excited singlet and triplet fullerene are observed in the transient absorption spectra. This might be explained by an additional energy transfer from the dye stack to the fullerene unit (Figure 60d). However, these signals might also arise from excitation by the pump laser pulse, which has to be clarified by additional measurements with plain C_{60}. Additionally, the excited triplet fullerene might be formed upon charge recombination (Figure 60d). The transient absorption

spectra of monomeric merocyanine-C_{60} conjugate **34** and aggregated bis(merocyanine)-C_{60} conjugate **33** with two different types of chromophores reveal a lifetime of the charge separated state in the same order of magnitude as for bis(merocyanine)-C_{60} conjugate **32**. Thus, the expected stabilization of the positive charge in the oxidized dye stack of **33** towards long timescales could not be achieved. The reason for this might be the flexible spacer between the dye stack and the fullerene moiety, which enables a short distance between the hole and electron formed upon charge separation. The short lifetime of the charge separated state observed for both bis(merocyanine)-C_{60} conjugates might explain the moderate power conversion efficiencies of organic solar cells based on merocyanines in combination with fullerene derivatives.

In conclusion, the results of this thesis confirm a strong exciton coupling between different types of chromophores, which significantly influences the optical properties of dye heteroaggregates as present *e.g.* in bulk heterojunction solar cells. These insights may inspire the design of dye aggregates with exceptional absorption properties by using different types of chromophores to cover a broad spectral range, which should be beneficial for harvesting solar light. In addition, exciton coupling indicates a coherent energy transfer between chromophores resulting in fast and efficient energy transport. Based on the insights gained in this thesis, further investigations by two-dimensional optical spectroscopy and quantum dynamical calculations seem promising.

7.2 Zusammenfassung

Die elektronische Kopplung zwischen Farbstoffen unter Ausbildung von exzitonischen Zuständen (exzitonische Kopplung) spielt eine wichtige Rolle für die funktionellen Eigenschaften von organischen Farbstoffen und Halbleitern sowie für deren Einsatz in (opto-)elektronischen Anwendungen und der organischen Photovoltaik. So beeinflusst sie wesentlich die Absorptions- und Emissionseigenschaften von Farbstoffaggregaten und ermöglicht wie im Fall der natürlichen Lichtsammelkomplexe einen kohärenten Energietransfer zwischen Chromophoren. Während die exzitonische Kopplung zwischen gleichen Chromophoren in den letzten Jahrzehnten umfangreich untersucht wurde, ist wenig über die Kopplung zwischen unterschiedlichen Chromophoren bekannt.

Daher bestand das wesentliche Ziel der vorliegenden Arbeit in der Untersuchung der exzitonischen Kopplung zwischen unterschiedlichen Chromophoren. Dazu wurde das Bis(merocyanin) **7** synthetisiert, das aus zwei Chromophoren mit unterschiedlicher Konjugationslänge besteht (Abbildung 1a). Die Verbrückungseinheit in **7** gewährleistet eine Präorganisation der beiden Farbstoffeinheiten, die eine Faltung der Chromophore in unpolaren Lösungsmitteln ermöglicht, sodass auf diese Weise ein Heterostapel aus zwei unterschiedlichen Merocyaninfarbstoffen entsteht. Bis(merocyanin) **6** mit zwei gleichen Chromophoren (Abbildung 1a) wurde als Referenzsystem verwendet. Lösungsmittelabhängige UV/Vis-Studien zeigten bei Zunahme des Anteils an unpolarem Lösungsmittel deutliche spektrale Veränderungen für beide Farbstoffsysteme, wobei die beobachteten Veränderungen in den UV/Vis-Spektren von Bis(merocyanin) **6** im Einklang mit der Entstehung eines H-Typ Aggregats stehen. Bemerkenswert ist, dass die beobachteten spektralen Veränderungen im Fall des Bis(merocyanin)-Farbstoffs **7**, welcher aus zwei unterschiedlichen Chromophoren besteht, nicht durch Solvatochromie erklärt werden können. Dies deutet auf eine starke Wechselwirkung der beiden Farbstoffeinheiten hin. Die konzentrationsabhängigen UV/Vis-Spektren beider Bis(merocyanin)-Farbstoffe zeigten bei Verdünnung der Lösungen keine spektralen Veränderungen, was darauf schließen lässt, dass eine intramolekulare Stapelung der π-Systeme vorliegt (Abbildung 1a). Die mittels DFT-Rechnungen erhaltenen geometrieoptimierten Strukturen weisen für beide Bis(merocyanin)-Farbstoffe π-Stapel der beiden Chromophore mit van-der-Waals-Abstand und antiparalleler Orientierung der Grundzustandsdipolmomente auf. Um die angeregten Zustände der Farbstoffstapel zu untersuchen, wurden zeitabhängige DFT-Rechnungen durchgeführt. Die aus diesen

Ergebnissen simulierten Absorptionsspekren waren in Übereinstimmung mit den experimentellen Spektren im unpolaren Lösungsmittel.

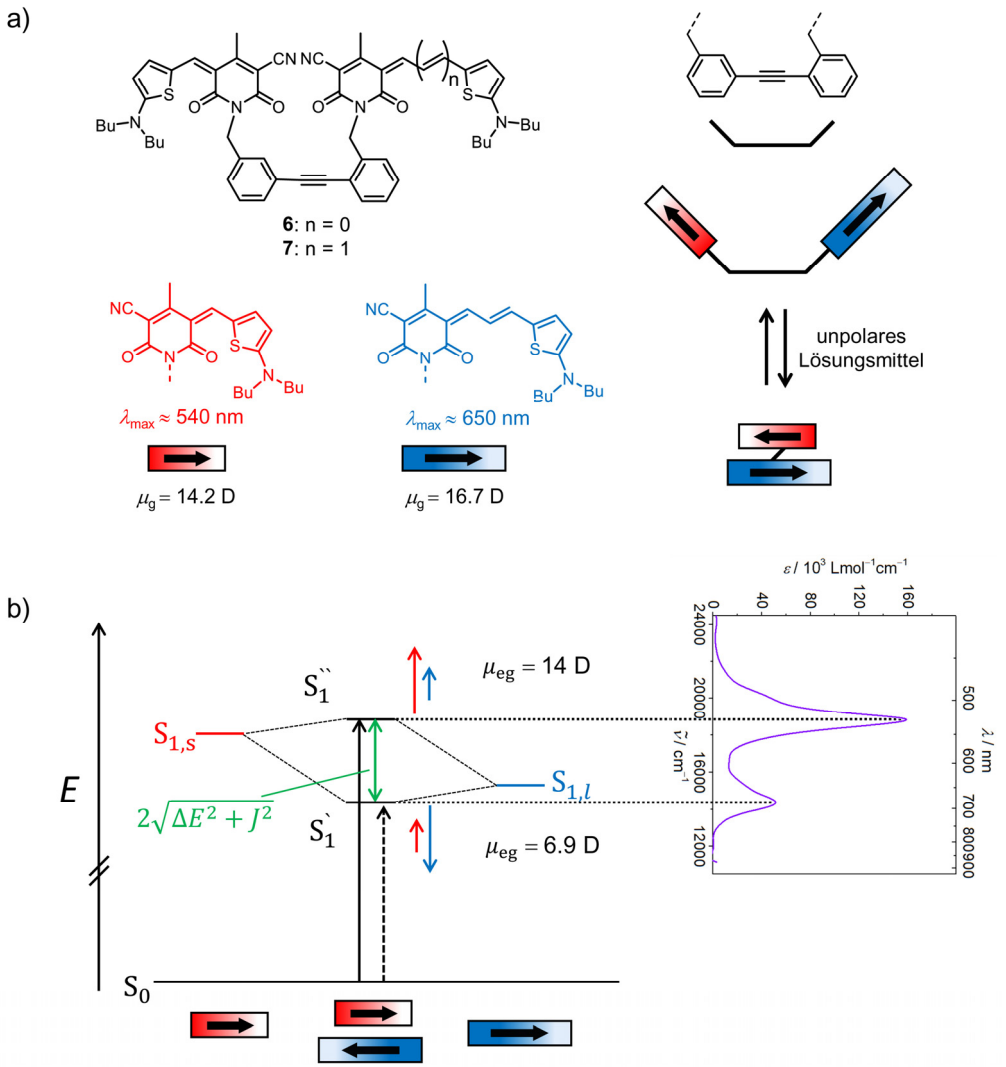

Abbildung 1. a) Chemische Struktur der Bis(merocyanin)-Farbstoffe **6** und **7** und schematische Darstellung des Faltungsprozesses von **7** zum Heterostapel im unpolaren Lösungsmittel. b) Diagramm mit exzitonischen Zuständen für den Heterostapel von **7**. Die Pfeile (rot für den kurzen und blau für den langen Chromophor) deuten die Phasenbeziehung der Übergangsdipolmomente an. Die Länge der Pfeile geben den Betrag der Koeffizienten der Übergangsdipolmomente wieder. $S_{1,s}$ steht für den ersten angeregten Zustand des kurzen Chromophors und $S_{1,l}$ entsprechend für den ersten angeregten Zustand des langen Chromophors, während J die exzitonische Kopplungsenergie repräsentiert. ΔE entspricht der halben Energiedifferenz zwischen den angeregten Zuständen $S_{1,s}$ und $S_{1,l}$. Weiterhin ist das UV/Vis-Spektrum von **7** in DCM/MCH 10:90 (c = 5 x 10^{-6} M) dargestellt.

Außerdem deuteten die erhaltenen Übergangsdichten beider Farbstoffstapel auf eine Kopplung der Übergangsdichten der einzelnen Chromophore in Phase bzw. außer Phase

für den höheren bzw. niedrigeren angeregten Zustand. Daher wurde für beide Farbstoffstapel die Exzitonentheorie angewandt unter der Annahme, dass auch eine exzitonische Kopplung zwischen den unterschiedlichen Chromophoren in Bis(merocyanin) **7** vorliegt. Auf diese Weise konnten die Absorptionseigenschaften des Heterostapels sowohl qualitativ als auch quantitativ erklärt werden (Abbildung 1b). Die mittels der Transition-Charge-Methode berechneten exzitonischen Kopplungsenergien stimmen gut mit den aus den UV/Vis-Daten ermittelten Werten überein. Demnach ist die Kopplung im Hetero-π-Stapel (1824 cm^{-1}) sogar stärker als im Fall des Homo-π-Stapels (1668 cm^{-1}). Somit kann eine starke exzitonische Kopplung nicht nur zwischen gleichen sondern auch zwischen unterschiedlichen Chromophoren vorliegen, die im Fall des Bis(merocyanin)-Farbstoffs **7** die Absorptionseigenschaften des Heterostapels maßgeblich beeinflusst.

Der zweite Teil der vorliegenden Arbeit befasst sich mit der exzitonischen Kopplung in Viererstapeln bestehend aus gleichen sowie unterschiedlichen Merocyaninchromophoren. Aus früheren Arbeiten ist bekannt, dass das symmetrische Bis(merocyanin) **21**, welches zwei gleiche Chromophore beinhaltet, in unpolaren Lösungsmitteln selbstassembliert und auf diese Weise Farbstoffstapel aus vier gleichen Chromophoren gebildet werden (Abbildung 2a). Aus diesem Grund wurde das unsymmetrische Bis(merocyanin) **22** mit zwei unterschiedlichen Chromophoren synthetisiert (Abbildung 2b) und dessen Aggregation mittels konzentrationsabhängiger UV/Vis-Spektroskopie in Chlorbenzol untersucht. Bei Erhöhung der Konzentration waren deutliche spektrale Veränderungen zu beobachten und die Absorptionsdaten konnten mithilfe des Dimer-Modells gefittet werden. Während für das symmetrische Bis(merocyanin) **21** nur eine Dimerstruktur möglich ist, können im Fall des unsymmetrischen Bis(merocyanin)-Farbstoffs **22** theoretisch drei Dimerstrukturen gebildet werden (Abbildung 2b). Die Struktur des Heteroaggregats konnte mittels verschiedener NMR-Techniken aufgeklärt und im Feststoff durch Röntgenstrukturanalyse eindeutig bestätigt werden. Demnach entsteht bei der Aggregation von Bis(merocyanin) **22** ausschließlich die Dimerstruktur, in der sich die beiden langen Chromophore in der Mitte des Stapels befinden, während die kurzen Chromophore im äußeren Bereich des Stapels liegen (Aggregattyp I in Abbildung 2b).

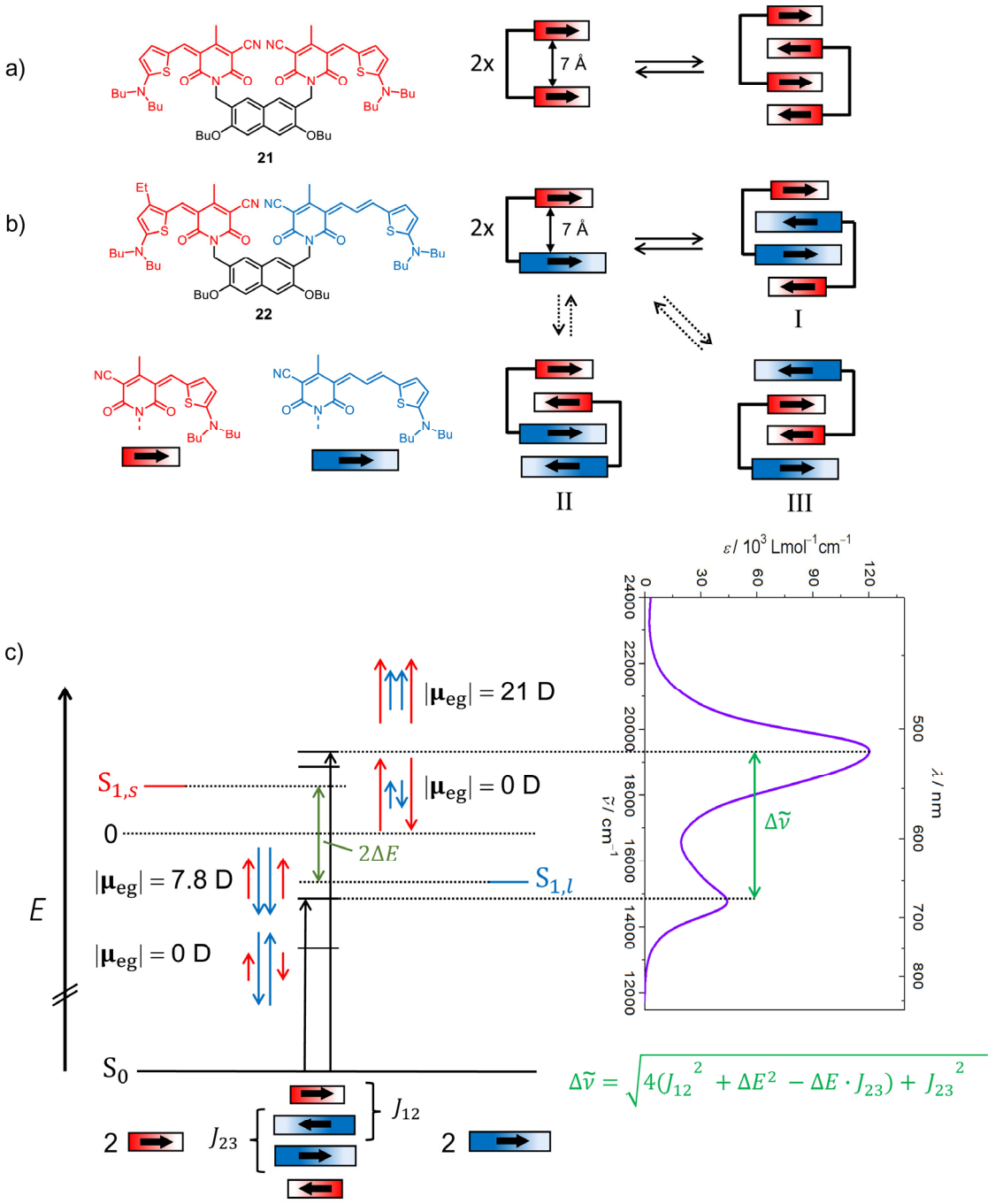

Abbildung 2. a) Chemische Struktur von Bis(merocyanin) **21** mit zwei gleichen Chromophoren und schematische Darstellung der Selbstassemblierung von **21** zum Homoaggregat. b) Chemische Struktur von Bis(merocyanin) **22** mit zwei unterschiedlichen Chromophoren und schematische Darstellung der Selbstassemblierung von **22** zu den drei möglichen Dimerstrukturen. c) Diagramm mit den exzitonischen Zuständen für den Viererstapel von **22**. Die Pfeile (rot für den kurzen und blau für den langen Chromophor) deuten die Phasenbeziehung der Übergangsdipolmomente an. Die Länge der Pfeile geben den Betrag der Koeffizienten der Übergangsdipolmomente wieder. Das aus den konzentrationsabhängigen UV/Vis-Spektroskopiemessungen in Chlorbenzol erhaltene Dimerspektrum ist dargestellt um die erlaubten Übergänge zu verdeutlichen. $S_{1,s}$ steht für den ersten angeregten Zustand des kurzen Chromophors und $S_{1,l}$ entsprechend für den ersten angeregten Zustand des langen Chromophors.

Der Farbstoffstapel weist unerwartete optische Absorptionseigenschaften auf, die sich deutlich von denen der monomeren Chromophore bzw. des Farbstoffstapels von **21** mit vier gleichen Chromophoren unterscheiden. Die auf der Basis von zeitabhängigen DFT-Rechnungen simulierten Absorptionsspektren des Homoaggregats von **21** sowie des Heteroaggregats von **22** waren in Übereinstimmung mit den entsprechenden experimentellen Spektren. Die Absorptionseigenschaften des Heteroaggregats können nicht dadurch erklärt werden, dass eine exzitonische Kopplung lediglich zwischen den gleichen Chromophoren im Stapel vorliegt. Aus diesem Grund wurde die Exzitonentheorie angewandt unter der Annahme, dass eine Kopplung zwischen benachbarten Chromophoren, und zwar auch zwischen unterschiedlichen Chromophoren vorliegt. Das daraus resultierende Diagramm mit den exzitonischen Zuständen stimmt gut mit den Ergebnissen aus den zeitabhängigen DFT-Rechnungen überein (Abbildung 2c). Die mittels Transition-Charge-Methode berechneten exzitonischen Kopplungsenergien deuten sogar auf eine stärkere Kopplung zwischen den unterschiedlichen Chromophoren ($J_{12} = 1861$ cm^{-1}) im Vergleich zur Kopplung zwischen den gleichen Chromophoren ($J_{23} = 1108$ cm^{-1}) im Viererstapel hin.

Anschließend wurde die exzitonische Kopplung zwischen unterschiedlichen Perylenbisimid (PBI)-Farbstoffen analysiert. Dafür wurden die optischen Eigenschaften von Cyclophan **or-CP** untersucht, welches ein am aromatischen Kern unsubstituiertes PBI-Chromophor („orangenes PBI“) sowie ein PBI-Chromophor mit *tert*-Butylphenoxy-Substituenten („rotes PBI“) beinhaltet (Abbildung 3c). Zum Vergleich wurden die PBI-Cyclophane **o2-CP** (Abbildung 3a) and **r2-CP** (Abbildung 3b) mit zwei orangenen bzw. roten PBI-Chromophoren in die Studien aufgenommen.
Alle drei Cyclophane (Abbildung 3d-f, schwarze durchgezogene Linien) weisen im Vergleich zu den jeweiligen monomeren Chromophoren (Abbildung 3d-f, schwarz gepunktete Linien) deutliche Unterschiede in den Absorptionsspektren auf, was auf eine starke Wechselwirkung zwischen den Chromophoren in den Cyclophanen hindeutet. Die mittels DFT-Rechnungen geometrieoptimierten Strukturen zeigen im van-der-Waals-Abstand π-gestapelte PBI-Chromophore mit Rotationsversatz (Abbildung 3a-c). Die Spektren der PBI-Cyclophane sind jedoch wesentlich komplexer als die der π-gestapelten Merocyaninfarbstoffe, was auf vibronische Beiträge zurückzuführen ist. Daher wurden für die PBI-Cyclophane quantendynamische Rechnungen unter Verwendung des Holstein-

Hamiltonoperators durchgeführt, der die optischen Absorptionseigenschaften von Farbstoffaggregaten mit exzitonisch-vibronischer Kopplung richtig beschreibt. Auf diese Weise konnten die Absorptionsspektren aller drei Cyclophane (Abbildung 3d-f, farbige Linien) in guter Übereinstimmung mit den experimentellen Spektren simuliert werden.

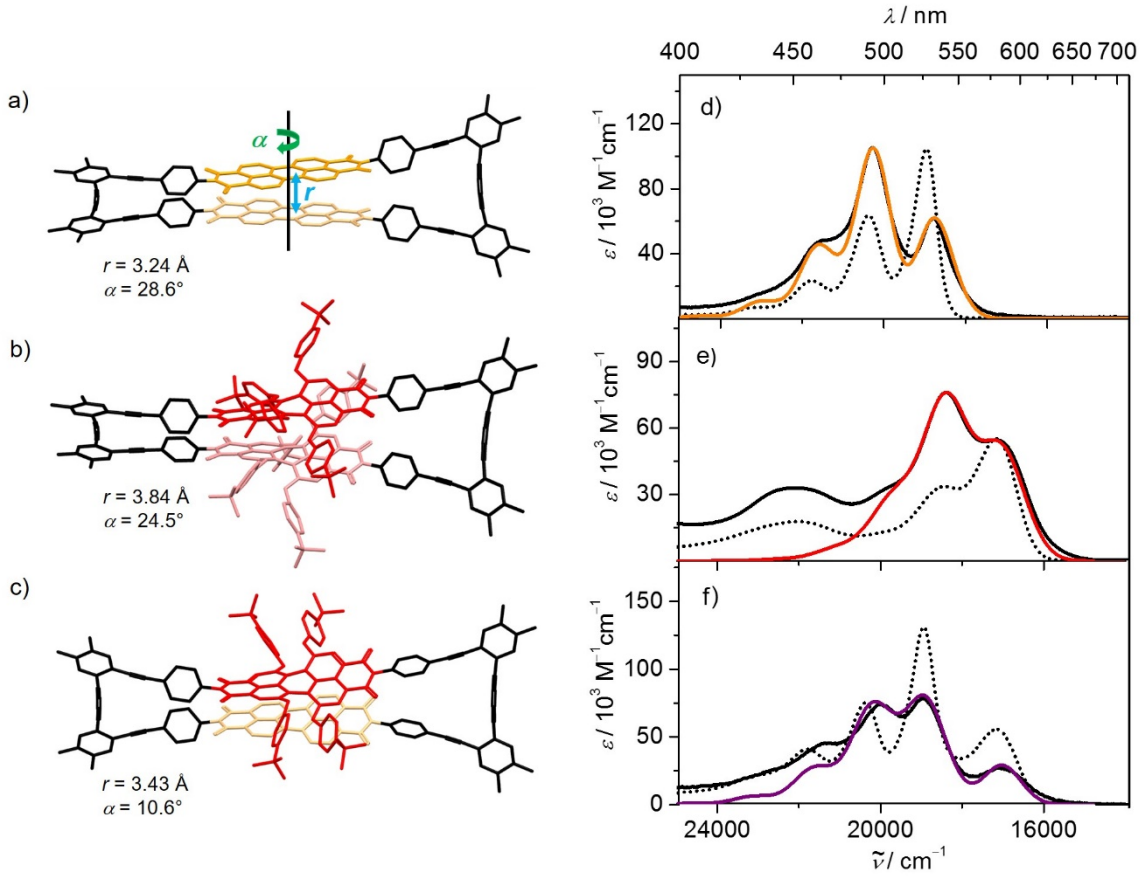

Abbildung 3. Geometrieoptimierte Strukturen der PBI-Cyclophane a) **o2-CP**, b) **r2-CP** und c) **or-CP** (B97D3, def2-SVP, Hexylgruppen wurden durch Methylgruppen ersetzt). Wasserstoffatome sind aus Gründen der besseren Übersicht nicht dargestellt. α steht für den Rotationsversatz und r für den Abstand zwischen den Chromophoren in den entsprechenden Cyclophanen wie in Abbildung 3a dargestellt. UV/Vis-Absorptionsspektren von d) monomerem orangenen PBI-Chromophor (schwarze gepunktete Linie) und Cyclophan **o2-CP** (schwarze durchgezogene Linie), e) monomerem roten PBI Chromophor (schwarze gepunktete Linie) und Cyclophan **r2-CP** (schwarze durchgezogene Linie) sowie f) Summe der Spektren von monomerem roten und orangenen PBI-Chromophor (schwarze gepunktete Linie) und das Spektrum von Cyclophan **or-CP** (schwarze durchgezogene Linie) in Dichlormethan ($c \approx 10^{-5}$ M) bei 298 K. Weiterhin sind die simulierten Absorptionsspektren der entsprechenden Cyclophane (farbige Linien) dargestellt. Die berechneten Spektren sind so normiert, dass jeweils die Intensität der intensivsten Absorptionsbande richtig wiedergegeben wird. Das verwendete Model berücksichtigt nicht den $S_0 \rightarrow S_2$ Übergang bei etwa 22000 cm^{-1} in Abbildung 3e,f.

Die erhaltenen exzitonischen Kopplungsenergien deuten auf eine ähnliche Kopplungsstärke für das Hetero-PBI-Cyclophan **or-CP** (427 cm^{-1}) im Vergleich zu den Kopplungsstärken in den Homo-PBI-Cyclophanen **o2-CP** (613 cm^{-1}) und **r2-CP** (500 cm^{-1}) hin. Die Kopplungsstärke ist vergleichbar mit der Streckmode des PBI-Kerns (≈1400 cm^{-1}), welche die vibronische Progression im Absorptionsspektrum hervorruft. Demnach befinden sich alle drei PBI-Stapel im sogenannten intermediären Kopplungsbereich.
Das wichtigste Ergebnis dieser Studie ist, dass eine exzitonisch-vibronische Kopplung auch im Hetero-PBI-Cyclophan **or-CP** vorliegt, welche die Absorptionseigenschaften des Heterostapels wesentlich beeinflusst.

Im letzten Teil der vorliegenden Arbeit wurde der photoinduzierte Elektronentransfer in wohldefinierten supramolekularen p/n-Heterogrenzflächen untersucht. Dazu wurden die beiden Bis(merocyanin)-C_{60}-Konjugate **32** und **33** (Abbildung 4a,b) synthetisiert, die gleiche bzw. unterschiedliche Chromophore aufweisen. Es wurde erwartet, dass beide Verbindungen eine Selbstassemblierung eingehen, sodass wie im Fall der Bis(merocyanin)-Farbstoffe **21** und **22** (Abbildung 2a,b) Farbstoffstapel aus vier Chromophoren mit den Fullereneinheiten in räumlicher Nähe der Stapel entstehen (Abbildung 4a,b). Nach Lichtanregung sollte ein Elektronentransfer vom Farbstoffstapel auf die Fullereneinheit stattfinden, was ein wichtiger Schritt zur Erzeugung von Ladungsträgern in organischen Solarzellen darstellt. Da das HOMO des Heteroaggregats von Bis(merocyanin) **22** auf den langen Chromophoren lokalisiert ist, sollte die positive Ladung, welche bei der Ladungstrennung entsteht, im Wesentlichen im inneren Bereich des Viererstapels lokalisiert sein. Aus diesem Grund weist das unsymmetrische Bis(merocyanin)-C_{60}-Konjugat **33** im Vergleich zum symmetrischen Bis(merocyanin)-C_{60}-Konjugat **32** nur eine Fullereneinheit auf, sodass der Abstand zwischen dem negativ geladenen Fulleren und der positiven Ladung im Viererstapel vergrößert wird. Auf diese Weise sollte ein langlebiger ladungsgetrennter Zustand realisiert werden.
Die Selbstassemblierung des symmetrischen Bis(merocyanin)-C_{60}-Konjugats **32** wurde mittels konzentrationsabhängiger UV/Vis-Studien untersucht, wobei ein Dimerisierungsprozess beobachtet werden konnte. Die Struktur des Viererstapels konnte mithilfe von 2D NMR-Spektroskopie nachgewiesen werden. Weiterhin ähnelten die Absorptionsspektren der beiden Bis(merocyanin)-C_{60}-Konjugate **32** und **33** in Toluol dem

idealen Dimerspektrum der Bis(merocyanin)-Farbstoffe **21** und **22**, sodass selbst bei niedriger Konzentration von einem fast ausschließlichen Vorliegen der aggregierten Spezies ausgegangen werden kann.

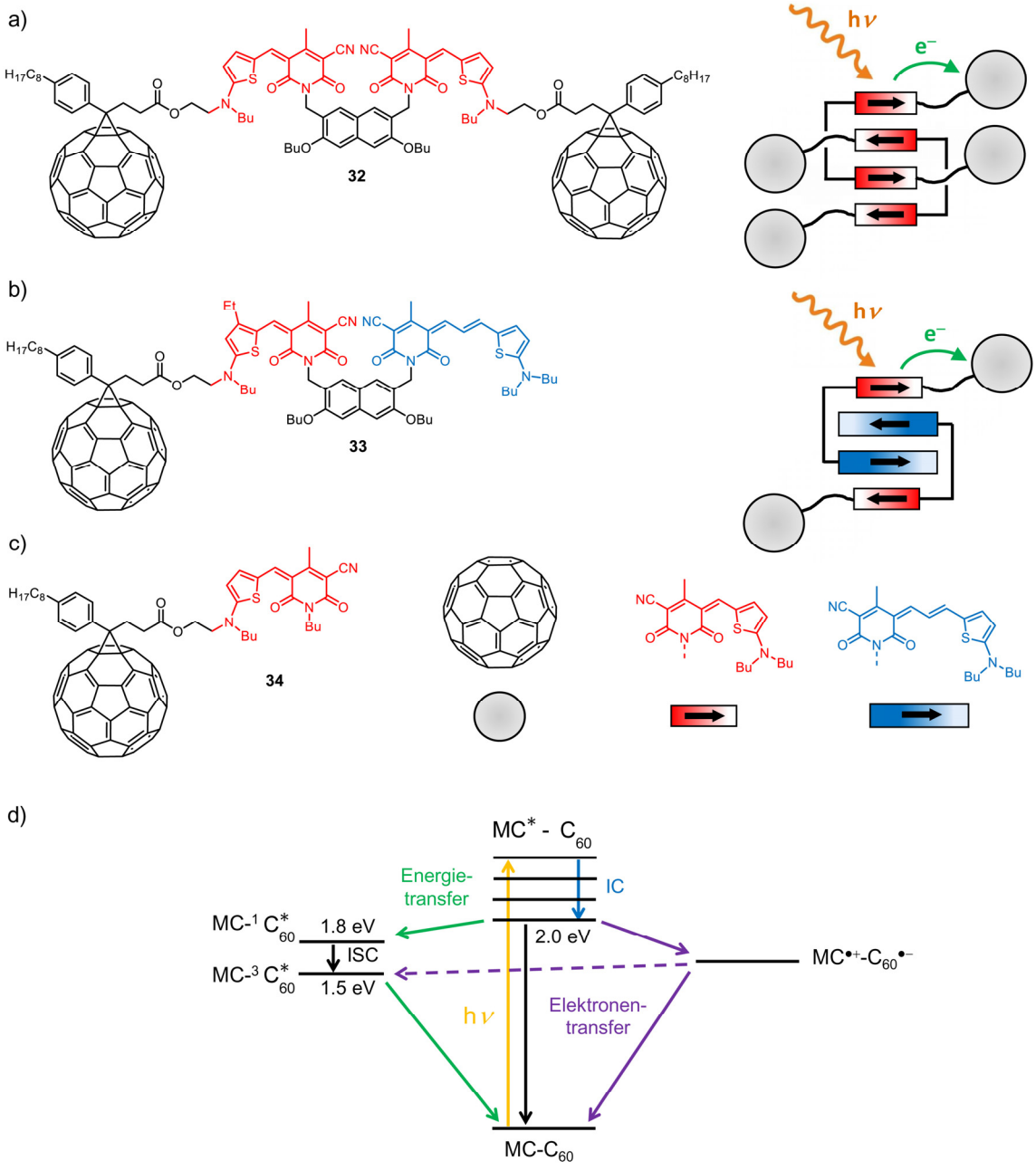

Abbildung 4. Chemische Struktur und schematische Darstellung des Dimeraggregats vom a) symmetrischen Bis(merocyanin)-C_{60}-Konjugat **32** und b) unsymmetrischen Bis(merocyanin)-C_{60}-Konjugat **33**. c) Chemische Struktur von Merocyanin-C_{60}-Konjugat **34**. d) Vermutetes Jablonski-Diagramm für das Dimeraggregat von Bis(merocyanin)-C_{60}-Konjugat **32**, das die vermeintlich konkurrierenden Prozesse des photoinduzierten Elektronen- und Energietransfers zeigt. Dabei ist zu beachten, dass das exakte Energieniveau des ladungsgetrennten Zustands unbekannt ist. MC bezeichnet den Farbstoffstapel aus vier gleichen Chromophoren, während IC und ISC für interne Konversion bzw. Intersystem Crossing steht.

Um den photoinduzierten Elektronentransfer vom Farbstoffstapel auf die Fullereneinheit für beide Bis(merocyanin)-C_{60}-Konjugate zu untersuchen, wurde Femtosekunden-zeitaufgelöste transiente Absorptionsspektroskopie in Toluol durchgeführt. Zum Vergleich erfolgten die Messungen ebenfalls für das neu synthetisierte Merocyanin-C_{60}-Konjugat **34** (Abbildung 4c) und das Dimeraggregat von Bis(merocyanin) **21**. Die transienten Spektren des Bis(merocyanin)-C_{60}-Konjugats **32** deuteten auf eine im Vergleich zum Bis(merocyanin) **21** deutlich schnellere Rückkehr des Farbstoffstapels in den Grundzustand nach Photoanregung hin. Demnach wird durch die Anwesenheit der Fullereneinheiten in **32** ein zusätzlicher Relaxationspfad ermöglicht. In den transienten Absorptionsspektren konnte eine spektrale Signatur beobachtet werden, die dem Fullerenradikalanion zugeordnet werden kann. Dies lässt einen Elektronentransfer vom angeregten Farbstoffstapel auf die Fullereneinheit vermuten (Abbildung 4d). Das Signal klingt auf einer Nanosekunden-Zeitskala ab und deutet auf einen relativ kurzlebigen ladungsgetrennten Zustand von < 7ns hin. Weiterhin konnten in den transienten Absorptionsspektren spektrale Signaturen von angeregtem Singulett- und Triplett-Fulleren beobachtet werden. Dies deutet auf einen zusätzlichen Energietransfer vom Farbstoffstapel auf das Fulleren hin (Abbildung 4d). Allerdings könnte dieses Signal auch durch den Pump-Laserpuls hervorgerufen werden, was durch zusätzliche Messungen an reinem C_{60} geklärt werden muss. Das angeregte Triplett-Fulleren könnte zudem auch durch Ladungsrekombination gebildet werden (Abbildung 4d). Die transienten Spektren von monomerem Merocyanin-C_{60}-Konjugat **34** und aggregiertem Bis(merocyanin)-C_{60}-Konjugat **33** mit zwei unterschiedlichen Chromophoren deuten ebenfalls auf einen ladungsgetrennten Zustand hin. Die Lebensdauer liegt in der gleichen Größenordnung wie für das Bis(merocyanin)-C_{60}-Konjugat **32**, sodass die erwartete deutliche Stabilisierung der positiven Ladung für den oxidierten Farbstoffstapel von **33** nicht beobachtet werden konnte. Ein Grund hierfür könnte die flexible Brückeneinheit zwischen dem Farbstoffstapel und der Fullereneinheit sein, die einen kurzen Abstand zwischen Loch und Elektron im ladungsgetrennten Zustand ermöglicht. Die für beide Bis(merocyanin)-C_{60}-Konjugate beobachtete kurze Lebensdauer des ladungsgetrennten Zustands könnte den mäßigen Wirkungsgrad von organischen Solarzellen auf Basis von Merocyanin-Farbstoffen in Kombination mit Fullerenderivaten erklären.

Zusammenfassend bestätigen die Ergebnisse dieser Arbeit eine starke exzitonische Kopplung zwischen unterschiedlichen Chromophoren. Diese beeinflusst wesentlich die optischen Eigenschaften von Heterofarbstoffaggregaten, wie sie zum Beispiel in Bulk-Heterojunction-Solarzellen vorliegen. Die Erkenntnisse könnten genutzt werden um Heterofarbstoffaggregate mit außergewöhnlichen optischen Absorptionseigenschaften zu realisieren. Die Verwendung unterschiedlicher Chromophore ermöglicht es, einen breiten Spektralbereich abzudecken, was für das Einfangen von Sonnenlicht von großem Vorteil ist. Weiterhin deutet die Anwesenheit der exzitonischen Kopplung auf einen kohärenten Energietransfer und damit auf einen schnellen und effizienten Energietransport zwischen den Chromophoren hin. Basierend auf den in dieser Arbeit gewonnenen Erkenntnisse erscheinen weitere Untersuchungen mittels zweidimensionaler optischer Spektroskopie und quantendynamischer Rechnungen vielversprechend.

References

[1] G. Scheibe, L. Kandler, H. Ecker, *Naturwissenschaften* **1937**, *25*, 75.

[2] G. Scheibe, *Angew. Chem.* **1937**, *50*, 212–219.

[3] E. E. Jelley, *Nature* **1936**, *138*, 1009–1010.

[4] E. E. Jelley, *Nature* **1937**, *139*, 631–632.

[5] A. S. Davydov, *Sov. Phys. Usp.* **1964**, *7*, 145–178.

[6] M. Kasha, *Radiat. Res.* **1963**, *20*, 55–70.

[7] E. G. McRae, M. Kasha, *Physical Processes in Radiation Biology*, Academic Press, N. Y., **1964**.

[8] M. Kasha, H. R. Rawls, M. A. El-Bayoumi, *Pure Appl. Chem.* **1965**, *11*, 371–392.

[9] F. Würthner, T. E. Kaiser, C. R. Saha-Möller, *Angew. Chem. Int. Ed.* **2011**, *50*, 3376–3410.

[10] T. Brixner, J. Stenger, H. M. Vaswani, M. Cho, R. E. Blankenship, G. R. Fleming, *Nature* **2005**, *434*, 625–628.

[11] R. J. Cogdell, A. Gall, J. Köhler, *Q. Rev. Biophys.* **2006**, *39*, 227–324.

[12] D. G. Lidzey, D. D. C. Bradley, M. S. Skolnick, S. Walker, *Synth. Met.* **2001**, *124*, 37–40.

[13] N. J. Hestand, R. V. Kazantsev, A. S. Weingarten, L. C. Palmer, S. I. Stupp, F. C. Spano, *J. Am. Chem. Soc.* **2016**, *138*, 11762–11774.

[14] S. Das, T. L. Thanulingam, K. G. Thomas, P. V. Kamat, M. V. George, *J. Phys. Chem.* **1993**, *97*, 13620–13624.

[15] Y. Kobuke, H. Miyaji, *J. Am. Chem. Soc.* **1994**, *116*, 4111–4112.

[16] M. Kirkus, L. Wang, S. Mothy, D. Beljonne, J. Cornil, R. A. J. Janssen, S. C. J. Meskers, *J. Phys. Chem. A* **2012**, *116*, 7927–7936.

[17] D. M. Eisele, C. W. Cone, E. A. Bloemsma, S. M. Vlaming, C. G. F. van der Kwaak, R. J. Silbey, M. G. Bawendi, J. Knoester, J. P. Rabe, D. A. Vanden Bout, *Nat. Chem.* **2012**, *4*, 655–662.

[18] Y. Wan, A. Stradomska, S. Fong, Z. Guo, R. D. Schaller, G. P. Wiederrecht, J. Knoester, L. Huang, *J. Phys. Chem. C* **2014**, *118*, 24854–24865.

[19] J. Megow, M. I. S. Röhr, M. Schmidt am Busch, T. Renger, R. Mitrić, S. Kirstein, J. P. Rabe, V. May, *Phys. Chem. Chem. Phys.* **2015**, *17*, 6741–6747.

[20] T. Fujii, H. Kashida, H. Asanuma, *Chem. Eur. J.* **2009**, *15*, 10092–10102.

[21] P. Ensslen, Y. Fritz, H.-A. Wagenknecht, *Org. Biomol. Chem.* **2015**, *13*, 487–492.

[22] M. M. Safont-Sempere, G. Fernández, F. Würthner, *Chem. Rev.* **2011**, *111*, 5784–5814.

[23] V. K. Praveen, C. Ranjith, E. Bandini, A. Ajayaghosh, N. Armaroli, *Chem. Soc. Rev.* **2014**, *43*, 4222–4242.

[24] R. Bhosale, J. Míšek, N. Sakai, S. Matile, *Chem. Soc. Rev.* **2010**, *39*, 138–149.

[25] A. Das, S. Ghosh, *Angew. Chem. Int. Ed.* **2014**, *53*, 2038–2054.

[26] H. Kashida, N. Higashiyama, T. Kato, H. Asanuma, *Bioorg. Med. Chem.* **2013**, *21*, 6191–6197.

[27] C. B. Winiger, S. M. Langenegger, G. Calzaferri, R. Häner, *Angew. Chem. Int. Ed.* **2015**, *54*, 3643–3647.

[28] K. Broch, U. Heinemeyer, A. Hinderhofer, F. Anger, R. Scholz, A. Gerlach, F. Schreiber, *Phys. Rev. B* **2011**, *83*, 245307.

[29] J. P. Reinhardt, A. Hinderhofer, K. Broch, U. Heinemeyer, S. Kowarik, A. Vorobiev, A. Gerlach, F. Schreiber, *J. Phys. Chem. C* **2012**, *116*, 10917–10923.

[30] S. F. Völker, A. Schmiedel, M. Holzapfel, K. Renziehausen, V. Engel, C. Lambert, *J. Phys. Chem. C* **2014**, *118*, 17467–17482.

[31] F. J. M. Hoeben, P. Jonkheijm, E. W. Meijer, A. P. H. J. Schenning, *Chem. Rev.* **2005**, *105*, 1491–1546.

[32] R. F. Fink, J. Seibt, V. Engel, M. Renz, M. Kaupp, S. Lochbrunner, H.-M. Zhao, J. Pfister, F. Würthner, B. Engels, *J. Am. Chem. Soc.* **2008**, *130*, 12858–12859.

[33] F. Würthner, *Pure Appl. Chem.* **2006**, *78*, 2341-2349.

[34] F. Würthner, *Acc. Chem. Res.* **2016**, *49*, 868–876.

[35] A. Zitzler-Kunkel, E. Kirchner, D. Bialas, C. Simon, F. Würthner, *Chem. Eur. J.* **2015**, *21*, 14851–14861.

[36] X. Zhan, A. Facchetti, S. Barlow, T. J. Marks, M. A. Ratner, M. R. Wasielewski, S. R. Marder, *Adv. Mater.* **2011**, *23*, 268–284.

[37] Z. Liu, G. Zhang, Z. Cai, X. Chen, H. Luo, Y. Li, J. Wang, D. Zhang, *Adv. Mater.* **2014**, *26*, 6965–6977.

[38] Y. Zhong, M. T. Trinh, R. Chen, G. E. Purdum, P. P. Khlyabich, M. Sezen, S. Oh, H. Zhu, B. Fowler, B. Zhang, W. Wang, C.-Y. Nam, M. Y. Sfeir, C. T. Black, M.

L. Steigerwald, Y.-L. Loo, F. Ng, X.-Y. Zhu, C. Nuckolls, *Nat. Commun.* **2015**, *6*, 8242.

[39] D. Meng, D. Sun, C. Zhong, T. Liu, B. Fan, L. Huo, Y. Li, W. Jiang, H. Choi, T. Kim, J. Y. Kim, Y. Sun, Z. Wang, A. J. Heeger, *J. Am. Chem. Soc.* **2016**, *138*, 375−380.

[40] J. Seibt, P. Marquetand, V. Engel, Z. Chen, V. Dehm, F. Würthner, *Chem. Phys.* **2006**, *328*, 354−362.

[41] J. Seibt, T. Winkler, K. Renziehausen, V. Dehm, F. Würthner, H.-D. Meyer, V. Engel, *J. Phys. Chem. A* **2009**, *113*, 13475−13482.

[42] R. A. J. Janssen, J. Nelson, *Adv. Mater.* **2013**, *25*, 1847−1858.

[43] J. Frenkel, *Phys. Rev.* **1931**, *37*, 17−44.

[44] M. Born, R. Oppenheimer, *Ann. Phys.* **1927**, *389*, 457−484.

[45] M. Ponder, R. Mathies, *J. Phys. Chem.* **1983**, *87*, 5090−5098.

[46] S. Ferdous, J. B. Lagowski, *J. Polym. Sci. Part B Polym. Phys.* **2007**, *45*, 1983−1995.

[47] B. Lasio, L. Malfatti, P. Innocenzi, *J. Photochem. Photobiol. A Chem.* **2013**, *271*, 93−98.

[48] S. Choi, J. Bouffard, Y. Kim, *Chem. Sci.* **2014**, *5*, 751−755.

[49] J. Gierschner, M. Ehni, H.-J. Egelhaaf, B. Milián Medina, D. Beljonne, H. Benmansour, G. C. Bazan, *J. Chem. Phys.* **2005**, *123*, 144914.

[50] X.-F. Zhang, Q. Xi, J. Zhao, *J. Mater. Chem.* **2010**, *20*, 6726−6733.

[51] L. Antonov, G. Gergov, V. Petrov, M. Kubista, J. Nygren, *Talanta* **1999**, *49*, 99-106.

[52] U. Rösch, S. Yao, R. Wortmann, F. Würthner, *Angew. Chem. Int. Ed.* **2006**, *45*, 7026−7030.

[53] D. Beljonne, J. Cornil, R. Silbey, P. Millié, J. L. Brédas, *J. Chem. Phys.* **2000**, *112*, 4749−4758.

[54] V. Czikklely, H. D. Försterling, H. Kuhn, *Chem. Phys. Lett.* **1970**, *6*, 207-210.

[55] J. C. Chang, *J. Chem. Phys.* **1977**, *67*, 3901−3909.

[56] C. Weiss, *J. Mol. Spectrosc.* **1972**, *44*, 37−80.

[57] K. A. Kistler, F. C. Spano, S. Matsika, *J. Phys. Chem. B* **2013**, *117*, 2032−2044.

[58] M. E. Madjet, A. Abdurahman, T. Renger, *J. Phys. Chem. B* **2006**, *110*, 17268–17281.

[59] R. L. Fulton, M. Gouterman, *J. Chem. Phys.* **1964**, *41*, 2280–2286.

[60] F. C. Spano, *Acc. Chem. Res.* **2010**, *43*, 429–439.

[61] E. J. Heller, *Acc. Chem. Res.* **1981**, *14*, 368–375.

[62] Z. Chen, V. Stepanenko, V. Dehm, P. Prins, L. D. A. Siebbeles, J. Seibt, P. Marquetand, V. Engel, F. Würthner, *Chem. Eur. J.* **2007**, *13*, 436–449.

[63] M. R. Philpott, *J. Chem. Phys.* **1971**, *55*, 2039–2054.

[64] F. C. Spano, *J. Chem. Phys.* **2002**, *116*, 5877–5891.

[65] F. C. Spano, *J. Chem. Phys.* **2005**, *122*, 234701.

[66] F. C. Spano, *J. Chem. Phys.* **2007**, *126*, 159901.

[67] F. C. Spano, *Chem. Phys.* **2006**, *325*, 22–35.

[68] F. C. Spano, *J. Chem. Phys.* **2003**, *118*, 981–994.

[69] K. Murata, S.-i. Kuroda, K. Saito, *Thin Solid Films* **1997**, *295*, 73–76.

[70] B. Z. Packard, D. D. Toptygin, A. Komoriya, L. Brand, *J. Phys. Chem. B* **1998**, *102*, 752–758.

[71] R. A. Garoff, E. A. Litzinger, R. E. Connor, I. Fishman, B. A. Armitage, *Langmuir* **2002**, *18*, 6330–6337.

[72] S. Bernacchi, E. Piémont, N. Potier, A. v. Dorsselaer, Y. Mély, *Biophys. J.* **2003**, *84*, 643–654.

[73] A. Yamaguchi, N. Kometani, Y. Yonezawa, *Thin Solid Films* **2006**, *513*, 125–135.

[74] I. V. Astakhova, V. A. Korshun, J. Wengel, *Chem. Eur. J.* **2008**, *14*, 11010–11026.

[75] Y. N. Teo, J. N. Wilson, E. T. Kool, *J. Am. Chem. Soc.* **2009**, *131*, 3923–3933.

[76] V. Czikkely, G. Dreizler, H. D. Försterling, H. Kuhn, J. Sondermann, P. Tillmann, J. Wiegand, *Z. Naturforsch. A* **1969**, *24*, 1821–1830.

[77] C. Lambert, T. Scherpf, H. Ceymann, A. Schmiedel, M. Holzapfel, *J. Am. Chem. Soc.* **2015**, *137*, 3547–3557.

[78] F. Bloch, *Z. Phys.* **1929**, *52*, 555–600.

[79] G. H. Wannier, *Phys. Rev.* **1937**, *52*, 191–197.

[80] M. Born, T. v. Kármán, *Physik. Zeits.* **1912**, *13*, 297–309.

[81] S. F. Völker, T. Dellermann, H. Ceymann, M. Holzapfel, C. Lambert, *J. Polym. Sci. A Polym. Chem.* **2014**, *52*, 890–911.

[82] E. W. Knapp, *Chem. Phys.* **1984**, *85*, 73–82.

[83] J. Knoester, *Proc. Int. Sch. Phys. "Enrico Fermi"* **2002**, *149*, 149–186.

[84] P. B. Walczak, A. Eisfeld, J. S. Briggs, *J. Chem. Phys.* **2008**, *128*, 044505.

[85] J. A. Leegwater, *J. Phys. Chem.* **1996**, *100*, 14403–14409.

[86] A. Ojala, H. Bürckstümmer, M. Stolte, R. Sens, H. Reichelt, P. Erk, J. Hwang, D. Hertel, K. Meerholz, F. Würthner, *Adv. Mater.* **2011**, *23*, 5398–5403.

[87] T. Katoh, Y. Inagaki, R. Okazaki, *J. Am. Chem. Soc.* **1998**, *120*, 3623–3628.

[88] L. Lu, R. J. Lachicotte, T. L. Penner, J. Perlstein, D. G. Whitten, *J. Am. Chem. Soc.* **1999**, *121*, 8146–8156.

[89] A. Zitzler-Kunkel, M. R. Lenze, K. Meerholz, F. Würthner, *Chem. Sci.* **2013**, *4*, 2071–2075.

[90] E. Kirchner, Master thesis, (Würzburg), **2013**.

[91] A. Varela-Fernández, J. A. Varela, C. Saá, *Adv. Synth. Catal.* **2011**, *353*, 1933–1937.

[92] D. Prim, G. Kirsch, J.-F. Nicoud, *Synlett* **1998**, *4*, 383–384.

[93] H. Bürckstümmer, E. V. Tulyakova, M. Deppisch, M. R. Lenze, N. M. Kronenberg, M. Gsänger, M. Stolte, K. Meerholz, F. Würthner, *Angew. Chem. Int. Ed.* **2011**, *50*, 11628–11632.

[94] A. Zitzler-Kunkel, M. R. Lenze, N. M. Kronenberg, A.-M. Krause, M. Stolte, K. Meerholz, F. Würthner, *Chem. Mater.* **2014**, *26*, 4856–4866.

[95] F. Würthner, S. Yao, T. Debaerdemaeker, R. Wortmann, *J. Am. Chem. Soc.* **2002**, *124*, 9431–9447.

[96] V. G. Machado, R. I. Stock, C. Reichardt, *Chem. Rev.* **2014**, *114*, 10429–10475.

[97] F. Effenberger, F. Würthner, *Angew. Chem. Int. Ed. Engl.* **1993**, *32*, 719-721.

[98] F. Würthner, G. Archetti, R. Schmidt, H.-G. Kuball, *Angew. Chem. Int. Ed.* **2008**, *47*, 4529–4532.

[99] S. Grimme, J. Antony, S. Ehrlich, H. Krieg, *J. Chem. Phys.* **2010**, *132*, 154104.

[100] F. Weigend, R. Ahlrichs, *Phys. Chem. Chem. Phys.* **2005**, *7*, 3297–3305.

[101] J.-D. Chai, M. Head-Gordon, *J. Chem. Phys.* **2008**, *128*, 084106.

[102] T. Lu, F. Chen, *J. Comput. Chem.* **2012**, *33*, 580–592.

[103] Gaussian 09, Revision D.01, M. J. Frisch, G. W. Trucks, H. B. Schlegel, G. E. Scuseria, M. A. Robb, J. R. Cheeseman, G. Scalmani, V. Barone, B. Mennucci, G.

A. Petersson, H. Nakatsuji, M. Caricato, X. Li, H. P. Hratchian, A. F. Izmaylov, J. Bloino, G. Zheng, J. L. Sonnenberg, M. Hada, M. Ehara, K. Toyota, R. Fukuda, J. Hasegawa, M. Ishida, T. Nakajima, Y. Honda, O. Kitao, H. Nakai, T. Vreven, J. A. Montgomery Jr., J. E. Peralta, F. Ogliaro, M. J. Bearpark, J. Heyd, E. N. Brothers, K. N. Kudin, V. N. Staroverov, R. Kobayashi, J. Normand, K. Raghavachari, A. P. Rendell, J. C. Burant, S. S. Iyengar, J. Tomasi, M. Cossi, N. Rega, N. J. Millam, M. Klene, J. E. Knox, J. B. Cross, V. Bakken, C. Adamo, J. Jaramillo, R. Gomperts, R. E. Stratmann, O. Yazyev, A. J. Austin, R. Cammi, C. Pomelli, J. W. Ochterski, R. L. Martin, K. Morokuma, V. G. Zakrzewski, G. A. Voth, P. Salvador, J. J. Dannenberg, S. Dapprich, A. D. Daniels, Ö. Farkas, J. B. Foresman, J. V. Ortiz, J. Cioslowski, D. J. Fox, Gaussian, Inc., Wallingford, CT, USA, **2009**.

[104] E. A. Cobar, R. Z. Khaliullin, R. G. Bergman, M. Head-Gordon, *Proc. Natl. Acad. Sci.* **2007**, *104*, 6963–6968.

[105] GaussView, Version 5, R. Dennington, T. Keith, J. Millam, *Semichem Inc.*, Shawnee Mission, KS, **2009**.

[106] A. Zitzler-Kunkel, PhD thesis, (Würzburg), **2014**.

[107] A. Lohr, M. Grüne, F. Würthner, *Chem. Eur. J.* **2009**, *15*, 3691–3705.

[108] M. R. Detty, D. S. Hays, *Heterocycles* **1995**, *40*, 925–937.

[109] H. Günther, *NMR Spectroscopy. Basic Principles, Concepts, and Applications in Chemistry*, 3rd ed., WILEY-VCH, Weinheim, **2013**.

[110] G. M. Sheldrick, *Acta Crystallogr. Sect. A* **2008**, *64*, 112–122.

[111] D. Bialas, E. Kirchner, F. Würthner, *Chem. Commun.* **2016**, *52*, 3777–3780.

[112] D. Bialas, A. Zitzler-Kunkel, E. Kirchner, D. Schmidt, F. Würthner, *Nat. Commun.* **2016**, *7*, 12949.

[113] W. Herbst, K. Hunger, *Industrial Organic Pigments: Production, Properties, Applications*, 2nd ed., WILEY-VCH, Weinheim, **1997**.

[114] F. Würthner, *Chem. Commun.* **2004**, 1564–1579.

[115] C. Huang, S. Barlow, S. R. Marder, *J. Org. Chem.* **2011**, *76*, 2386–2407.

[116] F. Würthner, C. R. Saha-Möller, B. Fimmel, S. Ogi, P. Leowanawat, D. Schmidt, *Chem. Rev.* **2016**, *116*, 962–1052.

[117] S. Yagai, T. Seki, T. Karatsu, A. Kitamura, F. Würthner, *Angew. Chem. Int. Ed.* **2008**, *47*, 3367–3371.

[118] H. Yoo, J. Yang, A. Yousef, M. R. Wasielewski, D. Kim, *J. Am Chem. Soc.* **2010**, *132*, 3939–3944.

[119] K. A. Kistler, C. M. Pochas, H. Yamagata, S. Matsika, F. C. Spano, *J. Phys. Chem. B* **2012**, *116*, 77–86.

[120] F. Gao, Y. Zhao, W. Liang, *J. Phys. Chem. B* **2011**, *115*, 2699–2708.

[121] J. Idé, R. Méreau, L. Ducasse, F. Castet, Y. Olivier, N. Martinelli, J. Cornil, D. Beljonne, *J. Phys. Chem. B* **2011**, *115*, 5593–5603.

[122] A. L. Sisson, N. Sakai, N. Banerji, A. Fürstenberg, E. Vauthey, S. Matile, *Angew. Chem. Int. Ed.* **2008**, *47*, 3727–3729.

[123] A. D. Shaller, W. Wang, H. Gan, A. D. Q. Li, *Angew. Chem. Int. Ed.* **2008**, *47*, 7705–7709.

[124] M. Weiser, H.-A. Wagenknecht, *Chem. Commun.* **2015**, *51*, 16530–16533.

[125] D. Veldman, S. M. A. Chopin, S. C. J. Meskers, M. M. Groeneveld, R. M. Williams, R. A. J. Janssen, *J. Phys. Chem. B* **2008**, *112*, 5846–5857.

[126] J. M. Giaimo, A. V. Gusev, M. R. Wasielewski, *J. Am. Chem. Soc.* **2002**, *124*, 8530–8531.

[127] J. Feng, Y. Zhang, C. Zhao, R. Li, W. Xu, X. Li, J. Jiang, *Chem. Eur. J.* **2008**, *14*, 7000–7010.

[128] K. E. Brown, W. A. Salamant, L. E. Shoer, R. M. Young, M. R. Wasielewski, *J. Phys. Chem. Lett.* **2014**, *5*, 2588–2593.

[129] F. Schlosser, PhD thesis, Julius-Maximilians-Universität Würzburg (Würzburg), **2012**.

[130] F. Schlosser, M. Moos, C. Lambert, F. Würthner, *Adv. Mater.* **2013**, *25*, 410–414.

[131] F. Würthner, C. Thalacker, S. Diele, C. Tschierske, *Chem. Eur. J.* **2001**, *7*, 2245–2253.

[132] J. Gershberg, F. Fennel, T. H. Rehm, S. Lochbrunner, F. Würthner, *Chem. Sci.* **2016**, *7*, 1729–1737.

[133] P. Osswald, D. Leusser, D. Stalke, F. Würthner, *Angew. Chem. Int. Ed.* **2005**, *44*, 250–253.

[134] P. Osswald, F. Würthner, *Chem. Eur. J.* **2007**, *13*, 7395–7409.

[135] P. Osswald, F. Würthner, *J. Am. Chem. Soc.* **2007**, *129*, 14319–14326.

[136] E. Fron, G. Schweitzer, P. Osswald, F. Würthner, P. Marsal, D. Beljonne, K. Müllen, F. C. De Schryver, M. Van der Auweraer, *Photochem. Photobiol. Sci.* **2008**, *7*, 1509–1521.

[137] R. Gvishi, R. Reisfeld, Z. Burshtein, *Chem. Phys. Lett.* **1993**, *213*, 338–344.

[138] M. J. Ahrens, M. J. Tauber, M. R. Wasielewski, *J. Org. Chem.* **2006**, *71*, 2107–2114.

[139] P. Leowanawat, A. Nowak-Król, F. Würthner, *Org. Chem. Front.* **2016**, *3*, 537–544.

[140] C. Hippius, I. H. M. van Stokkum, E. Zangrando, R. M. Williams, M. Wykes, D. Beljonne, F. Würthner, *J. Phys. Chem. C* **2008**, *112*, 14626–14638.

[141] T. Holstein, *Ann. Phys.* **1959**, *8*, 325–342.

[142] N. J. Hestand, F. C. Spano, *J. Chem. Phys.* **2015**, *143*, 244707.

[143] C. Brüning, K. Renziehausen, V. Engel, *J. Chem. Phys.* **2013**, *139*, 054303.

[144] L. Huang, M. Stolte, H. Bürckstümmer, F. Würthner, *Adv. Mater.* **2012**, *24*, 5750–5754.

[145] A. Liess, M. Stolte, T. He, F. Würthner, *Mater. Horiz.* **2016**, *3*, 72–77.

[146] N. M. Kronenberg, V. Steinmann, H. Bürckstümmer, J. Hwang, D. Hertel, F. Würthner, K. Meerholz, *Adv. Mater.* **2010**, *22*, 4193–4197.

[147] H. Bürckstümmer, N. M. Kronenberg, M. Gsänger, M. Stolte, K. Meerholz, F. Würthner, *J. Mater. Chem.* **2010**, *20*, 240–243.

[148] V. Steinmann, N. M. Kronenberg, M. R. Lenze, S. M. Graf, D. Hertel, H. Bürckstümmer, F. Würthner, K. Meerholz, *Appl. Phys. Lett.* **2011**, *99*, 193306.

[149] V. Steinmann, N. M. Kronenberg, M. R. Lenze, S. M. Graf, D. Hertel, K. Meerholz, H. Bürckstümmer, E. V. Tulyakova, F. Würthner, *Adv. Energy Mater.* **2011**, *1*, 888–893.

[150] A. Ojala, H. Bürckstümmer, J. Hwang, K. Graf, B. von Vacano, K. Meerholz, P. Erk, F. Würthner, *J. Mater. Chem.* **2012**, *22*, 4473–4482.

[151] F. Würthner, K. Meerholz, *Chem. Eur. J.* **2010**, *16*, 9366–9373.

[152] Y. Lin, Y. Li, X. Zhan, *Chem. Soc. Rev.* **2012**, *41*, 4245–4272.

[153] G. Sauvé, R. Fernando, *J. Phys. Chem. Lett.* **2015**, *6*, 3770–3780.

[154] J. C. Hummelen, B. W. Knight, F. LePeq, F. Wudl, J. Yao, C. L. Wilkins, *J. Org. Chem.* **1995**, *60*, 532–538.

[155] D. Bialas, Master thesis, Julius-Maximilians-Universität Würzburg (Würzburg), **2012**.

[156] A. Verley, *Bull. Soc. Chim. Fr.* **1899**, *21*, 414–418.

[157] O. Doebner, *Chem. Ber.* **1900**, *33*, 2140–2142.

[158] R. V. Bensasson, E. Bienvenüe, C. Fabre, J.-M. Janot, E. J. Land, S. Leach, V. Leboulaire, A. Rassat, S. Roux, P. Seta, *Chem. Eur. J.* **1998**, *4*, 270–278.

[159] K. Kordatos, T. Da Ros, M. Prato, R. V. Bensasson, S. Leach, *Chem. Phys.* **2003**, *293*, 263–280.

[160] N. D. McClenaghan, Z. Grote, K. Darriet, M. Zimine, R. M. Williams, L. De Cola, D. M. Bassani, *Org. Lett.* **2005**, *7*, 807–810.

[161] E. M. Pérez, L. Sánchez, G. Fernández, N. Martín, *J. Am. Chem. Soc.* **2006**, *128*, 7172–7173.

[162] S. Barazzouk, H. Lee, S. Hotchandani, P. V. Kamat, *J. Phys. Chem. B* **2000**, *104*, 3616-3623.

[163] D. A. Steinhurst, A. P. Baronavski, J. C. Owrutsky, *J. Phys. Chem. B* **2002**, *106*, 3160-3165.

[164] S. Verma, A. Ghosh, A. Das, H. N. Ghosh, *J. Phys. Chem. B* **2010**, *114*, 8327–8334.

[165] D. D. Nuzzo, A. Aguirre, M. Shahid, V. S. Gevaerts, S. C. J. Meskers, R. A. J. Janssen, *Adv. Mater.* **2010**, *22*, 4321–4324.

[166] D. M. Guldi, M. Prato, *Acc. Chem. Res.* **2000**, *33*, 695–703.

[167] J. W. Arbogast, A. P. Darmanyan, C. S. Foote, Y. Rubin, F. N. Diederich, M. M. Alvarez, S. J. Anz, R. L. Whetten, *J. Phys. Chem.* **1991**, *95*, 11–12.

[168] H. Isla, B. Grimm, E. M. Pérez, M. Rosario Torres, M. Ángeles Herranz, R. Viruela, J. Aragó, E. Ortí, D. M. Guldi, N. Martín, *Chem. Sci.* **2012**, *3*, 498–508.

[169] P. C. Y. Chow, S. Albert-Seifried, S. Gélinas, R. H. Friend, *Adv. Mater.* **2014**, *26*, 4851–4854.

[170] Y.-X. Liu, M. A. Summers, S. R. Scully, M. D. McGehee, *J. Appl. Phys.* **2006**, *99*, 093521.

[171] M. J. S. Dewar, E. G. Zoebisch, E. F. Healy, J. J. P. Stewart, *J. Am. Chem. Soc.* **1985**, *107*, 3902–3909.

[172] A. Weller, *Z. Phys. Chem.* **1982**, *133*, 93–98.

[173] R. M. Williams, J. M. Zwier, J. W. Verhoeven, *J. Am. Chem. Soc.* **1995**, *117*, 4093–4099.

Danksagung

An dieser Stelle möchte ich mich bei allen Personen bedanken, die mich während der Doktorarbeit unterstützt haben.

Mein besonderer Dank gilt meinem Doktorvater Herrn Prof. Dr. F. Würthner für seine Unterstützung, das entgegengebrachte Vertrauen und die damit verbundene Freiheit im Rahmen der Forschung. Die zahlreichen Diskussionen und die exzellenten Rahmenbedingungen in seiner Arbeitsgruppe haben wesentlich zum Gelingen dieser Arbeit beigetragen. Weiterhin möchte ich mich für seine Unterstützung bei der Bewerbung für ein Chemiefonds-Stipendium bedanken.

Mein weiterer Dank gilt Herrn. Prof. Dr. V. Engel und Herrn. Prof. Dr. C. Lambert für die Zusammenarbeit auf den verschiedenen Projekten und die hilfreichen Diskussionen.

Außerdem möchte ich mich bei der Stiftung des Verbandes der Chemischen Industrie e.V. für die Unterstützung der Doktorarbeit im Rahmen eines Chemiefonds-Stipendiums bedanken.

Herrn Dr. Christoph Brüning danke ich für die Durchführung der zeitabhängigen quantenmechanischen Simulationen. Weiterhin möchte ich mich bei Herrn Alexander Schmiedel für die Messungen der zeitaufgelösten transienten Absorptionsspektren bedanken sowie Frau Dr. Franziska Fennel und Herrn Dr. Marco Holzapfel für die Auswertung und Analyse der Daten.

Für das Korrekturlesen dieser Arbeit möchte ich mich bei Herrn Dr. Chantu Saha-Möller, Frau Dr. Agnieszka Nowak-Król, Herrn Dr. Vincenzo Grande, Frau Dr. Franziska Fennel, Frau Eva Kirchner, Herrn Dr. Matthias Stolte, Herrn Dr. Marco Holzapfel, Herrn Dr. Sven Markert und Frau Agathe Bialas bedanken. Ein großer Dank gilt Herrn Dr. Chantu Saha-Möller für das gründliche Korrekturlesen der Publikationsmanuskripte.

Bei Fragen und Problemen bei quantenmechanischen Rechnungen konnte ich jederzeit auf die Hilfe von Herrn Dr. Michael Winkler, Herrn Dr. Torsten Bruhn und Frau Dr. Merle Röhr zurückgreifen. Dafür ein herzliches Dankeschön!

Herrn Dr. David Schmidt danke ich für das Lösen der Kristallstrukturen. Für die Messungen der NMR-Spektren danke ich Frau Eva Kirchner, Herrn Dr. Matthias Grüne,

Frau Elfriede Ruckdeschel und Frau Patricia Altenbeger. Weiterhin bedanke ich mich bei Herrn Dr. Michael Büchner, Herrn Fritz Dadrich und Frau Juliane Adelmann für die Aufnahme und Analyse der Massenspektren.

Für die zahlreichen fachlichen Diskussionen bedanke ich mich bei Herrn Dr. Matthias Stolte, Frau Dr. Franziska Fennel, Herrn Dr. Florian Beuerle, Frau Dr. Agnieszka Nowak-Król und Frau Eva Kirchner. Herrn Dr. Bartolome Soberats danke ich für die Hilfe und Tipps bei der Erstellung von Graphiken.

Die Hilfsbereitschaft von Herrn Joachim Bialas, Herrn Christian Simon, Herrn Johannes Thein und Frau Jennifer Begall bei Problemen im Laboralltag war nahezu grenzenlos. Dafür ein herzliches Dankeschön.

Außerdem möchte ich mich bei Frau Dr. Agnieszka Nowak-Król, Herrn Reinhard Hecht, Frau Christina Kaufmann und Herrn Christian Simon für die unterhaltsame Atmosphäre im Labor bedanken.

Für die synthetische Unterstützung bedanke ich mich bei Frau Lisa Otter, Herrn Johannes Thein und bei den Bachelorstudenten Herrn Niklas Noll und Frau Anna Hanft sowie bei den Praktikumsstudenten Frau Lena Breitschwerdt, Herrn Kevin Bold und Herrn Marius Wehner.

Der gesamten Arbeitsgruppe Würthner danke ich für das sehr gute Arbeitsklima und die abendlichen Unternehmungen. Der „Lunch Group“ ein großer Dank für das tägliche unterhaltsame Mittagessen!

Von ganzem Herzen möchte ich mich bei meiner Familie und meinen Freunden bedanken, die mich immer unterstützt und das Leben außerhalb des Labors bereichert haben.

List of Publications

Exciton-Vibrational Couplings in Homo- and Heterodimer Stacks of Perylene Bisimde Dyes within Cyclophanes: Studies on Absorption Properties and Theoretical Analysis
D. Bialas, C. Brüning, F. Schlosser, B. Fimmel, J. Thein, V. Engel, F. Würthner, *Chem. Eur. J.* **2016**, *22*, 15011–15018.

Structural and quantum chemical analysis of exciton coupling in homo- and heteroaggregate stacks of merocyanines
D. Bialas, A. Zitzler-Kunkel, E. Kirchner, D. Schmidt, F. Würthner, *Nat. Commun.* **2016**, *7*, 12949.

Folding-induced exciton coupling in homo- and heterodimers of merocyanine dyes
D. Bialas, E. Kirchner, F. Würthner, *Chem. Commun.* **2016**, *52*, 3777–3780.

Organic Semiconductors based on Dyes and Color Pigments
M. Gsänger, D. Bialas, L. Huang, M. Stolte, F. Würthner, *Adv. Mater.* **2016**, *28*, 3615–3645.

Spacer-Modulated Differentiation Between Self-Assembly and Folding Pathways for Bichromophoric Merocyanine Dyes
A. Zitzler-Kunkel, E. Kirchner, D. Bialas, C. Simon, F. Würthner, *Chem. Eur. J.* **2015**, *21*, 14851–14861.

Ambient Stable Zwitterionic Perylene Bisimde-Centered Radical
D. Schmidt, D. Bialas, F. Würthner, *Angew. Chem. Int. Ed.* **2015**, *54*, 3611–3614.

Synthesis and Properties of a New Class of Fully Conjugated Azahexacene Analogues
W. Yue, S.-L. Suraru, D. Bialas, M. Müller, F. Würthner, *Angew. Chem. Int. Ed.* **2014**, *53*, 6159–6162.

Thiophene-functionalized isoindigo dyes bearing electron donor substituents with absorptions approaching the near infrared region

D. Bialas, S.-L. Suraru, R. Schmidt, F. Würthner, *Org. Biomol. Chem.* **2011**, *9*, 6127–6132.

Synthesis and Characterization of Optical and Redox Properties of Bithiophene-Functionalized Diketopyrrolopyrrole Chromophores

H. Bürckstümmer, A. Weissenstein, D. Bialas, F. Würthner, *J. Org. Chem.* **2011**, *76*, 2426–2432.